Metal-Organic Framework Nanosheets:
A New Dimension in Photovoltaics Research

Kezia Sasitharan

170120454

A thesis submitted to the University of Sheffield in partial fulfilment of the requirements for the Degree of Doctor of Philosophy

November 2020

Department of Chemistry, The University of Sheffield

Acknowledgements

I have been very fortunate to have received the University of Sheffield faculty of science doctoral academy scholarship to pursue my PhD in a very supportive environment. I am very grateful to my supervisor **Dr Jona Foster** for supporting my scholarship application and giving me the opportunity to undertake this research work. I particularly thank him for providing direction, advice, feedback, and for facilitating a network of brilliant scientists across departments in Sheffield, that has led to the successful completion of this PhD. I will always appreciate your inputs towards improving the coherence and clarity in my writing. It has been a privilege to work for a supportive supervisor who champions the success of his students. Thank you so much.

I would like to thank **Prof David Lidzey** for making me feel welcome in the electronic and photonic molecular materials group at Sheffield without which I would not have been able to bring together my research. Thank you to **Dr Ahmed Iraqi** and **Dr Jenny Clark** for helping me with interpreting results. I am also grateful to **Prof Graham Leggett** for fulfilling his role as my independent advisor. Your inputs during my confirmation review viva and your kind and supportive feedback were very helpful in building my confidence.

Working within the Foster group has been a great experience. **Dave Ashworth** and **Josh Nicks**, I do not have enough words to express the incredible support you have both been since my first week in the department. You filled my PhD with so much fun and laughter. Thank you, **Mike**, **Freya**, **Millie,** and **Ram**, for creating the most relaxed work environment. The friendly and collaborative nature of everyone in the **EPMM group** made the completion of my work much easier. I am also grateful to **DAAD** for the RISE fellowship that enabled a research visit to **Helmholtz Zentrum Berlin** resulting in a fruitful collaboration with the department of interface design. Thanks to **Prof Marcus Baer** for supporting my application and to **Dr Johannes Frisch** for the continued support and mentorship.

Finally, I thank my family and friends back home in India. Mum, Dad and Kenu, I would not have come close to pursuing a PhD without all the great things you taught me. Aravind, thank you for being my best friend for life.

This PhD has been an incredible journey in finding my area of interest, developing my skills, and establishing my knowledge base, and I really look forward to continuing my research career in low-dimensional materials for solar cells.

Declaration

This research has been performed between the months of October 2017 and September 2020, within the Department of Chemistry at the University of Sheffield, under the supervision of Dr Jonathan Foster

Examiner 1   Prof Graham Leggett, The University of Sheffield

Examiner 2   Prof Jenny Nelson, Imperial College London

Note on the thesis format

This thesis is submitted in an alternative format approved by the University of Sheffield Research Services.

Chapter 4 of this thesis is a published paper which has already been peer-reviewed. To preserve continuity within this thesis, the paper has been typeset in word although the contents are unaltered from the peer-reviewed version. The DOI of the paper has been provided should the reader wish to access the journal's fully typeset PDF version. Chapters 5 and 6 present work which has not yet been published but are intended for submission and therefore presented in the format of a scientific paper. In each case, the experimental work, analysis of data and writing of the manuscript was primarily completed by the author (Kezia Sasitharan).

Abstract

In recent years, metal-organic framework nanosheets (MONs) have emerged as novel two-dimensional materials with enormous potential for use in advanced electronic devices. MONs comprise of organic linkers that are linked with metal ions or clusters in two-dimensions. They are most notable for their high surface area, nanoscopic dimensions, physical flexibility, and diverse chemical functionalities. With their modular design, MONs can be systematically modified through substitution of different ligands and metal ions which allows for systematic tuning of their optoelectronic properties. In this thesis, MONs are explored as potential materials for enhancing the performance of a range of organic photovoltaic (OPV) devices.

Chapter 1 introduces photovoltaics, outlining the background theory of OPVs, their performance mechanism and provides an overview of the progress in ternary OPVs. **Chapter 2** is an introduction to MONs, detailing their structure, synthesis, and applications in electronics. This chapter also covers the aims and objectives of this thesis. **Chapter 3** is the experimental methods chapter,

In **Chapter 4**, $Zn_2(ZnTCPP)$ MONs (where TCPP = tetracarboxyphenyl porphyrin) were synthesised using liquid exfoliation. The MONs were found to approach monolayer thicknesses and their optoelectronic properties were found to be ideally suited for incorporation into the active layer a polythiophene-fullerene based OPVs. P3HT-MON-PCBM ternary blend bulk heterojunctions were therefore developed. Upon optimisation, the ternary OPV devices were found to outperform the reference devices with the champion MON devices at 5.2% PCE as compared to the references at 2.6%. Detailed mechanistic investigations were carried out to probe their performance enhancement. The incorporation of MONs was found to lead to creation of highly crystalline P3HT domains in the films, which resulted in improved light absorption, higher hole mobility and reduced grain sizes. This work provides the first example of incorporation of MONs into the active layer of an OPV device and demonstrates their potential as additives for enhancing the performance of OPVs.

In **Chapter 5** the effect of different metal ions and ligands on the energy level alignment of MONs was explored. The aim was to identify the key structural and electronic features that should be considered while designing MONs for OPV applications. Upon comparing $Cu_2(CuTCPP)$ and $Cu_2(ZnTPyP)$, (where TCPP = tetracarboxyphenyl porphyrin and TPyP = tetraphenyl porphyrin) as additives in P3HT-PCBM system, the device performance doubled

with Zn$_2$(ZnTCPP), remained unaffected with Cu$_2$(ZnTPyP) and halved with Cu$_2$(CuTCPP). The energy level alignment in different systems was evaluated using photoemission techniques. The choice of metal ions was found to only have a small impact on the ionization energies of the MON and was not sufficient to explain the variations in device performances observed. The size of the nanosheets was found to play a significant role in influencing the device performance. Large sized nanosheets were detrimental to the power conversion efficiencies because they reduce the interface between the donor P3HT and acceptor PCBM. This work identified the key structural and electronic features to be considered while choosing MONs for OPV applications.

In **Chapter 6** the general applicability of MONs to other donor-acceptor OPV systems is investigated. A range of commonly used polymer-fullerene devices were selected ranging from fully amorphous to fully crystalline systems. The addition of MONs to devices based on fully crystalline or amorphous donor polymers showed only small or non-significant improvements in their PCE upon incorporation of MONs. In contrast, the addition of MONs to semi-crystalline polymers showed remarkable improvements in performance. In particular, the PCE of PffBT4T-2OD-PCBM based devices increased from 10.6% to 12.23 % with the inclusion of MONs resulting in the best performing fullerene based OPV reported so far. Detailed mechanistic investigations of these devices showed that MONs promote a higher degree of crystallinity in the films by forcing a more face-on orientation of the polymer chains. This favours the charge transport direction resulting in higher charge mobilities, better light absorption and smaller well-defined grain sizes. This study not only demonstrates the general applicability of MONs as templates for semi-crystalline polymers but also offers important insights towards improving the nanoscale morphology in OPVs.

Overall, this thesis demonstrates the application of MONs in OPVs as additives for improved device performance. In addition to enhancing absorption and acting as electron donors within OPV devices, MONs can act as templates that improve the morphology of semi-crystalline polymers resulting in significant improvements in performance. Matching the energy levels of the MONs to the OPV devices and optimising exfoliation to ensure monolayer nanosheets are used are key to designing MONs for thin-film OPV applications. With their tuneable properties and nanoscopic dimensions, MONs therefore have significant potential to enhance the performance of a wide range of organic electronic devices.

List of publications

Published manuscript

1. Metal-organic framework nanosheets for enhanced performance of organic photovoltaic cells

   Kezia Sasitharan, David G. Bossanyi, Naoum Vaenas, Andrew Parnell, Jenny Clark, Ahmed Iraqi, David G. Lidzey and Jonathan A. Foster

   J. Mater. Chem. A, 2020, 8**, 6067-6075**
   DOI: 10.1039/C9TA12313J.

Manuscript in preparation

1. Investigating the energy levels and active layer morphology in metal-organic framework nanosheets based organic photovoltaic cells
   Kezia Sasitharan, Johannes Frisch, Ahmed Iraqi, David G Lidzey, Marcus Baer, Jonathan A Foster

2. Metal-organic framework nanosheets enabling 12.3% efficiency in organic photovoltaics.
   Kezia Sasitharan, Rachel Kilbride, Emma Spooner, Ahmed Iraqi, Jenny Clark, David G. Lidzey and Jonathan A Foster

3. Metal-organic framework nanosheets (MONs): programmable two-dimensional materials for catalysis, sensing, electronics, and separation applications.
   Joshua Nicks, **Kezia Sasitharan**, Ram RR Prasad. David J Ashworth, Jonathan A Foster

4. Continuous room temperature synthesis of ultrathin metal-organic framework nanosheets for enhancing the performance of organic photovoltaic cells.
   David J Ashworth, Justin Driver, **Kezia Sasitharan**, Ram RR Prasad, Joshua Nicks, Siddharth V. Patwardhan and Jonathan A. Foster

List of conference presentations

Oral presentations

July 2020	'Two-dimensional metal-organic nanosheets: band gap tunable materials for new generation solar cells', Nanophotonics of 2D materials, (moved online, because of COVID-19)
June 2020	'Metal-organic nanosheets – a new dimension in PV research', SuperGen Supersolar ECR webinar.
Feb 2020	'Two-dimensional framework nanosheets for Organic Photovoltaics' IUPAC Global Women's breakfast – Sheffield Women in Science, **Best talk prize**, Sheffield, UK
Jan 2020	'Enhanced performance of bulk heterojunction solar cells by metal-organic nanosheets' RSC Next Generation Materials for Solar Photovoltaics, Burlington House, London, UK
Dec 2019	'Ultrathin metal-organic nanosheets for improved performance of OPVs 2nd Joint UK Solar Fuels Network-SuperSolar workshop on Solar Energy Conversion and Storage, Imperial College, London, UK
Sep 2019	Metal-organic nanosheets: A new dimension in solar cell research **Best Oral presentation prize** 5th International Fall School on Organic Electronics- 2019, Moscow, Russia
Jul 2019	'Two-dimensional nanomaterials for solar cells' DAAD Rise Professional Meeting 2019, Heidelberg, Germany
Apr 2019	'Metal-organic nanosheets for enhanced performance of bulk heterojunction solar cells' Flash presentation, RSC Sir Geoffrey Wilkinson Dalton symposium 2019, London, UK

Poster presentations

Sep 2019	**Kezia Sasitharan**, Ahmed Iraqi, David G Lidzey, Jonathan A. Foster, 'Metal-organic nanosheets: A new dimension in solar cell research' Advances in photovoltaics 2019, Institute of Physics, London, UK
Apr 2019	**Kezia Sasitharan**, Ahmed Iraqi, David G Lidzey, Jonathan A. Foster, 'Metal-organic nanosheets for enhanced performance of bulk heterojunction solar

cells', RSC Sir Geoffrey Wilkinson Dalton Poster Symposium, Burlington House, London, UK

Apr 2019   **Kezia Sasitharan**, Ahmed Iraqi, David G Lidzey, Jonathan A. Foster, 'Two-dimensional nanomaterials in Organic solar cells', 9th Chemical Nanoscience Symposium, Newcastle, UK

Mar 2019   **Kezia Sasitharan**, Ahmed Iraqi, David G Lidzey, Jonathan A. Foster, 'Metal-organic nanosheets: A new dimension in solar cell research', Faculty of Science Graduate School Showcase, Sheffield, UK

Sep 2018   **Kezia Sasitharan**, Ahmed Iraqi, David G Lidzey, Jonathan A. Foster, 'Metal-organic nanosheets: a new dimension in photovoltaics', Advances in photovoltaics, Loughborough, UK

Contents

COMMON ABBREVIATIONS

1D	One dimensional
2D	two dimensional
3D	three dimensional
AFM	atomic force microscopy
AM	Air-mass
ATR	attenuated total reflectance
BHJ	bulk heterojunction
CP	coordination polymer
CV	cyclic voltammetry
COF	covalent organic framework
CSD	Cambridge structural database
DFT	density functional theory
DMF	N,N-dimethylformamide
EEL	electron extraction layer
FF	fill-factor
FTIR	fourier-transform infrared
GIWAXS	grazing incidence wide angle X-ray scattering
HIB	hole injection barrier
HTM	hole transport material
MOF	metal-organic framework
MON	metal-organic framework nanosheets
MS	mass spectrometry
NFA	non-fullerene acceptors
NMP	N-methyl-2-pyrrolidone
NMR	nuclear magnetic resonance
NREL	National renewable energy laboratory
OLED	Organic light emitting diode
OPV	Organic photovoltaics
PL	photoluminescence
PV	Photovoltaics

PW   paddle-wheel

SBU   secondary building unit

SCLC   space-charge limited current

SD   standard deviation

TCPP   tetrakis(4-carboxy-phenyl) porphyrin

TEM   transmission electron microscopy

TGA   thermogravimetric analysis

TMD   transition metal dichalcogenide

UPS   Ultraviolet photoelectron spectroscopy

UV-Vis   ultraviolet-visible

Chapter 1

Introduction and Background Theory
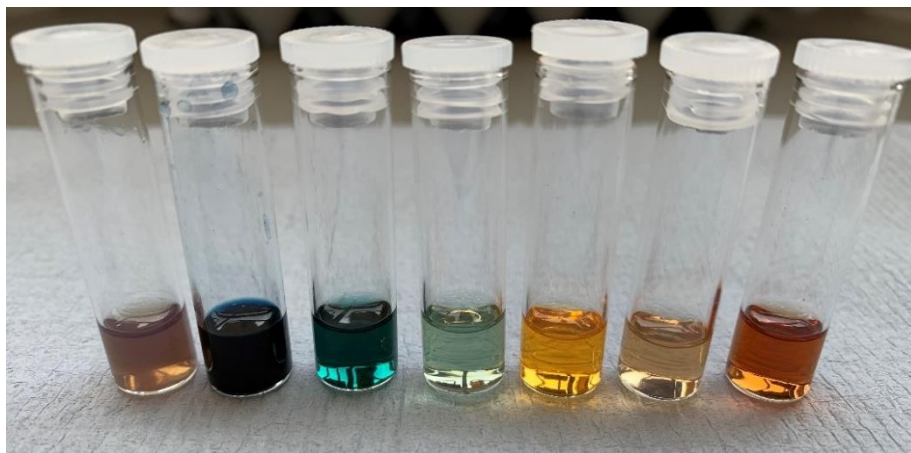
1.0 Introduction

Climate change cannot be ignored or refuted. It is true that Earth's climate has undergone changes throughout history, with several cycles of glacial advance and retreat, attributed to variations in earth's orbit that alter the amount of solar energy received by the earth.[1] The current warming trend however is significant because evidence shows that it is a result of human activity since mid-20th century.[2] This trend continues to proceed at an unprecedented rate as evidenced by global temperature rise, warming oceans, shrinking ice sheets, glacial retreat, decreased snow cover, sea level rise, declining arctic sea ice and ocean acidification.[3] The Intergovernmental Panel on Climate Change (IPCC) states that we are on track to reach 1.5 °C of global warming above pre-industrial levels, and a co-ordinated global effort to minimize CO_2 emissions to net zero by 2055 alone can enable avoidance of potentially irreversible environmental damage.[4]

1.1 Introduction to Photovoltaics

Solar power has the potential to be one of the fastest growing sources of renewable energy to tackle problems of climate change whilst also meeting the growing energy demands of the world. The average solar flux striking the earth's surface is 174.7 W/m^2.[5] The theoretical potential of solar power (the integral of the average flux over the earth's surface area) is 89,300 terawatts (TW) which represents more solar energy striking the earth's surface than the annual consumption from all sources combined (157,481 TWh, equivalent to about 18 TW).[6] Evidently this reservoir of solar energy shadows all other renewable resources but there are limitations in that solar irradiance depends on time of the day, shading, and seasonal changes. However, in combination with advanced energy storage systems, solar power can provide up to 20 TW years annual global energy consumption.[7]

Solar cells (also known as photovoltaic devices) convert light into electrical energy. The earliest demonstration of solar power conversion dates to 1839 when Antoine-Cesar Becquerel successfully showed the production of voltage in a chemical battery upon exposure to sunlight.[8] The next important discovery in this field is credited to Willoughby Smith who reported the photosensitivity of the element selenium in the year 1873.[9] This was followed by Charles Fritts's invention of gold coated selenium for photovoltaic conversion in the 1880s.[10] Advanced research in diodes and transistors eventually paved the way for Bell scientists Gordon Pearson, Darryl Chapin and Cal Fuller to develop the first-generation solid-state silicon solar cell with 4% power conversion efficiency.[11] The underlying physical concepts that are essential to understand the PV effect are explained in this chapter. This technology from Bell labs later became the basis for commercial solar panels.

Silicon: the benchmark PV technology

Silicon solar cells have increased in efficiency to 26% since the 1970s and currently commercial panels are rated at 20% efficiency for 25 years (with 0.5% decrease in efficiency per year).[12–14] Since Si is an indirect band gap semiconductor and not a very good absorber of light, the cells must be made around 100 µm thick to effectively absorb the incident light, unless light scattering/trapping mechanisms are used.[15–17] Silicon wafers also require high temperature processing and purification, resulting in expensive manufacturing and very long energy payback times.[18–22]

Advent of thin-film PV structures

Competing with these traditional silicon module materials is the thin-film light absorbing semiconductor research community where simpler processing and low temperatures are expected to give shorter payback times.[23] Even though decades of research has not yet resulted in any technology capable of displacing silicon PV, there are a few good candidates occupying upto 5% of the PV market share. Cadmium telluride (CdTe) is a direct band gap (1.5 eV) thin film compound semiconductor which is 100 times more absorbing than Silicon. It can be used as a polycrystalline thin film fabricated by close space sublimation, radio frequency sputtering or metal-organic chemical vapour deposition.[24] CdTe grain boundaries are highly complex as chemical composition will depend on deposition method, deposition conditions, post-growth treatment and contacting. CdTe modules exhibit a light conversion efficiency of about 18.6%.[25] However, the environmental concerns related to limited supply of tellurium and the toxic impact of cadmium release at the stage of panel disposal are the major limitations of this technology. CIGS (II-III-VI chalcopyrite materials i.e. $CuInGa(Se)_2$, $CuInGaS_2$) and CZTS (Kesterite structures (Cu_2ZnSnS_4; $Cu_2ZnSnSe_4$) based solar cells are other inorganic direct band gap materials that span the useable solar spectral region and have absorption coefficients typically greater than 10^5 cm^{-2}.[26,27]

Emerging PV technologies

Dye-sensitized solar cells in which a dye sensitizer with a broad absorption band is covalently linked to a semiconductor (nanocrystalline TiO_2) emerged as the first alternative competitor to inorganic PV.[28] The key step involves interfacial electron transfer following selective excitation of a surface-bound molecular chromophore. The excited dye electrons are injected onto the semiconductor layer and diffuse through the network of the sintered particles, permeate through an electrolyte solution containing a redox couple and are gathered at the transparent conducting oxide electrode.[29–32] The dye molecules are regenerated through reduction. This proved to be a cost-effective PV technology with good performance even under low lighting conditions. The main disadvantages however are low current efficiency, degradation of the dye upon exposure to UV rays, limited lifetime, temperature stability issues associated with the liquid electrolyte.[33]

A big surprise in the solar cell community was the perovskite sensitised solar cell developed in 2006, based on a metal-organic hybrid semiconductor within a nanoporous TiO_2 layer with 2.2% power conversion efficiency.[34,35] The metal-organic material used was $CH_3NH_3PbBr_3$ perovskite, an ABX_3 type structure where A is an organic cation, B is a big inorganic cation and X is an anion. The research on perovskites has exploded in the last decade with the world-record perovskite solar cell at the time of writing demonstrating a record efficiency of 25.2% and a perovskite/silicon tandem solar cell showing an impressive efficiency of 29.1%.[36] The stability of these devices over operational lifetime is still under investigation and the use of lead is a major issue with alternative structures that are as efficient yet to be discovered.[36–42]
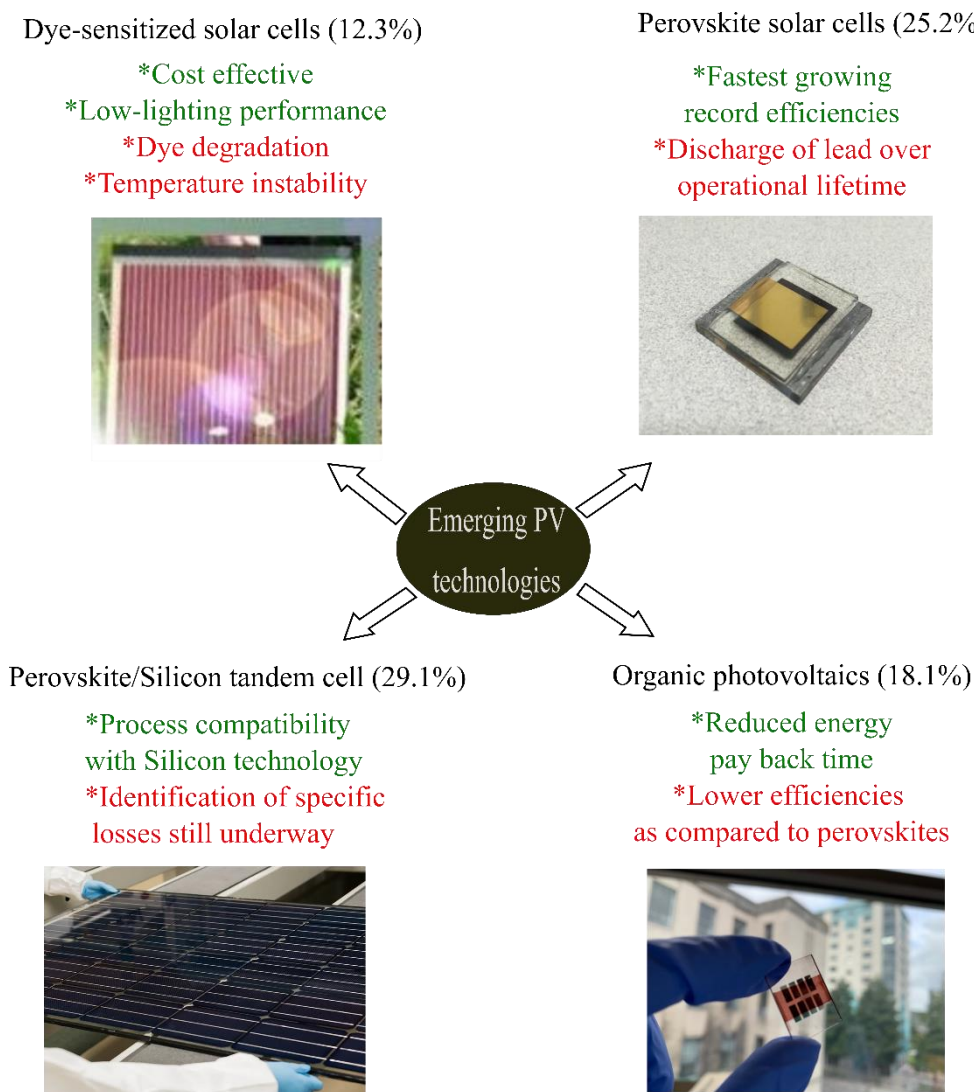

Figure 1.1. An overview of the emerging photovoltaic technologies listing the record efficiencies, key advantages, and challenges

1.2 Introducing Organic Photovoltaics

A class of PV cells with active layer comprised of organic-only components was discovered as early as 1906 with the investigations of photoelectric behaviour in Anthracene.[43] However, it was not until 1986 that Tang et al made significant contribution towards device performance by employing a planar junction of two organic materials each with different ionization potential and electron affinity.[44] Organic semiconductors are materials having a delocalized π-electron system that absorb sunlight and create photogenerated charge carriers (excitons). Conjugated electrons in the organic materials can be easily polarised. This gives rise to large absorption coefficients as compared to inorganic materials, leading to the use of thinner absorption layer thus decreasing the cost of the PV technology.[45]

Use of organic polymers with tuneable electronic properties as active layers in thin film photovoltaics has emerged as a promising technology that opens the direction towards flexible, lightweight devices.[46] Because of the negligibly low intrinsic charge carrier density of these organic polymers, a large electric field is required for extraction of charges which can be achieved by maintaining a lower film thickness of ~200 nm (F=V/d). Spin coating, doctor blading, screen printing, inkjet printing etc are the common approaches used for casting these blends into films. The ultra-thin layers of OPVs are favourable as they can be easily scaled up to large area devices and flexible cells can be created using roll-to-roll processing techniques.

This opens a new avenue of applications in foldable electronics, integrated devices into fabrics and enabling charging on the go. The record efficiency from OPVs currently stands at 18%, a significant improvement in the last 20 years, but still short of the ~25% PCE of perovskite and silicon technologies.[47,48] However, the fact that they can be processed quickly and cheaply from solutions offers other exciting opportunities. The expected reduction in production costs and energy payback time can easily offset the lower efficiency and OPVs may well represent the future of flexible electronics.

1.3 Design and Operation of Organic Photovoltaic Devices

Organic photovoltaics are prepared on a supporting substrate like glass or plastic typically coated with a conducting material that can act as an electrode. On top of the electrode is the photoactive material, followed by a thin buffer layer and a second electrode (**Figure 1.2**). It is important that one of these electrodes is transparent to facilitate photoexcitation of the

active material(s).[49] The energy conversion process in an organic photovoltaic cell can be grouped into five fundamental steps:[50]
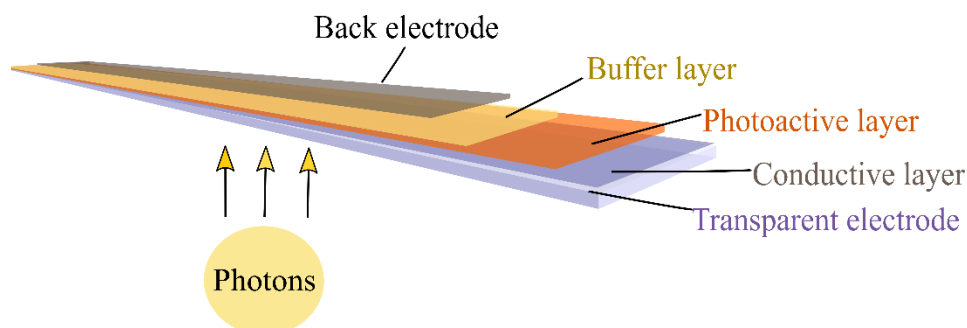
Figure 1.2. General structure and components in an organic photovoltaic device

1.3.1 Light absorption

Photons are absorbed in the photoactive layer resulting in generation of excitons. Organic polymers offer very high absorption coefficients but the absorption bands are relatively narrow thereby limiting the fraction of solar spectrum being absorbed.[51] The desired absorption band of an ideal donor-acceptor blend is 350–826 nm (3.5–1.5 eV), which can lead to 41% of the sun's photons being harnessed. Changing the polymer bandgap is not as straightforward in practice as a lot of other factors need to be managed/optimised such as solubility, film formation, carrier mobility to cumulatively result in enhanced performance. Other strategies to increase light absorption include anti-reflection coatings, engineering optical interference inside the device and introduction of ternary components with complementary absorption.[52–55]

1.3.2 Exciton generation

When photons of energy equal to or larger than the band gap of the photoactive layer are absorbed, an electron-hole pair (known as exciton) is generated. The exciton binding energy in inorganic semiconductors is small enough to be overcome by thermal energy at room temperature. This is due to the large dielectric constant that affects the screening of the coulomb interaction, resulting in delocalized charge carriers, band to band electronic transitions leading to the formation of weakly bound Mott-Wannier type excitons. Organic semiconductors, owing to their structural disorder and low dielectric constants result in the formation of strongly bound

Frenkel-like excitons which are localized and have large binding energies.[55,56] Thus, exciton dissociation cannot take place by thermal energy alone and warrants the need of at least two different materials ('donor' and 'acceptor') with an offset of energy levels with the difference being greater than the exciton binding energy.
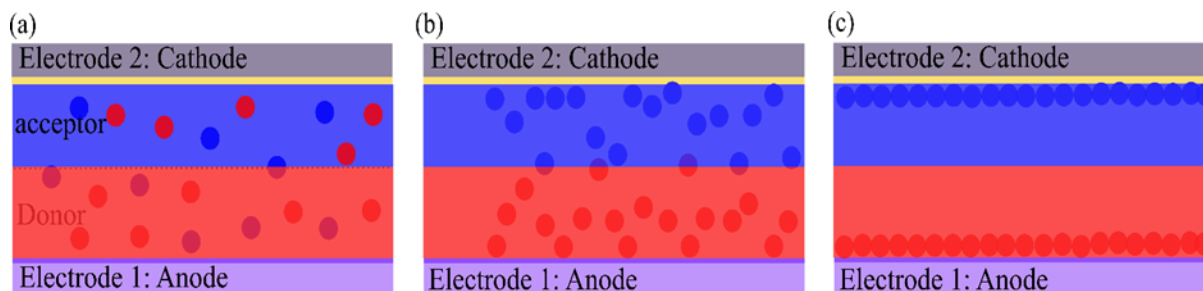
1.3.3 Exciton diffusion

Figure 1.3. A simplified illustration of the (a) exciton diffusion, (b) dissociation and (c) transport in a planar bi-layer OPV, showing the separated charges travelling through the appropriate material towards the electrodes.

Once created, the excitons diffuse through the OPV component to the donor -acceptor interface. The offset between the LUMO levels of the components will drive the exciton dissociation.[57] Exciton diffusion is characterized by the exciton lifetime – the distance that the exciton can diffuse before the excited electron returns to the empty hole (recombination). To ensure that the rate of charge-carrier recombination is not in competition with charge carrier generation, the design of the photoactive layer becomes important. For as long as OPV technology was dominated by bilayer devices, the decreased active donor/acceptor interface led to low performing devices because of competing recombination rates (**Figure 1.3**). In 1995, several independent groups demonstrated the making of donor-acceptor blends (bulk heterojunctions) by dissolving a hole conducting polymer with an electron acceptor in a common solvent. The difference in electron affinities between the blended materials creates the driving force for splitting of the photogenerated excitons.[57–61] The typical exciton diffusion length is 10 nm in organics. This bulk-heterojunction approach enables a uniform distribution of the donor-acceptor interface throughout the device making it likely for all excitons to find an interface within the diffusion length limit and split before recombining (**Figure 1.4**).
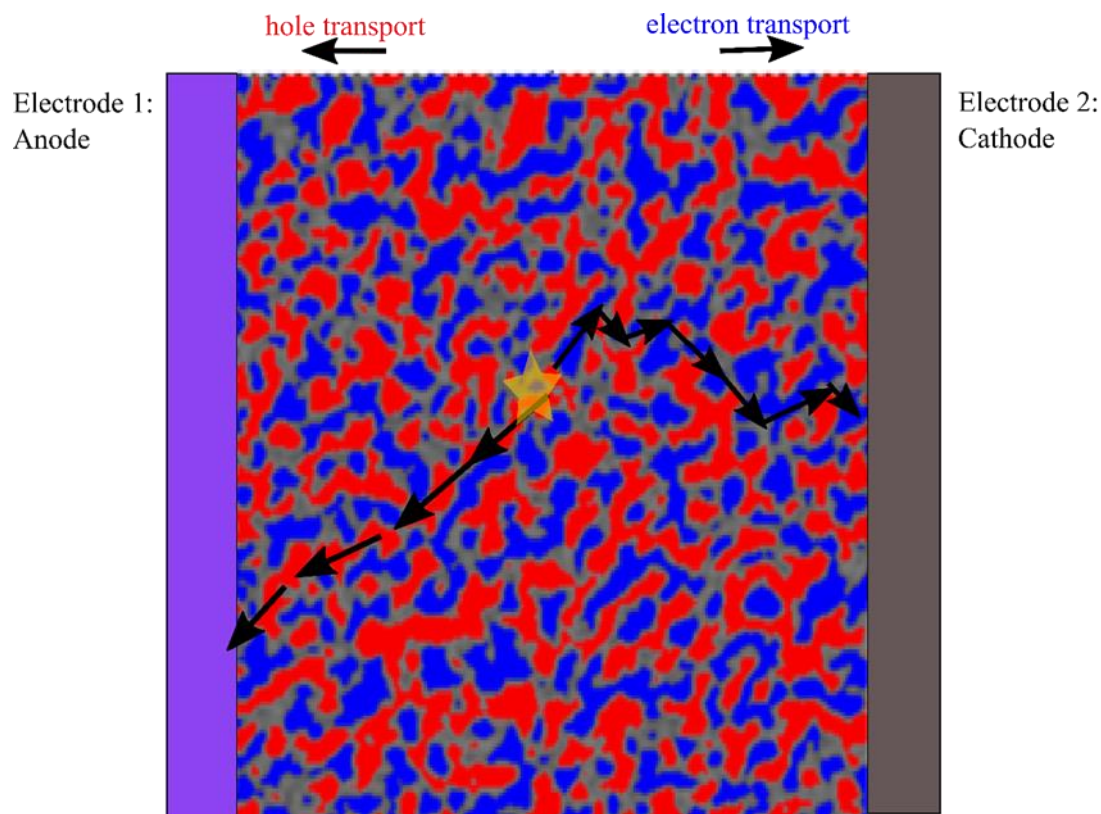
1.3.4 Exciton dissociation

Figure 1.4. A bulk heterojunction photoactive layer showing a uniform distribution of the donor-acceptor interfaces throughout the device

Once at the donor-acceptor interface the electron will move to the acceptor material and the hole will remain on the donor material. These charges form a charge-transfer state (they will still be attracted) and are known as geminate pairs. The word geminate denotes that the electron and the hole are the product of the same photoexcitation process that took place in the preceding step(s). As the distance between the charges increases across the bulk heterojunction, the binding energy of the geminate pair reduces and is eventually overcome by thermal energy resulting in the formation of a charge-separated state.[56,62]

1.3.5 Charge-carrier transport

The work-function difference in the electrodes 1 and 2 creates a built-in electric field in the organic layer. This leads to the charge carriers either diffusing or drifting towards their respective electrodes. For a pure bulk-heterojunction, with the donor and acceptor interfaces

distributed randomly, the drift component dominates.[63] Charge-carriers are prone to getting trapped in the tail states of density of states or in deeper-lying trap states (structural defects can result in the formation of energy states in the gap between the HOMO and LUMO) which leads to slower charge transport. At this stage, the free charge carriers can also encounter each other again and undergo non-geminate recombination (recombination of free electrons and holes across the interface, regardless of their source). It is imperative that the charges be collected before the non-geminate encounter.

1.3.6 Charge carrier-extraction

This is the final step where the charge-carriers from the photoactive layer are collected at the electrodes. Buffer layers such as a hole-blocking layer or an electron blocking layer are added between the photoactive layer and the electrode to prevent the extraction of the wrong carrier type. These layers facilitate a favourable energy level positioning to promote the extraction of the right of type of charge carrier at the respective electrode.[64]

1.4 Characterising Solar Cells

A PV device placed in the dark behaves like a diode. The nature of a simple PV device can thus be modelled by the Shockley ideal photodiode equation (**Equation 1.1**) and the solar cell equivalent circuit (**Figure 1.5a**).

$$J_D(V) = J_{dark}\left[\exp\left(\frac{eV}{k_BT}\right) - 1\right] \qquad \textbf{Equation 1.1}$$

Where.

J_D = the current through the diode;

e = the electron charge;

V= the diode voltage;

k_B= Boltzmann constant;

T= Absolute temperature of the diode.

Minority carriers can drift (in dark) across the device to produce a very small but measurable current J_{dark} (the dark saturated current).[65]

1.4.1 Current-voltage measurements

Current-voltage sweeps are used to determine the device performance metrics of a solar cell. A current-voltage curve can be thought of as a superposition of the solar cell diode in the dark under illumination. Upon illumination, the solar cell produces charge carriers through the absorption of photons in the active layer, which upon dissociation and transport give rise to a photocurrent in the direction opposite to that of the dark current.[65,66]

Upon illumination the solar cell diode equation 1 becomes,

$$J(V) = J_D - J_{SC} = J_{dark}\left[\exp\left(\frac{eV}{k_B T}\right) - 1\right] - J_{SC} \qquad \textbf{Equation 1.2}$$

1.4.2 Short circuit current density (J_{SC})

J_{SC} (written as the current per unit area i.e., mA cm^{-2}) can be defined as the photocurrent density provided by the solar cell when there is no applied voltage. Photocurrent being proportional to the incoming photons, is higher for photoactive layers with a small band gap. In OPVs, Jsc can be reduced by unwanted geminate and non-geminate charge recombination pathways. The primary way to increase J_{SC} is to enhance the light absorption of the photoactive layer and to find the best-fit charge extraction layers for a particular donor-acceptor combination.[67–73] Photocurrent is given a negative value to distinguish it from the current produced by the cell under forward bias (V>0V). As the forward bias voltage increases, it starts compensating for the reverse photocurrent produced by the incident light and at an applied voltage the current produced by the cell raises to zero.

1.4.3 Open circuit voltage (V_{OC})

When the current produced by the illuminating cell is zero, the forward bias fully compensates for the reverse photocurrent, hence the applied bias at that value is considered the open circuit voltage, V_{OC}. Typically, this is the voltage provided by the solar cell when there is no current flowing. In the context of OPVs, V_{OC} is dependent on the energy levels of the donor-acceptor, work function of the electrodes and charge carrier recombination rate.[74–76]

1.4.4 Fill Factor (FF)

The fill factor is the ratio of the actual power of the cell to what it's power would be if there were no series resistance and infinite shunt resistance. This is ideally as close as possible to 1, and can be calculated using the following equation:

$$FF = J_{MP}V_{MP}/J_{SC}V_{OC} \qquad \textbf{Equation 1.3}$$

Here, J_{MP}, V_{MP} are the current density and voltage of the cell at maximum power, respectively. A good solar cell has a high FF and this performance metric should always be maximized during fabrication optimisation. High fill factors of upto 80% are achievable but reliant on obtaining low series and shunt resistance.[77–81]

1.4.5 Power conversion efficiency (PCE)

The power conversion efficiency is a percentage of the power that a solar cell can generate relative to the power that is incident onto the solar cell. PCE is calculated from the ratio of powers, where the power of the incident light is P_{in} and the P_{MP} is calculated from the product of V_{MP} and current J_{MP} (refer **Figure 1.5c**). PCE is governed by all other important device metrics described above (Jsc, Voc, FF) and the parameters governing those metrics.

$$PCE = \frac{P_{out}}{P_{in}} = \frac{P_{MP}}{P_{in}} = \frac{V_{MP}J_{MP}}{P_{in}} = V_{OC}J_{SC}FF/P_{in} \quad \textbf{Equation 1.4}$$

1.4.6 Shunt resistance (R$_{SH}$)

The Shunt resistance accounts for the existence of alternate current leak pathways through a photovoltaic cell. The shunt resistance is the resistance against current bypassing the photoactive absorbing layer or any charge transport layers employed in a solar cell. Roughness of films and presence of pinholes rising during the film formation process leads to currents that can bypass those incomplete layers resulting in a loss.[82] Shunt resistance lowers the FF and V_{OC} of the device.

1.4.7 Series resistance (R$_S$)

This resistance accounts for all the resistances that arise from energetic barriers at interfaces and bulk resistance within layers – any process that opposes charge extraction from the solar cell. This can be caused by low charge carrier mobilities of the layers, too-thick charge

extraction layers (if the charge carriers have to travel a long distance before being extracted, the tendency of getting trapped or recombining is higher) and non-ideal charge affinity alignment between layers. Large series resistance lowers the FF of the device.[83]

Accounting for the series resistance and shunt resistance in the diode equation transforms Equation 2 as,

$$J(V) = J_{dark}\left[\exp\left(\frac{e(V+JR_S)}{nk_BT}\right) - 1\right] + V + JR_S/R_{SH} - J_{SC} \qquad \textbf{Equation 1.5}$$

Where n is the ideality factor – a dimensionless constant that indicates how close the diode (the working solar under illumination) behaves to that of an ideal diode.
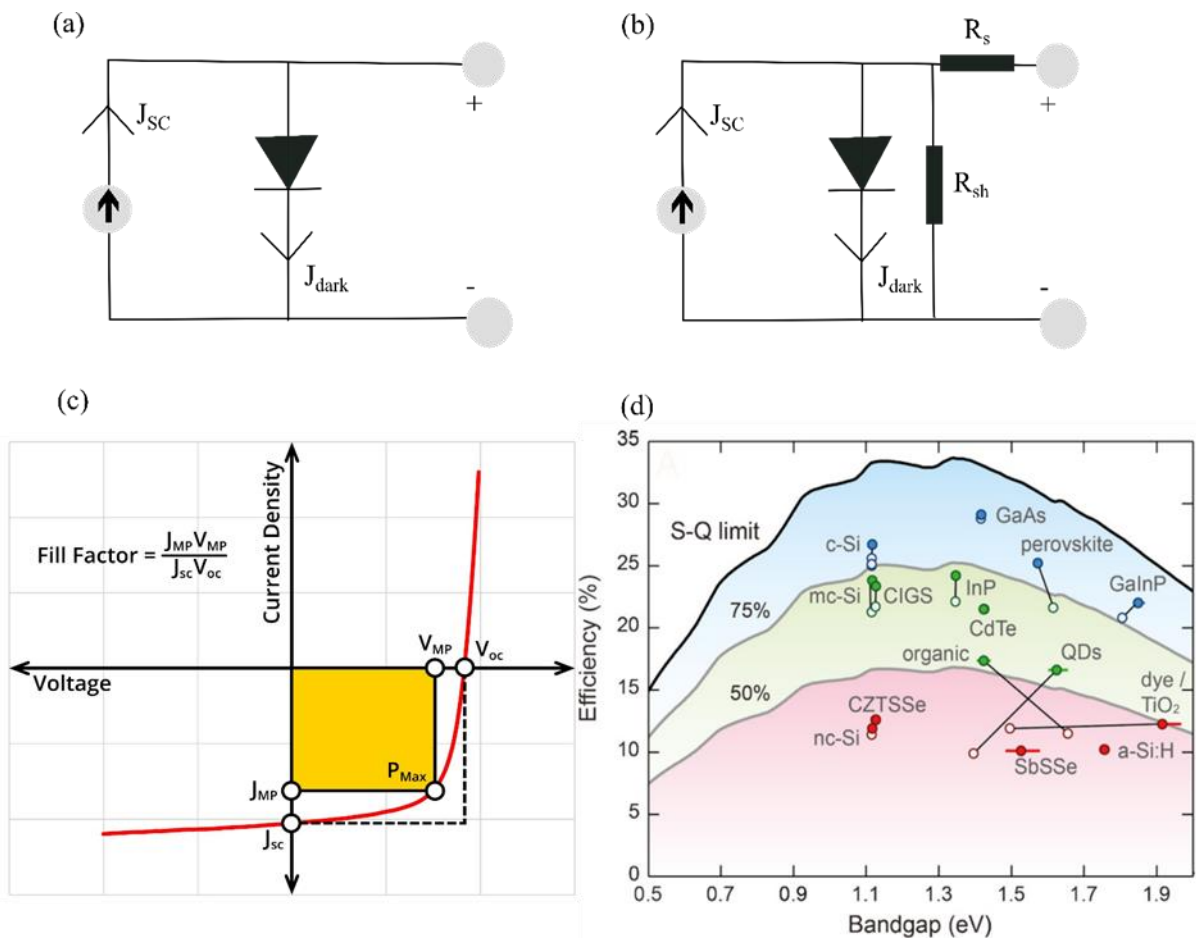

Figure 1.5. (a Equivalent circuit model of an ideal solar cell; (b) Equivalent circuit model of a non-ideal solar cell; (c) Typical IV curve of a solar cell plotted using current density, highlighting the short circuit density (Jsc), open-circuit voltage (Voc), current and voltage at maximum power (Jmp and Vmp respectively), maximum power point (Pmax) and fill factor (FF) (d)Record efficiency of solar cells against their bandgap in comparison to the Shockley-Quiesser limit taken and adapted from ACS Energy Lett. 2020, 5, 9, 3029-3033

1.4.8 Quantum efficiency

The internal quantum efficiency (IQE) is a more traditional indicator of solar cell performance. This is the percentage of the number of photons absorbed by the solar cell relative to the number of photogenerated charges extracted from the solar cell. It characterises all of the processes which suppress charge generation, transport and transfer from the photoactive absorbing layer.[84–86]

The external quantum efficiency (EQE) is a more applicable performance metric to compare solar cells. This is the number of extracted charges relative to the number of incident photons at every specific wavelength. It can be calculated from **equation 1.6** where P(λ) is the incident power of photons as a function of wavelength, (hc/λ) is the energy of one photon, J is the photocurrent and e is the electronic charge.

$$EQE(\lambda) = Jhc/P(\lambda)\lambda e \qquad \textbf{Equation 1.6}$$

EQE takes into account all of the photons that do not reach or are not absorbed by the active layer. In context of thin film OPVs this loss of incident photons is mainly caused by parasitic absorption and reflection occurring from the front facing encapsulation surface and electrodes.[83,87–89]

1.4.9 The Shockley Quiesser Limit

The maximum theoretical efficiency of a single junction solar cell is limited by fundamental physical constraints. This efficiency limit is Shockley-Quiesser limit named after the physicists who initially calculated it in 1961.[90,91] According to these calculations the fundamental causes of losses that can reduce the amount of energy a photovoltaic device can convert into useful electricity are.

a. Spectrum losses: Any photons with energy less than the band of the chosen semiconductor will not be absorbed and therefore all that flux of solar energy is lost. If a semiconductor with a large band gap is chosen, more photons will be absorbed but any photons with energy greater than the band gap will loose that excess energy via thermalization to the band edge.[92]

b. Thermodynamic losses: Any object above zero Kelvin must radiate energy in the form of blackbody radiation, which increases the temperature of the object. As a result of

this fundamental thermodynamic consideration, a percentage of solar flux on the device is lost as heat, and this loss increases with the rise in operating temperature of the solar cell.[9394]

Shockley and Quiesser determined the best theoretical power conversion efficiency for a given band gap (shown in **Figure 1.5d**, along with the record efficiencies obtained so far). A real solar cell however, will never have perfect absorption and will never fully reach the Shockley-Quiesser Limit.[90,91,93]
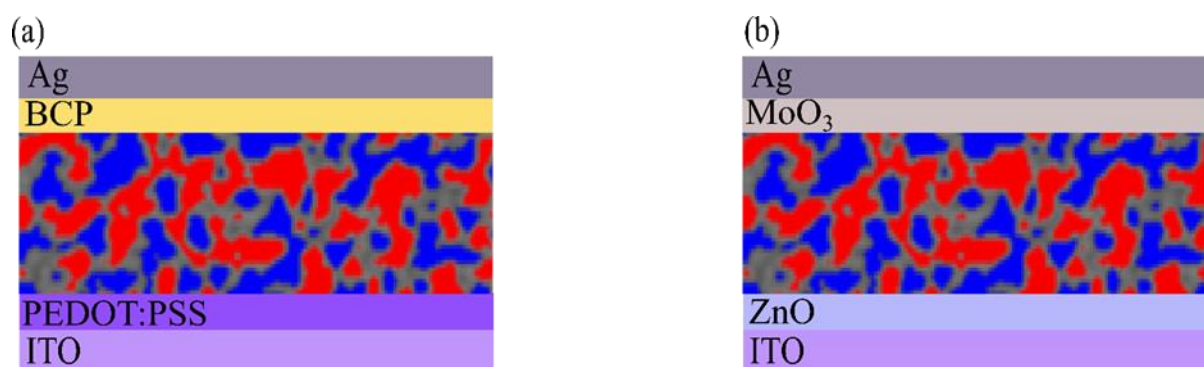
1.5 Device architectures

Figure 1.6. An illustration of (a) Conventional OPV stack and (b) Inverted OPV stack

Modern OPV research consists of solution processed bulk-heterojunctions where the architecture can be conventional or inverted (**Figure 1.6**) depending on the orientation of the electrodes. Planar bilayer junctions are also studied but where the intention is to illustrate specific interactions between materials and not performance enhancement. This thesis consists of all of the above-mentioned device architectures fabricated onto Indium Tin Oxide coated glass substrates (the transparent conducting electrode).

The conventional OPV devices employ poly(3,4-ethylenedioxythiophene) polystyrene sulfonate (PEDOT:PSS) as the interfacial layer. PEDOT:PSS is the benchmark material for lowering the barrier for hole injection. PEDOT is an electrochemically stable conjugated polymer system, which when oxidised and doped with PSS displays high electrical conductivity and maintains moderate transparency making it the ideal hole transport material for OPVs and OLEDs for well over a decade.[95,96] The acidity of the PSS chain is known to cause degradation in the devices and a number of neutral analogues and alternatives have been explored like graphene oxide, transition metal dichalcogenides, metal sulphides, Spiro-

OMeTAD, etc. But the easy orthogonal processing and compatibility in reducing the surface roughness when coating on top of ITO makes PEDOT:PSS the go-to hole transport material.[97,98]
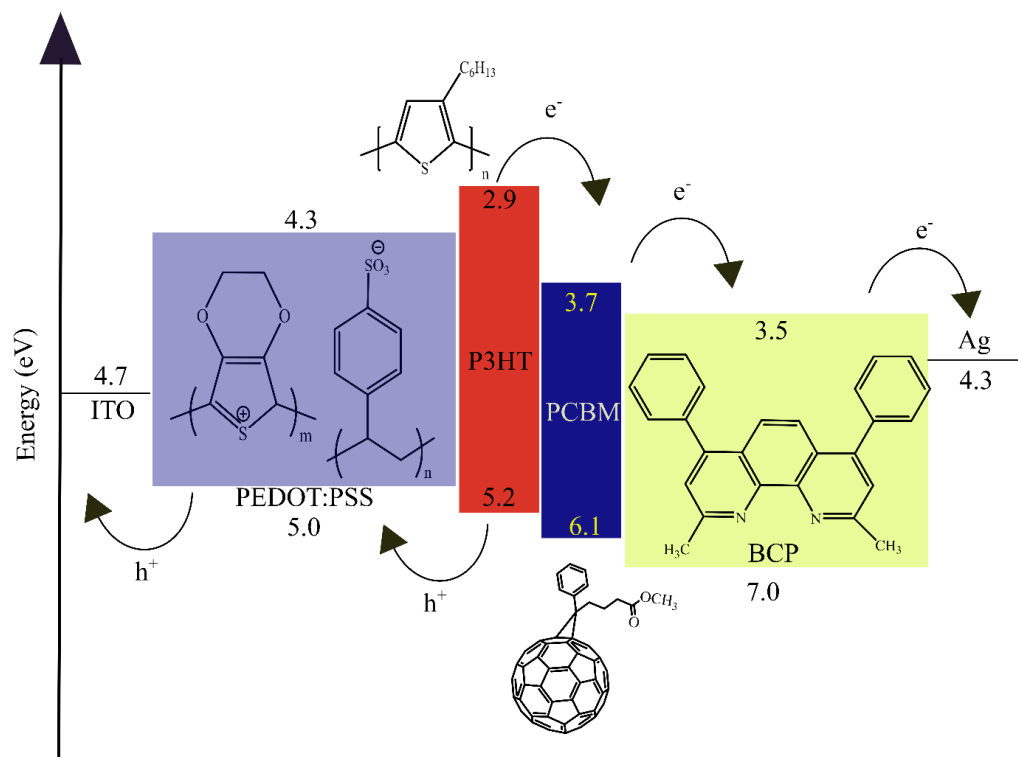

Figure 1.7. Transport of electrons and holes in a conventional OPV facilitated by the energy cascade of the components.

On top of the PEDOT:PSS layer, the device active layer consisting of the donor and the acceptor (and additives) is deposited followed by BCP/Ag as the buffer layer/back electrode. Bathocuproine (BCP) is the commercial name of a wide-band gap and high electron affinity material 2,9-Dimethyl-4,7-diphenyl-1,10-phenanthroline. Its role as the buffer layer here is to act as a hole-blocking barrier between the active layer and the cathode, thus improving the electron injection/collection efficiency, curbing the non-radiative recombination rate.[99–101] **Figure 1.7** shows the transport of electrons and holes in a conventional OPV device facilitates by the energy cascade of the components.

The inverted OPVs fabricated in this thesis employ sol-gel derived Zinc Oxide (ZnO) as the electron selective layer and MoO_3 as the anode buffer layer. MoO_3 can act as a good hole transport material while also serving as electron blocking layer.

Photoactive materials in OPVs

The molecular design of the organic semiconductors (small molecules and conjugated polymers) plays an important role in OPVs. The key phenomena in an OPV – intramolecular charge transport, intermolecular charge transport, light absorption, photoluminescence, charge injection and extraction are controlled by the energies and distribution of frontier molecular orbitals in a π-conjugated molecule. The electron density and delocalization of the π-electrons throughout the π-conjugated backbone determine the energy of the HOMO. Substituents that donate electron density mesomerically (lone pair donation from S, O, N heteroatoms) or inductively (alkyl chains), can raise the HOMO energy (decrease in solid state ionization potential); whereas electron withdrawing groups can lower both HOMO and LUMO energies leading to a rise in solid state electron affinity.[102,103,112–115,104–111] This control of the energy gap through molecular design has led to the synthesis of a wide range of conducting polymers for OPVs.

Poly(3-hexylthiophene) (P3HT) is one of the most important π-conjugated polymers and a standard building block in conducting polymers, thanks to its ability to be prepared with controlled regioregularity and precise end group functionality.[52] Along with [6,6]-phenyl C61 butyric acid methyl ester (PC60BM), P3HT, forms the benchmark donor-acceptor bulk heterojunction blend where the donor-acceptor energetic offset is large enough to overcome the P3HT exciton binding energy.[59] Thus, this system fulfils the fundamental requirements of the necessary driving force for charge separation, visible light absorption, and intermixed active layer morphology. PC60BM was succeeded by PC70PM where the non-symmetrical C70 cage enables energetic transitions that are forbidden in C60 and therefore exhibits improved absorption over PC60BM. 1',1'',4',4''-tetrahydro-di[1,4]methanonaphthaleno[5,6]fullerene-C60, (ICBA) is another fullerene derivative designed with a higher lying LUMO, which enables increased open circuit voltage. However, these modifications with acceptor structures only lead to marginal performance enhancements because of the relatively fixed electron affinities and ionization energies of fullerenes, thus offering very little window for V_{OC} improvement.[116] Thus, the OPV research direction rapidly shifted from the homopolymer P3HT to electron donors with hybridized molecular orbitals comprising alternating π-conjugated electron rich and electron-poor repeat units. This led to the development of push-pull polymers with narrower bandgap absorbing a greater proportion of incoming photons and increased Jsc. Using this polymer design strategy in conjunction with fullerenes, the field developed to efficiencies up to 11%.[117] Some of the widely used photovoltaic polymers and their energy gap are shown in **Figure 1.8**. It is noteworthy that a

number of small molecule electron donors such as the pyridalthiadiazole based p-DTS(PTTh$_2$)$_2$ p-DTS(FBTTh$_2$)$_2$, DR3TSBDT etc exist but are outside the scope of this thesis.

In the last four years the major research in OPVs is driven by the development of non-fullerene acceptors (NFA) which enable tunable frontier orbitals energies, better light absorption and high Jsc values leading the efficiencies to >12%.[118–122] The Calamitic π-conjugated molecule with a central fused electron rich aromatic core flanked by electron deficient units lead to the advent of a new boost in NFA based devices and efficiencies. Various electron-rich and electron deficient π-conjugated spacers can be introduced between the core and flanking groups to generate design variations. Thus, in comparison to fullerenes, NFAs offer a large window
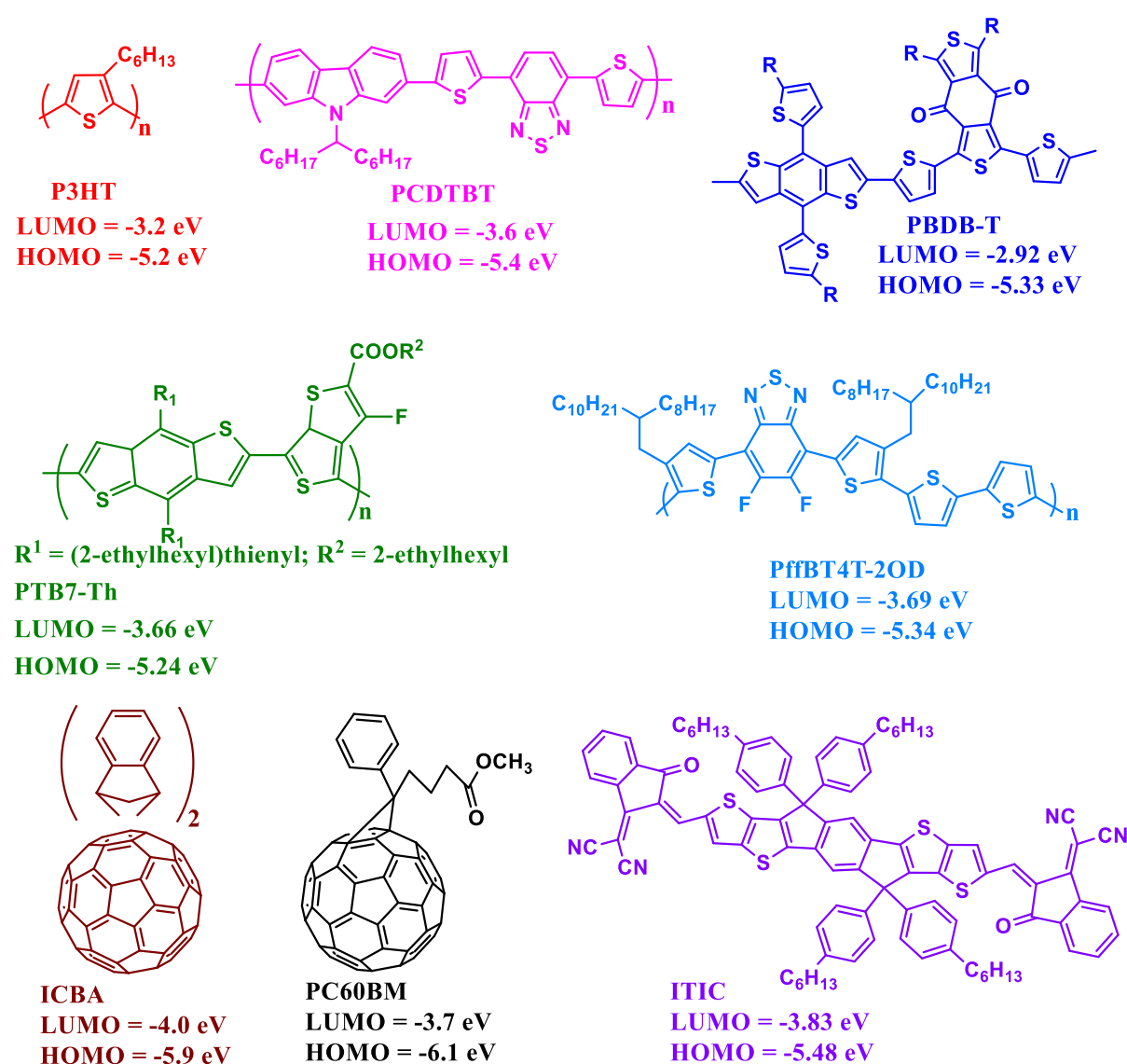

Figure 1.8. Structures of commonly used donors and acceptors in OPVs

for modifying the electron affinities and Voc (more electron withdrawing units as the flanking

groups can decreased the electron affinity and increase the Voc value). IDTBR and ITIC are the most popular calamitic NFAs incorporated in champion devices.[123,124] The most recent development that lead to >17% efficiencies is the non-linear Y6 acceptor whose larger dipole moment, higher electron mobility and absorption >900 nm, makes it the most desirable electron acceptor at the moment.[125,126] In spite of efficiencies surpassing the fullerene-based devices, there is a large scope of work still required in terms of controlling the nanomorphology, minimizing recombinations and extending the long term stability of these devices.

1.6 Ternary OPVs – Interest and Progress

Amongst several strategies explored to improve the efficiencies of OPVs is the ternary concept. A ternary OPV consists of a three-component photoactive layer, i.e. an additional donor or acceptor in the active layer as compared to the traditional binary systems that were discussed in the previous section. The third component is usually a minor ratio in the blend and can therefore be referred to as the guest in the bulk heterojunction.[127]

1.6.1 Operating modes of ternary OPVs

a. Cascade charge transfer mechanism:

Typically, a small amount of the ternary component (D2) is incorporated into the binary blend. This usually improves the nanomorphology of either D1 through enhanced crystallization, changes in domain sizes etc which improves the microstructure and favours charge transport, resulting in increased FF and J_{SC}.[128] When the energy level of the third component is located at the interface of the donor and the acceptor, a charge cascade mechanism is favoured.[129] Within this model, the ionization potential and electron affinity of the ternary component are between those of the D1 and A1, such that the ternary component facilitates the transport of holes to the anode and electrons to the cathode (**Figure 1.9i**).

b. Energy transfer mechanism:

When the energy gap of the third component is larger than the corresponding donor and the acceptor, it can act as a sensitiser to extend the absorption range (**Figure 1.9ii**). In competition with the charge transfer model is the energy transfer model where the excited sensitiser transfers energy to either the donor or the acceptor through Dexter or Forster resonance energy transfer (FRET) mechanism.[130,131] A pre-requisite for this mechanism is that there should be

significant overlap between the emission of the sensitizer and the absorption of the donor (or acceptor) to allow efficient energy transfer.

These two mechanisms can be intertwined and sometimes the same ternary system can simultaneously exhibit both energy transfer and charge relay processes. Time-resolved photoluminescence (PL) spectroscopy and transient absorption spectroscopy are key techniques to distinguish these processes. Both the mechanisms lead to increase in Jsc (because of complementary absorption and efficient charge generation).[132,133]

c. Parallel-like and alloy-like models

The energy cascade model does not suffice to account for the ternary examples where both J_{SC} and V_{OC} evolve. In the systems where V_{OC} appears to be scaled by the composition of the blend rather than the V_{OC} being pinned by the HOMO of the donor or LUMO of the acceptor, the mechanism is still under debate and has been attributed to two dominant nanomorphology
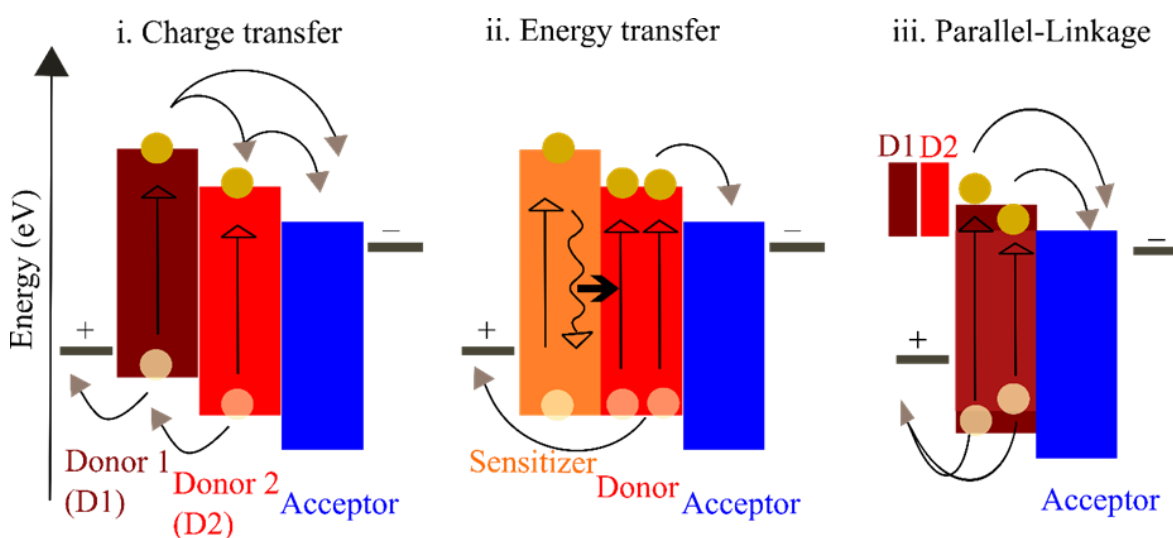

Figure 1.9. Different mechanism/operating modes observed in ternary OPVs

models – the parallel-like and alloy-like models (**Figure 1.9iii**). In the parallel-like model, each donor forms its own independent transport network. Both the donors absorb light, generate excitons and transport holes, which subsequently get transported through the donor matrix to the anode (and electrons through the acceptor matrix to the cathode). The Voc of such systems lie between that of the binary systems (i.e Voc of D1:D2:A1 > Voc of D1:A1 and Voc of D2:A1). The Jsc of such models are nearly the sum of the two binary cells. In contrast, the formation of an organic alloy model proposes that the D1 and D2 intermix electronically to form an electronic alloy (charge transfer state) that have a single IP (or an intermixed A1:A2 with a single EA).[127] However, the parallel-like model has very limited examples and the alloy-

like model has shown deviation upon increasing the concentration of the ternary component. Moreover, in many cases all the aforementioned models can co-exist thus further complicating the prediction of the operating mode.

1.6.2 The role of the third component

The key advantages or routes for performance enhancement with the use of ternary systems are:

a. **Extended light absorption:** Light absorption can be extended to the near IR region for wide/medium band gap polymers and to shorter wavelengths for low bandgap polymers. This enhanced sunlight harvesting translates to higher J_{SC}. The first work on ternary OPVs followed this route wherein a near-IR absorbing polymer, PCPDTBT was added as D2 to the well-known P3HT-PCBM blend resulting in extended absorption (up to 800nm) and improved device performance.[134] Modified versions of PCPDTBT such as Si-PCDTBT also showed similar ternary behaviour. With the advent of novel mid-bandgap and low band gap polymers, small molecule additives have become popular as a choice of ternary component in OPVs.[135] As compared to polymeric semiconductors, these molecular ones have well defined structures, high intrinsic carrier mobility and offer ease of modifications. In particular, p-DTS(FBTTh$_2$)$_2$ has demonstrated a concomitant increase in J_{SC} and FF when incorporated as D2.[136] Non-fullerene acceptors such as IDTBR and ITIC derivatives have been designed to exhibit panchromatic absorption from the visible to IR region and have been successfully used in record Jsc ternary devices.[122–124,137] However, the low absorption co-efficient in the 400-600 nm region, results in lower EQE in this wavelength range, and offers scope for incorporation of novel sensitizers that can absorb in the high energy region.

b. **Energy cascade alignment:** With the careful choice of the third component on the basis of the HOMO-LUMO levels (relative energies of frontier orbitals), it is possible to enable the formation of a cascade of the energy levels in the photoactive layer. This can improve charge separation and transport leading to decreased charge recombination. However, the major advantage of the energy cascade alignment in ternary systems is the opportunity to alleviate the trade-off between V_{OC} and J_{SC}. This trade-off defined as $(E_g/q)-V_{OC}=0.6V$ (where q is the elementary charge) limits the PCE of OPVs to 20%.

The introduction of a third component with suitable energy levels to form an energy cascade alignment with the binary components leads to creation of efficient charge extraction channels within the photoactive layer, contributing to increase in V_{OC} without compromising the J_{SC}.[127,138,139] Fullerene derivative IC60BA which has an high electron affinity than PC70BM showed an increased V_{OC} when used as A2 (acceptor 2) in binary devices. A similar effect has also been observed in some all-polymer ternary systems as well where the bridging role of the ternary component seems to improve donor-acceptor charge transfer, reduce the density of traps without disrupting the nanomorphology.

Nanomorphology: The nanoscale morphology of the donor-acceptor blend is of prime importance in bulk heterojunctions. Mixing in new components can change/disrupt the nanomorphology. This can alter charge transport and recombination pathways and bring down the charge extraction efficiency. The impact of nanomorphology is known to affect FF and V_{OC} but the exact impact on PCE is not fully understood yet in binary OPVs. With the introduction of additional components as in ternary systems, things get further complicated and information around this topic remains nascent. The third component could be fully embedded within donor 1, form its own network channels, be located at the donor: acceptor interface, or alloy with the donor/acceptor material. Therefore, all individual reports of performance enhancement remain system dependent and a generalized optimization guideline for ternary OPVs still does not exist in literature.[138–145]

1.7 Conclusion and Outlook

Solar power, being one of the fastest growing renewable energy sources, has the potential to help tackle climate change issues. The commercial front of this technology has been dominated by silicon solar cells with their well-established scale-up protocols, device stability and performance. However, their longer energy payback times and cost of processing have driven researchers to look for alternative thin film PV structures. OPVs, based on tuneable organic polymers are favourable for large scale processing with their ultra-thin active layers. With current record efficiencies at 18%, OPVs offer exciting opportunities in flexible and foldable electronic devices, with their lower energy payback times being an added advantage. Despite such a rapid growth in efficiencies and material development within this field, there is a lot of

scope in ongoing research for controlling the nanomorphology, minimizing recombinations and extending the long-term stability of these devices.

Ternary OPV is a very useful concept where-in by a careful choice of the material and thorough understanding of the fundamental processes, a simultaneous enhancement of all the photovoltaic parameters (J_{SC}, V_{OC}, FF, PCE) is possible without affecting the production cost and time. [128–133,146–149] The dual requirement of an ideal ternary component is optimised energy cascade for maximized voltage and broader spectral coverage whilst enabling favourable nanoscale interactions in the photoactive layer. A feedback loop between the fundamental understanding of ternary systems and design rules for material selection is necessary to realize the true potential of ternary OPVs to break the theoretical efficiency limit in single junction OPVs.

This thesis reports the work done between 2017-20 on the incorporation of porphyrin-based metal organic nanosheets (MONs) as a novel ternary component in OPVs, with the first working example shown in conjunction with the archetypal P3HT-PCBM system, followed by a careful analysis of the properties and design rules that can enable performance enhancement. This is followed by the application of MONs to enable the record efficiency of 12.3% for a fullerene based OPV device- the highest for this class of OPV till date. A detailed account of MONs, their synthesis, and their role as emerging materials in electronics is given in the next chapter.

1.8 References

1. Hegerl, G. C. *et al.* Causes of climate change over the historical record. *Environmental Research Letters* **14**, 123006 (2019).

2. Wei, Y. M. *et al.* Self-preservation strategy for approaching global warming targets in the post-Paris Agreement era. *Nature Communications* **11**, 1–13 (2020).

3. NASA Technical Reports Server (NTRS).

4. Sutton, R. T. & Hawkins, E. ESD Ideas: Global climate response scenarios for IPCC assessments. *Earth System Dynamics* **11**, 751–754 (2020).

5. Wang, Z., Song, H., Liu, H. & Ye, J. Coupling of Solar Energy and Thermal Energy for Carbon Dioxide Reduction: Status and Prospects. *Angewandte Chemie International Edition* **59**, 8016–8035 (2020).

6. Kreider, J. F. & Kreith, F. Solar energy handbook. (1981).

7. Heusinger, J., Broadbent, A. M., Sailor, D. J. & Georgescu, M. Introduction, evaluation

and application of an energy balance model for photovoltaic modules. *Solar Energy* **195**, 382–395 (2020).

8. Rothwarf, A. & Böer, K. W. Direct conversion of solar energy through photovoltaic cells. *Progress in Solid State Chemistry* **10**, 71–102 (1975).

9. Willoughby Smith. The Action of Light on Selenium. *The British Library* 1–8 (1856).

10. Fritts, C. On a New Form of Selenium Cell, and some Electrical Discoveries made by its use. *American Journal of Science* Vol. 26, Iss. 156 (1883).

11. Fraas, L. M. Low-cost solar electric power. *Low-Cost Solar Electric Power* **9783319075**, 1–181 (2014).

12. Zhao, J., Wang, A., Green, M. A. & Ferrazza, F. 19.8% Efficient 'Honeycomb' Textured Multicrystalline and 24.4% Monocrystalline Silicon Solar Cells. *Applied Physics Letters* **73**, 1991–1993 (1998).

13. Swanson, R. M. A vision for crystalline silicon photovoltaics. *Progress in Photovoltaics: Research and Applications* **14**, 443–453 (2006).

14. Liu, Z. *et al.* Revisiting thin silicon for photovoltaics: A technoeconomic perspective. *Energy and Environmental Science* **13**, 12–23 (2020).

15. Tool, C. J. J., Burgers, A. R., Manshanden, P., Weeber, A. W. & Van Straaten, B. H. M. Influence of wafer thickness on the performance of multicrystalline Si solar cells: An experimental study. *Progress in Photovoltaics: Research and Applications* **10**, 279–291 (2002).

16. Kowalczewski, P. & Andreani, L. C. Towards the efficiency limits of silicon solar cells: How thin is too thin? *Solar Energy Materials and Solar Cells* **143**, 260–268 (2015).

17. Needleman, D. B. *et al.* Economically sustainable scaling of photovoltaics to meet climate targets. *Energy and Environmental Science* **9**, 2122–2129 (2016).

18. Powell, D. M. *et al.* Crystalline silicon photovoltaics: A cost analysis framework for determining technology pathways to reach baseload electricity costs. *Energy and Environmental Science* **5**, 5874–5883 (2012).

19. Yoshikawa, K. *et al.* Silicon heterojunction solar cell with interdigitated back contacts for a photoconversion efficiency over 26%. *Nature Energy* **2**, (2017).

20. Sandor, D., Fulton, S., Engel-Cox, J., Peck, C. & Peterson, S. System dynamics of polysilicon for solar photovoltaics: A framework for investigating the energy security of renewable energy supply chains. *Sustainability (Switzerland)* **10**, (2018).

21. Liu, J., Yao, Y., Xiao, S. & Gu, X. Review of status developments of high-efficiency crystalline silicon solar cells. *Journal of Physics D: Applied Physics* **51**, 123001 (2018).

22. Yamaguchi, M., Lee, K. H., Araki, K. & Kojima, N. A review of recent progress in heterogeneous silicon tandem solar cells. *Journal of Physics D: Applied Physics* **51**, 133002 (2018).

23. Chopra, K. L., Paulson, P. D. & Dutta, V. Thin-film solar cells: An overview. *Progress in Photovoltaics: Research and Applications* **12**, 69–92 (2004).

24. Putra, N. M. D., Sugianto, Marwoto, P., Murtafiatin, R. & Rizaldi, P. D. Performance

profile analysis of ZnO/CdS/CdTe solar cells thin film : A review of absorber thickness and device temperature. in *Journal of Physics: Conference Series* **1567**, 22007 (Institute of Physics Publishing, 2020).

25. Britt, J. & Ferekides, C. Thin-film CdS/CdTe solar cell with 15.8% efficiency. *Applied Physics Letters* **62**, 2851–2852 (1993).

26. Ramanujam, J. & Singh, U. P. Copper indium gallium selenide based solar cells - A review. *Energy and Environmental Science* **10**, 1306–1319 (2017).

27. Ravindiran, M. & Praveenkumar, C. Status review and the future prospects of CZTS based solar cell – A novel approach on the device structure and material modeling for CZTS based photovoltaic device. *Renewable and Sustainable Energy Reviews* **94**, 317–329 (2018).

28. Grätzel, M. Dye-sensitized solar cells. *Journal of Photochemistry and Photobiology C: Photochemistry Reviews* **4**, 145–153 (2003).

29. O'Regan, B. & Gratzel, M. A Low-Cost, High-Efficiency Solar-Cell Based on Dye-Sensitized Colloidal TiO$_2$ Films. *Nature* **353**, 737–740 (1991).

30. Hagfeldt, A., Boschloo, G., Sun, L., Kloo, L. & Pettersson, H. Dye-sensitized solar cells. *Chemical Reviews* **110**, 6595–6663 (2010).

31. Grätzel, M. Recent advances in sensitized mesoscopic solar cells. *Accounts of Chemical Research* **42**, 1788–1798 (2009).

32. Chung, I., Lee, B., He, J., Chang, R. P. H. & Kanatzidis, M. G. All-solid-state dye-sensitized solar cells with high efficiency. *Nature* **485**, 486–489 (2012).

33. Bisquert, J. Dilemmas of dye-sensitized solar cells. *ChemPhysChem* **12**, 1633–1636 (2011).

34. Green, M. A., Ho-Baillie, A. & Snaith, H. J. The emergence of perovskite solar cells. *Nature Photonics* **8**, 506–514 (2014).

35. Green, M. A. & Ho-Baillie, A. Perovskite Solar Cells: The Birth of a New Era in Photovoltaics. *ACS Energy Letters* **2**, 822–830 (2017).

36. Jošt, M., Kegelmann, L., Korte, L. & Albrecht, S. Monolithic Perovskite Tandem Solar Cells: A Review of the Present Status and Advanced Characterization Methods Toward 30% Efficiency. *Advanced Energy Materials* **10**, 1904102 (2020).

37. Chen, B. *et al.* Blade-Coated Perovskites on Textured Silicon for 26%-Efficient Monolithic Perovskite/Silicon Tandem Solar Cells. *Joule* **4**, 850–864 (2020).

38. Wang, C., Song, Z., Li, C., Zhao, D. & Yan, Y. Low-Bandgap Mixed Tin-Lead Perovskites and Their Applications in All-Perovskite Tandem Solar Cells. *Advanced Functional Materials* **29**, (2019).

39. Wolff, C. M., Caprioglio, P., Stolterfoht, M. & Neher, D. Nonradiative Recombination in Perovskite Solar Cells: The Role of Interfaces. *Advanced Materials* **31**, (2019).

40. Werner, J., Niesen, B. & Ballif, C. Perovskite/Silicon Tandem Solar Cells: Marriage of Convenience or True Love Story? – An Overview. *Advanced Materials Interfaces* **5**, (2018).

41. Saliba, M., Correa-Baena, J. P., Grätzel, M., Hagfeldt, A. & Abate, A. Perovskite Solar Cells: From the Atomic Level to Film Quality and Device Performance. *Angewandte Chemie - International Edition* **57**, 2554–2569 (2018).

42. Jones-Albertus, R., Feldman, D., Fu, R., Horowitz, K. & Woodhouse, M. Technology advances needed for photovoltaics to achieve widespread grid price parity. *Progress in Photovoltaics: Research and Applications* **24**, 1272–1283 (2016).

43. Moore, W. & Silver, M. Generation of free carriers in photoconducting anthracene. I. *The Journal of Chemical Physics* **33**, 1671–1676 (1960).

44. Tang, C. W. Two-layer organic photovoltaic cell. *Applied Physics Letters* **48**, 183–185 (1986).

45. Wöhrle, D. & Meissner, D. Organic Solar Cells. *Advanced Materials* **3**, 129–138 (1991).

46. Scharber, M. C. *et al.* Design rules for donors in bulk-heterojunction solar cells - Towards 10 % energy-conversion efficiency. *Advanced Materials* **18**, 789–794 (2006).

47. yuanbao Lin *et al.* Self-assembled Monolayer Enables HTL-free Organic Solar Cells with 18% Efficiency and Improved Operational Stability. *ACS Energy Letters* (2020). doi:10.1021/acsenergylett.0c01421

48. Cui, Y. *et al.* Organic photovoltaic cell with 17% efficiency and superior processability. *National Science Review* **7**, 1239–1246 (2019).

49. Li, G. *et al.* High-efficiency solution processable polymer photovoltaic cells by self-organization of polymer blends. *Nature Materials* **4**, 864–868 (2005).

50. Roncali, J. & Roncali, J. ChemInform Abstract : Molecular Bulk Heterojunctions : An Emerging Approach to Organic Solar Cells Molecular Bulk Heterojunctions : An Emerging Approach to Organic Solar Cells. **42**, (2009).

51. Shaheen, S. E., Ginley, D. S. & Jabbour, G. E. Organic-Based Photovoltaics: Toward Low-Cost Power Generation. *MRS Bulletin* **30**, 10–19 (2005).

52. Yang, X. *et al.* Nanoscale morphology of high-performance polymer solar cells. *Nano Letters* **5**, 579–583 (2005).

53. Arias, A. C. *et al.* Photovoltaic performance and morphology of polyfluorene blends: A combined microscopic and photovoltaic investigation. *Macromolecules* **34**, 6005–6013 (2001).

54. Roncali, J. Synthetic principles for bandgap control in linear π-conjugated systems. *Chemical Reviews* **97**, 173–205 (1997).

55. Günes, S., Neugebauer, H. & Sariciftci, N. S. Conjugated polymer-based organic solar cells. *Chemical Reviews* **107**, 1324–1338 (2007).

56. Yang, F. & Forrest, S. R. Photocurrent generation in nanostructured organic solar cells. *ACS Nano* **2**, 1022–1032 (2008).

57. Mohan, S. R., Singh, M. P., Joshi, M. P. & Kukreja, L. M. Monte carlo simulation of carrier diffusion in organic thin films with morphological inhomogeneity. *Journal of Physical Chemistry C* **117**, 24663–24672 (2013).

58. Eisenmenger, N. D., Delaney, K. T., Ganesan, V., Fredrickson, G. H. & Chabinyc, M.

L. Energy Transfer Directly to Bilayer Interfaces to Improve Exciton Collection in Organic Photovoltaics. *Journal of Physical Chemistry C* **119**, 19011–19021 (2015).

59. Pensack, R. D., Guo, C., Vakhshouri, K., Gomez, E. D. & Asbury, J. B. Influence of acceptor structure on barriers to charge separation in organic photovoltaic materials. *Journal of Physical Chemistry C* **116**, 4824–4831 (2012).

60. Clark, M. D., Jespersen, M. L., Patel, R. J. & Leever, B. J. Predicting vertical phase segregation in polymer-fullerene bulk heterojunction solar cells by free energy analysis. *ACS Applied Materials and Interfaces* **5**, 4799–4807 (2013).

61. Jang, S. & Montoya-Castillo, A. Charge Hopping Dynamics along a Disordered Chain in Quantum Environments: Comparative Study of Different Rate Kernels. *Journal of Physical Chemistry B* **119**, 7659–7665 (2015).

62. Beljonne, D. *et al.* Electronic processes at organic-organic interfaces: Insight from modeling and implications for opto-electronic devices. *Chemistry of Materials* **23**, 591–609 (2011).

63. Ratcliff, E. L., Zacher, B. & Armstrong, N. R. Selective interlayers and contacts in organic photovoltaic cells. *Journal of Physical Chemistry Letters* **2**, 1337–1350 (2011).

64. Allen, J. E. & Black, C. T. Improved power conversion efficiency in bulk heterojunction organic solar cells with radial electron contacts. *ACS Nano* **5**, 7986–7991 (2011).

65. Giebink, N. C., Wiederrecht, G. P., Wasielewski, M. R. & Forrest, S. R. Ideal diode equation for organic heterojunctions. I. Derivation and application. *Physical Review B* **82**, 155305 (2010).

66. Sinton, R. A. & Cuevas, A. Contactless determination of current-voltage characteristics and minority-carrier lifetimes in semiconductors from quasi-steady-state photoconductance data. *Applied Physics Letters* **69**, 2510–2512 (1996).

67. Fernandez, D. *et al.* Understanding the Limiting Factors of Solvent-Annealed Small-Molecule Bulk-Heterojunction Organic Solar Cells from a Chemical Perspective. *ChemSusChem* **10**, 3118–3134 (2017).

68. Sandén, S., Wilson, N. M., Sandberg, O. J. & Österbacka, R. Characterization of the dominating bulk recombination in bulk-heterojunction blends using photoinduced absorption. *Applied Physics Letters* **108**, (2016).

69. Collins, S. D., Ran, N. A., Heiber, M. C. & Nguyen, T. Q. Small is Powerful: Recent Progress in Solution-Processed Small Molecule Solar Cells. *Advanced Energy Materials* **7**, (2017).

70. Wang, T. *et al.* High sensitivity, fast response and low operating voltage organic photodetectors by incorporating a water/alcohol soluble conjugated polymer anode buffer layer. *RSC Advances* **7**, 1743–1748 (2017).

71. Kiriy, A. & Krebs, F. C. Synthesis of conjugated polymers with complex architecture for photovoltaic applications. in *Advances in Polymer Science* **272**, 351–376 (Springer New York LLC, 2017).

72. Zonno, I., Martinez-Otero, A., Hebig, J. C. & Kirchartz, T. Understanding Mott-Schottky Measurements under Illumination in Organic Bulk Heterojunction Solar Cells. *Physical Review Applied* **7**, (2017).

73. Cha, H. *et al.* Influence of Blend Morphology and Energetics on Charge Separation and Recombination Dynamics in Organic Solar Cells Incorporating a Nonfullerene Acceptor. *Advanced Functional Materials* **28**, (2018).

74. Wang, T. *et al.* Work-function-controlled operation mode transition between photodiode and photoconductor modes in organic photodetectors. *Organic Electronics* **64**, 138–145 (2019).

75. Mäckel, H. & MacKenzie, R. C. I. Determination of Charge-Carrier Mobility in Disordered Thin-Film Solar Cells as a Function of Current Density. *Physical Review Applied* **9**, (2018).

76. Wu, J., Fischer, A. & Reineke, S. Investigating Free Charge-Carrier Recombination in Organic LEDs Using Open-Circuit Conditions. *Advanced Optical Materials* **7**, (2019).

77. Shuttle, C. G., Hamilton, R., Nelson, J., O'Regan, B. C. & Durrant, J. R. Measurement of charge-density dependence of carrier mobility in an organic semiconductor blend. *Advanced Functional Materials* **20**, 698–702 (2010).

78. Padilla, M., Michl, B., Thaidigsmann, B., Warta, W. & Schubert, M. C. Short-circuit current density mapping for solar cells. *Solar Energy Materials and Solar Cells* **120**, 282–288 (2014).

79. Liu, S., Liang, Q., Yan, J., Wu, H. & Cao, Y. Distinguishing limits on the fill factor in organic solar cells processed from different solvents: Charge recombination kinetics vs. charge extraction. *Organic Electronics* **59**, 427–431 (2018).

80. Yang, T. *et al.* Understanding, Optimizing, and Utilizing Nonideal Transistors Based on Organic or Organic Hybrid Semiconductors. *Advanced Functional Materials* **30**, (2020).

81. Xiao, B. *et al.* Relationship between Fill Factor and Light Intensity in Solar Cells Based on Organic Disordered Semiconductors: The Role of Tail States. *Physical Review Applied* **14**, (2020).

82. Kang, J. W. *et al.* Reduction of series resistance in organic photovoltaic using low sheet resistance of ITO electrode. *Electrochemical and Solid-State Letters* **12**, H64 (2009).

83. Wu, J. *et al.* Tail state limited photocurrent collection of thick photoactive layers in organic solar cells. *Nature Communications* **10**, (2019).

84. Ostroverkhova, O. Organic Optoelectronic Materials: Mechanisms and Applications. *Chemical Reviews* **116**, 13279–13412 (2016).

85. Pelzer, K. M. *et al.* Molecular dynamics and charge transport in organic semiconductors: a classical approach to modeling electron transfer. *Chemical Science* **8**, 2597–2609 (2017).

86. Heiber, M. C. *et al.* Measuring the competition between bimolecular charge recombination and charge transport in organic solar cells under operating conditions. *Energy and Environmental Science* **11**, 3019–3032 (2018).

87. Azzouzi, M. *et al.* Overcoming the Limitations of Transient Photovoltage Measurements for Studying Recombination in Organic Solar Cells. *Solar RRL* **4**, (2020).

88. Wu, J. *et al.* Exceptionally low charge trapping enables highly efficient organic bulk heterojunction solar cells. *Energy and Environmental Science* **13**, 2422–2430 (2020).

89.   Kaiser, W., Albes, T. & Gagliardi, A. Charge carrier mobility of disordered organic semiconductors with correlated energetic and spatial disorder. *Physical Chemistry Chemical Physics* **20**, 8897–8908 (2018).

90.   Rühle, S. Tabulated values of the Shockley-Queisser limit for single junction solar cells. *Solar Energy* **130**, 139–147 (2016).

91.   Harder, N. P. & Würfel, P. Theoretical limits of thermophotovoltaic solar energy conversion. *Semiconductor Science and Technology* **18**, (2003).

92.   Martí, A. & Araújo, G. L. Limiting efficiencies for photovoltaic energy conversion in multigap systems. *Solar Energy Materials and Solar Cells* **43**, 203–222 (1996).

93.   Kirchartz, T., Taretto, K. & Rau, U. Efficiency limits of organic bulk heterojunction solar cells. *Journal of Physical Chemistry C* **113**, 17958–17966 (2009).

94.   Nelson, J., Kirkpatrick, J. & Ravirajan, P. Factors limiting the efficiency of molecular photovoltaic devices. *Physical Review B - Condensed Matter and Materials Physics* **69**, (2004).

95.   Huang, J. *et al.* Investigation of the effects of doping and post-deposition treatments on the conductivity, morphology, and work function of poly(3,4-ethylenedioxythiophene)/poly(styrene sulfonate) films. *Advanced Functional Materials* **15**, 290–296 (2005).

96.   Nardes, A. M., Kemerink, M. & Janssen, R. A. J. Anisotropic hopping conduction in spin-coated PEDOT:PSS thin films. *Physical Review B - Condensed Matter and Materials Physics* **76**, (2007).

97.   Vitoratos, E. *et al.* Thermal degradation mechanisms of PEDOT:PSS. *Organic Electronics* **10**, 61–66 (2009).

98.   Choulis, S. A., Choong, V. E., Patwardhan, A., Mathai, M. K. & So, F. Interface modification to improve hole-injection properties in organic electronic devices. *Advanced Functional Materials* **16**, 1075–1080 (2006).

99.   Patil, B. R. *et al.* Area dependent behavior of bathocuproine (BCP) as cathode interfacial layers in organic photovoltaic cells. *Scientific Reports* **8**, 12608 (2018).

100.   Vogel, M., Doka, S., Breyer, C., Lux-Steiner, M. C. & Fostiropoulos, K. On the function of a bathocuproine buffer layer in organic photovoltaic cells. *Applied Physics Letters* **89**, 1–4 (2006).

101.   Gommans, H. *et al.* On the role of bathocuproine in organic photovoltaic cells. *Advanced Functional Materials* **18**, 3686–3691 (2008).

102.   Opoku, H. *et al.* Configurationally Random Polythiophene for Improved Polymer Ordering and Charge-Transporting Ability. *ACS Applied Materials & Interfaces* (2020). doi:10.1021/acsami.0c11165

103.   M Planells BC Schroeder, I. M. Effect of chalcogen atom substitution on the optoelectronic properties in cyclopentadithiophene polymers. *Macromolecules* **47**, 5889–5894 (2014).

104.   CB Nielsen AJP White, I. M. Effect of fluorination of 2,1,3-benzothiadiazole. *J. Org. Chem.* **80**, 5045–5048 (2015).

105. Usta, H. Design, synthesis, and characterization of ladder-type molecules and polymers. air-stable, solution-processable n-channel and ambipolar semiconductors for thin-film transistors via experiment and theory. *J. Am. Chem. Soc.* **131**, 5586–5608 (2009).

106. DM Leeuw MMJ Simenon, A. R. B. R. E. F. E. Stability of n-type doped conducting polymers and consequences for polymeric microelectronic devices. *Synth. Met.* **87**, 53–59 (1997).

107. KJ Thorley, I. M. Why are S–F and S–O non-covalent interactions stabilising? *J. Mater. Chem. C* **6**, 12413–12421 (2018).

108. Abbaszadeh, D. Electron trapping in conjugated polymers. *Chem. Mater.* **31**, 6380–6386 (2019).

109. Warnan, J. & Reisner, E. Synthetic Organic Design for Solar Fuel Systems. *Angewandte Chemie - International Edition* (2020). doi:10.1002/anie.202006013

110. G Yu J Gao, J. C. H. F. W. A. J. H. Polymer photovoltaic cells: enhanced efficiencies via a network of internal donor–acceptor heterojunctions. *Science* **270**, 1789–1791 (1995).

111. Conboy, G. To bend or not to bend — are heteroatom interactions within conjugated molecules effective in dictating conformation and planarity? *Mater. Horiz.* **3**, 333–339 (2016).

112. Bronstein, H., Nielsen, C. B., Schroeder, B. C. & McCulloch, I. The role of chemical design in the performance of organic semiconductors. *Nature Reviews Chemistry* **4**, 66–77 (2020).

113. McCulloch, I. Liquid-crystalline semiconducting polymers with high charge-carrier mobility. *Nat. Mater.* **5**, 328–333 (2006).

114. Nikolka, M. High operational and environmental stability of high-mobility conjugated polymer field-effect transistors through the use of molecular additives. *Nat. Mater.* **16**, 356–362 (2016).

115. NS Sariciftci L Smilowitz, A. J. H. F. W. Photoinduced electron transfer from a conducting polymer to buckminsterfullerene. *Science* **258**, 1474–1476 (1992).

116. Liu, T. & Troisi, A. What makes fullerene acceptors special as electron acceptors in organic solar cells and how to replace them. *Advanced Materials* **25**, 1038–1041 (2013).

117. NS Sariciftci, L. S. A. J. H. F. W. *et al.* Configurationally Random Polythiophene for Improved Polymer Ordering and Charge-Transporting Ability.

118. Lin, Y. *et al.* An electron acceptor challenging fullerenes for efficient polymer solar cells. *Advanced Materials* **27**, 1170–1174 (2015).

119. Yao, H. *et al.* Achieving Highly Efficient Nonfullerene Organic Solar Cells with Improved Intermolecular Interaction and Open-Circuit Voltage. *Advanced Materials* **29**, (2017).

120. Jung, J. W. *et al.* Fluoro-substituted n-type conjugated polymers for additive-free all-polymer bulk heterojunction solar cells with high power conversion efficiency of 6.71%. *Advanced Materials* **27**, 3310–3317 (2015).

121. Liu, Y. *et al.* NDI-Based Small Molecule as Promising Nonfullerene Acceptor for

Solution-Processed Organic Photovoltaics. *Advanced Energy Materials* **5**, (2015).

122. Yu, R., Yao, H. & Hou, J. Recent Progress in Ternary Organic Solar Cells Based on Nonfullerene Acceptors. *Advanced Energy Materials* **8**, (2018).

123. Liang, R.-Z. *et al.* Carrier Transport and Recombination in Efficient "All-Small-Molecule" Solar Cells with the Nonfullerene Acceptor IDTBR. *Advanced Energy Materials* **8**, 1800264 (2018).

124. Yang, Y. *et al.* Side-Chain Isomerization on an n-type Organic Semiconductor ITIC Acceptor Makes 11.77% High Efficiency Polymer Solar Cells. *Journal of the American Chemical Society* **138**, 15011–15018 (2016).

125. Meng, L. *et al.* Organic and solution-processed tandem solar cells with 17.3% efficiency. *Science* **361**, 1094–1098 (2018).

126. Perdigón-Toro, L. *et al.* Barrierless Free Charge Generation in the High-Performance PM6:Y6 Bulk Heterojunction Non-Fullerene Solar Cell. *Advanced Materials* **32**, 1906763 (2020).

127. Ameri, T., Khoram, P., Min, J. & Brabec, C. J. Organic ternary solar cells: A review. *Advanced Materials* **25**, 4245–4266 (2013).

128. Liu, T. *et al.* Ternary Organic Solar Cells Based on Two Compatible Nonfullerene Acceptors with Power Conversion Efficiency >10%. *Advanced Materials* **28**, 10008–10015 (2016).

129. Zhan, L. *et al.* Over 17% efficiency ternary organic solar cells enabled by two non-fullerene acceptors working in an alloy-like model. *Energy and Environmental Science* **13**, 635–645 (2020).

130. Gupta, V., Bharti, V., Kumar, M., Chand, S. & Heeger, A. J. Polymer-Polymer Förster Resonance Energy Transfer Significantly Boosts the Power Conversion Efficiency of Bulk-Heterojunction Solar Cells. *Advanced Materials* **27**, 4398–4404 (2015).

131. Zhao, W., Li, S., Zhang, S., Liu, X. & Hou, J. Ternary Polymer Solar Cells based on Two Acceptors and One Donor for Achieving 12.2% Efficiency. *Advanced Materials* **29**, (2017).

132. Fan, B. *et al.* Improved Performance of Ternary Polymer Solar Cells Based on A Nonfullerene Electron Cascade Acceptor. *Advanced Energy Materials* **7**, (2017).

133. Li, H., Lu, K. & Wei, Z. Polymer/Small Molecule/Fullerene Based Ternary Solar Cells. *Advanced Energy Materials* **7**, (2017).

134. Koppe, M. *et al.* Near IR sensitization of organic bulk heterojunction solar cells: Towards optimization of the spectral response of organic solar cells. *Advanced Functional Materials* **20**, 338–346 (2010).

135. Ameri, T. *et al.* Performance enhancement of the p3ht/pcbm solar cells through nir sensitization using a small-bandgap polymer. *Advanced Energy Materials* **2**, 1198–1202 (2012).

136. Lu, L., Xu, T., Chen, W., Landry, E. S. & Yu, L. Ternary blend polymer solar cells with enhanced power conversion efficiency. *Nature Photonics* **8**, 716–722 (2014).

137. He, E. *et al.* Indacenodifuran-Based Non-Fullerene Electron Acceptors for Efficient

Polymer Solar Cells. *ACS Applied Energy Materials* **3**, 6133–6138 (2020).

138. Lami, V., Hofstetter, Y. J., Butscher, J. F. & Vaynzof, Y. Energy Level Alignment in Ternary Organic Solar Cells. *Advanced Electronic Materials* **6**, (2020).

139. Gasparini, N., Salleo, A., McCulloch, I. & Baran, D. The role of the third component in ternary organic solar cells. *Nature Reviews Materials* **4**, 229–242 (2019).

140. Wadsworth, A. *et al.* Critical review of the molecular design progress in non-fullerene electron acceptors towards commercially viable organic solar cells. *Chemical Society Reviews* **48**, 1596–1625 (2019).

141. J-L Brédas EH Sargent, G. D. S. Photovoltaic concepts inspired by coherence effects in photosynthetic systems. *Nat. Mater.* **16**, 35–44 (2016).

142. I McCulloch A Salleo, M. C. Avoid the kinks when measuring mobility. *Science* **352**, 1521–1522 (2016).

143. Wang, Z. *et al.* Mechanistic Investigation into Dynamic Function of Third Component Incorporated in Ternary Near-Infrared Nonfullerene Organic Solar Cells. *Advanced Functional Materials* **30**, (2020).

144. Leo, K. Organic photovoltaics. *Nat. Rev. Mater.* **1**, 16056 (2016).

145. Liu, L., Chao, P., Mo, D. & He, F. Chlorinated polymer solar cells simultaneously enhanced by fullerene and non-fullerene ternary strategies. *Journal of Energy Chemistry* **54**, 620–625 (2021).

146. Yu, R. *et al.* Two Well-Miscible Acceptors Work as One for Efficient Fullerene-Free Organic Solar Cells. *Advanced Materials* **29**, (2017).

147. Lu, H. *et al.* Ternary-Blend Polymer Solar Cells Combining Fullerene and Nonfullerene Acceptors to Synergistically Boost the Photovoltaic Performance. *Advanced Materials* **28**, 9559–9566 (2016).

148. Zhong, L. *et al.* High Efficiency Ternary Nonfullerene Polymer Solar Cells with Two Polymer Donors and an Organic Semiconductor Acceptor. *Advanced Energy Materials* **7**, (2017).

149. Duan, L. & Uddin, A. Progress in Stability of Organic Solar Cells. *Advanced Science* **7**, (2020).

Chapter 2

Metal-Organic Framework Nanosheets: Emerging Two-Dimensional Materials in Electronics

Layered bulk MOF   Exfoliated MONs
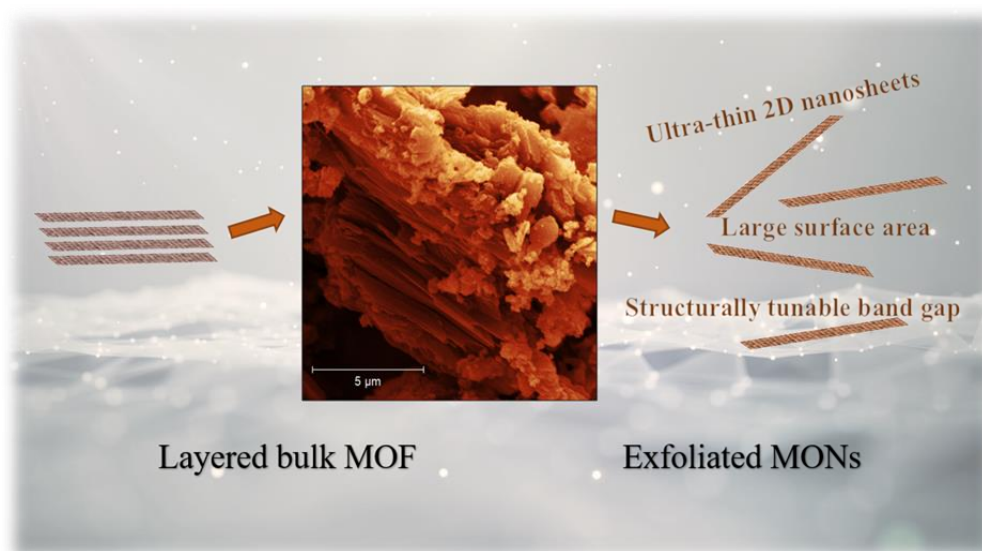
2.0 Introducing MONs

Metal-organic materials are coordination polymers comprising organic ligands as linkers coordinated with metal ions resulting in the formation of readily-tuneable structures.[1] Using this approach, a wide variety of architectures have been created ranging from discrete complexes and cages to extended polymers, gels and liquid crystals.[2–7] Of these metal-organic materials, the Cambridge structural database (CSD) lists greater than 99,000 metal-organic frameworks (MOFs) many of which are reported to have a layered structure.[8] Isolating the individual layers and stabilizing them to result in a uniform crystalline sheet with single unit thickness (extending infinitely in the other two dimensions) is the basis for designing metal-organic nanosheets (MONs). Although this ideal single-unit thickness is not always achieved

(just like any other 2D material), MONs approaching monolayer and few layer thicknesses have emerged as the most recent form-factor for metal-organic materials. In a review published by our group in the year 2018, a systematic definition for MONs was proposed as, *"1. Organic ligands coordinated to metal ions or clusters with continuous connectivity in two-dimensions but only non-covalent interactions in the third-dimension; 2. highly anisotropic materials with one-dimension approaching monolayer thickness and the others being at least an order of magnitude larger and approximately equal in size; 3. materials which can be isolated in a form with the dimensions outlined above as free standing sheets, not attached to a surface or other scaffold or as layers in a bulk material."* Thus, any metal-organic material that has the potential to display a sheet-like structure and upon optimisation of the preparation process can eventually form isolated free-standing monolayers can fall under the category of MONs. MONs have established themselves in recent years as promising two-dimensional materials with large surface area that also bring with them the structural diversity, tunable band gaps and chemical tailorability of MOFs. [9–12]

2.1 Structure and Design of MONs

MONs have strong directional interactions within the plane and weak interactions between the layers in bulk material.[13] Design of MON structures depends on the topology of the framework, the inorganic metal centre and the organic ligands. Typical 2D topological networks (**Figure 2.1**) include square lattice (sql), hexagonal lattice (hxl), honey-comb lattice (hcb), Kagomé (kgm), four eight squares (fes), etc.[12] By choosing the appropriate ligands and metal nodes according to the topological network of choice, 2D MONs can be assembled.
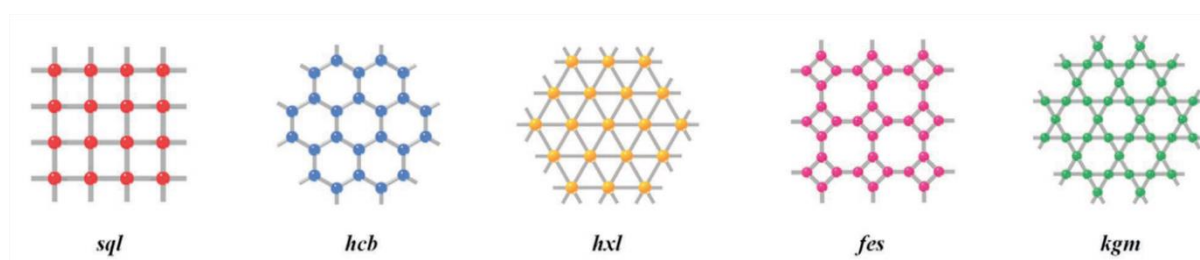

Figure 2.1.Typical 2D topological networks

The structural building unit (SBU), for the construction of MONs with ideal network topologies include metal ions, metal clusters and molecular complexes.[13] In comparison to free metal ions which contain little directional information, metal clusters are preferred for MOF construction owing to their rigidity and clearer bonding directions which enhances the robustness of the resulting framework.[14] The paddle-wheel dual-core cluster formed by tetracarboxybimetallic ions $[M_2(COO)_4]$, μ_4-oxohexacarboxy $[M_4(\mu_4-O)(COO)_6]$ tetrahedral cluster and μ_3-oxy/hydroxyhexacarboxy bridge $[M_3(\mu_3-O/OH)(COO)_6]$ triangle cluster are some of the most commonly used SBUs.[15,16] Hf $^{4+}$ cluster $[Hf_6(\mu_3-O)_4(\mu_3-OH)_4(carboxylate)_{12}]$, $M_6O_4(OH)_4$ clusters of Hf and Zr, $Hf_{12}O_8(OH)_{14}$ double cluster are other SBUs used in literature to create 2D MONs.[17–19] The paddlewheel dual-core SBU is used in this thesis. Metal ions such as Cd(II), Fe(II), Co(II), Cu(II), Zn(II) can form the paddlewheel motif. This SBU has a D4h symmetry with four carboxylate ligands organised in a plane around two metal ions, capped with axial ligands.

Organic ligands impart the tunability and diversity of organic chemistry to MONs allowing their structures to be systematically changed and new functional groups added. The different geometries and functional groups of organic ligands offer opportunities to construct a diverse range of structures.[13] As with MOFs, polycarboxylates are the most popular organic ligands for MONs because of their directional coordination chemistry. The first layered MOF to be exfoliated to MONs was made of 1,4-benzene dicarboxylate (BDC) coordinated via Zn paddlewheels with water molecules in the axial positions.[16] Isostructural MONs are reported with various metal ions such as Cu, Zn, Co and ligands such as 1,4-BDC, functionalised BDC with weakly interacting alkyl-ether chains, functionalized ligands of 2,5-bis(alkoxy)benzene-1,4-dicarboxylates etc.[20,21] Longer alkyl chain substitutions are known to reduce the interlayer interactions and favour the formation of thinner nanosheets. Benzene-1,3,5-tribenzoate (BTB) moieties, tetraphenylethylene-based tetracarboxylate (TCBPE) and tritopic carboxylates are other ligands that have proved popular in being used to create 2D MONs.[17,22–24]

N-donor based MONs are constructed using layered ZIFs (ZIF= zeolitic imidazole framework), with the compositions such as $Zn_2(bim)_4$, $Zn(bim)(OAc)$, $Co(mim)_2$, where (bim = benzimidazolate; mim = methylimidazolate). These sheets have found applications in gas separation, catalysis, and templating. Other N-donor ligands used in MON synthesis are the 4,4-bipyridine system, tri and hexa-dentate terpyridine coordinated to M(II) ions, tri, or tetra dipyrrinato ligands coordinated to tetrahedral Zn ions.[25–28]

Planar metal-dithiolene complexes with periodic 2D network topology are synthesised and evaluated for their electronic properties. Benzenehexathiol (BHT) when reacted with Ni(II) and Pd(II) created planar nanosheets with strong charge delocalization. Expanded versions of these structures are the isostructural Co-THT and Fe-THT (THT = 2,3,6,7,10,11-triphenylenehexathiolate) MONs which exhibit temperature-dependant charge transport properties.[29–37] Their amino analogues such as hexaminobenzene, hexaminotriphenylene and mixed amine/thiolene MONs with related structures also formed semiconducting networks.[37]

2.2 Porphyrin-Paddlewheel MONs
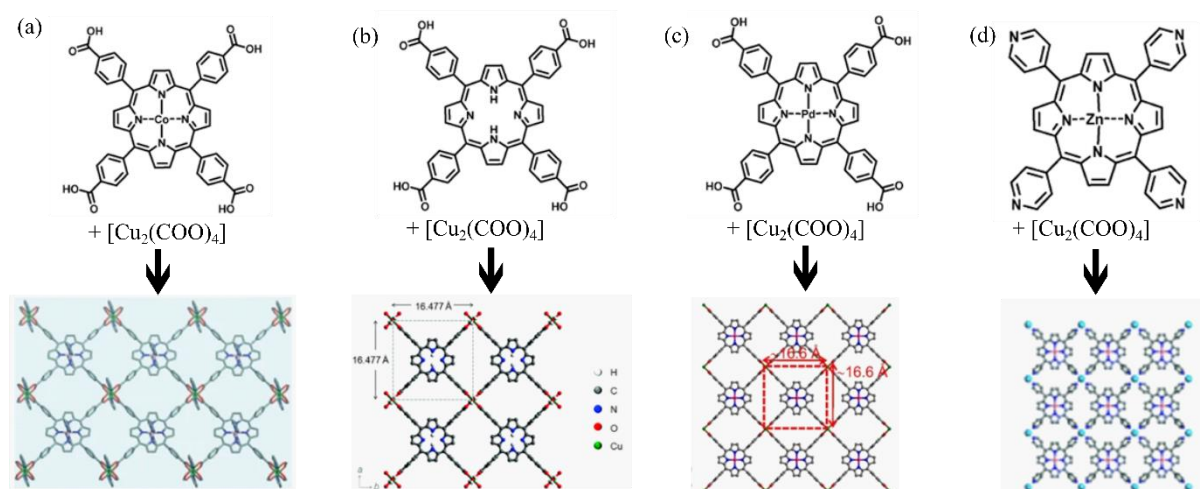
Figure 2.2. Porphyrin organic linkers commonly used in combination with planar paddlewheel SBUs for MON formation.

Porphyrins are another class of commonly employed planar ligands that have proven to be useful for constructing MONs. Porphyrins are well-known for their role in biological functions and have been widely investigated in photocatalysis, light harvesting and oxygen transportation.[38] Their delocalized π-conjugated structure and strong coordination capabilities towards metal ions makes them ideal in MON synthesis. They are well-suited for constructing 2D networks, thanks to the square planar shape of the conjugated tetrapyrrolic macrocycle which offers a high degree of connectivity, rigidity and robustness to the structure.[39–45] **Figure 2.2(a-d)** represents some of the candidates from the huge variety of available porphyrin derivatives incorporating different centre-coordinated metals and various functional groups. This allows fine control over the structure and property of the resulting MONs. While most examples of porphyrin MONs are assembled using the prototypical TCPP system with different metal combinations, some examples include other tetracarboxyporphyrin units such as tetrakis [4-(carboxymethyleneoxy)phenyl]-porphyrin (TCMOPP), 5,10,15,20-tetra(4-pyridyl)-

porphinato zinc(II) (ZnTPyP), trans-5,15-diphenyl-10,20-di(4-carboxyphenyl)porphine (trans-H_2DCPP), 5,10,15,20-tetrakis[4-(4-carboxyphenylethynyl)phenyl] porphine (H_2TCPEPP), 5,10,15,20-tetrakis[4'-(terpyridinyl)phenyl]porphyrin (TTPP) and 5,10,15,20-tetrakis[4'-(terpyridinyl)-1,1'-biphenyl]porphyrin (TTBPP) etc.[41,46–49] This thesis primarily includes the prototypical TCPP ligand in combination with the planar paddlewheel SBUs described earlier, to form MONs for light harvesting applications. In this kind of MON, the TCPP ligand is linked by four paddlewheel metal nodes ($M_2(COO)_4$) to form a square-grid layered motif. During the reaction, the centre of the TCPP ligand is also metallized by the M^{2+} ions. The layered sheets are further stacked in an AB pattern, in which metal atoms in the centre of the porphyrin ligand are aligned with the metal atoms in the paddlewheel metal nodes, forming a 2D MON structure.

The diverse chemistry that arises out of the metal-organic composition of MONs is a distinctive advantage over the simple inorganic nanosheets. While the choice of linkers imparts the functionality to the MONs, several other factors like lateral size, thickness, defects, crystallinity, and surface properties have the potential to affect the performance of MONs. These factors are controlled by the preparation methods used for obtaining MONs, discussed in the following section.

2.3 Synthetic Approaches for MONs

There are two distinct methodologies to approach the synthesis of MONs: "Bottom-up" techniques in which MONs are assembled directly as discreet entities by arresting the crystallisation process and "top-down" approaches in which the nanosheets are exfoliated from bulk layered materials. These techniques have been extensively reviewed elsewhere.[9,13,50] In this section a very brief account of the various techniques most relevant to the thesis is provided.

2.3.1 Bottom-up synthesis

In this approach, MONs are directly self-assembled from solutions of metal ions and ligands. The important step in this method is to promote the growth in two-dimensions (lateral directions) whilst arresting the growth in the third dimension (vertical directions).[14] This approach has resulted in the preparation of large area MONs.
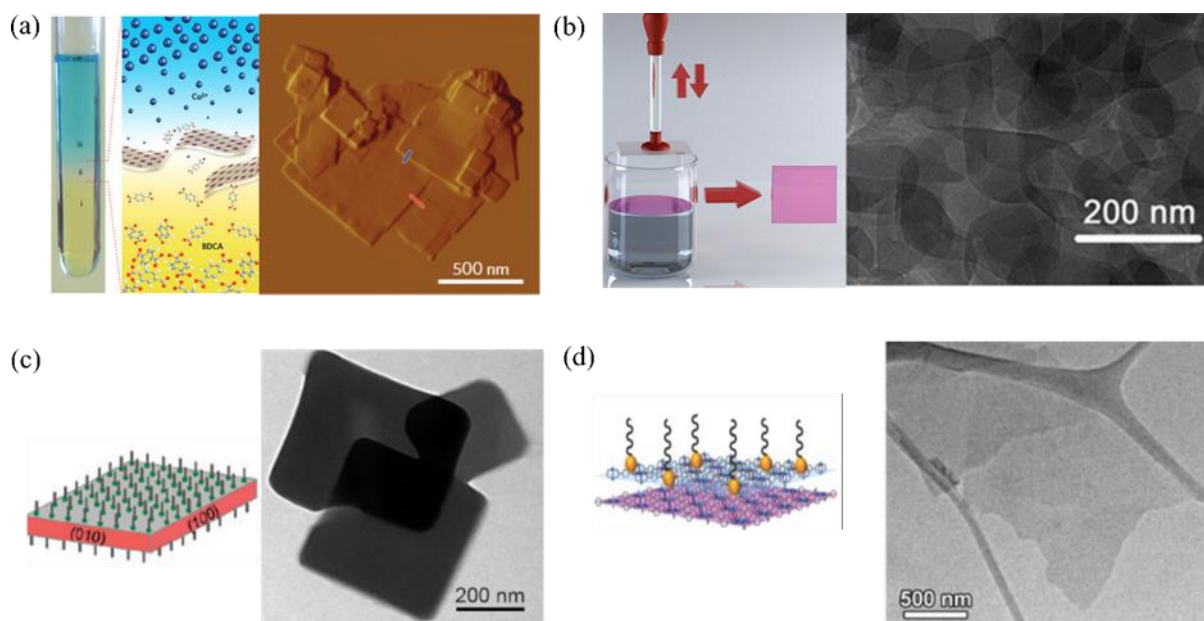
Figure 2.3. (a) Spatial arrangement of different liquid layers and AFM image of the synthesised Cu-BDC nanosheets; (b) MON film assembled onto quartz via stamping, and the corresponding TEM image of the nanosheets; (c)Selective modulation towards MON synthesis and TEM images of the MONs prepared; (d) Surfactant-assisted synthetic method showing the selective attachment of surfactant on the surface of MOFs leading to anisotropic growth resulting in the formation of ultrathin MONs and the corresponding TEM image.

Interfacial synthesis is the most widely used bottom-up methods for MON preparation. This method forces the growth of MONs at the confined interface where the reaction between organic ligand and the metal ions can occur prior to the crystal growth spreading horizontally. The different types of interfaces used to synthesise MONs are liquid/liquid, liquid/air and liquid/solid interface.[30,33] For liquid/liquid interfacial synthesis, two immiscible liquids are used to dissolve the metal ions and the organic ligands (such as water/DCM; water/ethyl acetate). At the interface of the solvents, the metal ions encounter the ligands and lead to MON formation. The thickness of the nanosheets are tuned by the concentration of the ligand solutions, with the reported MON sizes being about 100nm in thickness.[36,51–56]

Liquid/air interface has been successful in yielding ultra-thin MONs. In this method, a small amount of organic solvent is added to the surface of water. After evaporation of the organic solvent, the liquid/air interface is formed. The reaction takes place on the water surface, and the well-dispersed organic ligands give rise to monolayer MONs.[30,47,48,57,58] One of the first synthetic methods for porphyrin MON formation was the layer-by-layer fabrication coupled with the Langmuir Blodgett technique (liquid/air interface).[42] This method resulted in highly crystalline large area MONs that were ~20nm thick. Later studies optimised the dependence of

the number of cycles to the layer thickness and resulted in monolayer MONs.[59–62] A limitation of the interfacial method is that since the interface size determines the yield of MONs, it is not a viable method for large scale synthesis.

Layering is another bottom-up method of synthesis in which ligands and metal ions are dissolved in different ratios of solvents to produce solutions of different densities which are layered on top of each other with a buffer layer in between. The synthesis medium contains two miscible solvents, and the buffer layer determines the diffusion speed of the ligands and the metal ions.[2,63,72–75,64–71] The solvents are vertically aligned to begin with, and the slow diffusion of the ligand and metal ions into the buffer layer produces preferential growth in two-dimension to produce nanosheets which then sink as a result of gravity into a metal ion deficient layer, preventing further growth as shown in **Figure 2.3a**.[2] This method facilitates the formation of high aspect ratio MONs. This three-layer method also gives a higher yield of MONs, as unlike in interfacial method, the MON growth is not limited by the interface area.

The layer-by-layer assembly technique was further improved by a two-step MON film technique where a 'modularization' step precedes the 'assembly step'. Here, solvothermally prepared MONs were drop cast onto water which served as a perfectly flat substrate. The MON films formed on water were then transferred to substrates of choice by a stamping technique.[76] This method enabled faster growth of MON films. (**Figure 2.3b**).[77] But not all linkers with the desired properties can be pre-disposed towards forming 2D structures. In the cases were 3D crystals are preferentially formed, addition of small molecule crystal growth modifiers can compete with pillaring units to result in formation of large area MONs. In a classic example shown in [$Cu_2(NDC)_2(DABCO)$] (where NDC = 1,4-naphthalene dicarboxylate and DABCO = 1,4-diazabicyclo[2.2.2.]octane), addition of pyridine competes with the pillaring ligand resulting in the formation of about $500nm^2$ MONs (**Figure 2.3c**). Modulator-assisted synthesis has also been explored for Zn-TCPP based systems.[78–81] With the use of 4,4'-biphenyldicarboxylic acid (BPDC), selective coordination took place between the carboxyl functional groups of BPDC and the zinc ions. This coordination bond acted as a nucleation modulator for the controlled growth of MONs.[81] In another similar method using formic acid as modulators, ultrathin (1.5nm) MONs were synthesised with Ni-TCPP and Zirconium paddlewheels.[79] [5] In these cases, the modulators can become incorporated in the nanosheet structure. Sometimes this is not favourable as the modulators can disrupt the optoelectronic properties of the MONs.

Use of surfactants like polyvinyl pyrrolidone (PVP), where they bind to the surface of MONs and prevent re-stacking is another commonly employed method favouring the 2D morphology. **Figure 2.3d** shows the approach used by Zhang and co-workers to form PVP assisted growth of ZnTCPP MONs that were approximately 8 layers thick.[82] Surfactants decrease the surface tension between the phases. The selective attachment of the surfactant molecules on the surface of the MOFs promotes growth in the horizontal direction and prevents re-stacking of the layers. This method can provide a higher yield of MONs. The surfactant molecules (PVP) selectively attach on the surface of the MONs leading to anisotropic growth and formation of ultrathin sheets. The size of the nanosheets obtained by this method was ~7.6 nm.[82] In a facile attempt towards the synthesis of ultrathin MONs that also possess large lateral sizes in high yield, an elevated temperature approach was applied.[39] This was also a PVP-assisted approach, wherein the increase in crystallization temperature from 60°C to 150°C led to a gradual decline in layer thickness (2-3 layers), gradual increase in lateral size with high aspect ratio MONs and increased yield from 7.4% to 73.2%. The higher temperature was reported to enlarge the interlayer distance and accelerate the crystal growth along the lateral direction.

2.3.2 Top down synthesis

The 'top-down' synthetic approaches are inspired by the way that layers of graphite can be separated (or exfoliated) to form nanosized sheets of graphene. Preferentially breaking apart

(a)

(b)
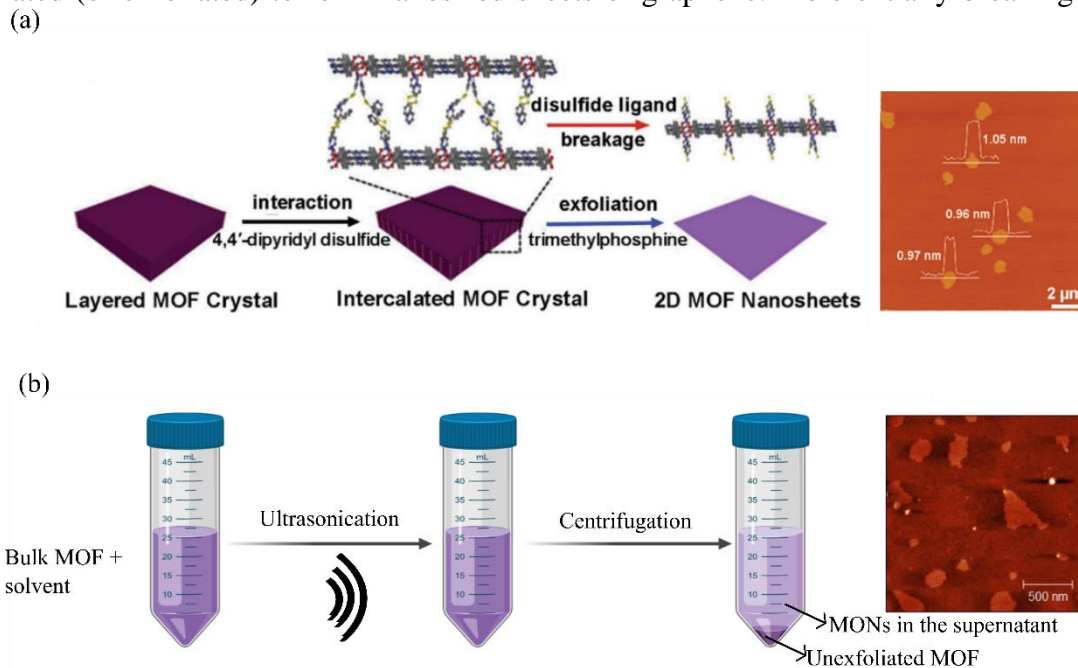
Figure 2.4. Schematic representation of the top-down exfoliation techniques for the preparation of MONs.

weak interactions between the layers, without disrupting strong bonding interactions within them is the principle underlying the top-down approaches.[83] This method of synthesis involves two-types of exfoliation techniques – physical exfoliation and chemical exfoliation. In the case of 3D MOFs, chemical exfoliation techniques are required for the decomposition or structural modification of the pillaring unit between layers.[14] 2D frameworks are chosen for physical exfoliation because they involve non-covalent interactions such as hydrogen bonding, π-π interaction etc that can be easily overcome.[13]

The intercalation of molecular/ionic species between MOF layers is an approach to form large quantities of free-standing MONs. This method induced exfoliation by increasing the interlayer distance and thereby converting a 3D or 2D MOF into MONs. In the case shown in **Figure 2.4a**, 4,4' dipyridyl disulfide (DPDS) molecule was introduced to coordinate with the metal nodes of layered porphyrin-based MOF crystals. By chemical scissoring of the disulfide bond in DPDS, the layers expand leading to weakening of the interlayer interactions. The cleavage of the intercalated disulphide groups occurs rapidly and is capable of controlling the MON thickness.[45] When subjected to ultrasonication, this resulted in the formation of ultrathin (~1 nm thickness) MONs with a ~57% yield. Another example was the case of lithium ion intercalation, wherein the intercalated MOFs were subject to sonication and the forced hydration of the lithium forced the layers apart.[84]

Physical exfoliation has so far been achieved through a wide range of methods including the 'scotch-tape' method, mechanical grinding and ball milling.[85–87] Ultrasonic liquid exfoliation (**Figure 2.4b**) is the most widely adopted method of MOF exfoliation and is the method used in this thesis. It is known to give sizable quantities of MONs. Typically, ultrasonicators provide an energy input of 20-80 kHz with powers of 80-750 W and have demonstrated layer separation with the penetration of solvent. This method resulted in smaller crystallite fragments and subsequently broader particle size distribution. Along with exfoliation, sonication also results in fragmentation of MONs, warranting the use of low energy-input. The role of solvents and coordinated water is yet to be understood fully in this process. The key factors to be considered for the choice of the exfoliating solvent are – stability of the MOF in the corresponding solvent and the matching of surface energy between the solvent and MOF. The stability of the MOF in the solvent is necessary to help maintain the structural integrity of MON during and after the ultrasonic treatment. Matched surface energy results in easy penetration of the solvent between the layers of the MOF. As the solvent gets into and between the layers of the MOF, expansion of the distances between the layers takes

place, leading to production of free-standing MONs. The matched surface energy between the solvent and the MON also helps to stabilize the exfoliated MONs and prevent their re-stacking once the ultrasonication is stopped. While this is a popular method for MON production, the lack of uniformity in sizes and the increased fragmentation of the units are some of the disadvantages of this technique.[13,20,88] Usually, this technique is combined with centrifugatin to remove the larger unexfoliated particles.[89] Despite the challenges in yield and stabilization of the exfoliated nanosheets, top-down methods remain an effective and simple way to prepare clean and highly crystalline MONs.

Bottom-up methods generally give larger, thicker nanosheets with a narrower size distribution in low quantities, whereas top-down methods give smaller, more irregularly shaped nanosheets that with a broader size distribution. Optimisation is required for each MON system to identify the best working exfoliation technique for it. The use of surfactants can aid nanosheet formation, but block pores and active sites and can be difficult to remove. The chemical and thermal stability of the MONs within the medium of exfoliation are another factor to be considered before selecting an appropriate MON preparation technique. The preferred method of synthesis will also depend on the properties required for a particular application. For instance, electronics applications require ultrathin MONs for optimum device performances, whereas for separation related application, higher aspect ratios are desired.

2.4 Applications of MONs

The 2D structure and the topological and functional tunability of MONs makes them a versatile class of materials which have been explored for applications as diverse as gas storage, water purification, catalysis, drug-delivery, sensing, imaging and electronics.[8–11] The versatile composition that can be obtained by changing the metal-node/organic ligands offers the advantage of tailoring a MON for a particular application. MONs have been used as ultra-permeable and highly selective membranes for gas separation, heterogenous catalysts resulting in higher reaction rates than bulk MOFs, highly sensitive and selective sensing platforms and as nanocarriers for the delivery and release of nucleic acids and drugs. Hybridization of MONs with other nanomaterials resulting in functional composites/heterostructures have also shown promise for various electrocatalytic applications.

2.5 Emerging Interest in MONs for Electronics

Chapter 1 clearly established that more efficient energy harvesting and storage technologies are urgently needed to address the climate crisis and that this is further catalysing research into new materials. The silicon-centred paradigm in electronics is recently being challenged by the commercialization of OLED technology, increasing interest in hybrid perovskites for light harvesting and new types of graphene based integrated photonics. Layered materials like graphite, oxides, chalcogenides and clays have been of profound interest in materials chemistry because of their opto-electronic and mechanical properties.[93–97] The enhanced surface areas of the exfoliated materials as compared to the bulk materials, the quantum confinement of electrons in two-dimensions transforming the band structure and their nanosized dimensions are desirable characteristics that led to increasing interest in exfoliated materials.[98] Ultrathin 2D materials have exhibited unconventional emission, light sensitivity, plasmonic effects, carrier mobility etc.[11] Hybrid organic-inorganic materials offer advantages over inorganic materials in being solution processable and forming at lower temperatures, potentially allowing for lower production costs.[99] Interfacing between organic-inorganic materials also allows for a more diverse range of properties and greater tuning of their electronic and optical properties such as their dielectric properties, [100] electrical resistance, [101] redox activity and band gap. [102–105] The ability to control the structure of active materials at the nanoscale level is important for the optimization of electronic devices and the nanoscale dimensions of MONs open up new opportunities for use in thin-film devices not available to bulk MOFs.[106] This section focuses on the progress that has been made in the use of MONs within sensors, batteries, supercapacitors, solar fuels, light emitting diodes and photovoltaics. In each case the different roles that MONs have been shown to play in literature have been discussed.

2.5.1 Sensor devices

MONs have been cast as films onto interdigitated electrodes and used as chem-resistive sensors. These devices monitor the changes in resistance to quantitatively detect the analyte gas molecules. Dinca and co-workers demonstrated the use of conductive MONs of $Cu_3(HITP)_2$ where HITP = hexaminotriphenylene as ammonia sensors via potentiostatic measurements (**Figure 2.5a**).[107] These MONs with intrinsic pi-conjugation and charge de-localization within the plane, showed a conductivity of 0.2 Scm^{-1}. Similar chemresistive sensors with isomorphic MONs- $Ni_3(HITP)_2$ and $Cu_3(HHTP)_2$ where HHTP is (2,3,6,7,10,11-hexahydroxytriphenylene), were shown to reliably distinguish between different categories of
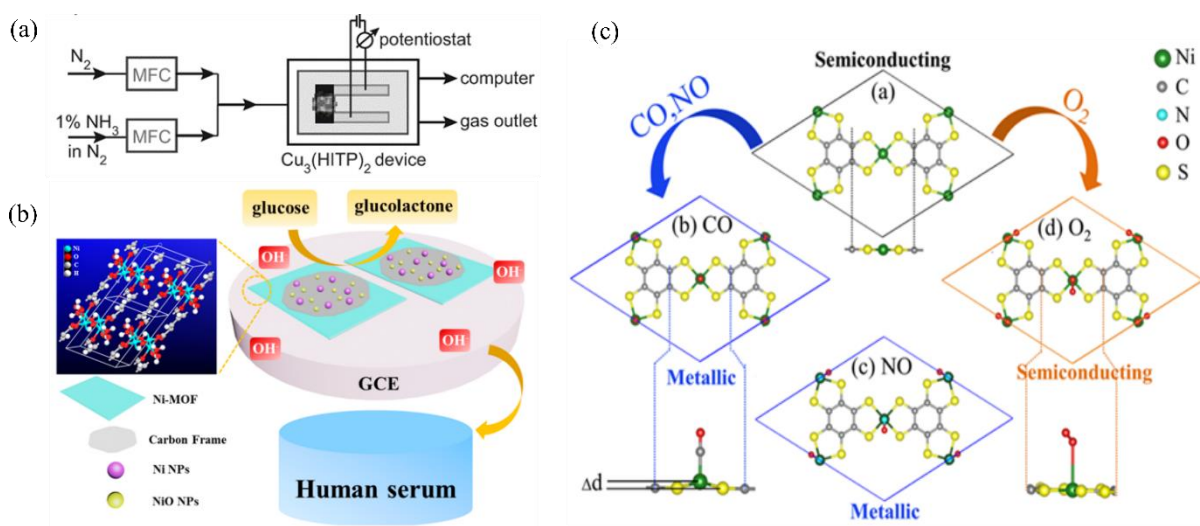
Figure 2.5. (a) Scheme of a MON based chem-resistive device for ammonia sensing;[107] (b)Schematic of the Ni-MOF/Ni/NiO/C nanocomposite glucose sensor for human serum samples; (c)Schematic representation of change in electronic nature of MONs upon gas adsorption.[109]

volatile organic compounds. The authors attributed either charge transfer or hydrogen bonding as the possible mechanisms for the various sensing responses observed. [108]

SC Marinescu and co-workers in a first principles calculation study showed that the selectivity of semiconducting MONs towards gas sensing arose from the increased electronic states near the fermi level due to adsorption of the gas molecules onto MONs (**Figure 2.5c**). The authors stated that the resulting up-shifted fermi level is expected to change the electronic property of the MONs from semi-conducting to metallic – leading to the chem-resistive response.[109]

Hu and co-workers demonstrated the use of Ni-BDC MONs (where BDC= 1,4 benzenedicarboxylic acid) when composited with Ni/NiO/C as a non-enzymatic glucose sensor with high sensitivity of 367.45 mA M^{-1} cm^{-2} (**Figure 2.5b**).[110] Other notable examples include Co-TCPP(Fe) MONs as amperometric sensors for H_2O_2 detection, AuNCs@521-MOF (where NC= nanocrystal) for detection of cocaine by electrochemical impedence spectroscopy and Zn-TCPP MONs for amperometric sensing of nitrite.[111–113]

Layered MOFs with conductive networks have also been assembled as a transducer device for molecular recognition via capacitive response. NH$_2$-MIL-53(Al) (where MIL-53 is a MOF topology based on inorganic trans-connected AlO$_4$(μ_2-OH)$_2$ octahedra forming linear chains) was synthesised as nanosheets and nanoparticles by Gascon et al using surfactant-assisted arrested crystallization technique and cast as films over *p*-doped silicon substrates to obtain planar capacitive electrodes.[114] The authors showed that the conductive network in the

nanosheets being oriented along the shortest particle dimension enabled better capacitive sensing with reduced response time.

2.5.2 Electrodes for energy storage

MONs have been explored as potential materials for electrodes in high performance lithium-ion batteries (LIB). The accessible redox active centres in MONs offer enhanced Li^+ ion insertion/desertion when used within the anodes of LIB. Hu and co-workers demonstrated this strategy in nickel 1,4-benzenedicarboxylic acid ($Ni_2(OH)_2BDC$) MONs, manganese 1,4-benzenedicarboxylic acid ($Mn_2(OH)_2BDC$) MONs and cobalt thiophenedicarboxylic acid (Co-TDA) MONs (**Figure 2.6a-c**).[115,116] The authors proposed that the lithiation/de-lithiation mechanism in these systems showed the involvement of both, the metal centre and the chelating ligands, in the reduction/oxidation process, thereby providing a high theoretical electron storage capacity for the electrode. The ultra-thin morphology of the MONs offered shorter ion diffusion distances to the internal electroactive sites. This effective ion transportation in the MON based anodes resulted in 100% coulombic efficiency, outstanding rate capability and long-term cyclic performance - key performance parameters in LIBs. [115–117]

MONs have also been used in conjunction with conductive supports to form high performing hybrid electrodes. Yao et al demonstrated the use of nickel 2,6-naphthalene dicarboxylic acid (Ni-2,6 NDC) MONs grown on carbon nanotube fibres as a barrier free cathode to form a fiber-aqueous rechargeable nickel-zinc (FAR Ni-Zn) battery (**Figure 2.6d-f**).[118] The prepared device displayed high rate capacity and stability with up to 89% retention in capacity after 600 cycles of operation. Zong and co-workers studied the use of bimetallic porphyrin MONs/reduced graphene oxide (CoNi-MON/rGO) composite as the air electrode in zinc-air batteries. The authors attributed the superior performance and stability of this electrode to the optimised electronic conductivity of the bifunctional MON/rGO composite.[119]

MONs with high electrical conductivity have been reported as high performing electrodes in supercapacitors. Wei et all demonstrated the pseudocapacitive behaviour of conductive Co-MOF nanosheets (**Figure 2.6 g-i**).[120] The study showed that the large interlayer distance in the MON structure provided enough space for electrolyte storage and ensured efficient OH^- intercalation and de-intercalation. The conductive network frame acted as an electron transport channel. The authors demonstrated that with a conductivity of 3.75×10^{-3} S cm^{-1}, the MONs helped accelerate the transfer of electrons at the electrode-electrolyte interface. Bu and co-workers demonstrated faradaic properties in a Ni-Co bimetallic MOF electrode

deposited on Ni foam. This electrode showed lower series resistance and faster electron transfer rate during
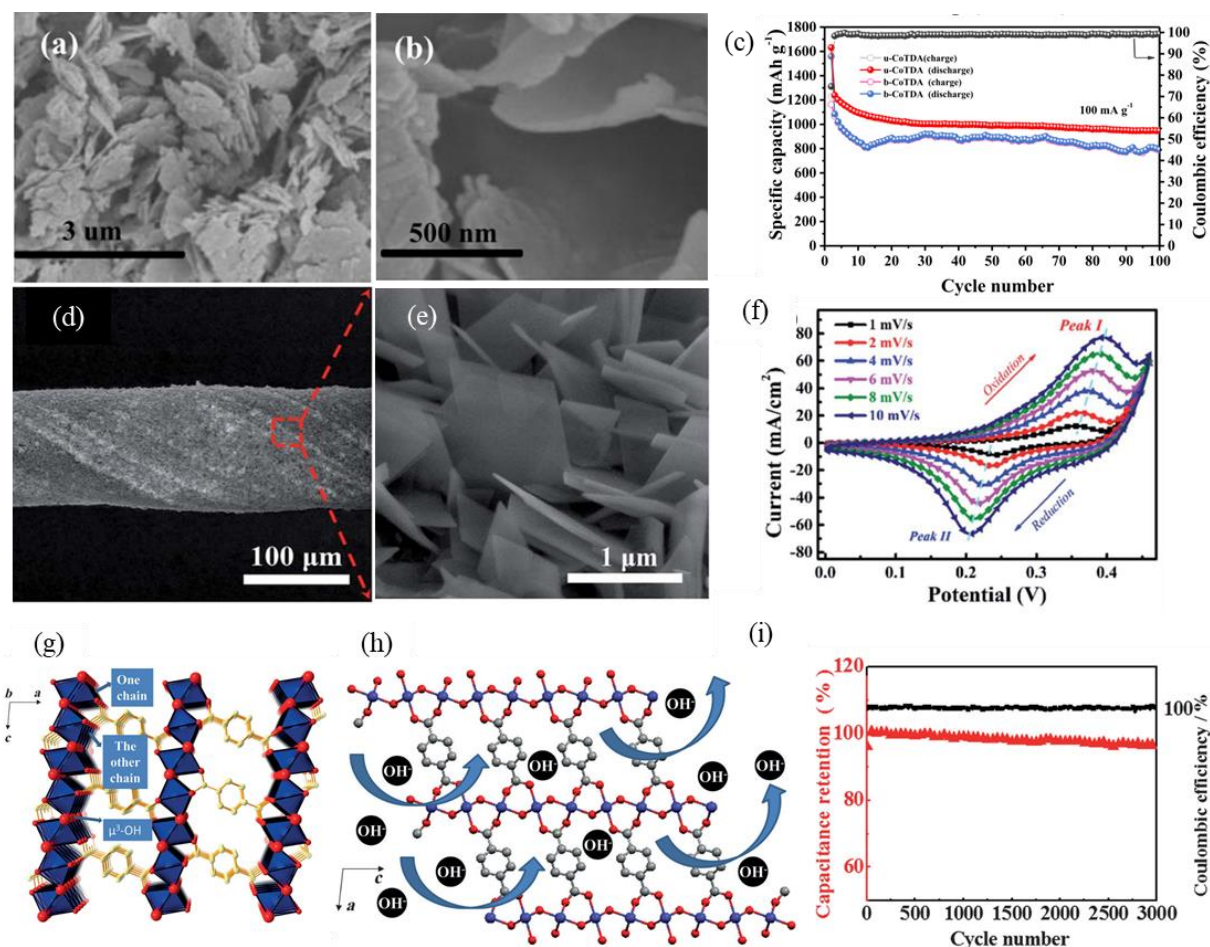

Figure 2.6. MONs in energy storage applications (a) and (b) SEM images of Co-TDA MONs employed as anodes in Lithium ion batteries;[115] (c) Cycling performance of CoTDA MONs (u-CoTDA) compared with the bulk MOF (b-CoTDA) at a current density of 100 mA/g versus Li+/Li with the corresponding Coulombic efficiency;[115] (d-e) SEM images of Ni-MOF/CNTF showing nanostructured hybrid composites of MONs;[118] (f) The cyclic voltammetry curve of the corresponding MON based FAR Ni-Zn battery;[118] (g) Structure of the Co MON with a layered structure and a conductive network frame used as a supercapacitor electrode;[120] (h) Schematic representation of Intercalation/de-intercalation process of OH-1 in the layered structure of the Co-MOF crystal.[120] (i) Charge–discharge profile (black line) and specific capacitance (red line) at a current density of 2A/g of the Co-MOF electrode.[120]

the charge/discharge procedure.[121] The electrochemical performance was shown to be better than the single ion MOFs due to the improved conductivity. In another study by Li and group, Ni-Co BDC MONs displayed strong coupling between the Ni^{2+} and Co^{2+} species which facilitated charge transfer during electrochemical reaction leading to high pseudocapacitive behaviour.[122] Nickel-cobalt terephthalic acid (Ni-Co PTA) MONs on activated carbon were used to create asymmetric supercapacitors in another similar work by Yang et al.[123]

With a vast number of MONs exhibiting limited electrical conductivity, compositing them with other conductive nanomaterials is also a typical approach in supercapacitors. Zheng and co-workers demonstrated that NiTCPPfilm/CNT composites (TCPP =tetracarboxy phenylporphyrin; CNT= carbon nanotubes) exhibit 1.8 times and 14 times higher specific capacitance than pure NiTCPP and pure CNT electrodes respectively.[124] The authors showed that the hybrid nanostructures reduced the aggregation of individual components and provided a shorter route between each component thereby improving electron transfer. Liu and co-workers developed 2D NiCo-MOF ultrathin nanosheets/rGO hybrid electrode. The authors showed that the rGO facilitated the ionic and electronic conductive pathway while the redox active sites of the MONs provided an additional pseudocapacitive component.[125] Zhang et al demonstrated electrostatically self-assembled TCPP/GO (tetracarboxyphenyl porphyrin/ graphene oxide) electrode as a flexible asymmetric supercapacitor. The electropositive TCPP MONs and electronegative GO sheets when composited together showed bending tolerance and good conductivity.[126]

MONs have also been employed as substrates to host electrode materials. Zhao et al demonstrated the electrochemical polymerization of polypyrrole (PPy) onto wrinkled 2D ultrathin CuTCPP nanosheets to construct a flexible CuTCPP/PPy hybrid film. The authors attributed the enhanced supercapacitive performance to intense electronic interaction between the CuTCPP MONs and polypyrrole and the porous film structure that facilitated sufficient immersion of the electrolyte.[127] Detailed mechanistic investigations showed that PPy offered a conductive network for fast electron transport and enhanced the electrochemical kinetics. In a similar work, polypyrrole nanotubes have also shown success when used in conjunction with MONs to impede aggregation, boost conductivity and enhance the pseudocapacitance behaviour.[128] In another example, Pang and co-workers used the porous Cu-BTC (BTC =1,3,5 benzene tricarboxylic acid) MON as an inert host for pseudocapacitive MnO_2 nanoparticles. The authors attributed the resulting superior charge-discharge performance to the film formation in the MON/nanoparticle composite that favoured the diffusion path of ions.[129]

2.5.3 Generation of solar fuels

Solar fuels generated via photocatalysis (artificial photosynthesis) are considered a promising energy generation method. MONs have the potential to play a role in the light absorption, charge funnelling and redox reactions as part of these systems.[130] Qiao at al used a 2D Ni-based MOF (NMF) [Ni(phen)(oba)]$_n$·$0.5n$H$_2$O (phen = 1,10-phenanthroline, oba = 4,4′-

oxybis(benzoate)), as a platform to host CdS photocatalyst resulting in the best performing example (highest activity) of a noble-metal free photocatalytic H_2 generation of this kind (**Figure 2.7a**).[131]
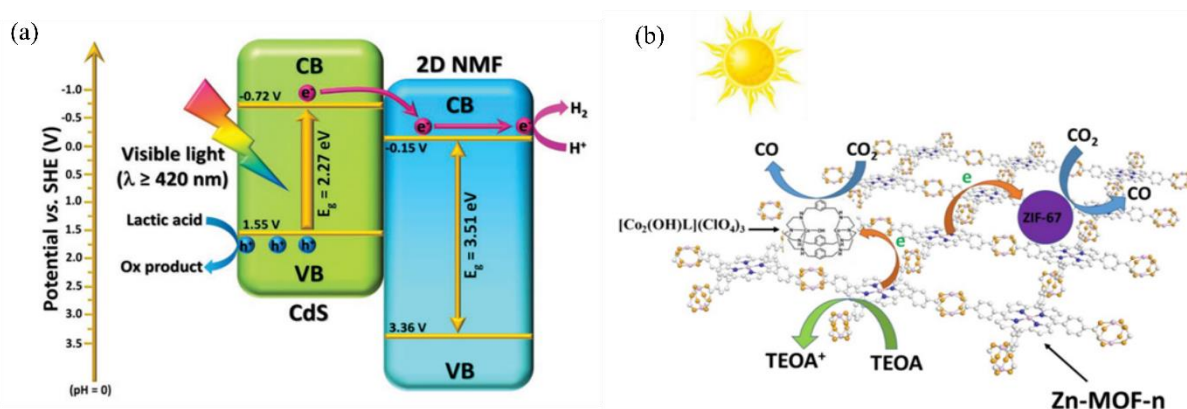

Figure 2.7. MONs for generation of solar fuels (a) The excitons dissociation and transfer in the 2D NMF/CdS heterostructure under visible-light irradiation. The pink and blue spheres denote photoinduced electrons and holes, respectively.[131] (b) A MON/complex or MON/ZIF system for CO_2 photoreduction with Zn-MOF nanosheets as the photosensitizer;[133]

The authors demonstrated the formation of a staggering-type heterojunction between the MONs and CdS. Upon visible-light illumination, the photo-induced electrons transfer from the conduction band of CdS and migrate to active centres on the surface of the MONs that reduce protons to generate H_2 gas. The photo-induced holes remain on the valence band of CdS for the oxidation of lactic acid. Duan et al demonstrated the loading of plasmonic Au nanoparticles on Co-PPF3 MONs (Co-TCPP with Bpy (bipyridine) pillars prepared by surfactant assisted method) for photocatalytic CO_2 generation.[132] The authors showed that the hot electrons generated by surface plasmon resonance excitation of the nanoparticles have higher fermi levels and can easily be injected into the Co^{2+} centres of the MON leading to a higher photocatalytic efficiency. The plasmon resonance energy transfer effect was found to become weaker with increasing thickness of the MONs. Efficient photoelectrochemical reduction of CO_2 was demonstrated by Sun and co-workers using ZnTCPP MONs as semiconducting photosensitizers along with ZIF-67 (ZIF= zeolitic imidazolate framework) as co-catalyst (**Figure 2.7b**).[133] Photoelectrochemical impedance measurements from the fabricated device and steady state PL measurements showed that MONs enabled better charge transport, efficient separation and longer lifetime of the photogenerated charge-carriers.

In all the previously described examples, the hybrid catalysts are assembled via physical/electrostatic interactions. Liu et al show that the attachment of carbon nitride quantum dots via coordination to the Co active sites in CoTCPP based photosensitizer improves

directional transfer of the photogenerated electrons from the quantum dots to the Co sites for efficient photocatalytic reduction of CO_2.[134] The low dimensionality of both the components enabled spatial separation of the photoexcited charge carriers and acceleration of charge transfer.

2.5.4 MONs in light emitting devices

MONs have also been used in a couple of ways to create light emitting devices. In a recent work by Nishihara and co-workers, bis(dithiolato)nickel (NiDT) nanosheets on ITO were employed as the hole buffer layer within OLED devices. The devices showed comparable efficiencies to conventional OLEDs and nearly 2-fold enhancement in device lifetime compared to the standard PEDOT:PSS based devices.[36] Another promising example of MONs in emissive applications is by Lin et al[80] who used TCBPE-Zr cluster based MONs to create visible light communication devices. The bi-layered nanosheets display favourable photophysical properties, high quantum yields and restricted internal motion of the fluorescent struts owing to the network structure. However, there is a drop of 30% in output power following 168 hours of operation, which the authors attribute to degradation of the linker upon light-exposure in the presence of oxygen.

2.5.5 MONs in photovoltaic devices

The first example of MONs used in a functional solar cell was as a buffer layer by Huang and co-workers. Tellurophene based MON was mixed with a polymer surfactant PEIE (polyethylenimine ethoxylate) to form a hybrid ink that was integrated as an electron extraction layer along with ZnO into organic solar cells (**Figure 2.8a**).[135] UPS measurements showed that the work function of ZnO decreased with the addition of PEIE , whilst adding the MONs increased it to a medium work function that improved device performance. The study showed this as a widely applicable approach by employing this MON based electron extraction layer in two important types of solar cells – P3HT-PCBM the workhorse of semiconducting devices – the most well characterised and largely accepted standard OPV[136]; and PBDB-T-ITIC the best performing non-fullerene OPV at the time.[137] MONs have also been used to form liquid-junction solar cell. Jiang et al showed that porphyrin-based MONs could be assembled onto ITO and embedded with fullerenes to form a functioning device. The high surface area and porous structure of the photoactive MONs enhanced charge transfer to the electron accepting fullerenes resulting in a quantum efficiency of <0.5% (**Figure 2.8b**).[138] .

Recently, A.K.Y Jen and co-workers demonstrated the use of MONs as an electron extraction layer at the perovskite/cathode interface leading to a 22.02% efficient perovskite solar cell.[139] The MONs enabled improved long-term operational stability with up to 90% retention in power conversion efficiency under accelerated testing conditions. The thiol functionalized zirconium 1,3,5-Tris(4-carboxyphenyl) benzene MON formed intimate contact with the silver electrode to extract electrons efficiently from the perovskite solar cell. The authors also demonstrated that the thiol functionalization trapped the mobile Pb^{2+} ions at the perovskite/electrode interface – a major step to mitigate the potential impact of perovskites on environmental sustainability.
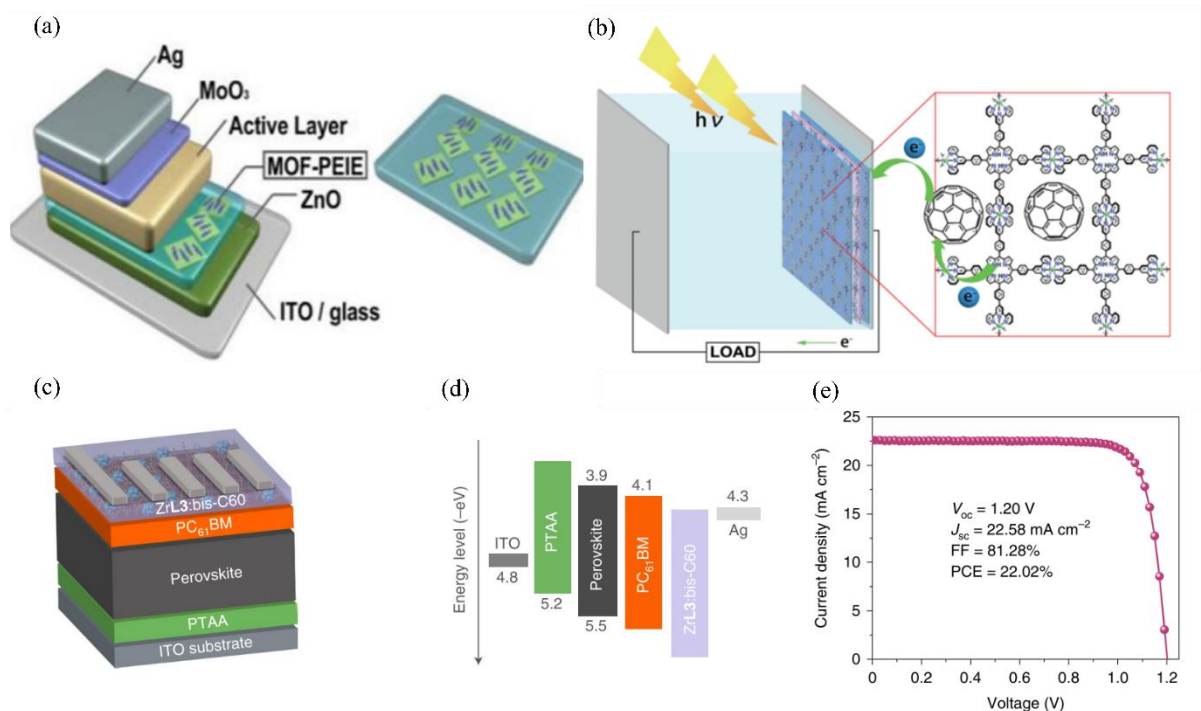
Figure 2.8. MONs in light harvesting devices; (a) Device structure of solar cells investigated with a MON based electron extraction layer;[135] (b) Schematic representation of the porphyrin based liquid junction solar cell with incorporated fullerene;[138](c) device structure of the inverted MON based perovskite solar cell; (d) the energy level alignment of the used materials in c; (e) the J-V curve of the best performing perovskite solar cell with the MON electron extraction layer.

A study published by our group (Chapter 4 in this thesis) is the first example showing incorporation of MONs into the photoactive layer of OPV bulk heterojunctions.[89] Porphyrin MONs as a ternary blend within the archetypal P3HT-PCBM architecture resulted in the formation of a ternary blend solar cell which showed a doubling in device power conversion efficiency (PCE).[89] Detailed investigations into the morphology of the active layer using AFM, wide angle X-ray and dark injection measurements showed that the relative proportion of crystalline regions in the thin films is improved upon incorporation of MONs. Thus, MONs act as templates to increase the crystallinity of the otherwise semi-crystalline polymer P3HT

leading to more balanced charge mobility and device performance metrics. Subsequent studies will be reported shortly showing how this approach can be generalised to other semi-crystalline polymers leading to higher performing devices.

2.6 Perspective and Conclusion

In the past decade, MONs have established themselves as promising materials combining the advantages of two-dimensional materials and metal-organic frameworks. The diverse chemistry that arises out of their metal-organic composition is an advantage as compared to the simple inorganic compositions of other two-dimensional materials such as graphene and MoS_2. MONs can be designed for a particular application by selecting the structural building units of desired properties. Selecting an appropriate MON preparation route is equally important because the factors like lateral size, thickness, defects, crystallinity, and surface properties are vital in controlling the performance of MONs. Though MONs have shown enormous potential in applications such as catalysis and separation, in this chapter a detailed look into the applications of MONs in electronic devices was provided.

Their distinct combination of properties has allowed them to be used in a variety of roles within different electronic devices. The growing number of examples of 2D conducting and semiconducting MONs offer a wide opportunity for MON-integrated sensors and other resistance-based devices. MONs have been shown to outperform their bulk counterparts when incorporated as electrodes in energy storage devices. As MONs approach monolayer thicknesses, they offer shorter diffusion paths for the electrons/ions and improve the rate performance. The higher surface area also increases the number of coordinatively unsaturated redox sites leading to higher capacity of the electrodes. The porous nature of MONs is advantageous to help in the transport of the electrolyte ions in energy storage applications. While not all MONs are electronically conducting, they are physically flexible enough to stick closely with substrates, thereby opening the opportunity to integrate insulating MONs with conductive substrates in many high performing batteries and supercapacitors. The ability of MONs to act as scaffolds to host pseudocapacitive materials and nanoparticles opens versatile options for integrating them into device architectures.

MONs have also shown success when incorporated as platforms for light harvesting catalysts in solar fuel generation. The band gap tunability of MONs expands their role from being inert scaffolds for the photocatalyst to promoting electron transport when incorporated as a

heterojunction. The higher light scattering, and lower charge mobility of MONs are some limitations for this type of application, however the porous nature of MONs offers the distinctive advantage of allowing higher rate of diffusion of the redox carriers through the device. The band gap tunability of MONs is also the main factor allowing for their incorporation in OLEDs and photovoltaics for performance enhancement. MONs have shown tremendous promise as electron extraction layers, templates for favoured crystallization, and as electron donors. Most recent studies on the utilization of diverse chemical functionalities of MONs prove that not only can they impart structural and electronic improvements to the devices but also trap the release of toxic heavy metals and improve environmental sustainability of the device.

Table 2.1 provides a SWOT (Strength, Weaknesses, Opportunities and Threats) analysis of MONs for electronic applications.

Table 2.1. SWOT analysis of MONs in the context of their applications in electronic devices

Strengths	1.The modular design offers band gap tunability 2. Functionality can be tailored for specific application. 3. Nanoscopic dimensions enable easy integration into existing device architectures 4. The simple organic-inorganic building blocks offer ease of synthesis and processing
Weaknesses	1. The thickness and lateral sizes are difficult to control, especially with top-down methods 2. Large area fabrication techniques are still in early stages of research and need further development 3. Disparate materials make it hard to generalize - no single example to illustrate the class of material as a whole
Opportunities	1. There is an increased interest in 2D material integrated photonics, and MONs offer diverse functionality 2. Electronics research is shifting towards organic-inorganic hybrids and the metal-organic linkage in MONs imparts unique opto-electronic features. 3. Breakthroughs have already been demonstrated with MONs across different sectors within electronics (Electrodes, sensors, light harvesters and emitters, memory devices)

	4. With great success in many applications, there is an increased scope for applying computational tools to model and screen the MON properties
Threats	1. Other recent 2D materials (Perovskites, M-Xenes) have already established their focus areas and directions whereas the interest in MONs still remains broad. Choosing a couple of winning applications and pursuing them further is key. 2. Standardised measurement techniques for electronic properties for MONs as a class of materials is still under progress.

In conclusion, MONs have enabled breakthroughs in all major sectors of electronic applications thanks to their modular design and nanoscopic size. The development of large area growth of MON films and standardized measurements across the field are still in progress. However, the short span of time in which most of these developments have grown from ideas to high performing and stable devices is extraordinary. The coming years will determine which of these MON-based electronic applications end up making the transition from lab-based prototypes to a practical manufacturing environment.

2.7 Thesis aims

This thesis aims to explore MONs as potential materials for enhancing the performance of organic photovoltaic (OPV) devices. The porphyrin-paddlewheel MON system provides good absorption features to be incorporated into OPV devices. This thesis is structured around three papers that test hypotheses on the effect of incorporating MONs into the photoactive layers of different OPV systems.

1. How do monolayer MONs with complimentary absorption when added to an OPV device as a ternary component affect its performance? (**Chapter 4**)
2. How does changing the metal/ligand composition of MONs affect its optoelectronic and morphological properties and the resulting photovoltaic performance? (**Chapter 5**)
3. What is the general applicability of MONs to the commonly employed donor-acceptor systems in OPVs? What is the mechanism involved in the cases where MONs result in performance enhancement? (**Chapter 6**)

2.8 References

1   H. C. Zhou, J. R. Long and O. M. Yaghi, *Chemical Reviews*, 2012, **112**, 673–674.

2   T. Rodenas, I. Luz, G. Prieto, B. Seoane, H. Miro, A. Corma, F. Kapteijn, F. X. Llabrés I Xamena and J. Gascon, *Nature Materials*, 2015, **14**, 48–55.

3   H. C. Streit, M. Adlung, O. Shekhah, X. Stammer, H. K. Arslan, O. Zybaylo, T. Ladnorg, H. Gliemann, M. Franzreb, C. Wöll and C. Wickleder, *ChemPhysChem*, 2012, **13**, 2699–2702.

4   D. S. Germack, C. K. Chan, B. H. Hamadani, L. J. Richter, D. A. Fischer, D. J. Gundlach and D. M. Delongchamp, *Applied Physics Letters*, 2009, **94**, 1–4.

5   M. H. Pham, G. T. Vuong, F. G. Fontaine and T. O. Do, *Crystal Growth and Design*, 2012, **12**, 3091–3095.

6   T. Hasobe, K. Saito, P. V. Kamat, V. Troiani, H. Qiu, N. Solladié, K. S. Kim, J. K. Park, D. Kim, F. D'Souza and S. Fukuzumi, *Journal of Materials Chemistry*, 2007, **17**, 4160.

7   S. Dong, H. Tian, D. Song, Z. Yang, D. Yan, Y. Geng and F. Wang, *Chemical Communications*, 2009, 3086.

8   P. Z. Moghadam, A. Li, X. W. Liu, R. Bueno-Perez, S. D. Wang, S. B. Wiggin, P. A. Wood and D. Fairen-Jimenez, *Chemical Science*, 2020, **11**, 8373–8387.

9   W. Zhao, J. Peng, W. Wang, S. Liu, Q. Zhao and W. Huang, *Coordination Chemistry Reviews*, 2018, **377**, 44–63.

10   J. Liu, X. Song, T. Zhang, S. Liu, H. Wen and L. Chen, *Angewandte Chemie - International Edition*, 2020, 2–15.

11   S. Wang, X. Yang, L. Zhou, J. Li and H. Chen, , DOI:10.1039/c9tb02845e.

12   Y. Zheng, F. Sun, X. Han, J. Xu and X. Bu, *Advanced Optical Materials*, 2020, 2000110.

13   D. J. Ashworth and J. A. Foster, *Journal of Materials Chemistry A*, 2018, **6**, 16292–16307.

14   M. Zhao, Y. Huang, Y. Peng, Z. Huang, Q. Ma and H. Zhang, *Chemical Society Reviews*, 2018, **47**, 6267–6295.

15   J. J. Perry, J. A. Perman and M. J. Zaworotko, *Chemical Society Reviews*, 2009, **38**, 1400–1417.

16   H. Li, M. Eddaoudi, T. L. Groy and O. M. Yaghi, *Journal of the American Chemical Society*, 1998, 120, 8571–8572.

17   Z. Hu, E. M. Mahdi, Y. Peng, Y. Qian, B. Zhang, N. Yan, D. Yuan, J. C. Tan and D. Zhao, *Journal of Materials Chemistry A*, 2017, **5**, 8954–8963.

18   M. J. Cliffe, E. Castillo-Martínez, Y. Wu, J. Lee, A. C. Forse, F. C. N. Firth, P. Z. Moghadam, D. Fairen-Jimenez, M. W. Gaultois, J. A. Hill, O. V. Magdysyuk, B. Slater, A. L. Goodwin and C. P. Grey, *Journal of the American Chemical Society*, 2017, **139**, 5397–5404.

19   L. Cao, Z. Lin, W. Shi, Z. Wang, C. Zhang, X. Hu, C. Wang and W. Lin, *Journal of the*

American Chemical Society, 2017, **139**, 7020–7029.

20 D. J. Ashworth, A. Cooper, M. Trueman, R. W. M. Al-Saedi, L. D. Smith, A. J. H. M. Meijer and J. A. Foster, *Chemistry - A European Journal*, 2018, **24**, 17986–17996.

21 D. J. Ashworth, T. M. Roseveare, A. Schneemann, M. Flint, I. D. Bernáldes, P. Vervoorts, R. A. Fischer, L. Brammer and J. A. Foster, *Inorganic Chemistry*, 2019, **58**, 10837–10845.

22 X. Hu, Z. Wang, B. Lin, C. Zhang, L. Cao, T. Wang, J. Zhang, C. Wang and W. Lin, *Chemistry - A European Journal*, 2017, **23**, 8390–8394.

23 L. Zhao, B. Dong, S. Li, L. Zhou, L. Lai, Z. Wang, S. Zhao, M. Han, K. Gao, M. Lu, X. Xie, B. Chen, Z. Liu, X. Wang, H. Zhang, H. Li, J. Liu, H. Zhang, X. Huang and W. Huang, *ACS Nano*, 2017, **11**, 5800–5807.

24 Y. Wang, L. Li, L. Yan, X. Gu, P. Dai, D. Liu, J. G. Bell, G. Zhao, X. Zhao and K. M. Thomas, *Chemistry of Materials*, 2018, **30**, 3048–3059.

25 Y. Peng, Y. Li, Y. Ban, H. Jin, W. Jiao, X. Liu and W. Yang, *Science*, 2014, **346**, 1356–1359.

26 S. C. Junggeburth, L. Diehl, S. Werner, V. Duppel, W. Sigle and B. V. Lotsch, *Journal of the American Chemical Society*, 2013, **135**, 6157–6164.

27 H. L. Liu, Y. J. Chang, T. Fan and Z. Y. Gu, *Chemical Communications*, 2016, **52**, 12984–12987.

28 Y. Lo and D. Y. Kang, *Journal of Materials Chemistry A*, 2016, **4**, 4172–4179.

29 K. Hoshiko, T. Kambe, R. Sakamoto, K. Takada and H. Nishihara, *Chemistry Letters*, 2014, **43**, 252–253.

30 T. Kambe, R. Sakamoto, K. Hoshiko, K. Takada, M. Miyachi, J. H. Ryu, S. Sasaki, J. Kim, K. Nakazato, M. Takata and H. Nishihara, *Journal of the American Chemical Society*, 2013, **135**, 2462–2465.

31 R. Dong, M. Pfeffermann, H. Liang, Z. Zheng, X. Zhu, J. Zhang and X. Feng, *Angewandte Chemie - International Edition*, 2015, **54**, 12058–12063.

32 P. J. Beldon, S. Tominaka, P. Singh, T. Saha Dasgupta, E. G. Bithell and A. K. Cheetham, *Chemical Communications*, 2014, **50**, 3955–3957.

33 A. J. Clough, N. M. Orchanian, J. M. Skelton, A. J. Neer, S. A. Howard, C. A. Downes, L. F. J. Piper, A. Walsh, B. C. Melot and S. C. Marinescu, , DOI:10.1021/jacs.9b06898.

34 A. J. Clough, J. W. Yoo, M. H. Mecklenburg and S. C. Marinescu, *Journal of the American Chemical Society*, 2015, **137**, 118–121.

35 C. Hermosa, B. R. Horrocks, J. I. Martínez, F. Liscio, J. Gómez-Herrero and F. Zamora, *Chemical Science*, 2015, **6**, 2553–2558.

36 S. Liu, Y.-C. Wang, C.-M. Chang, T. Yasuda, N. Fukui, H. Maeda, P. Long, K. Nakazato, W.-B. Jian, W. Xie, K. Tsukagoshi and H. Nishihara, *Nanoscale*, 2020, 0–7.

37 Q. Zeng, L. Wang, Y. Huang, S.-L. Zheng, Y. He, J. He, W.-M. Liao, G. Xu, M. Zeller and Z. Xu, *Chemical communications (Cambridge, England)*, 2020, 2–5.

38   M. G. Walter, A. B. Rudine and C. C. Wamser, *Journal of Porphyrins and Phthalocyanines*, 2010, **14**, 759–792.

39   M. Jian, H. Liu, T. Williams, J. Ma, H. Wang and X. Zhang, *Chemical Communications*, 2017, **53**, 13161–13164.

40   L. Ye, Y. Gao, S. Cao, H. Chen, Y. Yao, J. Hou and L. Sun, *Applied Catalysis B: Environmental*, 2018, **227**, 54–60.

41   R. Makiura, R. Usui, Y. Sakai, A. Nomoto, A. Ogawa, O. Sakata and A. Fujiwara, *ChemPlusChem*, 2014, **79**, 1352–1360.

42   H. L. Zheng, S. L. Huang, M. B. Luo, Q. Wei, E. X. Chen, L. He and Q. Lin, *Angewandte Chemie - International Edition*, , DOI:10.1002/anie.202012019.

43   X. Zhao, J. Bai, X. Bo and L. Guo, *Analytica Chimica Acta*, 2019, **1075**, 71–80.

44   Z. W. Jiang, Y. C. Zou, T. T. Zhao, S. J. Zhen, Y. F. Li and C. Z. Huang, *Angewandte Chemie - International Edition*, 2020, **621900**, 3300–3306.

45   Y. Ding, Y. P. Chen, X. Zhang, L. Chen, Z. Dong, H. L. Jiang, H. Xu and H. C. Zhou, *Journal of the American Chemical Society*, 2017, **139**, 9136–9139.

46   A. Karmakar and I. Goldberg, *CrystEngComm*, 2010, **12**, 4095–4100.

47   R. Makiura and O. Konovalov, *Dalton Transactions*, 2013, **42**, 15931–15936.

48   E. V. Ermakova, I. N. Meshkov, Y. Yu. Enakieva, A. I. Zvyagina, A. A. Ezhov, A. A. Mikhaylov, Y. G. Gorbunova, V. V. Chernyshev, M. A. Kalinina and V. V. Arslanov, *Surface Science*, 2017, **660**, 39–46.

49   C. Liu, C. Wang, H. Wang, T. Wang and J. Jiang, *European Journal of Inorganic Chemistry*, 2019, 1–6.

50   C. Tan, X. Cao, X. J. Wu, Q. He, J. Yang, X. Zhang, J. Chen, W. Zhao, S. Han, G. H. Nam, M. Sindoro and H. Zhang, *Chemical Reviews*, 2017, **117**, 6225–6331.

51   R. Sakamoto, T. Yagi, K. Hoshiko, S. Kusaka, R. Matsuoka, H. Maeda, Z. Liu, Q. Liu, W. Y. Wong and H. Nishihara, *Angewandte Chemie - International Edition*, 2017, **56**, 3526–3530.

52   X. Sun, K.-H. Wu, R. Sakamoto, T. Kusamoto, H. Maeda and H. Nishihara, *Chemistry Letters*, 2017, **46**, 1072–1075.

53   T. Tsukamoto, K. Takada, R. Sakamoto, R. Matsuoka, R. Toyoda, H. Maeda, T. Yagi, M. Nishikawa, N. Shinjo, S. Amano, T. Iokawa, N. Ishibashi, T. Oi, K. Kanayama, R. Kinugawa, Y. Koda, T. Komura, S. Nakajima, R. Fukuyama, N. Fuse, M. Mizui, M. Miyasaki, Y. Yamashita, K. Yamada, W. Zhang, R. Han, W. Liu, T. Tsubomura and H. Nishihara, *Journal of the American Chemical Society*, 2017, **139**, 5359–5366.

54   K. Takada, R. Sakamoto, S. T. Yi, S. Katagiri, T. Kambe and H. Nishihara, *Journal of the American Chemical Society*, 2015, **137**, 4681–4689.

55   R. Sakamoto, K. Hoshiko, Q. Liu, T. Yagi, T. Nagayama, S. Kusaka, M. Tsuchiya, Y. Kitagawa, W. Y. Wong and H. Nishihara, *Nature Communications*, 2015, **6**, 1–9.

56   Z. Sun, L. Hui, W. Ran, Y. Lu and D. Jia, *New Journal of Chemistry*, 2016, **40**, 1100–1103.

57   N. Lahiri, N. Lotfizadeh, R. Tsuchikawa, V. V. Deshpande and J. Louie, *Journal of the American Chemical Society*, 2017, **139**, 19–22.

58   Y. N. Li, S. Wang, Y. Zhou, X. J. Bai, G. S. Song, X. Y. Zhao, T. Q. Wang, X. Qi, X. M. Zhang and Y. Fu, *Langmuir*, 2017, **33**, 1060–1065.

59   A. Ciesielski, S. Colella, L. Zalewski, B. Bruchmann and P. Samorì, *CrystEngComm*, 2011, **13**, 5535–5537.

60   S. Motoyama, R. Makiura, O. Sakata and H. Kitagawa, *Journal of the American Chemical Society*, 2011, **133**, 5640–5643.

61   G. Xu, K. Otsubo, T. Yamada, S. Sakaida and H. Kitagawa, *J. Am. Chem. Soc.*, 2013, **135**, 7438–7441.

62   R. Makiura and O. Konovalov, *Scientific Reports*, 2013, **3**, 1–8.

63   S. Hu, J. Yan, X. Huang, L. Guo, Z. Lin, F. Luo, B. Qiu, K. Y. Wong and G. Chen, *Sensors and Actuators B: Chemical*, 2018, **267**, 312–319.

64   L. Yan, O. J. Silveira, B. Alldritt, O. Krejčí, A. S. Foster and P. Liljeroth, 2020, 1–18.

65   F. Yang, M. Wu, Y. Wang, S. Ashtiani and H. Jiang, *ACS Applied Materials and Interfaces*, 2019, **11**, 990–997.

66   X. Song, X. Wang, Y. Li, C. Zheng, B. Zhang, C. Di, F. Li, C. Jin, W. Mi, L. Chen and W. Hu, *Angewandte Chemie International Edition*, 2019, 10.1002/anie.201911543.

67   Z. Zeng, I. S. Flyagina and J.-C. Tan, *Nanoscale Advances*, , DOI:10.1039/d0na00475h.

68   R. Dai, X. Zhang, M. Liu, Z. Wu and Z. Wang, *Journal of Membrane Science*, 2019, **573**, 46–54.

69   A. C. Elder, A. B. Aleksandrov, S. Nair and T. M. Orlando, *Langmuir*, 2017, **33**, 10153–10160.

70   Z. Bai, S. Liu, G. Cheng, G. Wu and Y. Liu, *Microporous and Mesoporous Materials*, 2020, **292**, 109763.

71   Y. Yang, G.-B. Hu, W.-B. Liang, L.-Y. Yao, W. Huang, Y.-J. Zhang, J.-L. Zhang, J.-M. Wang, R. Yuan and D.-R. Xiao, *Nanoscale*, 2020, **12**, 5932–5941.

72   C. Liu, X. Huang, J. Liu, J. Wang, Z. Chen, R. Luo, C. Wang, J. Li, L. Wang, J. Wan and C. Yu, *Advanced Science*, , DOI:10.1002/advs.201901480.

73   A. C. Elder, S. Bhattacharyya, S. Nair and T. M. Orlando, *Journal of Physical Chemistry C*, 2018, **122**, 10413–10422.

74   Y. Cheng, X. Wang, C. Jia, Y. Wang, L. Zhai, Q. Wang and D. Zhao, *Journal of Membrane Science*, 2017, **539**, 213–223.

75   L. Zhao, B. Dong, S. Li, L. Zhou, L. Lai, Z. Wang, S. Zhao, M. Han, K. Gao, M. Lu, X. Xie, B. Chen, Z. Liu, X. Wang, H. Zhang, H. Li, J. Liu, H. Zhang, X. Huang and W. Huang, *ACS Nano*, 2017, **11**, 5800–5807.

76   G. Xu, T. Yamada, K. Otsubo, S. Sakaida and H. Kitagawa, *Journal of the American Chemical Society*, 2012, **134**, 16524–16527.

77   G. Xu, T. Yamada, K. Otsubo, S. Sakaida and H. Kitagawa, *Journal of the American Chemical Society*, 2012, **134**, 16524–16527.

78   Z. Gao, Y. Li, Y. Zhang, K. Cheng, P. An, F. Chen, J. Chen, C. You, Q. Zhu and B. Sun, *ACS applied materials & interfaces*, 2020, **12**, 1963–1972.

79   T. He, B. Ni, S. Zhang, Y. Gong, H. Wang, L. Gu, J. Zhuang, W. Hu and X. Wang, *Small*, 2018, **14**, 1–6.

80   X. Hu, Z. Wang, B. Lin, C. Zhang, L. Cao, T. Wang, J. Zhang, C. Wang and W. Lin, *Chemistry - A European Journal*, 2017, **23**, 8390–8394.

81   Y. Zhao, L. Jiang, L. Shangguan, L. Mi, A. Liu and S. Liu, *Journal of Materials Chemistry A*, 2018, **6**, 2828–2833.

82   M. Zhao, Y. Wang, Q. Ma, Y. Huang, X. Zhang, J. Ping, Z. Zhang, Q. Lu, Y. Yu, H. Xu, Y. Zhao and H. Zhang, *Advanced Materials*, 2015, **27**, 7372–7378.

83   C. Backes, T. M. Higgins, A. Kelly, C. Boland, A. Harvey, D. Hanlon and J. N. Coleman, *Chemistry of Materials*, 2017, 29, 243–255.

84   W.-J. Song, *Talanta*, 2017, **170**, 74–80.

85   A. Abhervé, S. Mañas-Valero, M. Clemente-León and E. Coronado, *Chemical Science*, 2015, **6**, 4665–4673.

86   Y. Peng, Y. Li, Y. Ban, H. Jin, W. Jiao, X. Liu and W. Yang, *Science*, 2014, **346**, 1356–1359.

87   M. J. Cliffe, E. Castillo-Martínez, Y. Wu, J. Lee, A. C. Forse, F. C. N. Firth, P. Z. Moghadam, D. Fairen-Jimenez, M. W. Gaultois, J. A. Hill, O. V. Magdysyuk, B. Slater, A. L. Goodwin and C. P. Grey, *Journal of the American Chemical Society*, 2017, **139**, 5397–5404.

88   J. A. Foster, S. Henke, A. Schneemann, R. A. Fischer and A. K. Cheetham, *Chem. Commun.*, 2016, **52**, 10474–10477.

89   K. Sasitharan, D. G. Bossanyi, N. Vaenas, A. J. Parnell, J. Clark, A. Iraqi, D. G. Lidzey and J. A. Foster, *Journal of Materials Chemistry A*, 2020, **8**, 6067–6075.

90   R. Kaur, K.-H. Kim, A. K. Paul and A. Deep, *J. Mater. Chem. A*, 2016, **4**, 3991–4002.

91   L. He, F. Duan, Y. Song, C. Guo, H. Zhao, J. Tian and Z. Zhang, .

92   P.-Z. Li, Y. Maeda and Q. Xu, *Chemical Communications*, 2011, **47**, 8436.

93   M. Cox, A. Gorodetsky, B. Kim, K. S. Kim, Z. Jia, P. Kim, C. Nuckolls and I. Kymissis, *Applied Physics Letters*, 2011, **98**, 2–5.

94   M. Shanmugam, T. Bansal, C. A. Durcan and B. Yu, *Applied Physics Letters*, 2012, **100**, 1–5.

95   G. D. Sharma, R. Srivastava, V. Gupta, R. Bhardwaj, N. Chaudhary and S. Chand, *Journal of the American Chemical Society*, 2011, **133**, 9960–9963.

96   S. Wang, B. M. Goh, K. K. Manga, Q. Bao, P. Yang and K. P. Loh, *ACS Nano*, 2010, **4**, 6180–6186.

97   Z. Liu, Q. Liu, Y. Huang, Y. Ma, S. Yin, X. Zhang, W. Sun and Y. Chen, *Advanced Materials*, 2008, **20**, 3924–3930.

98   V. Nicolosi, M. Chhowalla, M. G. Kanatzidis, M. S. Strano and J. N. Coleman, *Science*, 2013, 340.

99   Z. Zeng, Y. Xu, Z. Zhang, Z. Gao, M. Luo, Z. Yin, C. Zhang, J. Xu, B. Huang, F. Luo, Y. Du and C. Yan, *Chemical Society Reviews*, 2020, **49**, 1109.

100   G. Ding, Y. Wang, G. Zhang, K. Zhou, K. Zeng, Z. Li, Y. Zhou, C. Zhang, X. Chen and S. T. Han, *Advanced Functional Materials*, 2019, **29**, 1–11.

101   M. G. Campbell, D. Sheberla, S. F. Liu, T. M. Swager and M. Dincə, *Angewandte Chemie - International Edition*, 2015, **54**, 4349–4352.

102   W. Zhao, J. Peng, W. Wang, S. Liu, Q. Zhao and W. Huang, *Coordination Chemistry Reviews*, 2018, **377**, 44–63.

103   M. D. Allendorf, A. Schwartzberg, V. Stavila and A. A. Talin, *Chemistry - A European Journal*, 2011, **17**, 11372–11388.

104   I. Stassen, N. Burtch, A. Talin, P. Falcaro, M. Allendorf and R. Ameloot, *Chemical Society Reviews*, 2017, **46**, 3185–3241.

105   M. Yuan, R. Wang, W. Fu, L. Lin, Z. Sun, X. Long, S. Zhang, C. Nan, G. Sun, H. Li and S. Ma, *ACS Applied Materials and Interfaces*, 2019, **11**, 11403–11413.

106   J. F. Liao, W. Q. Wu, Y. Jiang, J. X. Zhong, L. Wang and D. Bin Kuang, *Chemical Society Reviews*, 2020, **49**, 354–381.

107   M. G. Campbell, D. Sheberla, S. F. Liu, T. M. Swager and M. Dincə, *Angewandte Chemie - International Edition*, 2015, **54**, 4349–4352.

108   M. G. Campbell, S. F. Liu, T. M. Swager and M. Dincə, *Journal of the American Chemical Society*, 2015, **137**, 13780–13783.

109   H. Liu, X. Li, L. Chen, X. Wang, H. Pan, X. Zhang and M. Zhao, *Journal of Physical Chemistry C*, 2016, **120**, 3846–3852.

110   Y. Shu, Y. Yan, J. Chen, Q. Xu, H. Pang and X. Hu, *ACS Applied Materials and Interfaces*, 2017, **9**, 22342–22349.

111   Y. Zhao, L. Jiang, L. Shangguan, L. Mi, A. Liu and S. Liu, *Journal of Materials Chemistry A*, 2018, **6**, 2828–2833.

112   F. Su, S. Zhang, H. Ji, H. Zhao, J. Y. Tian, C. Sen Liu, Z. Zhang, S. Fang, X. Zhu and M. Du, *ACS Sensors*, 2017, **2**, 998–1005.

113   Y. Wang, M. Zhao, J. Ping, B. Chen, X. Cao, Y. Huang, C. Tan, Q. Ma, S. Wu, Y. Yu, Q. Lu, J. Chen, W. Zhao, Y. Ying and H. Zhang, *Advanced Materials*, 2016, **28**, 4149–4155.

114   A. Pustovarenko, M. G. Goesten, S. Sachdeva, M. Shan, Z. Amghouz, Y. Belmabkhout, A. Dikhtiarenko, T. Rodenas, D. Keskin, I. K. Voets, B. M. Weckhuysen, M. Eddaoudi, L. C. P. M. de Smet, E. J. R. Sudhölter, F. Kapteijn, B. Seoane and J. Gascon, *Advanced Materials*, 2018, **30**, 1707234.

115   Y. Ning, X. Lou, C. Li, X. Hu and B. Hu, *Chemistry - A European Journal*, 2017, **23**,

15984–15990.

116   C. Li, X. Hu, W. Tong, W. Yan, X. Lou, M. Shen and B. Hu, *ACS Applied Materials and Interfaces*, 2017, **9**, 29829–29838.

117   C. Shi, Y. Gao, L. Liu, Y. Song, X. Wang, H. J. Liu and Q. Liu, *Journal of Nanoparticle Research*, , DOI:10.1007/s11051-016-3641-5.

118   C. Li, Q. Zhang, T. Li, B. He, P. Man, Z. Zhu, Z. Zhou, L. Wei, K. Zhang, G. Hong and Y. Yao, *Journal of Materials Chemistry A*, 2020, **8**, 3262–3269.

119   X. Zheng, Y. Cao, D. Liu, M. Cai, J. Ding, X. Liu, J. Wang, W. Hu and C. Zhong, *ACS Applied Materials and Interfaces*, 2019, **11**, 15662–15669.

120   J. Yang, Z. Ma, W. Gao and M. Wei, *Chemistry - A European Journal*, 2017, **23**, 631–636.

121   J. Wang, Q. Zhong, Y. Zeng, D. Cheng, Y. Xiong and Y. Bu, *Journal of Colloid and Interface Science*, 2019, **555**, 42–52.

122   H. M. Ma, J. W. Yi, S. Li, C. Jiang, J. H. Wei, Y. P. Wu, J. Zhao and D. S. Li, *Inorganic Chemistry*, 2019, **58**, 9543–9547.

123   Y. Wang, Y. Liu, H. Wang, W. Liu, Y. Li, J. Zhang, H. Hou and J. Yang, *ACS Applied Energy Materials*, 2019, **2**, 2063–2071.

124   W. Bai, S. Li, J. Ma, W. Cao and J. Zheng, *Journal of Materials Chemistry A*, 2019, **7**, 9086–9098.

125   L. G. Beka, X. Bu, X. Li, X. Wang, C. Han and W. Liu, *RSC Advances*, 2019, **9**, 36123–36135.

126   J. Cheng, S. Chen, D. Chen, L. Dong, J. Wang, T. Zhang, T. Jiao, B. Liu, H. Wang, J. J. Kai, D. Zhang, G. Zheng, L. Zhi, F. Kang and W. Zhang, *Journal of Materials Chemistry A*, 2018, **6**, 20254–20266.

127   W. Zhao, W. Wang, J. Peng, T. Chen, B. Jin, S. Liu, W. Huang and Q. Zhao, *Dalton Transactions*, 2019, **48**, 9631–9638.

128   Y. Liu, Y. Wang, Y. Chen, C. Wang and L. Guo, *Applied Surface Science*, 2020, **507**, 145089.

129   J. Xu, Y. Wang, S. Cao, J. Zhang, G. Zhang, H. Xue, Q. Xu and H. Pang, *Journal of Materials Chemistry A*, 2018, **6**, 17329–17336.

130   H. Wang, L. Zhang, Z. Chen, J. Hu, S. Li, Z. Wang, J. Liu and X. Wang, *Chemical Society Reviews*, 2014, **43**, 5234–5244.

131   S.-Z. Qiao, J. Qu, H. Wang, L. Song, S. Chen, T. Wen, R. Zheng, X. Zhang, H. Zhang, J. Ran and L. Jing, *Advanced Energy Materials*, 2019, **1803402**, 1803402.

132   L. Chen, Y. Wang, F. Yu, X. Shen and C. Duan, *Journal of Materials Chemistry A*, 2019, **7**, 11355–11361.

133   L. Ye, Y. Gao, S. Cao, H. Chen, Y. Yao, J. Hou and L. Sun, *Applied Catalysis B: Environmental*, 2018, **227**, 54–60.

134   C. Zheng, X. Qiu, J. Han, Y. Wu and S. Liu, *ACS Applied Materials and Interfaces*,

2019, **11**, 42243–42249.

135   W. Xing, P. Ye, J. Lu, X. Wu, Y. Chen, T. Zhu, A. Peng and H. Huang, *Journal of Power Sources*, 2018, **401**, 13–19.

136   G. Li, R. Zhu and Y. Yang, *Nature Photonics*, , DOI:10.1038/nphoton.2012.11.

137   P. Cheng, G. Li, X. Zhan and Y. Yang, *Nature Photonics*, 2018, **12**, 131–142.

138   C. Liu, C. Wang, H. Wang, T. Wang and J. Jiang, *European Journal of Inorganic Chemistry*, 2019, **2019**, 4815–4819.

139   S. Wu, Z. Li, M. Li, Y. Diao, F. Lin, T. Liu, J. Zhang, P. Tieu, W. Gao, F. Qi, X. Pan, Z. Xu, Z. Zhu and A. K. Jen, *Nature Nanotechnology*, , DOI:10.1038/s41565-020-0765-7.

Chapter 3

Experimental Methods
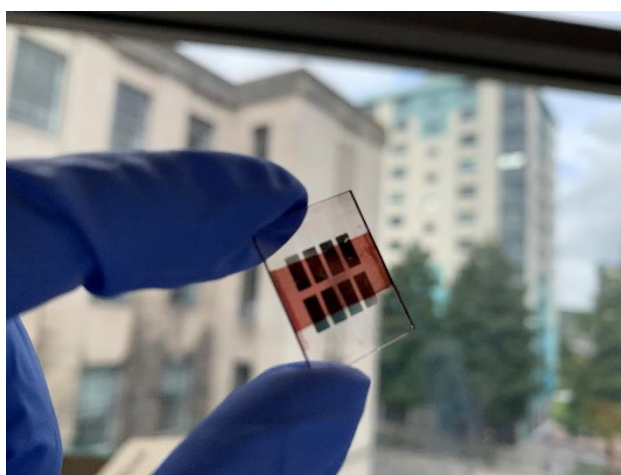
3.0 Introduction

In keeping with the alternative format theses, the experimental chapters 4-6 are presented in a publication format with their own comprehensive materials and methods section in the supplementary information which includes MON preparation procedures, solution preparation and OPV fabrication steps. Therefore, to avoid repeated content, this chapter presents a brief background to the physics behind the techniques employed to fabricate and characterise the MON incorporated OPVs.

3.1 OPV Fabrication Procedure

3.1.1 Pre-deposition treatments

Substrates mounted on a cleaning rack were immersed in in boiling DI water containing Hellmanex (Z805939, 5 vol %) solution and sonicated for 10 minutes. After this step, the substrates were immersed in boiling DI water and sonicated for 10 minutes to remove any excess Hellmanex. The substrates were then sonicated for 10 minutes in room temperature IPA. The substrates were then dried using nitrogen gun followed by solution deposition. For PV (photovoltaic) experiments the substrates were subjected to UV-ozone treatments (20 minutes) prior to deposition of the first layer (usually PEDOT:PSS or ZnO). When the sample is illuminated with UV in air, it leads to the formation of individual oxygen radicals which go on to form O_3.[1] The contaminants on the irradiated surface can undergo photoexcitation followed by reaction with ozone thereby liberating any organic material from the surface of the substrates.[2] This creates surface energy modifications on the substrates and helps with improved wettability and adhesion.[3] This fabrication step has been reported to remove excess carbon from the surface and increase the work function of ITO. For some non-PV experiments, UV-Ozone treatment was not used because the solution cleaning procedure was sufficient to allow a thin-film deposition.

3.1.2 Spin-coating

Spin-coating is a popular technique for fabricating small area thin-film devices. In this work, solutions are spin-coated using a single-step dynamic technique. In this typical deposition process, first a substrate is placed onto a chuck with an indentation or a vacuum feed to help hold the substrate in position.[4] Then the solution of choice is drop-cast from a pipette onto a spinning substrate in a single motion. The shear forces exerted on the top surface of the fluid, cause an expulsion of the fluid across the surface of the substrate. During this step, majority of the contents get flung away and the thickness of the fluid layer eventually becomes thin enough to rotate with the spinning substrate. When the substrate has reached its final rpm, the rotational acceleration balances the viscous drag of the fluid layer.[5,6] The air flow across the sample during the spinning, leads to drying of the remaining fluid. **Figure 3.1** shows the spin-coating process. The rate of thinning of the film is controlled by the viscous forces of the liquid. Any remaining solvent (especially the higher boiling ones) that is trapped within the film that can

affect the thickness of the films can be removed via a post-spin annealing step. Substrates can also be heated prior to the spin-coating step to accelerate the film formation.

The final film thickness can be calculated by the relationship

$$T \propto \frac{c\,\eta}{\sqrt{\omega}}$$ **Equation 3.1**

Where, T= thickness of the final film, c = solution concentration, η= solution viscosity and ω= the spin speed.

For most thin-film applications it is useful to fine tune the film thickness, T by simply adjusting the pain speed which follows the relationship

$$\omega = \omega_R \left(\frac{T_R}{T}\right)^2$$ **Equation 3.2**
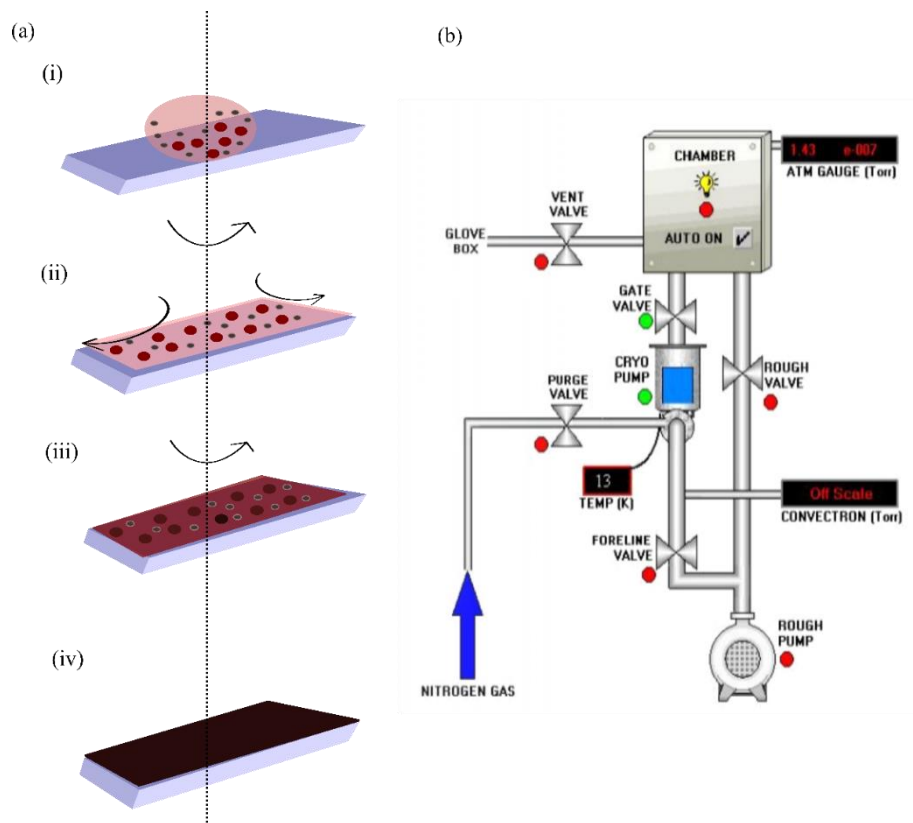
Figure 3.1. Representation of the techniques used to fabricate the different layers in OPV. (a) Spin-coating - (i) A substrate is placed onto chuck with vacuum feed/indentation; (ii) The chuck is rapidly accelerated and the precursor solution is dropped onto the substrate; (iii) the remaining film becomes more concentrated as more solvent is evaporated; (iv) a thin-film is left behind to dry.; (b) Schematic representation of a typical thermal evaporation system used to deposit the metal contacts onto the OPV devices.

This is a very cost-effective and a quick method for film formation suited for small area devices. When the substrate area increases, the forces on the edge of the substrate are higher which can lead to film fracture. Another limitation of this technique is that about 95-98% of the material that is pipetted onto the substrate is wasted. Several studies on the drying effects, edge effects and film-defects developed during spin-coating describe this process sin more detail.

3.1.3 Thermal evaporation

The transport layers and electrical contacts for the OPVs were deposited via thermal evaporation using an Angstrom thermal evaporator housed in a glovebox. The devices were loaded into he vacuum chamber. The high vacuum ensures that the evaporated molecules can travel unimpeded, without colliding with any gas molecules. The sample holder in an evaporator is usually a resistive boat, or a wire that can hold a crucible. Once a minimum pressure of 4×10^{-6} mbar is attained, the sample holders are heated by passing a large amount of current through it. This heats the source material until it evaporates and travels up to nucleate onto the substrate. A calibrated quartz crystal rate monitor, vibrating at a target known frequency, measures the rate of deposition, which can be controlled by changing the current passed through the sample holder. By mounting the substrates in an evaporation mask, the metal contacts formed can be patterned onto well-defined shapes. Some materials require an adhesion layer (for example a thin layer of chromium prior to deposition of gold). Typically, the substrates are rotated enabling a uniform deposition, and with a stable rate of evaporation the resulting films are compact.

3.1.4 Post-deposition treatments

Solvent annealing was explored to grow the grain sizes and thereby improve efficiency in the devices made in chapter 4 and 5. This process involves exposing the active layer to a solvent vapour at an elevated temperature (100-150°C). The solvent molecules diffuse into the active layer and increase the mobility of molecules within the active layer.[7] This re-organisation leads to effective control of morphology in the bulk-heterojunction mixture.[8] For solvent annealing, we held freshly prepared ITO/spin-coated active layer films in a chlorobenzene solvent atmosphere for 10 minutes at 120°C. Following this, they were further annealed under nitrogen to remove any residual chlorobenzene, after which device processing proceeded as normal.

3.2 Thin Film Characterisations

3.2.1 Surface profilometry

A Bruker Dektak surface profilometer was used to measure the film thickness and surface roughness. Here, a stylus is scanned in a line across the surface of a sample with a fixed force applied to it (3mg). The profiler measures the vertical displacement of the stylus in contact with the surface. By measuring the magnitude of the restoring force on the stylus, a line profile for the surface is produced. This measurement determines the depth and surface roughness of the film to be characterised. A step in the film is created by scratching a trench through the film and blowing a stream of N_2 over it to remove any excess material from the surface. Then by scanning over the trench an estimate for the film thickness can be obtained (**Figure 3.2**). A minimum of 4 profiles were taken for each sample and the values quoted in this thesis are the mean scratch depth and standard deviations from those line profiles. For surface roughness, a root-mean-square (RMS) value was determined between scratched regions of the film. The RMS values quoted in this thesis are calculated from a minimum of 4 line profiles as well. Calculating the film thickness and roughness is important in optimising the solar cell performance. Planarizing films can be done only after determining the pre-layer roughness, because the top layer's thickness needs to be higher than the underlying layer's roughness in order to effectively planarize it and reduce the chances of formation of a Schottky junction.
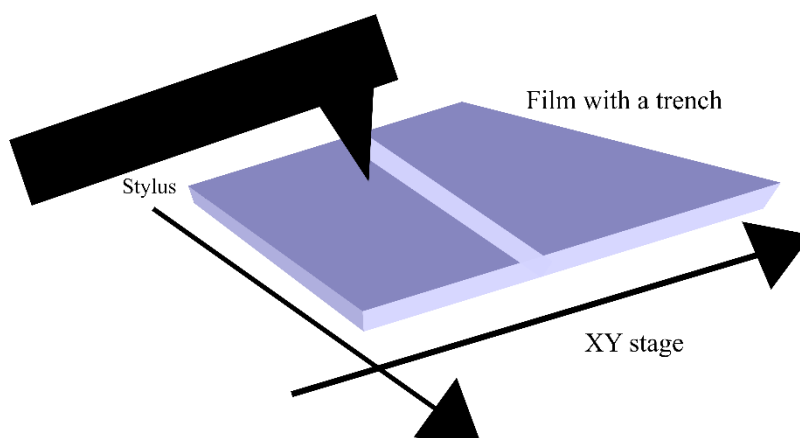
Figure 3.2 Schematics of surface profilometry

3.2.2 Atomic Force Microscopy

Tapping mode AFM was used for topographic mapping of the thin films. This technique operates by scanning a tip attached to the end of an oscillating cantilever across the sample surface. The cantilever is oscillated at or near its resonance frequency with an amplitude ranging typically from 20nm-100nm. The frequency of the oscillation can be at or on either side of the resonant frequency. The tip lightly taps on the sample surface during the scanning, contacting the surface at the bottom of its swing. The feedback loop maintains a constant oscillation amplitude by maintaining a constant RMS of the oscillation signal acquired by the split photodiode detector. The vertical position of the scanner at each (x, y) data point to maintain a constant setpoint amplitude is stored by the computer to form the topographic image of the sample surface. By maintaining a constant oscillation amplitude, a constant tip-sample interaction is maintained during the imaging. All the imaging was done in air.
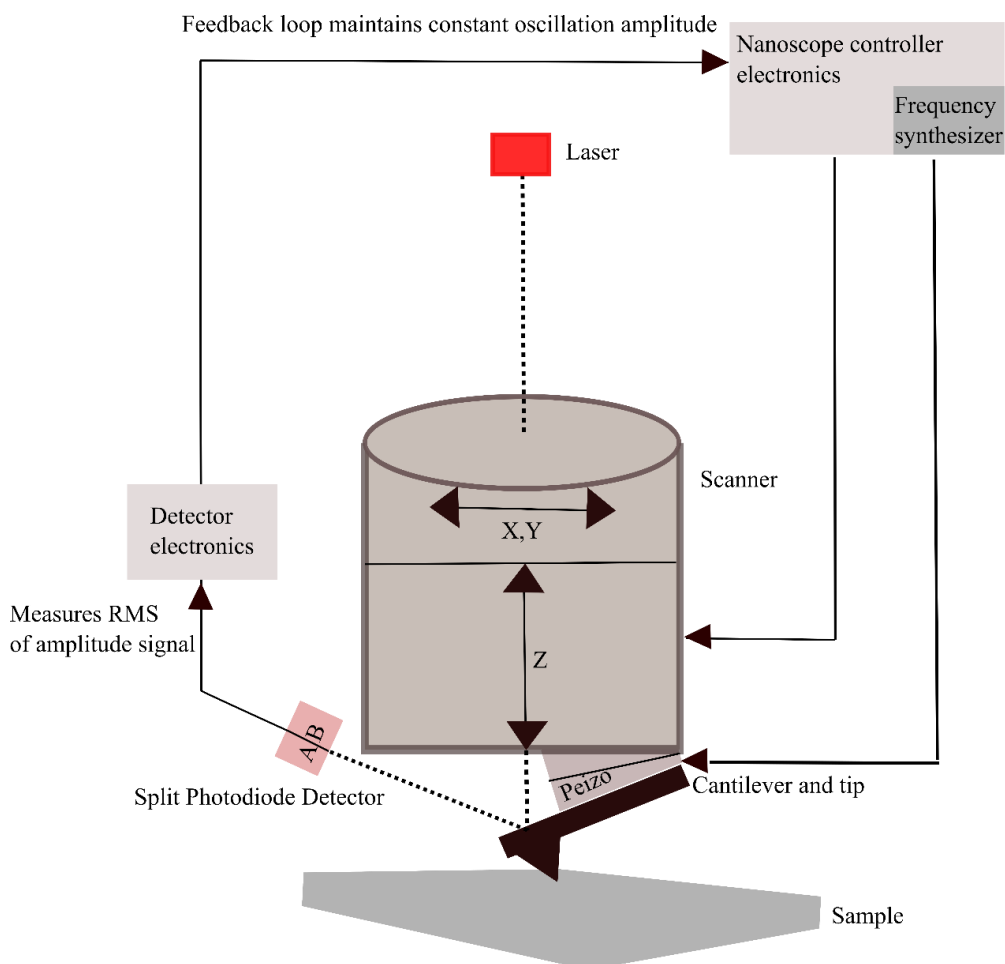
Figure 3.3. Schematics of atomic-force microscopy (AFM)

2D Fast-Fourier transform (FFT) function was performed on thin-film AFM images to obtain the power spectra of phase-separated structures. The 2D FFT decomposes when applied decomposes a signal into its harmonic components. This function transforms the X-Y representation to a polar representation (pixel information provided based on radial distances and angle with respect to the image centre). The output is obtained in the Modulus mode in Gwydion, which yields the absolute value of the complex Fourier coefficient, proportional to the square root of the power spectrum density function (PSDF). Thus, any periodicity in the image is represented at a certain radial distance (and angle) from the centre. Using this technique, the 2D height images when fast-Fourier transformed gave the characteristic length scale of phase separation in the films.

3.2.3 Grazing-Incidence Wide Angle X-ray Scattering (GIWAXS)

GI-WAXS makes use of diffraction patterns produced when incident X-rays are scattered from a sample. As the name suggests, GIWAXS is performed with the X-ray source aligned at a grazing incidence relative to the sample. Bragg's diffraction law (**equation 3.3**) provides an understanding of how X-rays will diffract through a crystalline or semi-crystalline material. Here, n is any integer, λ is the wavelength of the incident X-ray and the repeating crystal lattice of atoms has a distance d between diffraction planes.

$$n\lambda = 2d\,sin\theta \qquad\qquad (\textbf{Equation 3.3})$$
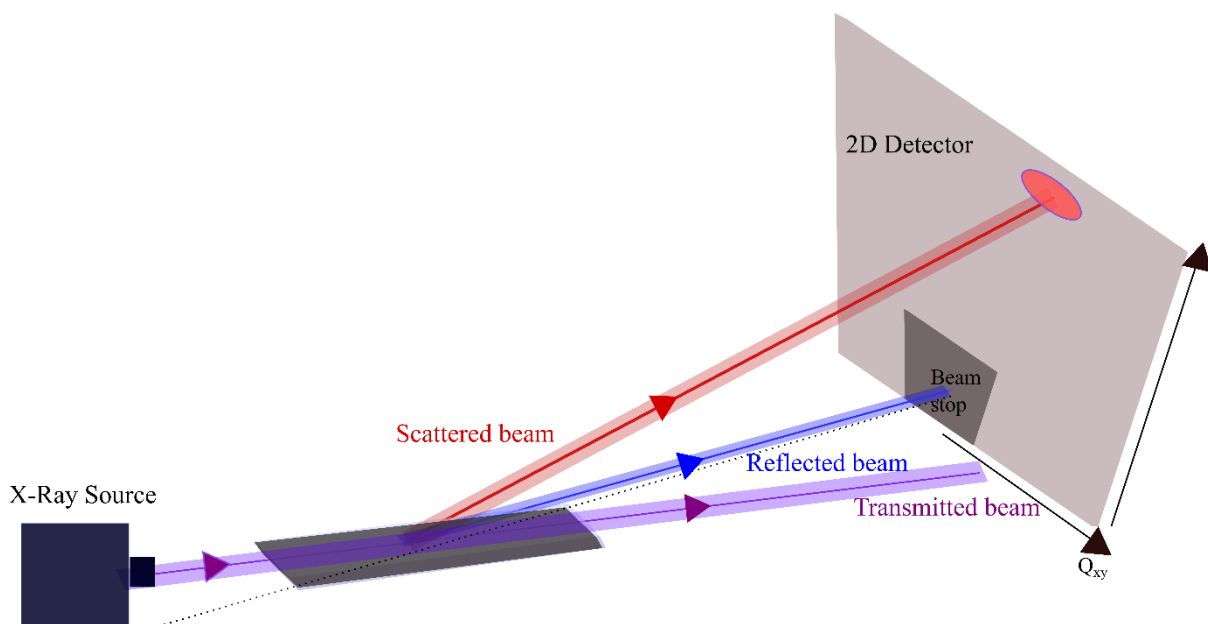
Figure 3.4. Schematics of the grazing-incidence wide angle x-ray scattering (GI-WAXS) set-up.

By scanning the detector around a chosen range of 2θ angles, the intensity at each angle can be found. The incident angle dictates how deep into the material gets probed, and there is a critical angle at which the X-rays will interact with the bulk of the material instead of its top surface. GIWAXS is typically used to observe structures in the range of nm to Å.

To ensure the X-rays reaching the detector are only from scattering, and not from the reflected or transmitted beam, a beam stop is used near the base of the detector. This occludes the direct beam and also some of the reflected intensity. GIWAXS typically uses a two-dimensional detector making it possible to collect the full diffraction pattern simultaneously. **Equation 3.4** demonstrates how the reciprocal space parameter q is related to angle of detected diffraction pattern and wavelength of incident X-rays

$$q = \frac{2\pi}{d} = \frac{4\pi sin\theta}{\lambda} \qquad\qquad \textbf{Equation 3.4}$$

Using these values, GIWAXS can be used to identify the strengths of various crystal orientations and phases, compare materials and collect data for indexing and modelling of crystal structure. For highly ordered samples the diffraction pattern appears as spots. For ordered samples with many directions of orientation, the diffraction pattern will manifest as arcs or rings on the 2D detector. The width of diffraction patterns is a good indication of the level of disorder of the various crystal structures within a sample.

The GIWAXS thin film measurements were performed with a Xeuss 2.0 system (Xenons, France). The Sheffield machine is fitted with a MetalJet (Excillum, Sweden) liquid gallium X-ray source, providing a 9.24 keV X-ray beam collimated to a beam spot of 400 µm laterally at the sample position, measuring the full sample length. X-ray diffraction patterns were acquired with a Pilatus3R 1M 2D detector (Dectris, Switzerland). The sample to detector distance was calibrated using a silver behenate calibrant standard in transmission geometry. Samples were measured in GI-WAXS geometry near the critical angle (calculated to probe the entire film thickness) and under vacuum atmosphere to minimise the background scatter.

3.2.4 Approaches to modelling the GI-WAXS data

The Matlab toolbox GIXSGUI, developed by Zhang Jiang was used for the GI-WAXS data visualization and reduction.[9] This package was developed for GIWAXS data visualisation and processing as well as for three-dimensional nanostructure indexing. The toolbox is designed

with a graphical user interface., based on the MATLAB handle class data type *gixsdata*. The data and experimental parameters are input and stored as properties of *gixsdata.* The data correction function to the 2D GIWAXS pattern to account for detection efficiency, flat-field incident X-ray polarization, solid-angle variation and the Lorentz effect. The 2D GI-WAXS data was reduced to 1-D profile with respect to the q component with the built-in linecut method, integrated with the MATLAB curve fitting. This reduced 1D profile was subjected to further structural analysis (lattice parameter, nanostructure size, shape analysis), as describe in the ESI of the chapters.

3.3 PV device characterisations

3.3.1 Current-voltage measurements

The device performance parameters (described in Chapter 1) are measured as followed. A Newport 92251A-1000 solar simulator was used to illuminate the OPV devices. The illumination was restricted to a 0.0256 cm^2 area via an aperture mask. Before each batch of measurements, the intensity of the solar simulator was calibrated to 100 mWcm^{-2} using an NREL certified silicon reference cell. The applied bias was swept from 0.0 V to +1.2 V and back again at 0.4 Vs^{-1}, with the help of a Keithley 237 source measure system.

3.3.2 External Quantum Efficiency (EQE)

The EQE was calculated by the method described in chapter 1. Figure 3.5 shows a schematic representation fo the EQE set-up which comprised of a halogen light source (L.O.T.-Oriel GmbH & Co, 10- 150 W halogen source), a monochromator grating (Spectral products, DK 240), and a calibration silicon photodetector (Newport 818-uv). EQE spectra were taken by measuring the generated photocurrent with a source measure unit (Ossila X-100) while irradiating with the monochromatic source.
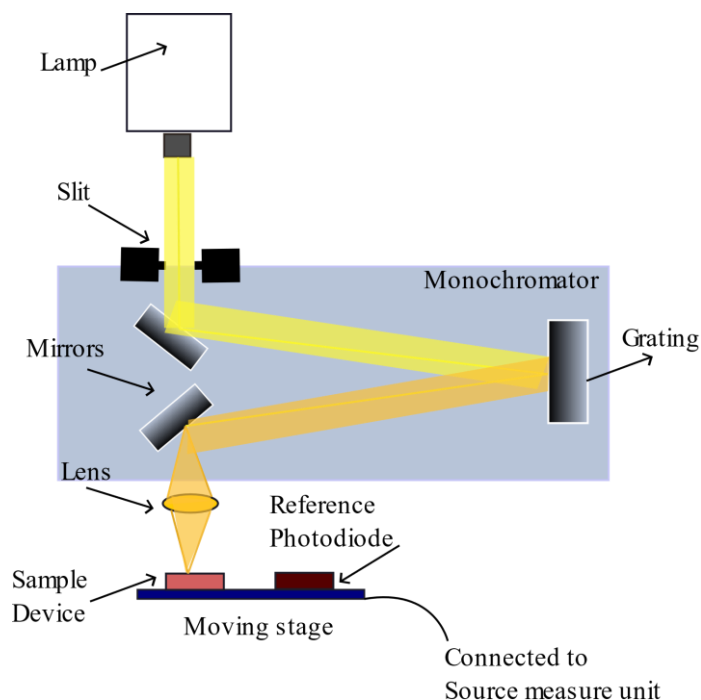
Figure 3.5. Schematic of external quantum efficiency (EQE) set-up

3.4 Other techniques used in this thesis

3.4.1 Cyclic voltammetry

Cyclic voltammetry is a type of potentiodynamic electrochemical measurement. In this thesis we used this technique for energy level estimation of organic materials. According to Koopman's theorem, in a closed shell Hartree-Fock theory, the first ionisation energy of a molecular system is equal to the negative of the orbital energy of the highest occupied molecular orbital (HOMO). In principle, during a CV measurement we are monitoring an oxidation or reduction, hence we measure the oxidation or reduction potential relative to the reference. Oxidation potential involves removing an electron from the molecule, and the lowest ionisation potential should come from the HOMO.[10–12]

In this thesis, the cyclic voltammetry experiments were run in an acetonitrile solution containing tetrabutylammonium perchlorate electrolyte. The reference electrode Ag/Ag$^+$ was immersed in the reaction cell. The working electrode was a glassy carbon electrode and the counter electrode was a Pt wire.

Under working conditions, the working electrode makes contact with the analyte. When the desired potential is applied in a controlled manner, it facilitates the transfer of charge to and from the analyte. The reference electrode is a half cell of known reduction potential. Its only role is to act as the reference in measuring and controlling the working electrode's potential. The counter electrode passes all the current needed to balance the observed current at the working electrode. During the run of the CV experiment, the working electrode potential is ramped linearly versus time. When the set potential is reached, the potential is ramped in the opposite direction to return to the initial position. The current at the working electrode is plotted vs the applied voltage to give the CV trace. The electrode potential ramps linearly vs time in cyclic phases. The rate of the voltage change over time during each of these phases is known as the experiment's scan rate. The potential is measured between the working electrode and the reference electrode. The current is measured between the working electrode and the counter electrode. The data is plotted as current vs applied potential.

3.4.2 Photoemission spectroscopy

Photoemission studies (also known as photoelectron spectroscopy) are a widely employed technique for studying the electronic and chemical properties of materials. The working principle is based on the external photoelectric effect, where electrons are excited by an incident light beam with monochromatic energy ($\hbar\omega$) and then emitted from the sample if the difference between the excitation energy ($\hbar\omega$) and their binding energy (E_{bin}) is larger than the work function of the sample (ϕ_s) i.e. $\hbar\omega$-E_{bin}>ϕ_s (Figure 3.6 a). The kinetic energy of the photoemitted electron $E_{kin} = \hbar\omega$- ϕ_s-E_B and its momentum (p) are then detected in a hemispherical analyser. For UPS, the energy of the incoming photon is in the ultraviolet regime (5-100 eV, UPS). An important feature is the increasing background created by secondary electrons that are generated by inelastic scattering processes of photoexcited electrons in the sample before they leave the surface and thereby lose energy. The background of the secondaries has a sharp cutoff at E_{kin} =0. This cutoff energy, measured with respect to the fermi energy can be used to determine the sample work function. Under experimental conditions, the sample holder and the electron detector in the analyser are electrically connected and in electronic equilibrium, therefore they both have the same fermi level (E_f) which is taken as the reference energy (Figure 3.6b). The exact position of the secondary electron cut-off cannot be measured unless a constant negative potential U_{seco} is applied to the sample when measuring the SECO (typically a few eV). The voltage that is needed to detect all low kinetic energy

electrons determines the work function difference between the sample and the electron detector in the analyzer. This difference also determines the measured kinetic energy (E'_{kin}) of the photoelectrons in the analyser, i.e.

$$E'kin = hv - (\phi_A - \phi_S) = hv - E_{bin} - \phi_A \quad \textbf{Equation 3.5}$$
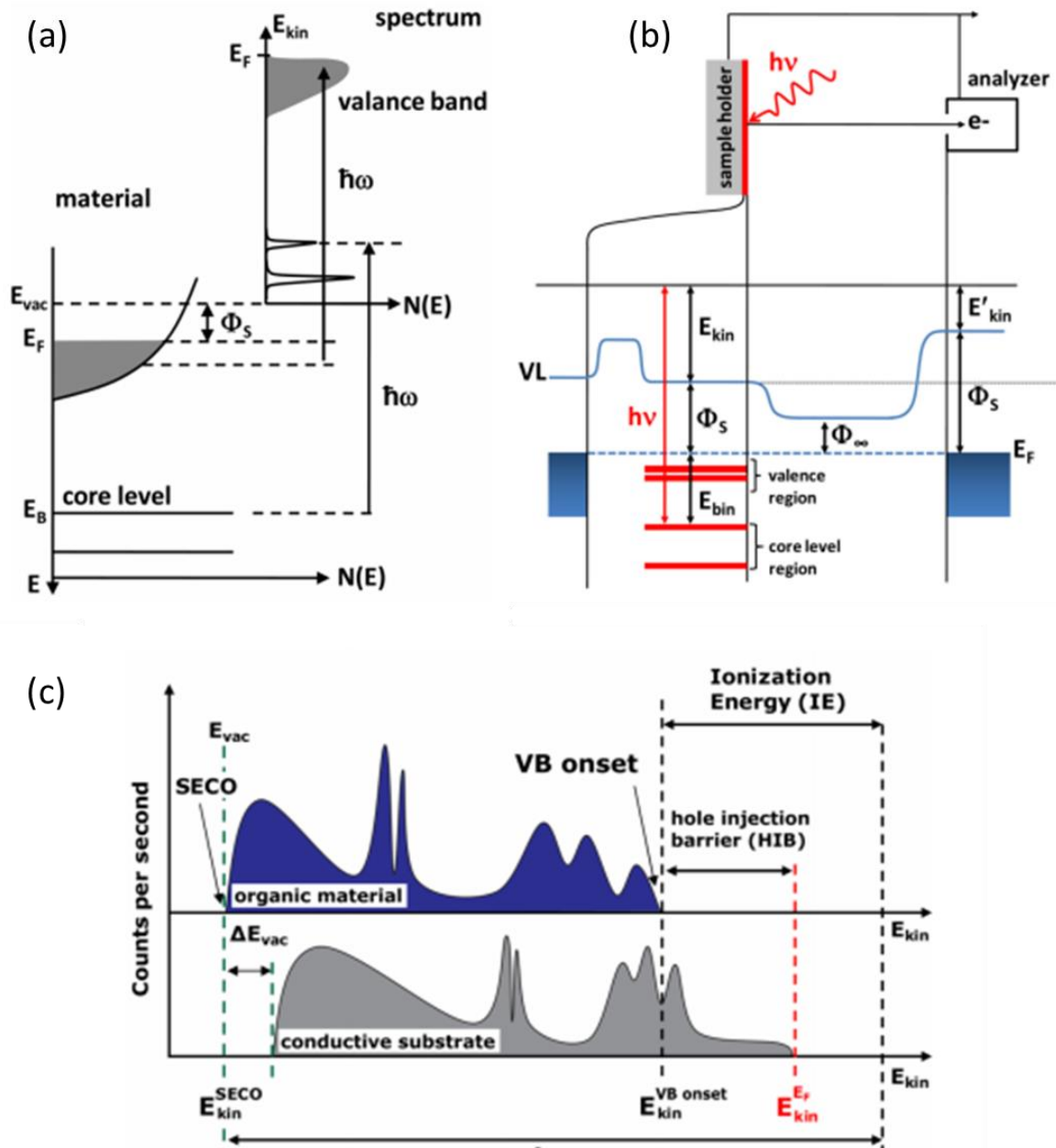
Figure 3.6 (a) Relation between the energy levels in a solid and the electron energy distribution produced by photons of energy ℏω. The abscissa is the kinetic energy with the zero corresponding to the vacuum level of the sample. E_B is the binding energy of the electrons which is referred to as E_f in solids. (b) Schematic energy level diagram for the sample and the electron energy analyzer in a photoelectron spectroscopy experiment; (c) Hypothetical energy distribution curve (EDC)obtained in a typical UPS experiment for a conductive substrate and a conjugated organic thin film. The onset of the valence band (VB onset) and the hole injection barrier (HIB), which is defined as the energetic difference between the fermi level (E_f) and VB onset, are shown. The vacuum level is shown as E_{VAC}, which enables the calculation of the work function of the sample. The change in work function is denoted as ΔE_{VAC}.

A typical energy distribution curve (EDC) obtained in a photoemission experiment has the number of counted photoelectrons plotted against their kinetic energy (Figure 3.6c). The electrons with the highest E_{kin} stem from the highest occupied states of the sample, which is the fermi level (E_f) for a metal or the VB (HOMO) onset for a polymer (molecule). At higher E_{kin} very distinct peaks can be observed that originate from the core levels of the individual atoms of the material. Without accounting for cross-section and selection rule effects, photoemission spectroscopy yields the density of the occupied levels of a solid. The photoelectrons in the valence region are thus related to the σ and π type orbitals of the polymers (molecules).

The sample work function ϕ_s can be calculated by subtracting the full width of the EDC from the provided energy of the photon:

$$\phi_S = hv - \left(E_{kin}^{Ef} - \left(E_{kin}^{SECO} - U_{SECO} \right) \right) \qquad \textbf{Equation 3.6}$$

The hole injection barrier (HIB) and the ionisation energy (IE) of the organic material that is the sum of HIB and ϕ_S can be extracted by

$$HIB = E_{kin}^{E_F} - E_{kin}^{VB_{onset}} \qquad \textbf{Equation 3.7}$$

and

$$IE = HIB + \phi_S \qquad \textbf{Equation 3.8}$$

3.5 References

1   F. Wang, G. Sun, C. Li, J. Liu, S. Hu, H. Zheng, Z. Tan and Y. Li, *ACS Applied Materials and Interfaces*, 2014, **6**, 9458–9465.

2   H. Awada, G. Mattana, A. Tournebize, L. Rodriguez, D. Flahaut, L. Vellutini, C. Lartigau-Dagron, L. Billon, A. Bousquet and S. Chambon, *Organic Electronics*, 2018, **57**, 186–193.

3   M. Saliba, J. P. Correa-Baena, C. M. Wolff, M. Stolterfoht, N. Phung, S. Albrecht, D. Neher and A. Abate, *Chemistry of Materials*, 2018, **30**, 4193–4201.

4   M. Reichenberger, D. Kroh, G. M. M. Matrone, K. Schötz, S. Pröller, O. Filonik, M. E. Thordardottir, E. M. Herzig, H. Bässler, N. Stingelin and A. Köhler, *Journal of Polymer Science Part B: Polymer Physics*, 2018, **56**, 532–542.

5   M. Reichenberger, D. Kroh, G. M. M. Matrone, K. Schoetz, S. Proeller, O. Filonik, M. E. Thordardottir, E. M. Herzig, H. Baessler, N. Stingelin and A. Koehler, *Journal of Polymer Science, Part B: Polymer Physics*, 2018, **56**, 532–542.

6 S. A. Choulis, V. E. Choong, A. Patwardhan, M. K. Mathai and F. So, *Advanced Functional Materials*, 2006, **16**, 1075–1080.

7 S. Lan, H. Yang, G. Zhang, X. Wu, Q. Chen, L. Chen, H. Chen and T. Guo, *ACS Applied Materials and Interfaces*, 2017, **9**, 20679–20685.

8 T. Wang, A. J. Pearson, D. G. Lidzey and R. A. L. Jones, *Advanced Functional Materials*, 2011, **21**, 1383–1390.

9 Z. Jiang, *Journal of Applied Crystallography*, 2015, **48**, 917–926.

10 V. Lami, A. Weu, J. Zhang, Y. Chen, Z. Fei, M. Heeney, R. H. Friend and Y. Vaynzof, *Joule*, 2019, **3**, 2513–2534.

11 G. Lan, Z. Li, S. S. Veroneau, Y. Y. Zhu, Z. Xu, C. Wang and W. Lin, *Journal of the American Chemical Society*, 2018, **140**, 12369–12373.

12 G. O. N. Ndjawa, M. R. Tchalala, O. Shekhah, J. I. Khan, A. E. Mansour, J. Czaban-Jóźwiak, L. J. Weselinski, H. A. Ahsaine, A. Amassian and M. Eddaoudi, *Materials*, , DOI:10.3390/ma12152457.

Chapter 4

Metal-Organic Framework Nanosheets for Enhanced Performance of Organic Photovoltaic cells

Kezia Sasitharan [a], **David G. Bossanyi** (iD)[b], **Naoum Vaenas** [b], **Andrew J. Parnell** (iD) [b], **Jenny Clark** [b], **Ahmed Iraqi** [a], **David G. Lidzey** (iD)[b] and **Jonathan A. Foster** (iD)*[a]

[a]*Department of Chemistry, The University of Sheffield, Dainton Building, Brook Hill, S3 7HF, Sheffield, UK.*
[b]*Department of Physics and Astronomy, The University of Sheffield, Hicks Building, Hounsfield Road, S3 7RH, Sheffield, UK*

Author contributions

Kezia Sasitharan   Synthesised and characterised the MONs, prepared the photovoltaic devices and carried out the related analyses, prepared samples for TA and GI-WAXS, analysed the experimental results and drafted the manuscript.

David G. Bossanyi   Measured and analysed the TA data.

Naoum A. Vaenas   Collected the EQE spectra.

Andrew J Parnell   Measured the GI-WAXS data and helped with editing of the manuscript.

Jenny Clark   Aided with data discussion and editing of the manuscript.

Ahmed Iraqi   Aided with data discussion and editing of the manuscript.

David G. Lidzey   Aided with data discussion and editing of the manuscript.

Jonathan A. Foster   Supervised the project, aided with data discussion and drafting of the manuscript.

4.1 Publication main text:

Metal–organic framework nanosheets for enhanced performance of organic photovoltaic cells†

Kezia Sasitharan [a], David G. Bossanyi [b], Naoum Vaenas [b], Andrew J. Parnell [b], Jenny Clark [b], Ahmed Iraqi [a], David G. Lidzey [b] and Jonathan A. Foster *[a]

[a]Department of Chemistry, The University of Sheffield, Dainton Building, Brook Hill, S3 7HF, Sheffield, UK. E-mail: jona.foster@sheffield.ac.uk
[b]Department of Physics and Astronomy, The University of Sheffield, Hicks Building, Hounsfield Road, S3 7RH, Sheffield, UK

Abstract

Metal–organic framework nanosheets (MONs) are an emerging class of two-dimensional materials whose diverse and readily tunable structures make them ideal for use in optoelectronic applications. Here, liquid exfoliation is used to synthesize ultrathin zinc-porphyrin based MONs with electronic and optical properties ideally suited for incorporation into a polythiophene–fullerene (P3HT–PCBM) organic solar cell. Remarkably, the addition of MONs to the photoactive layer of a photovoltaic device results in a power conversion efficiency of 5.2%, almost twice that for reference devices without nanosheets with a simultaneous improvement of J_{sc}, V_{oc} and FF. Our analysis indicates that the complimentary electronic, optical and structural properties of the MONs allows them to act as a surface to template the crystallization of P3HT leading to a doubling of the absorbance, a tenfold increase in hole mobility and reduced grain size. These results demonstrate the potential of MONs as a tunable class of two-dimensional materials for enhancing the performance of a broad range of organic solar cells and other electronic devices.

Introduction

Two-dimensional nanomaterials such as graphene hold enormous potential for use in advanced electronics, energy, separation and composite materials applications.[1–3] However, the simple chemical composition of many of these materials mean it can be difficult to optimize them for many applications. Metal-organic framework nanosheets (MONs) are an emerging class of two-dimensional nanomaterials composed of organic linkers co-coordinated to metal-ions or clusters.[4–7] MONs display the high surface area and aspect ratios of other two-dimensional materials but have a modular structure which readily allows for systematic tuning of their electronic, optical and mechanical properties and introduction of new chemical functionalities. A diverse range of MONs have been formed either bottom-up, via an arrested crystallization in the presence of a templating agent or interface, or "top-down" by mechanical or liquid exfoliation of layered metal-organic frameworks (MOFs). MONs have already shown significant promise for use in a variety of separation,[8,9] catalysis,[10,11] sensing[9,12–14] and electronics applications.[15–19]

Organic photovoltaics (OPV) offer a variety of attractive properties over current silicon technology including highly tuneable structures, low cost production, large area manufacturing capability and the potential to create flexible and semi-transparent devices.[20] Historically OPV has suffered from low power conversion efficiencies and poor stability but there has been renewed interest thanks to recent innovations such as new materials[21,22] device architectures[23] and multicomponent (ternary or quaternary) bulk heterojunction (BHJ) approaches.[24–29] In the latter case, a wide range of additives have been investigated whose complimentary optical or electronic properties enable them to enhance the range of light absorbed,[30–32] facilitate more efficient electron or hole transport[33] or modify the morphology of the devices leading to improvements in performance and stability.[34–36] Two-dimensional materials are ideal candidates for use as additives thanks to their large surface areas and distinct electronic and optical properties.[37–39] Transition metal dichalcogenides (TMDCs) in particular have attracted significant interest because of their thickness-dependant opto-electronic properties,[40] ambipolar charge transport,[41] chemical stability and direct band-gaps in the single layer form.[42] However, the difficulties in controlling layer thickness and scalability of these materials have so far limited their use in OPV applications.[43]

MONs possess a variety of characteristics that make them attractive candidates for use in photovoltaics, as outlined in the "MOF electronic roadmap".[44] Their diverse chemistry and modular structure allow for ready tuning of their optical and electronic properties. This means

MONs have the potential to perform roles in light absorption, carrier generation and transport within PV devices. MONs have a long range order which could help minimize the traps, dead ends and defects problematic in light-harvesting organic polymers. The nanoscopic dimensions of MONs open up new possibilities for their inclusion within the active layer of thin film devices and the highly anisotropic structure of MONs mean they are predisposed to align parallel to the surface.

Most work using MOFs for photovoltaics has focused on their use in dye-sensitized solar cells where they have been used to reduce structural disorder and increase charge mobility.[45–47] They have achieved this using either dyes or donor-acceptor molecules as ligands within the MOFs or by incorporating dyes or fullerenes within their pores with power conversion efficiencies reported up to 1.27%.[48,49] Epitaxially grown MOF films have also been employed as donor layers in planar light-harvesting devices.[50–53] MONs have shown promise in a variety of electronic applications,[18,54] however we are only aware of two reports of their use in solar cells. One recent report showed that tellurophene based MONs can be blended with ZnO-PEIE (polyethylenimine ethoxylate) to form a buffer layer which resulted in a small enhancement in the performance of two OPV devices.[55] In another recent study, porphyrin based MON films were formed on ITO using a Langmuir Blodgett approach and impregnated with C_{60} to form a liquid junction solar cell with quantum efficiency less than 0.1%.[56] To-date, there have been no-reports of the use of MONs or more generally MOFs within the active layer of bulk-heterojunction OPV devices.

Here, we explore a new approach to enhancing OPV bulk heterojunction devices by blending 2-D metal-organic nanosheets along with semi-conducting polymers and fullerene acceptors in the photoactive layer via a simple spin-coating procedure. We hypothesized that zinc-porphyrin based MONs would have good electronic and optical properties for inclusion in OPV devices and used ultrasonic liquid exfoliation to create predominantly monolayer nanosheets. Remarkably, addition of the MONs to a well-studied OPV system was found to result in an almost doubling of the device performance compared to the reference devices without MONs. Detailed studies were therefore undertaken in order to understand the role of the MONs on device performance, charge mobility, absorbance, thin film morphology and crystallinity. On the basis of these observations, we were able to put forward a model to explain the improvements in performance seen. We anticipate that the diverse and tunable properties of MONs will enable them to play an important role in enhancing the performance of a wide range of other OPV and electronic devices.

Results and discussion

Synthesis and characterisation of the zinc porphyrin MONs
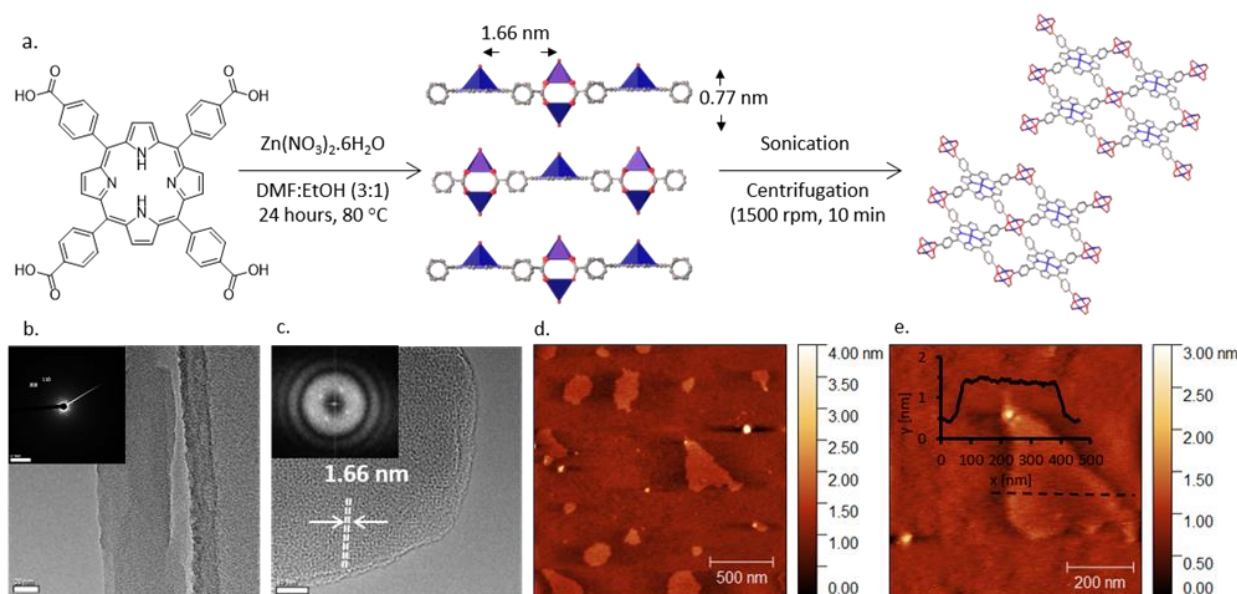
Figure 4.1. Synthesis and morphological characterisation of Zn2(ZnTCPP) MONs; a. Scheme showing synthesis of the layered MOF Zn2(ZnTCPP) followed by liquid exfoliation into MONs; b. Transmission electron micrograph of a single nanosheet on the TEM grid; b-inset: Single-area electron diffraction pattern of the nanosheets; c. HR-TEM image of a nanosheet showing lattice fringe distance =1.66 nm (inset: the corresponding FFT pattern); d. AFM topographical image of the MONs as observed under a 1.5 μm area scan; e. AFM image of a single MON with the corresponding height profile as inset (0.77 nm thickness; 300 nm lateral dimension).

The layered MOF Zn_2(ZnTCPP), where TCPP is tetrakis(4-carboxyphenyl)porphyrin, was synthesised solvothermally using a procedure adapted from Choi et al[57] (**Figure 4.1a**). TCPP was heated with zinc nitrate in a DMF:ethanol mixture at 80°C for 24h to produce a black microcrystalline powder. XRPD and other solid-state analysis (Figure S4.1-S4.3,ESI) showed a good match for the previously reported Zn_2(ZnTCPP) and analogous structures in literature.[13,58–62]

The layered MOF was suspended in chlorobenzene (5mg/mL), sonicated in an ultrasonic bath for 1 hour and centrifuged at 1500 rpm for 10 mins to remove larger particles. The resulting transparent suspension showed Tyndall scattering (Figure S4.4, ESI) consistent with the presence of nanoparticles. Atomic force microscopy (AFM) and Transmission Electron Microscopy (TEM) revealed the formation of ultra-thin nanosheets with lateral dimension of 300 ± 100 nm and a uniform thickness of 1±0.3nm corresponding to

Figure 4.2. Optoelectronic characterizations: a. Thin film absorption spectra of P3HT and PCBM spin-coated from chlorobenzene at 2000 rpm@60 seconds and $Zn_2(ZnTCPP)$ MONs dropcast (5mg/ml) and dried b. Comparison of absorption spectra of the polymer-fullerene, polymer-nanosheets and polymer-nanosheets-fullerene blends all spin-coated to achieve a layer thickness of ~150 nm; c. Photoluminescence spectra recorded from spin coated thin films (~150 nm) of P3HT, P3HT-$Zn_2(ZnTCPP)$ and P3HT-$Zn_2(ZnTCPP)$-PCBM blends, excited at 500nm. The weight ratios of the components in the blend films are stated in the legend. Refer to Figure S14 (ESI) for spin coating parameters used; d. Table showing key results from the band gap evaluation of $Zn_2(ZnTCPP)$ MONs (i. λonset values obtained by extrapolating the charge transfer peak to the x-axis (shown in Figure S10, ESI); ii. The charge transfer UV-Vis peak as observed in Fig S9; iii. A MON suspension (5mg/ml in ethanol) was dropcast onto a quartz substrate, followed by solvent evaporation prior to recording the UV-Vis spectra.

predominantly monolayer thickness (**Figure 4.1a**, FigureS4.5-S4.6, ESI). Fast Fourier Transform (FFT) of electron diffraction patterns (**Figure 4.1c**) show lattice fringes with spacing of 1.66 nm consistent with the Zn-Zn distance in the MON structure (**Figure 4.1c**). Electron energy loss spectroscopy (EELS) showed the zero-electron loss peak to be the most intense with an inelastic mean free path of 0.10, consistent with the observation of a sample of monolayer thickness (Figure S4.6c, ESI). It is worth noting that the MONs produced by our simple and scalable approach are thinner and have smaller lateral dimensions than those typically obtained from TCPP with Zinc and other metal ions (Cu, Co, Cd) including assembly at liquid interfaces,[59,60,62] intercalation of ligands[63] and surfactant assisted synthesis.[13] UV-Vis measurements of the $Zn_2(ZnTCPP)$ MONs in suspension show they are strongly absorbing with a characteristic π-π* soret band at 435nm and Q bands at 564 and 601 nm (Figure S4.7, ESI). **Figure 4.2a** shows the thin film UV-Vis spectra on quartz substrates in which the band at 440 nm is assigned as the π-π* peak, slightly red shifted compared to the MON in suspension, whilst Q bands are seen at 563 and 605 nm respectively.[64] The electrochemical properties of the MONs were studied in acetonitrile using cyclic voltammetry (CV) and the key results are

shown in **Figure 4.2d**. The HOMO-LUMO energy level calculations derived from the onset of oxidation and reduction are shown in Figure S4.8, ESI. The nanosheets show an electrochemical band gap of 1.8 eV making it a good material for light harvesting applications. Previous literature reports have shown that a minimum energy offset of 0.3 eV between the LUMO of the donor and acceptor is necessary to facilitate efficient exciton dissociation.[65] The LUMO level of the MONs was found to be -3.5 eV which makes it ideally positioned between that of the fullerene electron acceptor [6,6]-Phenyl-C61-butyric acid methyl ester (PCBM) at -3.80eV and electron donating organic polymer poly(3-hexylthiophene-2,5diyl) (P3HT) at -3.00 eV.[66] These finding lead us to evaluate P3HT-Zn_2(ZnTCPP)-$PC_{60}BM$ ternary blend organic photovoltaics where all three of the materials in the active layer display an energy offset in the excess of the 0.3 eV limit. Although the high band-gap of P3HT means that the performance of these systems is ultimately limited, as a well-studied BHJ system it provides an ideal test-bed to investigate our novel materials and rationally understand any changes in the observed performance.

Solution and thin-film photoluminescence (PL) studies were undertaken in order to understand the energy transfer characteristics between the MONs and the chosen donor-acceptor components. The MONs show a broad PL emission between 500-800 nm which was quenched upon gradual addition of PCBM (Figure S4.10, ESI). In the solution state PL, addition of MONs to P3HT resulted in 70% quenching of the P3HT signal and a 30% increase in the PL signal of the MONs (Figure S4.11, ESI). This observation is consistent with previous literature studies in ternary blend solar cells.[67,68] The PL intensity of pristine-P3HT films when compared with that of P3HT-MONs blend films was found to be quenched (69.6% quenching efficiency, obtained by integrating the area under curve) with the addition of MONs. When $PC_{60}BM$ is introduced into the blend, complete quenching of the PL signal is observed (**Figure 4.2c**). Figure S4.12, ESI shows the systematic study of PL quenching of P3HT thin films upon gradual increase in the weight ratio of incorporated MONs which saturates at a ratio of 1:0.5 P3HT:Zn_2(ZnTCPP).

Device fabrication, optimisation, and performance

The blends were deposited by spin coating on ITO coated glass substrates containing a 30-40 nm thick layer of PEDOT:PSS. The spin coating parameters were adjusted in order to obtain a ~150-200 nm thick photoactive layer. Finally, a 5 nm thick BCP (2,9-Dimethyl-4,7-diphenyl-1,10-phenanthroline, commonly known as bathocuproine) buffer layer and a 100 nm thick Ag electrode was thermally evaporated on top and the devices were encapsulated with glass covers.

The current density-voltage curves under illumination with a solar simulator (AM 1.5, 1SUN) for the blends P3HT:Zn$_2$(ZnTCPP):PCBM and control P3HT-PCBM are shown in **Figure 4.3b** for the optimised device. Remarkably, the power conversion efficiency (PCE) of the best performing optimised devices with nanosheets was 5.2%; the highest value reported in the literature for this type of device (**Figure 4.3b**) and twice that reported for the best performing device without nanosheets (2.67 %). The best performing optimised device with the nanosheets exhibited a short circuit current density (Jsc) of 10.8 mA/cm^2, open circuit voltage (Voc) of 0.69 V and fill factor (FF) of 69% corresponding to a PCE of 5.2%. These results are also remarkably reproducible with a low standard deviation of 0.12% PCE across 35 devices developed. The laser beam induced current (LBIC) mapping of the MON based devices shows uniform current distribution throughout the mapped region (**Figure 4.3c**).
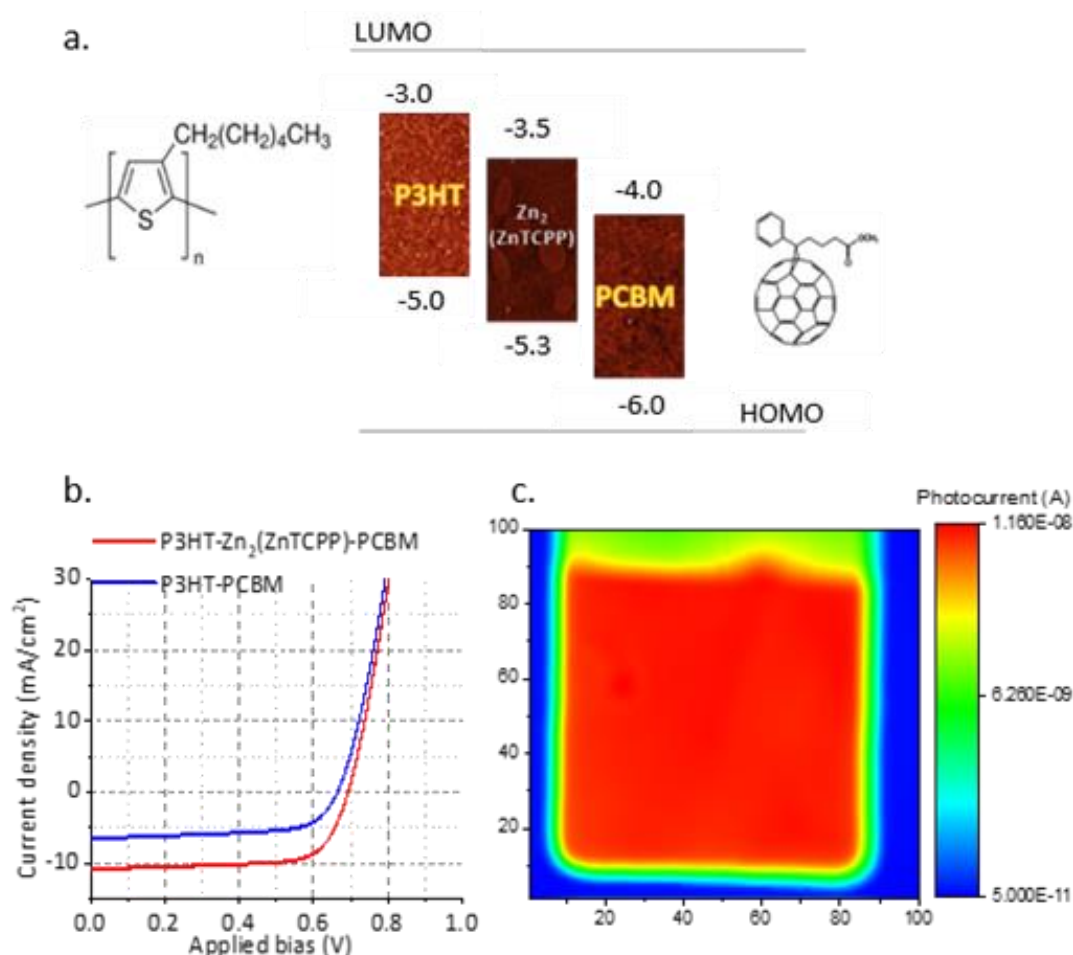
Figure 4.3. Device performance metrics; a. A representation of the HOMO-LUMO level alignment of the components of the ternary device; b. J-V curve of the best performing devices with and without the MONs; c. High resolution LBIC mapping of the P3HT-MON- PCBM device showing a uniform distribution of current over the entire mapped region, each division on the axes corresponds to the step size = 25microns)

Table S4.1(ESI) details the iterative development of the devices, varying the ratio of materials and annealing protocols. It is worth noting that as the concentration of MONs in the blend is increased from 1:0.25:1 to 1:0.5:1 (P3HT:Zn$_2$(ZnTCPP):PCBM) weight ratio Table S4.1(a-d), the Voc remains unchanged within error, and the Jsc increases by 2.08 mA/cm2 accompanied by a 2% increase in the fill factor which corresponds to higher power conversion efficiency. This increase in PCE with the gradual increase in the amount of MONs indicates that the MONs play a significant role in controlling the device performance. Upon further increase of the MON concentration (1:1:1), there is a significant drop in the FF and PCE. Thus 1:0.5:1 weight ratio of P3HT:Zn$_2$(ZnTCPP):PCBM was fixed as the optimum blend concentration for the nanosheet based devices. The reference devices produced under the same conditions without MONs were consistently lower across all metrics with the best performing optimised device without nanosheets exhibited a Jsc of 7.09 mA/cm^2, Voc of 0.66 V and FF of 57.44% corresponding to a power conversion efficiency of 2.67%. A comparison with data reported in the literature for P3HT-PCBM based device having active layer-BCP-Ag
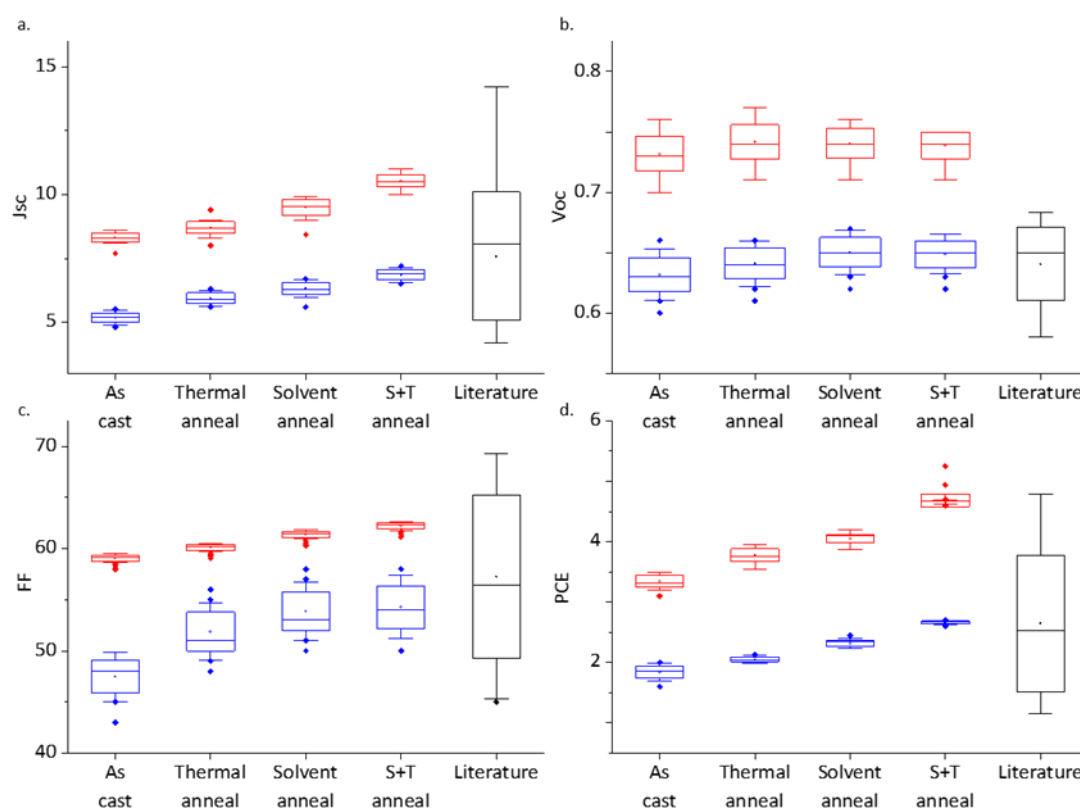
Figure 4.4. Statistical analysis of device performance metrics; Comparison of variation of -Jsc (a), Voc (b), FF (c) and PCE (d) of the MON based devices (Red) with the reference devices (blue) and previous literature reports (black) represented as box plot

configuration show a broad spread of values across the 38 device results statistically analysed in this work (Table S4.2, ESI). In addition to remarkably high PCE's, the Jsc values of our devices are notably high in comparison to previous literature reports indicating higher current density with the incorporation of MONs. Importantly, reference devices with the bulk unexfoliated MOF incorporated into the active layer were not found to function, presumably because of short circuiting due to the µm sized MOFs. This establishes that the nanoscopic dimensions of the monolayer MOF nanosheets play a key role in device performance. A control device was also made by incorporating the TCPP ligand in the P3HT-PCBM blend and the performance was comparable with the P3HT-PCBM devices with a PCE of 1.93% (Jsc=6.5 mA/cm2, Voc=0.54 V; FF=55%) (Figure S4.15c, ESI). Progressive enhancement in the Jsc and PCE and no change in Voc was observed when both sets of devices were subjected to thermal, solvent and solvent + thermal annealing conditions as shown in **Figure 4.4** and listed in Table S4.1, ESI. Interestingly, the fill factor for the as cast MON devices is significantly improved compared to the reference devices but the gap narrows slightly with the additional annealing processes.

Absorption and charge mobility

External quantum efficiency (EQE) measurements were done to compare the amount of current generation from the devices when irradiated in the wavelength range (400-700 nm). Comparison of EQE measurements for the MON-based devices with the control devices (**Figure 4.5a**) shows enhanced spectral response around 430-450 nm corresponding to π-π* transition absorption of the MONs and another well pronounced enhancement at 550-580 nm corresponding to the Q absorption band of the MONs.[64] A higher absorption in the region 600-630 nm corresponds to an increased percentage of crystalline polymer structures in the film.[69] A decrease in the amorphous P3HT region (**Figure 4.5b**) and the red-shifted λ_{max} of the normalized absorption spectra of the MON incorporated ternary blend (**Figure 4.5b**) supports this analysisNo obvious new transient-absorption (TA) features were observed when $Zn_2(ZnTCPP)$ was added to the blend. However, the signal for the sample with $Zn_2(ZnTCPP)$ added is roughly twice that of the sample without (**Figure 4.5c** and S4.17a-b ESI). This gives evidence of enhanced light absorption in the blend with the nanosheets, corresponding to higher current density in the solar cell performance. Evaluation of kinetics of the P3HT-PCBM and P3HT- $Zn_2(ZnTCPP)$-PCBM blends show no real change in the excited state dynamics upon addition of $Zn_2(ZnTCPP)$, at least on timescales ranging from 1 ps to 1 ns (Figure S4.18a). However, the kinetics of polaron pairs in P3HT shows that the addition of $Zn_2(ZnTCPP)$

indicates a large increase (more than twofold) in the population of charges in P3HT (Figure S4.17c).

The charge carrier mobility of electrons and holes after dissociation of excitons at the donor/acceptor interface is an important factor in bulk-heterojunction PV performance. Space-charge limited currents (SCLC) were fabricated and tested in hole only and electron only devices (Table S4.3,Figure S4.19a-S4.22b).[70]   In the absence of nanosheets, the electron mobility in P3HT-PCBM is higher by an order of magnitude than the hole mobility. This can lead to unbalanced charge transport and non-geminate recombination. The inclusion of MONs increases the hole mobility of the system by a factor of 10, improving the balance of hole and electron mobility within the devices. This enables more efficient extraction of charges during
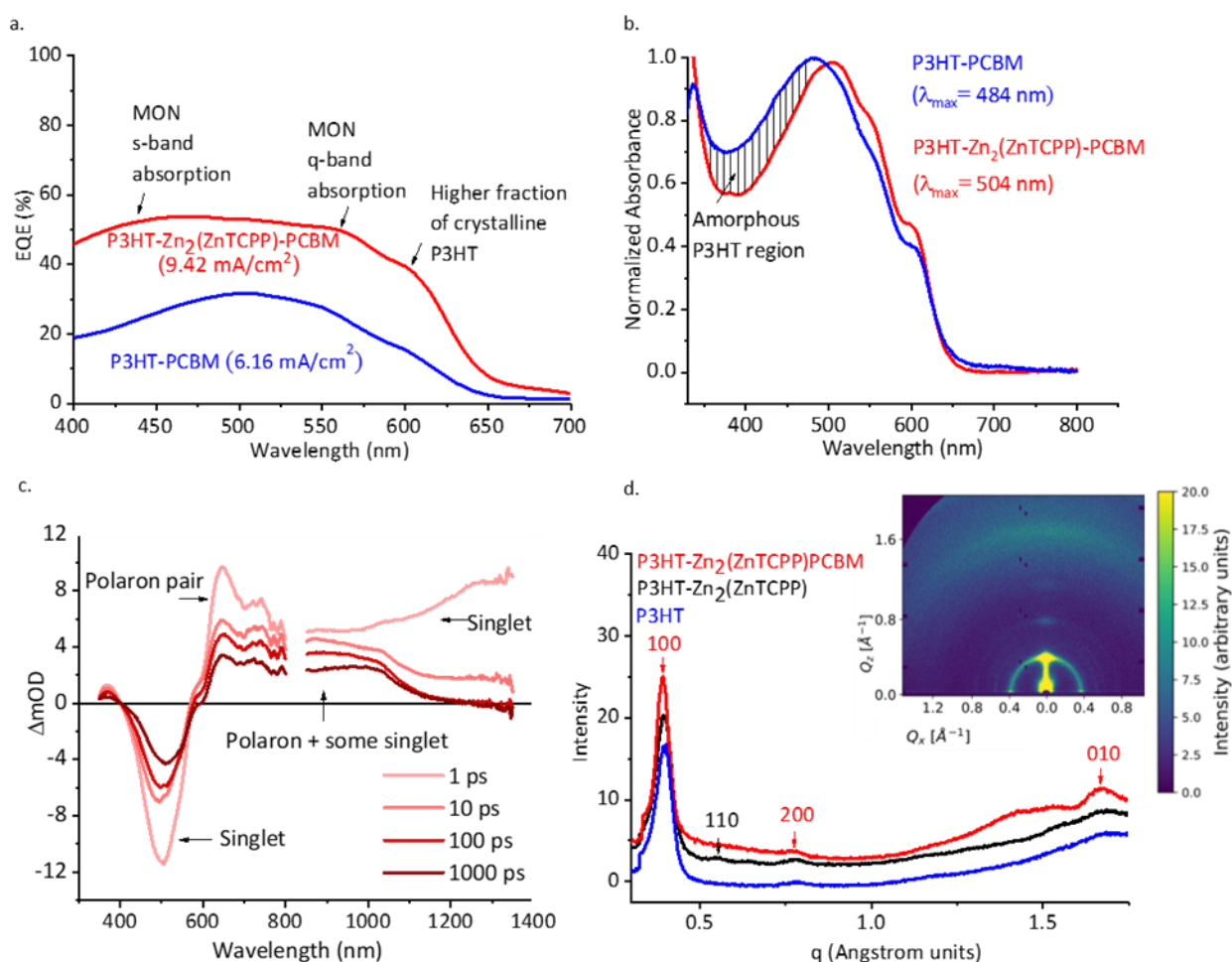
Figure 4.5. EQE, absorption and GI-WAXS results: a. EQE spectra of the MON based devices and the reference devices (with the integrated Jsc values); b. Comparison of the normalized absorption spectra of the reference active layer and the MON based ternary blend- showing a decrease in the amount of amorphous P3HT upon incorporation of MONs; c. Transient absorption spectra of from P3HT-Zn_2(ZnTCPP)-PCBM blend; d. The 1-D cross-sectional analysis of GI-WAXS signals from Pristine P3HT and P3HT-Zn_2(ZnTCPP) blend film overlaid with the signal from P3HT-Zn_2(ZnTCPP)-PCBM active layer blend processed according to the device optimisation procedure; (inset: . 2-D detector image of P3HT-Zn_2(ZnTCPP))

transport to the electrodes reducing the opportunity for free charges to encounter each other and recombine at the donor-acceptor interface.

Understanding the morphology – GIWAXS and AFM
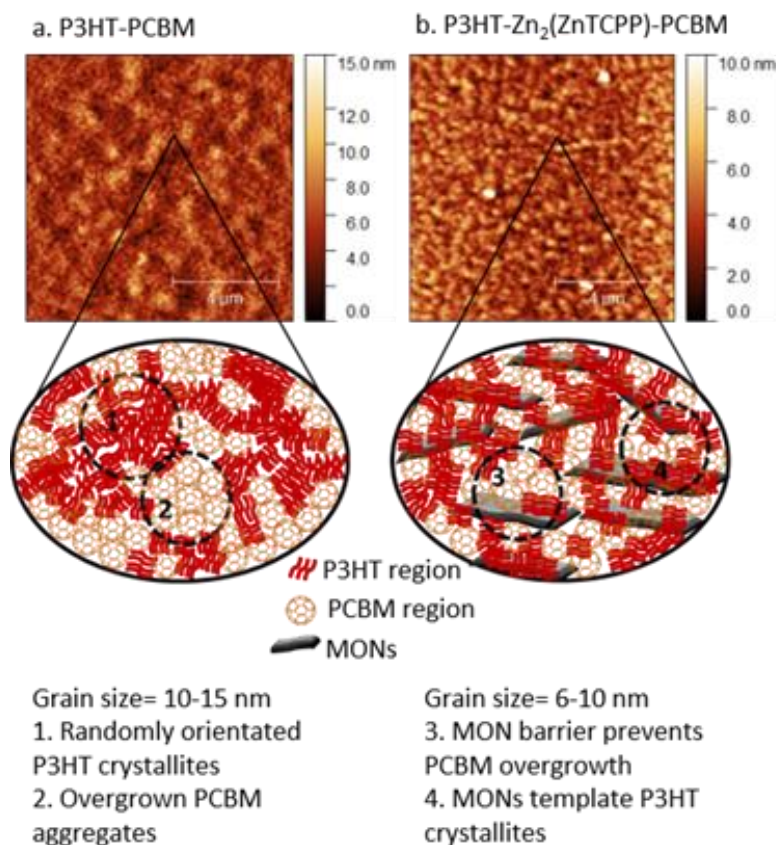
Figure 4.6. AFM images showing optimised devices following solvent and thermal annealing with (top) and without (bottom) MONs and corresponding cartoons highlighting the role of the nanosheets in creating smaller and more crystalline P3HT domains and inhibiting the overgrowth of PCBM aggregates.

Grazing Incidence Wide Angle X-ray Scattering (GI-WAXS) measurements were performed on ~150 nm thick films with and without nanosheet in order to probe the structure of the thin films used in the devices (**Figure 4.5d** and Figure S4.23). Peak at 0.55 Å corresponds to reflection peaks (110) from $Zn_2(ZnTCPP)$ nanosheets[71] which confirms that the nanosheets do not degrade in the presence of the polymer or during the high temperature anneal but facilitate a well-ordered arrangement of the polymer chains and enhance the crystallinity. The peak corresponding to (100) reflections of P3HT is observed with an enhanced intensity in the GI-WAXS signal from P3HT-ZnTCPP film. P3HT appears to have predominantly adopted a face on orientation with respect to the substrate with an intense lamellar stacking peak in plane (100) along q_x. The crystallite size of P3HT was calculated to be 13.59 nm from the 100 and 110 peaks using Scherrer analysis (Table S4.4, ESI). These observations indicate a higher fraction

of crystalline P3HT upon the inclusion of ZnTCPP, consistent   with the observed changes in absorption spectra. AFM imaging of P3HT-Zn_2(ZnTCPP)-PCBM spin coated blends shows the MONs to be homogeneously distributed throughout the matrix of P3HT-PCBM. Demixing of P3HT and PCBM during thin film formation leads to separate regions of P3HT rich and PCBM rich nanoscale domains.[72] A spatial Fourier transform was used to extract the phase separation length scales (grain size) from the AFM images (Figure S4.25-4.26,ESI). In the reference P3HT-PCBM active layer these are in the range of 10-15 nm, while in the presence of MONs the length scale is 6-10 nm. In the presence of MONs, the grain sizes are smaller and more well defined which we speculate favors charge carrier transport. It has been previously shown that the overgrowth of PCBM aggregates (in some literature reports micron sized PCBM crystallites have been observed) correlate with degraded power conversion efficiency and is a reason for detrimental performance in fullerene based systems.[73] The presence of an additional 2-D component which interacts closely with both P3HT and PCBM appears to inhibit their de-mixing and act as a barrier to prevent the formation of oversized PCBM aggregates.

Discussion of the role of MONs within the devices

The zinc-porphyrin MONs possess a number of features that make them ideally suited for incorporation as third component into the active layer of OPVs. The nanoscopic dimensions of the MONs, predominantly monolayer in thickness and ~300 nm wide, allows for their incorporation of at high concentrations (20 wt%) within the ~150 nm thick active layer of the devices. It is worth emphasising that devices based on the bulk MOF did not function and it is only because the predominantly monolayer nanosheets have thicknesses less than the exciton diffusion length that they are able to be incorporated into BHJ type architecture. The porphyrin units have an absorption maximum between that of PCBM and P3HT which means the ternary blends are able to capture a larger fraction of the incident solar spectrum, although this remains dominated by the more strongly absorbing P3HT. The LUMO of the MONs at -3.5 eV means they are ideally positioned between those of PCBM (-4.00 eV) and P3HT (-3.00 eV) with a greater than 0.3 eV offset potentially allowing the MONs to facilitate an energy cascade. However, the transient absorption spectra do not show any of the new features upon inclusion of the MONs that might be expected if the nanosheets are involved in the charge/energy transfer process. This indicates that either charge transfer to the MONs does not happen, or that it occurs faster than the limit of the experimental set-up. Never-the-less, there is typically a trade-off between improvements in Jsc/FF and Voc in ternary devices where additives improve device morphology, but the misaligned HOMO-LUMO levels between the

corresponding levels of the donor and acceptor materials leads to reduced exciton dissociation and charge transfer rates. The very strong device performance and in particular the fact that the Voc is close to the theoretical limit for this system indicates that intermediate HOMO-LUMO level of the MONs prevents geminate recombination losses which would otherwise limit device performance.

The addition of nanosheets also impacts significantly on the morphology of the device. Absorbance, EQE, GI-WAXS and ellipsometry studies indicates that incorporation of the nanosheets results in a larger fraction of crystalline P3HT regions whilst smaller P3HT-PCBM grain sizes are seen by AFM. These observations could also account for the increased hole mobility observed in charge mobility studies and the increase in the population of charges in P3HT observed in transient absorption studies in the presence of MONs. The improved matching of the hole and electron mobilities and smaller grain sizes would reduce the chances for charge carrier recombination during transport to the electrodes.[70] These observations indicate that the two-dimensional MONs act as a surface to template the formation of a larger fraction of crystalline P3HT domains and barriers to inhibit the overgrowth of PCBM aggregates leading to smaller grain sizes (**Figure 4.6**). Thus, the role of the MONs is to enhance the morphology of the active layer without hindering the formation, dissociation and transport of the charge carriers through the charge percolation pathways.

Conclusions

Here we have demonstrated the first example of a MON based bulk-heterojunction solar cell by incorporating monolayer $Zn_2(ZnTCPP)$ MONs in the active layer blend of P3HT: PCBM. The MONs' intermediate energy levels with respect to the donor and acceptor system means that they do not create traps for charges, as observed with the introduction of nanomaterials in other ternary systems. The efficiency of the best performing devices with a 20% loading of MONs was 5.2 %, almost double that of the reference devices without nanosheets (2.67%) and the highest performing devices of its class. Incorporation of the MONs leads to a significant improvement of the open circuit voltage, current density and fill factor of the solar cells. Absorption, EQE, GI-WAXS, ellipsometry and AFM studies show a tenfold increase in charge mobility, doubling of the absorbance, improved crystallinity of P3HT and reduced P3HT: PCBM domain sizes. We suggest that these observations are best explained by the MONs acting as a template to the formation of P3HT crystallites and as a barrier to prevent the over-growth of PCBM. These results demonstrate the potential of MONs as a new class of two-dimensional nanomaterials for use in optoelectronic devices.

The ease with which the electronic and optical properties of MONs can be tuned mean that the band-gap of these materials can potentially be optimized to blend with any polymer system of choice, potentially with non-fullerene acceptor polymers such as ITIC, IHIC, Y6, PM6 etc to result in higher performing fullerene-free OPVs. A range of other semi-crystalline OPV devices where MONs can be introduced as ternary blends to enhance crystallinity, improve blending and reducing domain size are immediate candidates for further investigation.

Author contributions

KS carried out the synthesis and characterisation of MONs, device fabrication, testing and related analysis and drafted the manuscript. DGB analysed the transient absorption data. NV carried out the L-BIC measurement. AJP carried out the GI-WAXS studies. JC, AJP, AI and DGL supported experimental design and data analysis and aided in drafting of the manuscript. JAF designed and coordinated the project and helped in drafting the manuscript.

Conflicts of interest

DGL is a co-founder and Chairman of the materials science company Ossila Ltd, that retails materials and equipment used in organic optoelectronic device research and development.

References

1   A. K. Geim and K. S. Novoselov, *Nature Materials*, 2007, **6**, 183–191.

2   K. Leng, I. Abdelwahab, I. Verzhbitskiy, M. Telychko, L. Chu, W. Fu, X. Chi, N. Guo, Z. Chen, Z. Chen, C. Zhang, Q. H. Xu, J. Lu, M. Chhowalla, G. Eda and K. P. Loh, *Nature Materials*, 2018, **17**, 908–914.

3   I. V. Vlassiouk, Y. Stehle, P. R. Pudasaini, R. R. Unocic, P. D. Rack, A. P. Baddorf, I. N. Ivanov, N. V. Lavrik, F. List, N. Gupta, K. V. Bets, B. I. Yakobson and S. N. Smirnov, *Nature Materials*, 2018, **17**, 318–322.

4   S. Kim, H. Wang and Y. M. Lee, *Angewandte Chemie International Edition*, , DOI:10.1002/anie.201814349.

5   D. J. Ashworth and J. A. Foster, *Journal of Materials Chemistry A*, 2018, **6**, 16292–16307.

6   M. Zhao, Y. Huang, Y. Peng, Z. Huang, Q. Ma and H. Zhang, *Chemical Society Reviews*, 2018, **47**, 6267–6295.

7   R. Sakamoto, K. Takada, T. Pal, H. Maeda, T. Kambe and H. Nishihara, *Chemical Communications*, 2017, **53**, 5781–5801.

8   Y. Peng, Y. Li, B. Yujie, H. Jin, W. Jiao, X. Liu and W. Yang, *Science*.

9   A. Pustovarenko, M. G. Goesten, S. Sachdeva, M. Shan, Z. Amghouz, Y. Belmabkhout, A. Dikhtiarenko, T. Rodenas, D. Keskin, I. K. Voets, B. M. Weckhuysen, M. Eddaoudi, L. C. P. M. de Smet, E. J. R. Sudhölter, F. Kapteijn, B. Seoane and J. Gascon, *Advanced Materials*, 2018, **30**, 1707234.

10   J. Huang, Y. Li, R. K. Huang, C. T. He, L. Gong, Q. Hu, L. Wang, Y. T. Xu, X. Y. Tian, S. Y. Liu, Z. M. Ye, F. Wang, D. D. Zhou, W. X. Zhang and J. P. Zhang, *Angewandte Chemie - International Edition*, 2018, **57**, 4632–4636.

11   T. He, B. Ni, S. Zhang, Y. Gong, H. Wang, L. Gu, J. Zhuang, W. Hu and X. Wang, *Small*, 2018, **14**, 1–6.

12   D. J. Ashworth, A. Cooper, M. Trueman, R. W. M. Al-Saedi, S. D. Liam, A. J. Meijer and J. A. Foster, *Chemistry - A European Journal*, 2018, **24**, 17986–17996.

13   Y. Wang, M. Zhao, J. Ping, B. Chen, X. Cao, Y. Huang, C. Tan, Q. Ma, S. Wu, Y. Yu, Q. Lu, J. Chen, W. Zhao, Y. Ying and H. Zhang, *Advanced Materials*, 2016, **28**, 4149–4155.

14   M. Zhao, Y. Wang, Q. Ma, Y. Huang, X. Zhang, J. Ping, Z. Zhang, Q. Lu, Y. Yu, H. Xu, Y. Zhao and H. Zhang, *Advanced Materials*, 2015, **27**, 7372–7378.

15   N. Lahiri, N. Lotfizadeh, R. Tsuchikawa, V. V. Deshpande and J. Louie, *Journal of the*

American Chemical Society, 2017, **139**, 19–22.

16   A. Abhervé, S. Mañas-Valero, M. Clemente-León and E. Coronado, *Chemical Science*, 2015, **6**, 4665–4673.

17   X. Sun, K.-H. Wu, R. Sakamoto, T. Kusamoto, H. Maeda and H. Nishihara, *Chemistry Letters*, 2017, **46**, 1072–1075.

18   X. Hu, Z. Wang, B. Lin, C. Zhang, L. Cao, T. Wang, J. Zhang, C. Wang and W. Lin, *Chemistry - A European Journal*, 2017, **23**, 8390–8394.

19   G. Wu, J. Huang, Y. Zang, J. He and G. Xu, *Journal of the American Chemical Society*, 2017, **139**, 1360–1363.

20   P. Cheng, G. Li, X. Zhan and Y. Yang, *Nature Photonics*, 2018, **12**, 131–142.

21   J. Zhao, Y. Li, G. Yang, K. Jiang, H. Lin, H. Ade and H. Yan, *Nature Energy*, , DOI:10.1038/NENERGY.2015.27.

22   S. Zhang, Y. Qin, J. Zhu and J. Hou, *Advanced Materials*, 2018, **1800868**, 1–7.

23   Y. Wang, X. Ke, Z. Xiao, L. Ding, R. Xia and H. Yip, *Science*, 2018, **1098**, 1094–1098.

24   C.-H. Tsai, Y.-A. Su, P.-C. Lin, C.-C. Shih, H.-C. Wu, W.-C. Chen and C. Chueh, *Journal of Materials Chemistry C*, , DOI:10.1039/c8tc01542b.

25   V. Sharapov, Q. Wu, A. Neshchadin, D. Zhao, Z. Cai, W. Chen and L. Yu, *The Journal of Physical Chemistry C*, 2018, **122**, 11305–11311.

26   Y. Cho, T. L. Nguyen, H. Oh, K. Y. Ryu and H. Y. Woo, *ACS Applied Materials & Interfaces*, 2018, **10**, 27757–27763.

27   M. Nam, H. Y. Noh, J. Cho, Y. Park, S. Shin, J. Kim, J. Kim, H. H. Lee, J. W. Shim and D. Ko, *Advanced Functional Materials*, 2019, **1900154**, 1–9.

28   M. Nam, M. Cha, H. H. Lee, K. Hur, K. Lee, J. Yoo, I. K. Han, S. J. Kwon and D. Ko, *Nature Communications*, 2017, **8**, 1–10.

29   K. Feron, M. N. Thameel, M. F. Al-Mudhaffer, X. Zhou, W. J. Belcher, C. J. Fell and P. C. Dastoor, *Applied Physics Letters*, , DOI:10.1063/1.4979181.

30   N. Gasparini, L. Lucera, M. Salvador, M. Prosa, G. D. Spyropoulos, P. Kubis, H.-J.

Egelhaaf, C. J. Brabec and T. Ameri, *Energy & Environmental Science*, , DOI:10.1039/c6ee03599j.

31   T. Ameri, J. Min, N. Li, F. Machui, D. Baran, M. Forster, K. J. Schottler, D. Dolfen, U. Scherf and C. J. Brabec, *Advanced Energy Materials*, 2012, 1198–1202.

32   F. Zhang, Q. An and M. Zhang, *Advanced Energy Materials*, , DOI:10.1002/aenm.201702854.

33   R. A. Street, D. Davies, P. P. Khlyabich, B. Burkhart and B. C. Thompson, *Journal of the American Chemical Society*, 2013, 1–4.

34   M. Garg and V. Padmanabhan, *Scientific Reports*, 2016, 1–12.

35   Y. Zhang and Z. Wei, *Nanotechnology*, , DOI:10.1088/0957-4484/26/30/309501.

36   B. Aïssa, M. Nedil, J. Kroeger and A. Ali, *Nanotechnology*.

37   M. M. Stylianakis, D. Konios, C. Petridis, G. Kakavelakis, E. Stratakis and E. Kymakis, *2D Materials*, , DOI:10.1088/2053-1583/aa8440.

38   W. Yang, Z. Ye, T. Liang, J. Ye and H. Chen, *Solar Energy Materials and Solar Cells*, 2019, **190**, 75–82.

39   R. Ahmad, R. Srivastava, S. Yadav, S. Chand and S. Sapra, *ACS Applied Materials and Interfaces*, , DOI:10.1021/acsami.7b08725.

40   H. J. Conley, B. Wang, J. I. Ziegler, R. F. Haglund, S. T. Pantelides and K. I. Bolotin, *Nano Letters*, 2013, **13**, 3626–3630.

41   shuangqing Fan, xiaodong tang, D. Zhang, X. Hu, J. Liu, L. Yang and J. Su, *Nanoscale*, , DOI:10.1039/C9NR05343C.

42   M. M. Ugeda, A. J. Bradley, S. F. Shi, F. H. Da Jornada, Y. Zhang, D. Y. Qiu, W. Ruan, S. K. Mo, Z. Hussain, Z. X. Shen, F. Wang, S. G. Louie and M. F. Crommie, *Nature Materials*, 2014, **13**, 1091–1095.

43   Q. H. Wang, K. Kalantar-Zadeh, A. Kis, J. N. Coleman and M. S. Strano, *Nature Nanotechnology*, 2012, **7**, 699–712.

44   I. Stassen, N. Burtch, A. Talin, P. Falcaro, M. Allendorf and R. Ameloot, *Chemical Society Reviews*, 2017, **46**, 3185–3241.

45   W. A. Maza, A. J. Haring, S. R. Ahrenholtz, C. C. Epley, S. Y. Lin and A. J. Morris, *Chem. Sci.*, 2016, **7**, 719–727.

46   S. Jin, H.-J. Son, O. K. Farha, G. P. Wiederrecht and J. T. Hupp, *Journal of the American Chemical Society*, 2013, **135**, 955–958.

47   C. Y. Lee, O. K. Farha, B. J. Hong, A. A. Sarjeant, S. T. Nguyen and J. T. Hupp, *Journal of the American Chemical Society*, 2011, **133**, 15858–15861.

48   D. Y. Lee, E. K. Kim, C. Y. Shin, D. V. Shinde, W. Lee, N. K. Shrestha, J. K. Lee and S. H. Han, *RSC Advances*, 2014, **4**, 12037–12042.

49   E. D. Spoerke, L. J. Small, M. E. Foster, J. Wheeler, A. M. Ullman, V. Stavila, M. Rodriguez and M. D. Allendorf, *Journal of Physical Chemistry C*, 2017, **121**, 4816–4824.

50   G. O. N. Ndjawa, M. R. Tchalala, O. Shekhah, J. I. Khan, A. E. Mansour, J. Czaban-Jóźwiak, L. J. Weselinski, H. A. Ahsaine, A. Amassian and M. Eddaoudi, *Materials*, , DOI:10.3390/ma12152457.

51   J. Liu, W. Zhou, J. Liu, Y. Fujimori, T. Higashino, H. Imahori, X. Jiang, J. Zhao, T. Sakurai, Y. Hattori, W. Matsuda, S. Seki, S. K. Garlapati, S. Dasgupta, E. Redel, L. Sun and C. Wöll, *Journal of Materials Chemistry A*, 2016, **4**, 12739–12747.

52   C. W. Kung, T. H. Chang, L. Y. Chou, J. T. Hupp, O. K. Farha and K. C. Ho, *Chemical Communications*, 2015, **51**, 2414–2417.

53   C. Zhang, X. Li, S. Z. Kang, L. Qin, G. Li and J. Mu, *Chemical Communications*, 2014, **50**, 9064–9067.

54   W. Zhao, J. Peng, W. Wang, S. Liu, Q. Zhao and W. Huang, *Coordination Chemistry Reviews*, 2018, **377**, 44–63.

55   W. Xing, P. Ye, J. Lu, X. Wu, Y. Chen, T. Zhu, A. Peng and H. Huang, *Journal of Power Sources*, 2018, **401**, 13–19.

56   J. J. Chenxi Liu, Chiming Wang, Hailong Wang, Tianyu Wang, *Eur. J. Inorg. Chem.*, , DOI:10.1002/ejic.201900940.

57   E.-Y. Choi, C. A. Wray, C. Hu and W. Choe, *CrystEngComm*, 2009, **11**, 553–555.

58   I. Goldberg, *Acta Crystallographica Section A Foundations of Crystallography*, 2000,

56, s122–s122.

59   R. Makiura and O. Konovalov, *Scientific Reports*, 2013, **3**, 1–8.

60   R. Makiura and O. Konovalov, *Dalton Transactions*, 2013, **42**, 15931–15936.

61   G. Xu, T. Yamada, K. Otsubo, S. Sakaida and H. Kitagawa, *Journal of the American Chemical Society*, 2012, **134**, 16524–16527.

62   S. Motoyama, R. Makiura, O. Sakata and H. Kitagawa, *Journal of the American Chemical Society*, 2011, **133**, 5640–5643.

63   Y. Ding, Y. P. Chen, X. Zhang, L. Chen, Z. Dong, H. L. Jiang, H. Xu and H. C. Zhou, *Journal of the American Chemical Society*, 2017, **139**, 9136–9139.

64   S. C. Jeoung, D. Kim and D. W. Cho, *Journal of Raman Spectroscopy*, 2000, **31**, 319–330.

65   A. Lefrançois, B. Luszczynska, B. Pepin-Donat, C. Lombard, B. Bouthinon, J. M. Verilhac, M. Gromova, J. Faure-Vincent, S. Pouget, F. Chandezon, S. Sadki and P. Reiss, *Scientific Reports*, 2015, **5**, 1–8.

66   D. Chen, A. Nakahara, D. Wei, D. Nordlund and T. P. Russell, *Nano Letters*, 2011, **11**, 561–567.

67   M. Koppe, H.-J. Egelhaaf, G. Dennler, M. C. Scharber, C. J. Brabec, P. Schilinsky and C. N. Hoth, *Advanced Functional Materials*, 2010, **20**, 338–346.

68   E. M. J. Johansson, A. Yartsev, H. Rensmo and V. Sundstro, 2009, 3014–3020.

69   J. Clark, J. F. Chang, F. C. Spano, R. H. Friend and C. Silva, *Applied Physics Letters*, 2009, **94**, 3–6.

70   J. C. Blakesley, F. A. Castro, W. Kylberg, G. F. A. Dibb, C. Arantes, R. Valaski, M. Cremona, J. Soo and J. Kim, *Organic Electronics*, 2014, **15**, 1263–1272.

71   E.-Y. Choi, C. A. Wray, C. Hu and W. Choe, *CrystEngComm*, 2009, **11**, 553–555.

72   B. A. Collins, J. R. Tumbleston and H. Ade, *Journal of Physical Chemistry Letters*, 2011, **2**, 3135–3145.

73   W. Wang, S. Guo, E. M. Herzig, K. Sarkar, M. Schindler, D. Magerl, M. Philipp and J. Perlich, *Journal of Materials Chemistry A*, 2016, 3743–3753.

4.2 Publication supplementary information

Metal-Organic Framework Nanosheets for Enhanced Performance of Organic Photovoltaic Cells

Kezia Sasitharan, David G. Bossanyi, Naoum Vaenas, Andrew J. Parnell, Jenny Clark, Ahmed Iraqi, David G. Lidzey, Jonathan A. Foster

Supplementary information

Table of contents

1. General experimental procedures

Commercial solvents and reagents were used without further purification. Synthesis of organic ligands was carried out in dry glassware with a nitrogen overpressure. Solvothermal synthesis of metal-organic frameworks was undertaken using borosilicate vials with Teflon faced rubber lined caps.

NMR spectra were recorded on a Bruker Advance DPX 400 spectrometer. Chemical shifts for ^{1}H are reported in ppm on the δ scale; ^{1}H chemical shifts were referenced to the residual solvent peak. All coupling constants are reported in Hz. Mass spectra were collected using a Bruker Reflex III MALDI-TOF spectrometer. Elemental analyses were obtained on a vario MICRO CHNS elemental analyzer equipped with a thermal conductivity detector. X-Ray powder diffraction patterns were collected using a Bruker D8 Advance powder diffractometer equipped with a copper K_α source (λ=1.5418 Å) operating at 40 kV and 40 mA. The instrument was fitted with an energy-dispersive LYNXEYE detector. Measurements were carried out using a fixed goniometer stage with a rotating flat plate sample holder. IR spectroscopy was performed on a Perkin-Elmer Pyris TGA from 30-600°C at 10°C min^{-1}, under a 20 mL min^{-1} nitrogen flow. UV-Vis absorption spectra were collected on a Cary 5000 UV-Vis-NIR instrument using a 1 cm internal length quartz cuvette. PL spectra were recorded using a Horiba FluoroMax spectrofluorometer using 500 nm excitation. The fluorescence emission was corrected for sample absorption at the excitation wavelength to produce an emission spectrum proportional to the fluorescence quantum efficiency.

Nanoscopic characterisation was performed using a Bruker Multimode 5 AFM, operating in soft-tapping mode under ambient conditions. Bruker OTESPA-R3 cantilever were used, with a drive amplitude and nominal resonance frequency of 20.4 mV and 290 kHz, respectively. Images were processed using standard techniques with free Gwyddion software. TEM images were obtained using a JEOL-2010F TEM operated at an accelerated voltage of 200 kV.

2. Syntheses

2.1 Synthesis of *meso-tetracarboxyphenyl porphyrin* (TCPP) ligand

10 mL of pyrrole (98%, light brown solution) was distilled under vacuum at 80°C to give 5 mL of a clear solution. 4-formylbenzoic acid (3.0 g, 20 mmol) was dissolved in propionic acid (100 mL) and freshly distilled pyrrole (1.4 mL, 20 mmol) was added by syringe. The solution immediately darkened and was refluxed for 15 hours. The mixture was chilled in a fridge for 10 hours before collection of the solid by vacuum filtration. The solid was washed with hot water (2 x 20 mL) and dried under vacuum to give the product as a black powder (3.23 g, 4.0 mmol, 80 %). Elemental Analysis calculated for $C_{48}H_{30}N_4O_8$: Expected: C, 72.91; H, 3.82; N, 7.09. Found: C, 72.95; H, 4.08; N, 6.82

λ_{max} (nm): 420 (π-π^*)

^{1}H-NMR (d$_6$-DMSO) δ/ppm: 8.85 (8H, s, β-pyrrolic H), 8.38 (8H, d, $J = 8.0$, Ar-H), 8.32 (8H, d, $J = 8.0$, Ar-H), -2.95 (2H, s, internal pyrrole NH).

MALDI-TOF: m/z 791.2 ([MH]$^+$)

2.2 Synthesis of bulk Zn_2(Zn-TCPP)(DMF)

H$_2$TCPP (7.9 mg, 0.03 mmol), Zn(NO$_3$)$_2$.3H$_2$O (8.9 mg, 0.09 mmol), DMF (1.5 mL) and ethanol (0.5 mL) were mixed at room temperature and heated at 80°C for 24 hours. Purple crystals were collected by centrifugation at 4500 RPM for 10 minutes and repeatedly washed in ethanol until the supernatant became clear (Yield 87%)

Elemental analysis $C_{48}H_{24}N_4O_8Zn_3(H_2O)_4(DMF)_3$: Expected C, 53.57; H, 4.50; N, 8.33 Found C, 52.76; H, 4.77; N, 8.88.

A slight excess of Zn around the edge of the MOF and possible nitrate counter ions could be the reason for lower carbon content and higher nitrogen.

2.3 Exfoliation of MOF into MONs

20 mg of Zn$_2$(ZnTCPP) MOF was added to a 10 mL glass vial along with 4 mL of the desired solvent. The sample was mixed in a vortex mixer for 30 seconds to disperse the sediment. The samples were sonicated using a Fisherbrand Elmasonic P 30H ultrasonic bath (2.75 L, 380/350 W, UNSPSC 42281712) filled with water. Samples were sonicated for 60 min at a frequency

of 80 kHz with 100% power and the temperature was thermostatically maintained at 16-20°C using a steel cooling coil. Sonication was applied using a sweep mode and samples were rotated through the water using an overhead stirrer to minimise variation due to ultrasound "hot-spots". Following sonication, the vials were transferred to centrifuge tubes and centrifuged at 1500 RPM for 10 minutes to remove non-exfoliated particles.

3. Structural characterisations

Figure S4.1 Powder diffraction pattern for as-synthesized $Zn_2(ZnTCPP)$ MON in comparison with the synthesized bulk MOF. The diffraction patterns are in accordance with the previous reports[1]

TGA
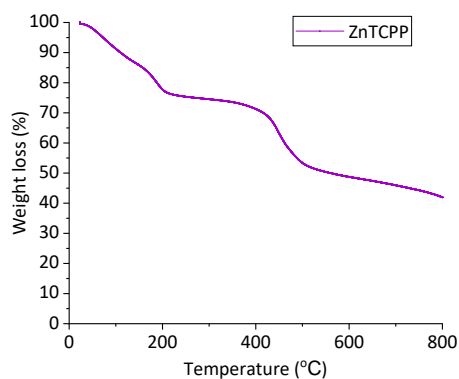
Figure S4.2 Thermo-gravimetric analysis of $Zn_2(ZnTCPP)(H_2O)_4(DMF)_3$ MOF

Loss of solvent (Calculated 22.89%; Experimental: 22.74%)
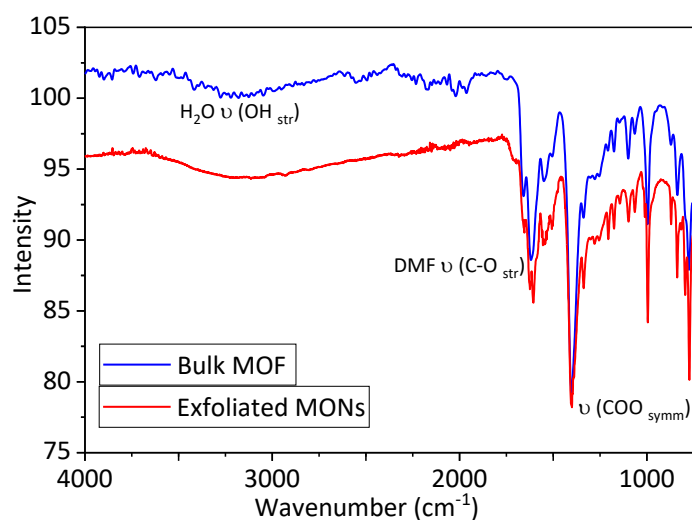
Figure S4.3 FTIR spectra of $Zn_2(ZnTCPP)$ bulk MOF in comparison with exfoliated MONs.

The tyndall scattering observed in the supernatant containing the MONs confirms their colloidal nature.
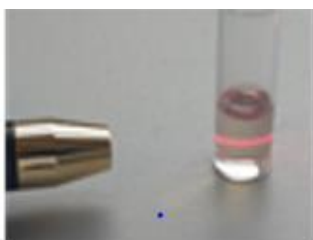
Figure S4.4. Tyndall scattering observed in a MON suspension

4. Morphological characterisations

4.1 AFM

AFM samples of the nanosheets were prepared through dropping aliquots (typically 2 x 5 µL drops) of a suspension onto freshly cleaved Mica, which had been stuck to a magnetic, stainless steel Agar scanning probe microscopy specimen disc for loading into the instrument.
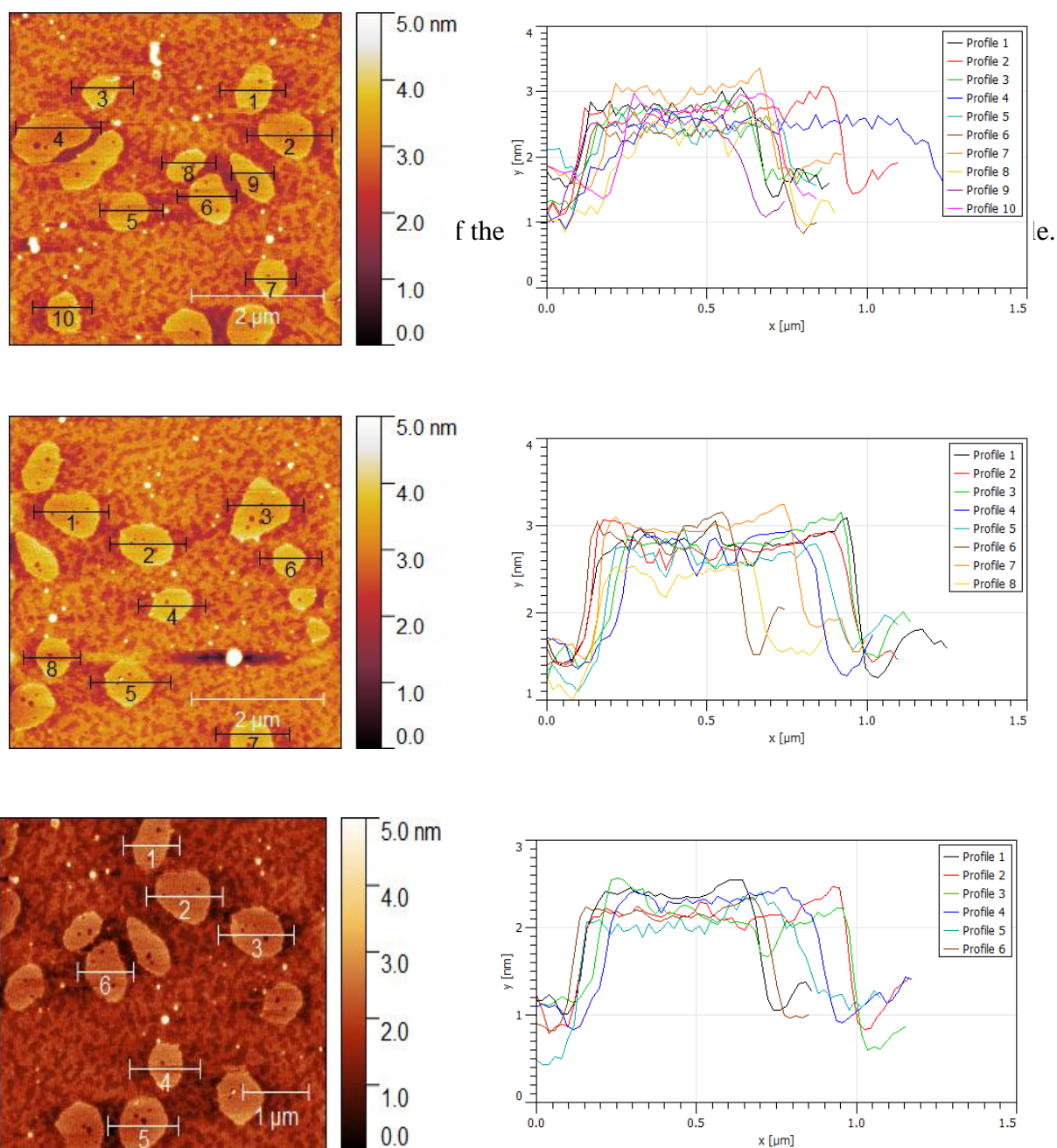
Figure S4.5 AFM images and the corresponding height profiles of the MONs

4.2 TEM and EELS

Prior to TEM characterisation, the suspension (10uL) of the nanosheets was dropcast onto holey C-coated Cu grid and allowed for evaporation of the solvent.
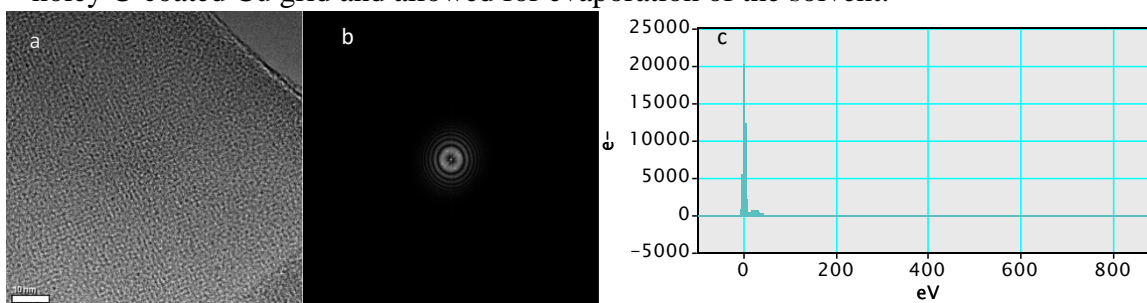
Figure S4.6. HRTEM and corresponding FFT (b) pattern of the MONs; c. Electron energy loss spectroscopy

5. Opto-electronic characterisation

5.1 UV-Vis in solution state
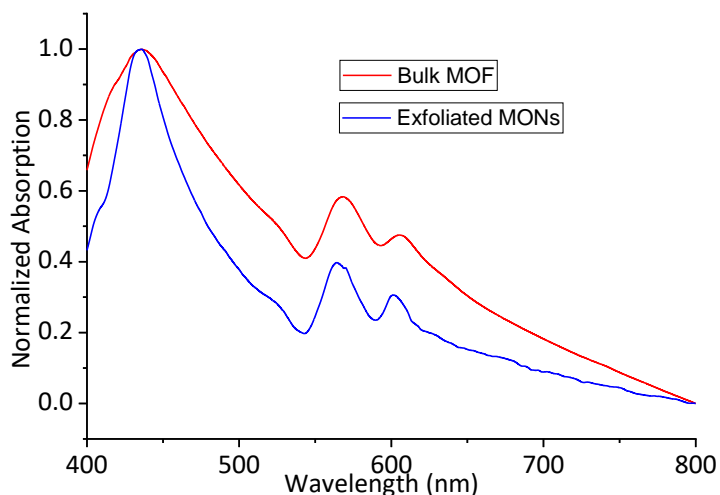
Figure S4.7. UV-Vis spectroscopy of suspension of the bulk MOF (in Ethanol) and MONs (in chlorobenzene); 0.1 mM concentration.

5.2 Cyclic voltammetry

The CV analysis was conducted in an acetonitrile solution containing tetrabutylammonium perchlorate electrolyte with Ag/Ag^+ as the reference electrode and Pt wire as the counter electrode. The nanosheets were drop cast as films onto the glassy carbon working electrode

and the measurements were performed under an inert atmosphere of Argon with a scan rate of 100 mVs^{-1}.
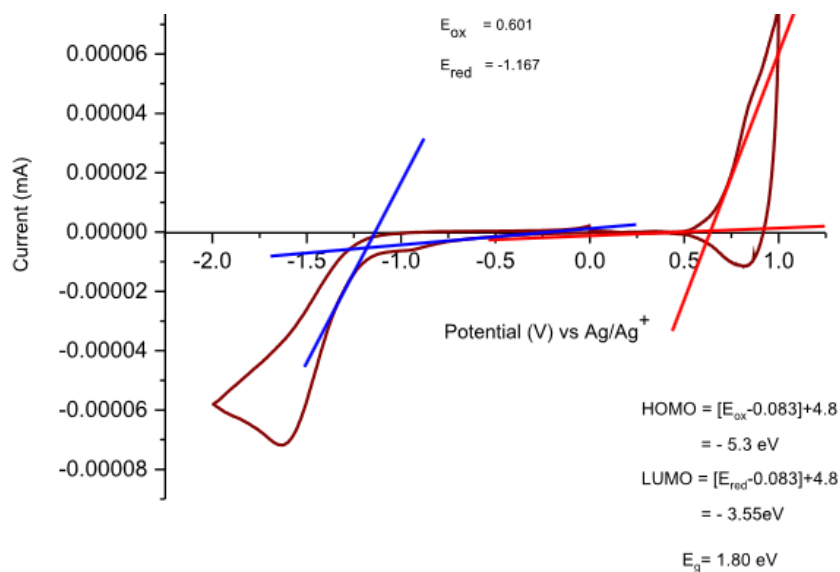
Figure S4.8 HOMO-LUMO level determination from the CV scan of Zn$_2$(ZnTCPP) MONs

5.3 Thin film UV-Vis for optical band gap evaluation
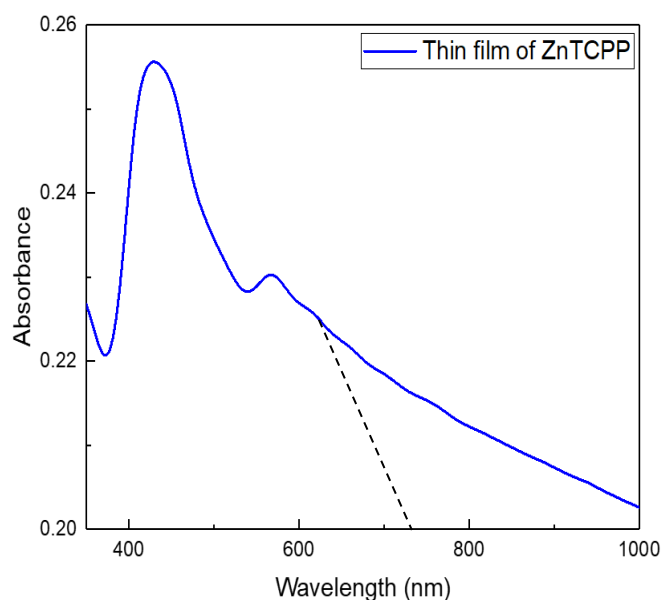
Figure S4.9. Thin film UV-vis spectra obtained by dropcasting a 5mg/ml suspension of MON in ethanol onto a quartz substrate, followed by evaporation of solvent resulting in a 40nm thin film (dektak).
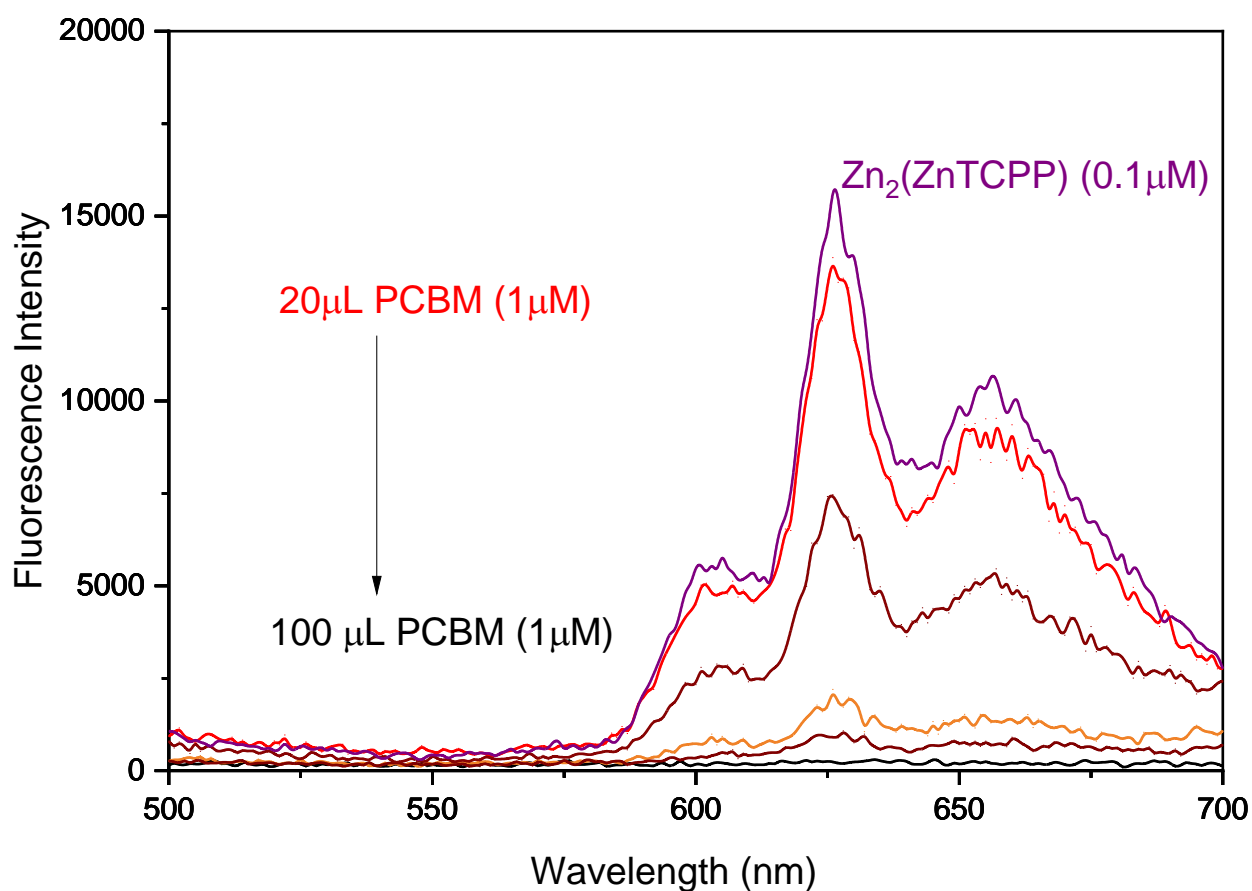
Figure S4.10 The fluorescence emission of a 0.1µM suspension of the MONs (concentration adjusted for Absorbance <0.1 OD) is quenched upon gradual addition of PCBM (1µM) indicating charge transfer between them. The addition of the PCBM solution was done in increments of 20µL (20µl, 40µl, 60µl, 80µl, 100µl). Excitation wavelength= 430nm
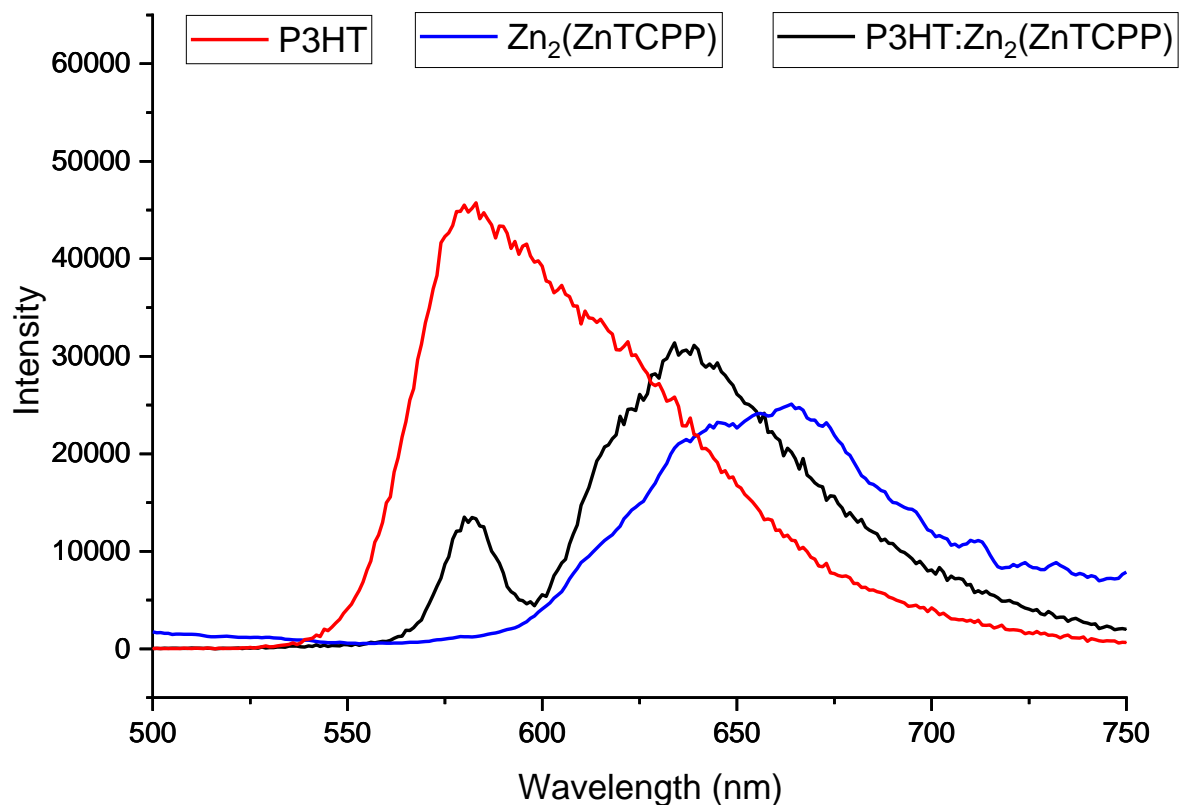
Figure S4.11 The fluorescence emission of 1µM P3HT solution; Zn$_2$(ZnTCPP) suspension and 1:0.5 volume ratio of P3HT: Zn$_2$(ZnTCPP) Excitation wavelength = 430nm

5.5 Thin film PL
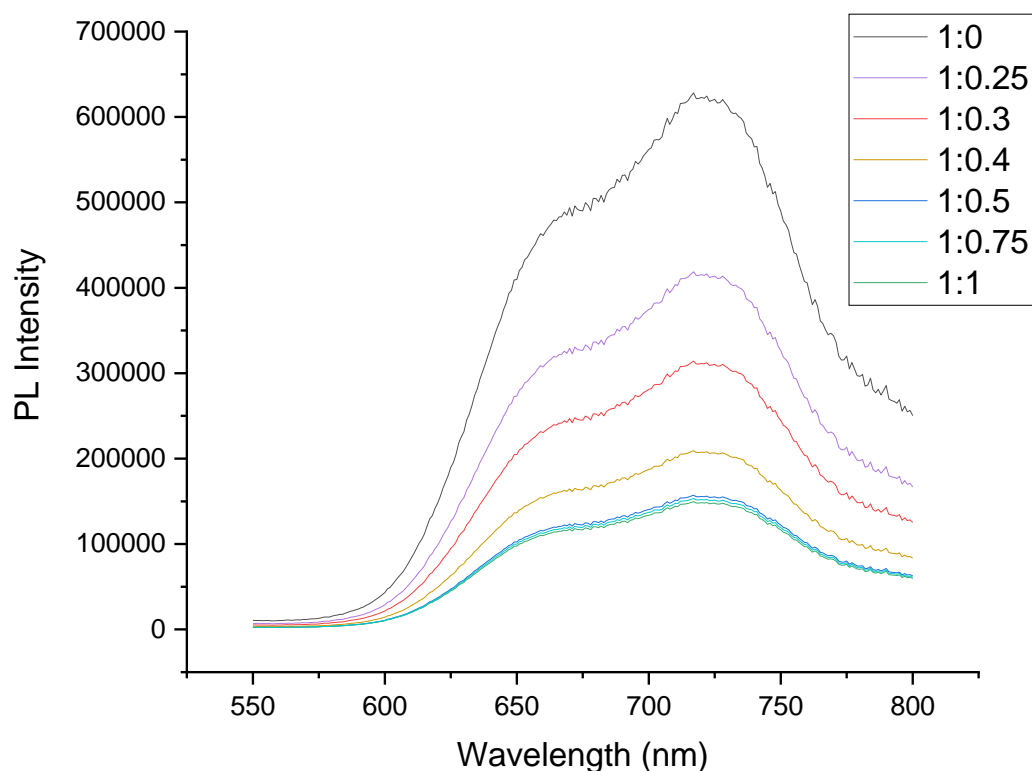
Figure S4.12 Thin film Photoluminescence spectra of P3HT:Zn_2(ZnTCPP). The weight ratios of the components in the film (P3HT:Zn_2(ZnTCPP) is listed in the legend. Excitation wavelength = 430 nm

P3HT (10mg/ml) was spin-coated onto Quartz slides (2000rpm, 60 s) and dried for solvent evaporation. Similarly P3HT: Zn_2(ZnTCPP) precursor solutions were prepared for the required weight ratios and spin coated (1500rpm, 60s), dried prior to PL measurements.

The PL intensity of P3HT is quenched by 70% upon addition of 1:0.5 weight ratio of the MONs and any further addition does not cause more quenching of the signal.

6. Casting of films

6.1 Optimization of spin parameters
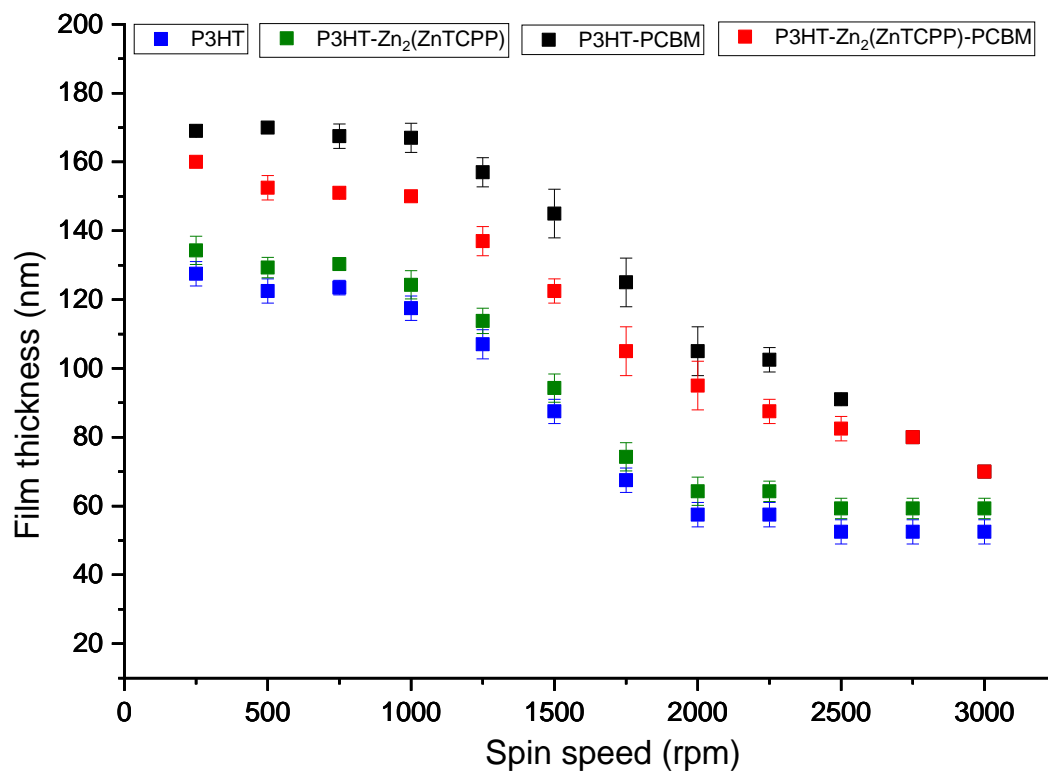
Figure S4.13 Calibration curve of thickness of the spin-coated films as a function of spin speed (t=60 seconds). Concentration of spin coat precursor solutions are: P3HT- 10 mg/ml; P3HT-Zn_2(ZnTCPP)- 10 mg/ml (1:0.5); P3HT:PCBM- 10 mg/ml (1:1); P3HT-Zn_2(ZnTCPP)-PCBM-10mg/ml (1:0.5:1)

6.2 AFM analysis of spin coated Pure P3HT and P3HT-Zn$_2$(ZnTCPP) films on Quartz substrate
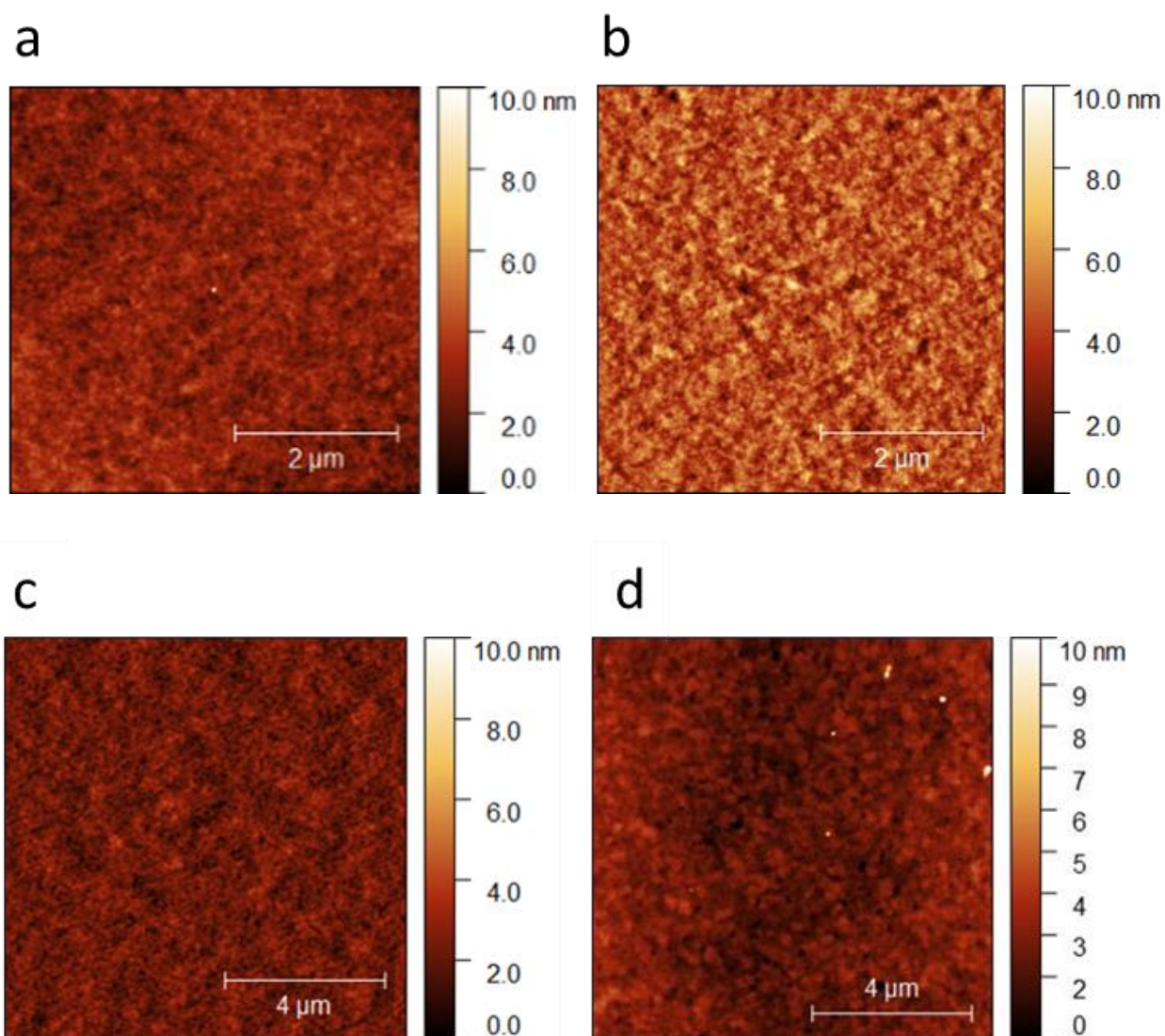
Figure S4.14 AFM topographical images of spin coated films

a) Pure P3HT on quartz substrate; b) P3HT-Zn$_2$(ZnTCPP) (1:0.5) on quartz substrate; c) As-cast P3HT-PCBM on ITO coated glass substrate; d) As-cast P3HT- Zn$_2$(ZnTCPP)-PCBM (1:0.5:1) on ITO coated glass substrate

7. Fabrication of devices

7.1 Preparation of substrates

Pre-patterned ITO Glass substrates (20 mm x 15 mm) of 20 ohm/square resistance (Ossila) were cleaned via hellmenex (1-3vol%) in boiling DI water (10-minute sonication), followed by further washing in boiling DI water (10-minute sonication) and finally 5-10 minutes sonication in isopropyl alcohol. The substrates were dried with a nitrogen gun and placed in a UV-Ozone cleaner for 10 minutes to ensure removal of any surface particulates.

7.2 Deposition of PEDOT:PSS

PEDOT:PSS solution (Al4083, Ossila) was brought to room temperature, filtered through a 0.45 µm PVDF filter into an amber vial and dynamically spin-coated (45 µL) onto room-temp substrates at 6000 rpm, to achieve a film ~25 nm. The PEDOT:PSS coated substrates were placed on a hotplate at 110 °C for 15 minutes. This was followed by further annealing in the glovebox at 110 °C for 15 minutes to remove any surface moisture. After 15 minutes annealing in the glovebox, the ITO/PEDOT samples were cooled to room temperature before active layer deposition.

7.3 Active layer deposition

P3HT (Sigma Aldrich) and PCBM (99% purity, supplied by Ossila) were used as received. P3HT (10mg/mL) was dissolved in chlorobenzene (CB) solvent. After heating at 60 °C for 10 minutes followed by cooling towards room temperature, the solution was filtered through a 0.45 um PTFE filter. The P3HT solution in chlorobenzene was then mixed with 5mg ZnTCPP MONs (1:0.5 wt/wt ratio of P3HT:ZnTCPP)) and stirred at 60 °C for an hour. Then 10 mg of PCBM was added and the final P3HT:ZnTCPP:PCBM (1:0.5:1 wt/wt ratio) was heated at 70°C for an hour and cooled to room temperature prior to spin coating. The solutions were then spin-cast onto ITO/PEDOT at 1000 rpm under a nitrogen atmosphere in a glove box, forming films of ~150 nm as determined by dektak. For control devices, 1:1(wt/wt) (P3HT:PCBM) were spin cast at 2000 rpm in the same method as above to give films of ~150nm. Solvent-vapour annealing of the films was carried out by placing the coated substrates in a sealed metal container containing 20uL of solvent chlorobenzene) for 5 minutes.

7.4 Top contact deposition and encapsulation

The ITO/PEDOT:PSS/Active layer substrates were placed under a vacuum of <2E-6 mBar before thermally evaporating BCP (5nm) and Silver (100nm) layers using a shadow mask. The devices were encapsulated using an epoxy resin (Ossila, E131).

7.5 Device testing

Device performance was determined under ambient conditions by measuring J–V curves using a Newport 92251A-1000 solar simulator, with devices illuminated through a 0.0256 cm^2 aperture mask. Before each set of measurements, the intensity was calibrated to 100 mW cm^{-2} using an NREL certified silicon reference cell. The applied bias was swept from 0.0 to +1.2 V and back again at a scan speed of 0.4 V s^{-1} using a Keithley 237 source measure unit.

External quantum efficiencies were measured using a white light source that was monochromated using a Spectral Products DK240 monochromator that was then imaged on the PSC active area. The intensity of the monochromated light was determined using a calibrated silicon photodiode having a known spectral response. The external quantum efficiency was measured in the spectral range 400-700 nm using an Xtralien X100 (Ossila) source measure unit to determine the PSC photocurrent.

Laser beam induced current (LBIC) mapping was performed on the ternary blend devices. The system comprised a mechanically chopped laser that was passed through a spatial filter before being focused to a spot size of ~1 μm onto the sample via a 50x Mitutoyo infinity-corrected long working distance objective. The sample was mounted on a computer controlled XY-stage, and moved in a sawtooth pattern in steps of 1 μm. A blue 3mW, 405 nm diode laser (power density of 27 W/cm^2)　used to generate photocurrent. Photocurrent was measured using a Stanford Research Systems SR830 lock-in amplifier referenced to the chopped laser.
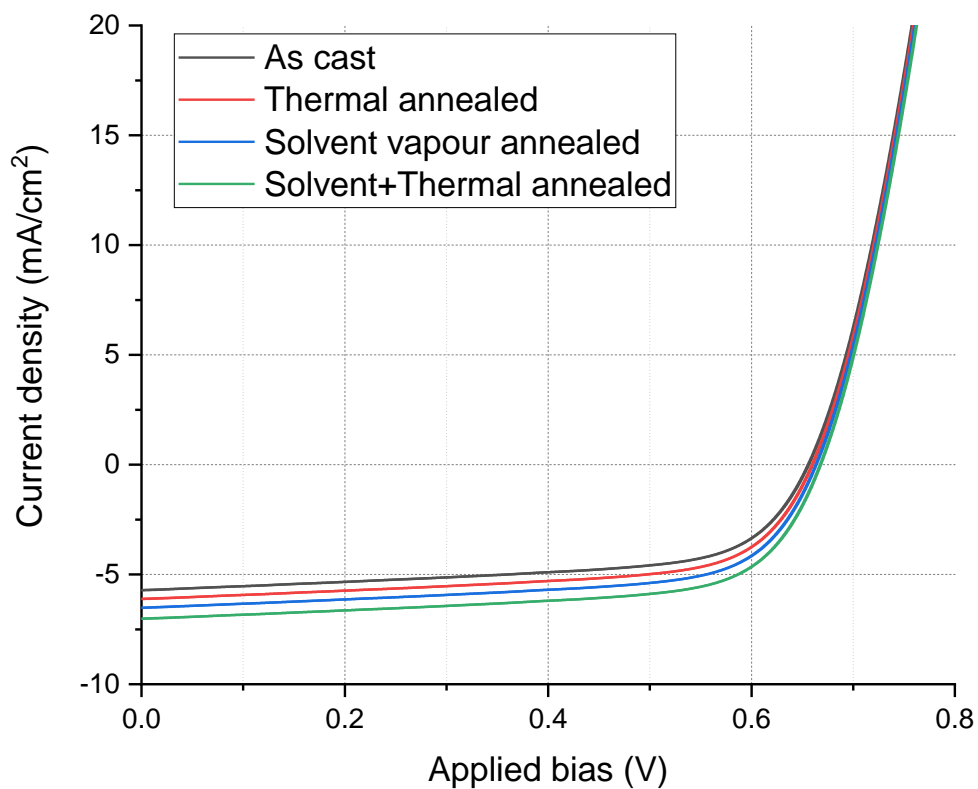
Figure S4.15a Current-density-voltage curves of P3HT-Zn_2(ZnTCPP)-PCBM devices.
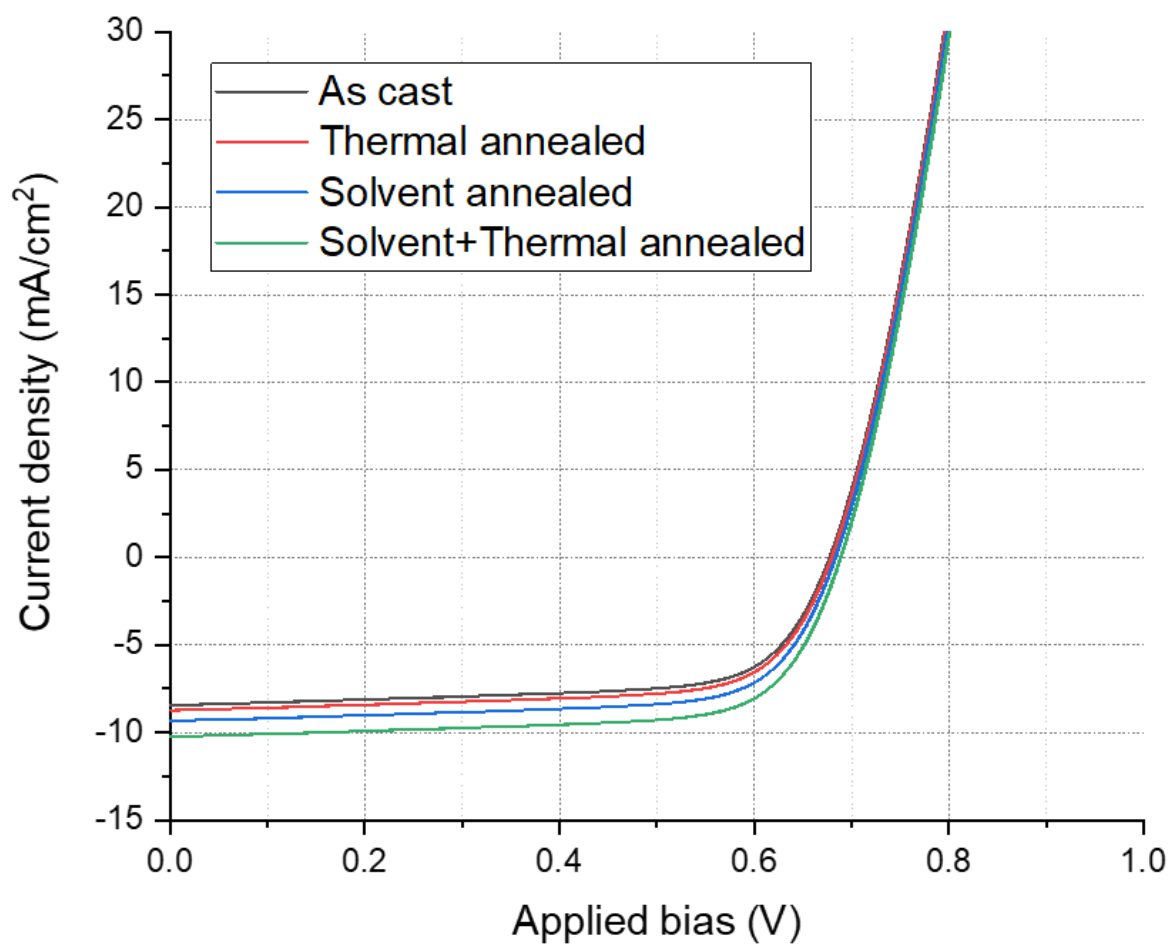
Figure S4.15b- Current-density-voltage curves of P3HT-PCBM devices

Table S4.1 Device performance metrics corresponding to the different blend ratios and processing conditions used in this work for optimization. All the results shown here are averaged values of data obtained from a set of 35 devices each.

	Active layer (P3HT:Zn$_2$ZnTCPP:PCBM)	J$_{sc}$ (mA/cm^2)	V$_{oc}$ (V)	FF (%)	PCE (%)	PCE (%) Champion device
	Varying composition of active layer					
a	1:0:1	5.25±0.31	0.64±0.06	49.21±2.50	1.94±0.14	2.02
b	1:0.25:1	6.34±0.21	0.64±0.02	50.26±1.40	2.27±0.23	2.50
c	1:0.5:1	8.42±0.20	0.69±0.05	59.17±1.27	3.24±0.35	3.60
d	1:1:1	7.23±0.12	0.66±0.07	35.87±3.20	1.87±0.02	1.90
	Thermal annealing					
e	1:0:1	6.11±0.40	0.66±0.05	51.64±2.74	2.04±0.04	2.09
f	1:0.5:1	8.72±0.32	0.70±0.04	60.12±0.85	3.63±0.15	3.96
	Solvent vapour annealed					
g	1:0:1	6.50±0.23	0.65±0.03	53.21±1.70	2.25±0.23	2.46
h	1:0.5:1	9.51±0.31	0.70±0.05	62.70±0.72	4.06±0.10	4.21
	Solvent + thermal annealed					
i	1:0:1	7.09±0.15	0.66±0.02	57.44±2.20	2.67±0.01	2.67
j	1:0.5:1	10.54±0.2	0.70±0.03	63.12±0.15	4.65±0.30	5.20

7.6 Analysis of device data reported in literature.

Scifinder search yielded 65 literature results containing the search keywords "P3HT", "PCBM" and "BCP". Out of these reports, devices with plasmon modified hybrid systems, with <1%

power conversion efficiencies or which were only reported as a patent were excluded. The remaining 38 device results from 18 papers are shown in figure S2 and used in for the statistical analysis given in Figure 3.

Table S4.2. The configuration and performance parameters of the devices used for statistical analysis in Figure 4.3

Configuration	Jsc	Voc	FF	PCE
P3HT-PC71BM/BCP/Al[2]	14.21	0.58	57.8	4.79
P3HT-PCBM/BCP/Ag/Wox[3]	6.33	0.54	60.2	2.07
P3HT-PCBM/Yb/BCP/Ag/Wox[3]	6.68	0.55	65.4	2.42
P3HT-PCBM/BCP/Al[4]	11.74	0.59	62.29	4.31
P3HT-PCBM/BCP/Al[5]	9.76	0.63	60	3.72
	9.55	0.65	57	3.52
	9.38	0.64	56	3.36
	10.02	0.64	41	2.61
	9.41	0.63	62.73	3.74
	10.22	0.64	63	4.11
P3HT-PCBM-PMMA/BCP/Al[6]	5.41	0.61	52.6	1.65
	4.18	0.61	45.5	1.16
P3HT-PCBM/BCP/Al[6]	4.35	0.59	52.2	1.34
	4.51	0.59	51.1	1.36
P3HT-PCBM/BCP/Al[7]	10	0.64	60	3
P3HT-PCBM/BCP/Al[8]	6.28	0.61	38	2.66
P3HT-PCBM/BCP/LiF/Al[9]	12.31	0.645	44.5	3.54

P3HT-PCBM/MoO3/ ZnPc/C60/BCP/LiF-Al[10]	4.76	0.457	56.6	1.21
	4.23	0.57	58.3	1.42
	5.68	0.48	56.0	1.53
P3HT-PCBM/Ca-Al/Subpc/C60/BCP/Ag[11]	8	0.55	60	3.00
P3HT-PCBM-BCP/LIF-Al[12]	8.88	0.59	39.1	2.05
P3HT-PCBM/BCP/Al[13]	9.64	0.63	61.2	3.72
P3HT-PCBM/BCP/LiF/Al[14]	10.83	0.56	65.2	3.74
P3HT-PCBM/BCP/Ag[15]	8	0.6	60	3.5
P3HT-PCBM/BCP/Al[16]	11.06	0.59	40	2.64
P3HT-PCBM/BCP-LiQ[16]	11.30	0.66	58	4.29
ZnO/BCP/P3HT-PCBM/MoO3/Al[17]	9.23	0.61	62	3.49
	8.53	0.50	35	1.50
	8.85	0.58	60	3.08
	8.68	0.59	55	2.82
CsCl/BCP/P3HT-PCBM/MoO3/Al[18]	9.43	0.59	54.1	3.00
	9.49	0.60	58.6	3.31
BCP/P3HT-PCBM/MoO3/Al[18]	9.24	0.53	50.1	2.50
P3HT-PCBM/BCP/Al[19]	4.51	0.65	42	1.24
	6.29	0.61	52	1.99
P3HT-PCBM/BCP-LiF/Al[19]	4.58	0.66	41	1.25
	6.12	0.61	49	1.85
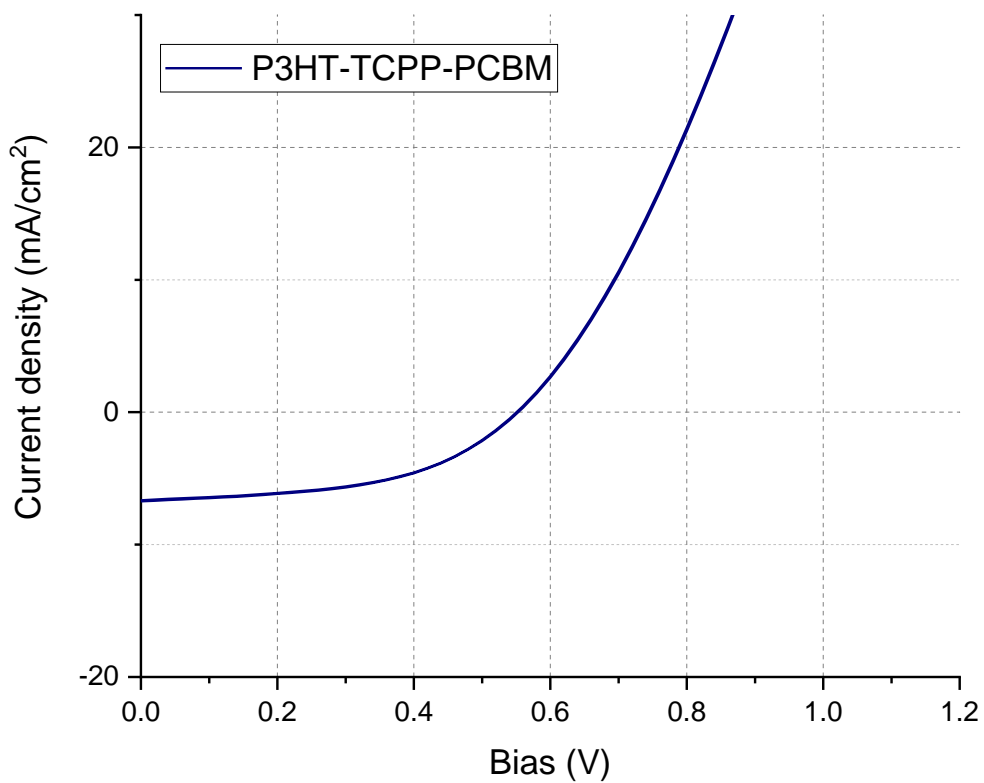
Figure S4.16. J-V curve of P3HT/TCPP-ligand/PCBM ternary device.

8. Transient absorption and Kinetics

We have recorded transient absorption spectra for P3HT-PCBM and P3HT/Zn$_2$(ZnTCPP)/PCBM samples with both NIR and UV probes. During the UV probe measurement both samples degraded. UV probe gives sensible TA data in the range 350nm-700nm and the NIR probe from 850nm-1300nm. TA signals are given in units of $\Delta mOD = 1000 \times \frac{OD_{pump\,on} - OD_{pump\,off}}{OD_{pump\,off}}$ where OD is optical density.

The following transient absorption features were observed:

1. Singlet exciton ground state bleach (GSB) 470-530nm (photogenerated exciton in P3HT);

2. Polaron pair photoinduced absorption (PIA) 600-700nm (charge-pairs in P3HT or charge-transfer state at P3HT/PCBM interface);

3. Polaron photoinduced absorption (PIA) 900-1000nm (free charges in P3HT overlapped with singlet PIA) and

4. Singlet exciton photoinduced absorption (PIA) 1000-1400nm (photogenerated exciton in P3HT).

No obvious new TA features were observed when Zn$_2$(ZnTCPP) was added to the blend. However, the signal for the sample with Zn$_2$(ZnTCPP) added is roughly twice that of the sample without (Figure S4.17a-b). This gives evidence of enhanced light absorption in the blend with the nanosheets, corresponding to higher current density in the solar cell performance. Of all the TA features, the singlet PIA feature around 1300nm increased less than the other features when ZnTCPP is added. Evaluation of kinetics of the P3HT-PCBM and P3HT-ZnTCPP-PCBM blends show no real change in the excited state dynamics upon addition of ZnTCPP, at least on timescales ranging from 1ps to 1ns (Figure S4.18a). Addition of PCBM results in a much longer lifetime of holes in the P3HT, as expected. Addition of ZnTCPP seems to cause a large increase (more than twofold) in the population of charges in P3HT (Figure S4.17c).
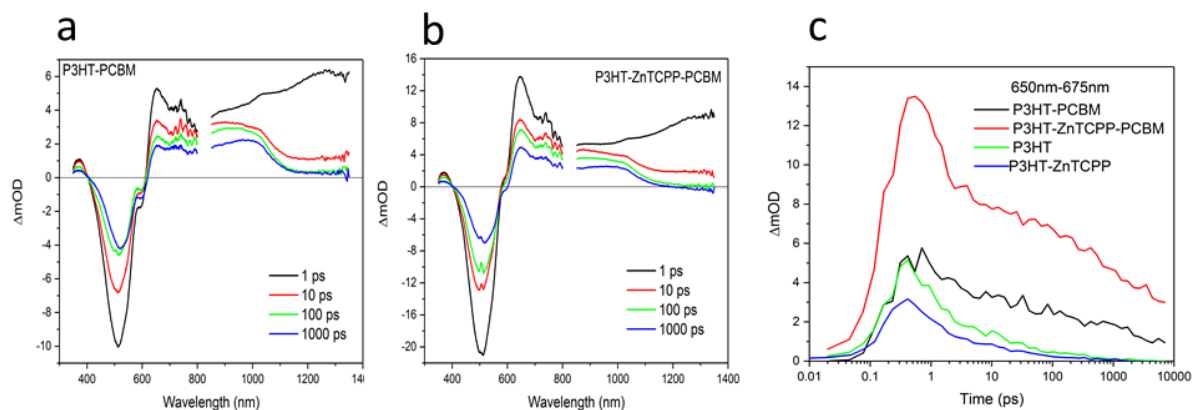
Figure S4.17. Transient absorption spectra of a. P3HT-PCBM film and b. P3HT-ZnTCPP-PCBM film; c. Kinetics of polaron pairs in P3HT
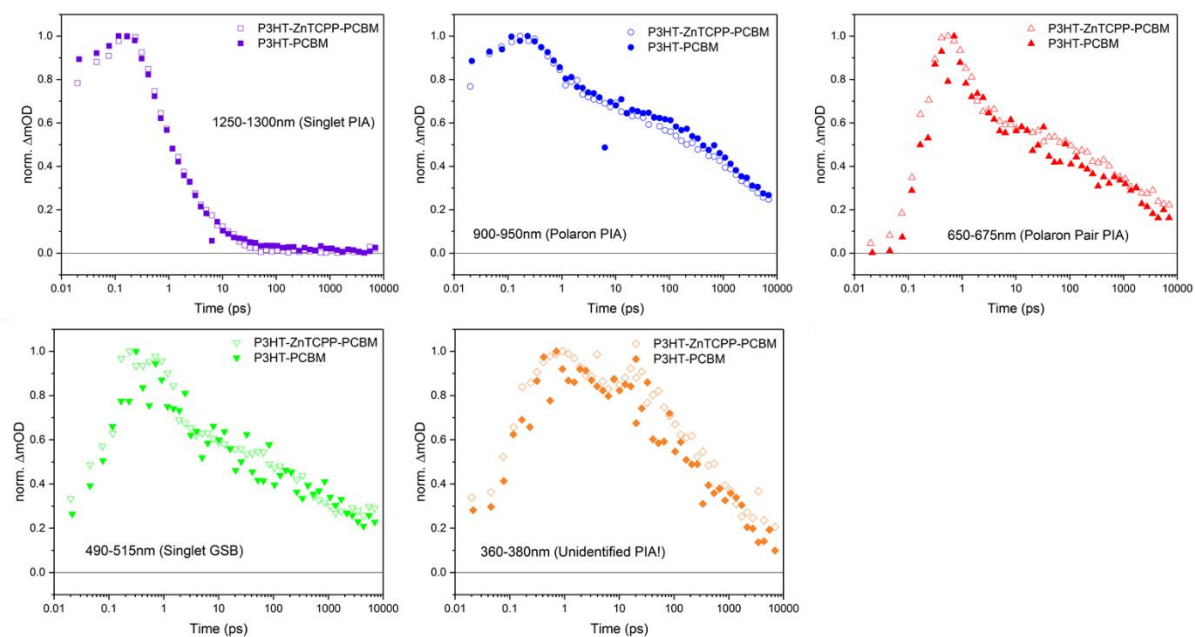

Figure S4.18a: Comparison of kinetics of the blends (normalized). No real change in the excited state dynamics upon addition of ZnTCPP, at least on timescales ranging from 1ps to 1ns.
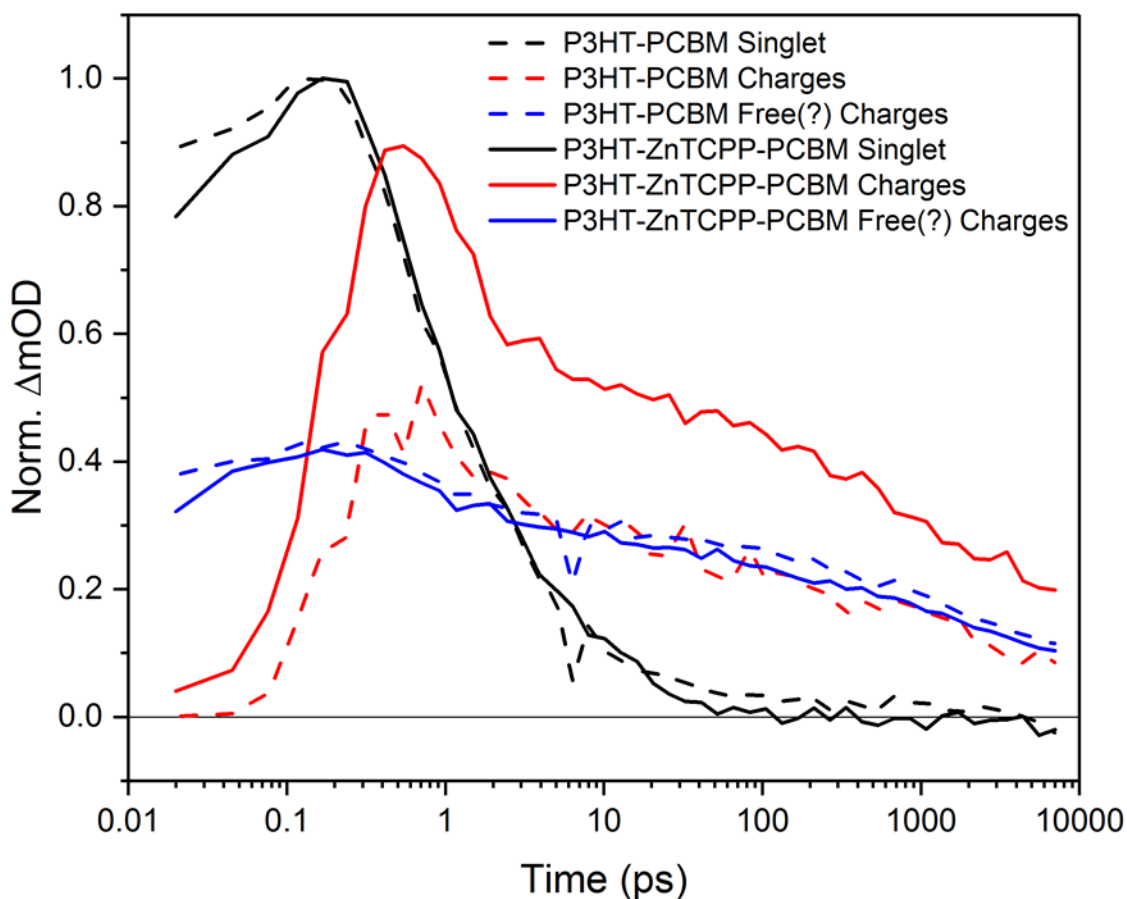
Figure S4.18b: Dynamics of excitons and charges in P3HT.

Here, the signal from PIA associated with charges (red and blue) has been normalised to the maximum (i.e. initial value) of the PIA associated with singlet excitons (black) It appears that the film with ZnTCPP has a much higher population of charge pairs (red) as a proportion of the photoexcited singlet exciton population. However, this doesn't seem to be replicated for the free-charge population (blue).
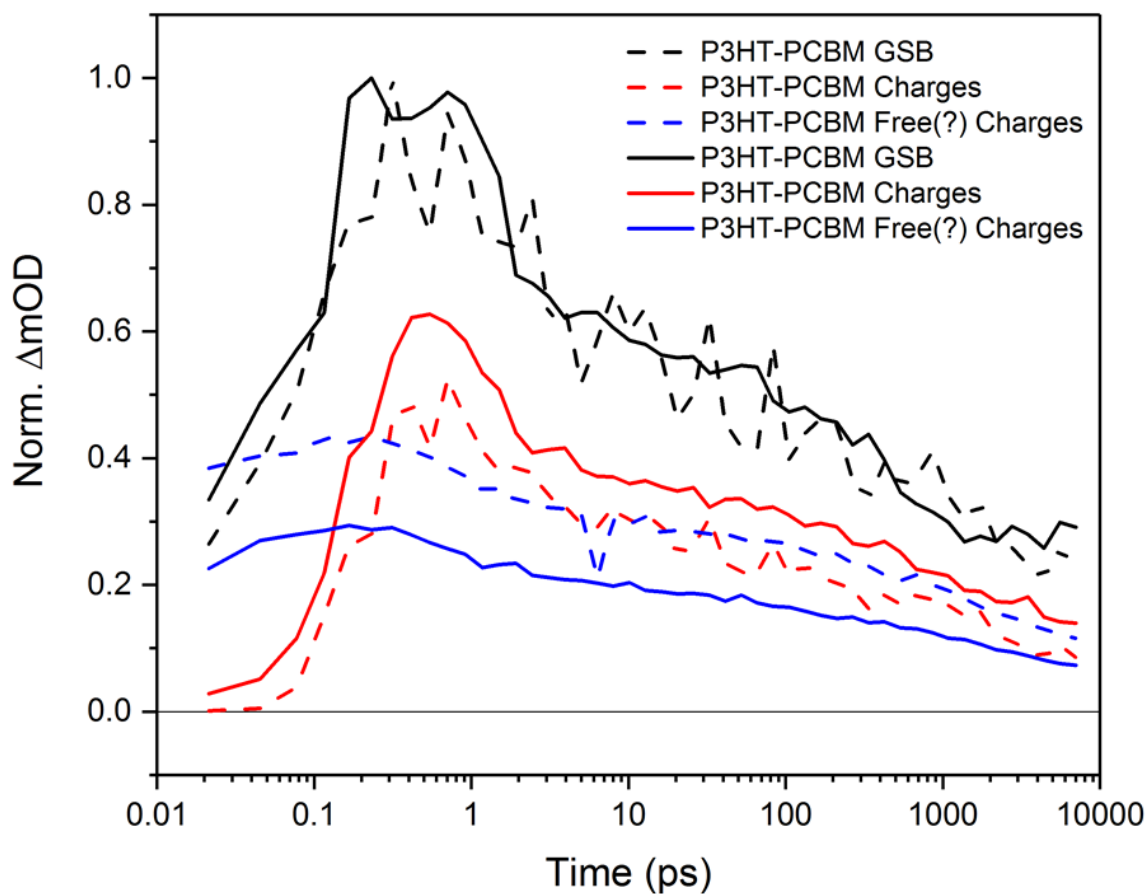
Figure S4.18c Dynamics of excitons and charges in P3HT normalized to the maximum of the ground state bleach (GSB).

It appears that the film with ZnTCPP has now only a slightly higher population of charge pairs (red) as a proportion of the photoexcited singlet exciton population.

9. SCLC devices for charge carrier mobility measurement

The investigation of space-charge limited electron-only or hole-only devices for extraction of mobility values is a well-known and reliable method. Space-charge limited currents were tested in hole only devices with the configuration ITO:PEDOT/PSS:active layer:MoO_3:Ag and a well-established protocol from literature was used for data fitting and analysis[20]. The hole mobility was determined by fitting the dark current to the model of a single carrier SCLC current with field dependent mobility based on Mott-Gurney law (Figure S19a-S22b, ESI). Electron only devices were fabricated with the configuration ITO:ZnO:Active layer:BCP:Ag to extract the electron mobility.

Table S4.3 Hole mobility and electron mobility extracted from SCLC holes only and electrons only devices for different thicknesses of active layer; Number of devices tested for each thickness=3.

Device configuration	Active layer (nm)	μ_h (cm^2/Vs)	μ_e (cm^2/Vs)
P3HT-PCBM	100	$(6.06\pm0.50)\times10^{-4}$	$(3.77\pm0.71)\times10^{-3}$
	150	$(1.13\pm0.17)\times10^{-4}$	$(1.35\pm0.07)\times10^{-3}$
P3HT-Zn$_2$(ZnTCPP)-PCBM	100	$(3.20\pm0.48)\times10^{-3}$	$(2.14\pm0.46)\times10^{-3}$
	150	$(2.12\pm0.34)\times10^{-3}$	$(2.13\pm0.14)\times10^{-3}$

Figure S4.19(a)-S4.22(b): The J–V characteristics of electron and hole only devices in different structures and active layer thickness. The bias is corrected for built-in voltage , arising from difference in the work function of the contacts, and the voltage drop due to substrate series resistance.

Status: **Complete**

1)

Raw data		
Filename:	**P3HT-PCBM (hole only device)**	

Selected data		
Description of selected data:	**ITO/PEDOT:PSS/P3HT-PCBM/MoO3/Ag**	

Film thickness, d	100	nm
Device area, A	0.025	cm²

2)

Series resistance compensation?	TRUE	
Series resistance, R_S	20	Ω
Excluded voltages V_int >	1000000	V

3)

Built in voltage compensation?	TRUE	
V_BI value	-0.1	V
Exclude V_int <	0.00	V

4)

Relative dielectric constant, ε_r	3.5	
Internal voltage range selected for fitting		
min	0.01	
max	1	

5)

Fitted?	TRUE	
Fit results:		
μ_0 =	3.19E-04	cm²/Vs
γ =	3.70E-03	cm$^{1/2}$/V$^{1/2}$
Field range of good fit:		
min	2.60E+04	V/cm
max	8.18E+04	V/cm
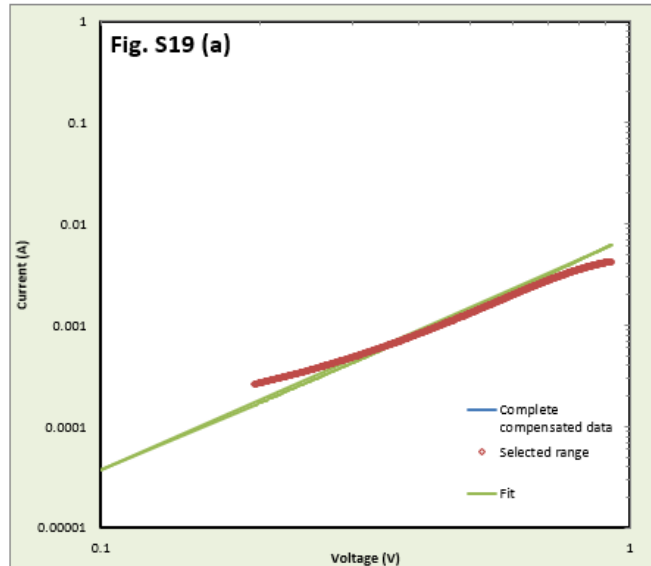
Mobility at selected electric field =	**6.06E-04**	**cm²/Vs**
at F =	3.00E+04	V/cm

Good fit at this electric field

Fig. S19 (a)

Status: **Complete**

1)

Raw data		
Filename:	**P3HT-PCBM electron only device**	

Selected data		
Description of selected data:	**ITO/ZnO/P3HT-PCBM/BCP/Ag**	

Film thickness, d	100	nm
Device area, A	0.025	cm²

2)

Series resistance compensation?	TRUE	
Series resistance, R_S	10	Ω
Excluded voltages V_int >	0.8	V

3)

Built in voltage compensation?	TRUE	
V_BI value	-0.1	V
Exclude V_int <	0.00	V

4)

Relative dielectric constant, ε_r	3.5	
Internal voltage range selected for fitting		
min	0.01	
max	0.8	

5)

Fitted?	TRUE	
Fit results:		
μ_0 =	1.58E-03	cm²/Vs
γ =	5.00E-03	cm$^{1/2}$/V$^{1/2}$
Field range of good fit:		
min	2.27E+04	V/cm
max	7.44E+04	V/cm
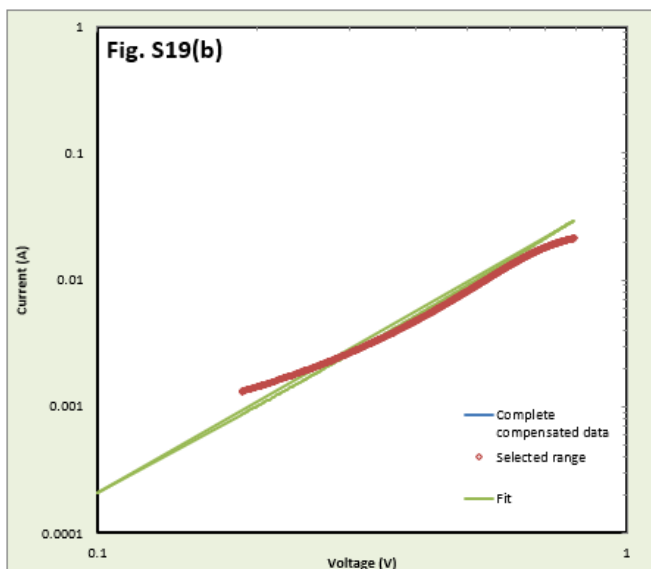
Mobility at selected electric field =	**3.77E-03**	**cm²/Vs**
at F =	3.00E+04	V/cm

Good fit at this electric field

Fig. S19(b)

Panel 1

Status: **Complete**

1)

Raw data	
Filename:	P3HT-PCBM hole only

Selected data	
Description of selected data:	ITO/PEDOT:PSS/P3HT-PCBM/MoO3/Ag

Film thickness, d	150	nm
Device area, A	0.025	cm^2

2)

Series resistance compensation?	TRUE	
Series resistance, R_s	10	Ω
Excluded voltages V_int >	1000000	V

3)

Built in voltage compensation?	TRUE	
V_BI value	-0.1	V
Exclude V_int <	0.00	V

4)

Relative dielectric constant, ε_r	3.5	
Internal voltage range selected for fitting		
min	0.01	
max	1	

5)

Fitted?	TRUE	
Fit results:		
μ_0 =	7.96E-05	cm^2/Vs
γ =	2.00E-03	cm$^{1/2}$/V$^{1/2}$
Field range of good fit:		
min	1.44E+04	V/cm
max	5.49E+04	V/cm

Mobility at selected electric field =	**1.13E-04**	**cm^2/Vs**
at F =	3.00E+04	V/cm

Good fit at this electric field

Fig. S20(a)

Panel 2

Status: **Complete**

1)

Raw data	
Filename:	P3HT-PCBM electron only

Selected data	
Description of selected data:	ITO/ZnO/P3HT-PCBM/BCP/Ag

Film thickness, d	150	nm
Device area, A	0.025	cm^2

2)

Series resistance compensation?	TRUE	
Series resistance, R_s	20	Ω
Excluded voltages V_int >	1000000	V

3)

Built in voltage compensation?	TRUE	
V_BI value	-0.2	V
Exclude V_int <	0.00	V

4)

Relative dielectric constant, ε_r	3.5	
Internal voltage range selected for fitting		
min	0.01	
max	1	

5)

Fitted?	TRUE	
Fit results:		
μ_0 =	1.13E-03	cm^2/Vs
γ =	1.00E-03	cm$^{1/2}$/V$^{1/2}$
Field range of good fit:		
min	1.97E+04	V/cm
max	6.81E+04	V/cm

Mobility at selected electric field =	**1.35E-03**	**cm^2/Vs**
at F =	3.00E+04	V/cm

Good fit at this electric field

Fig. S20(b)

1)

	Raw data			Selected data
Filename:	P3HT–Zn2(ZnTCPP)–PCBM hole only device		Description of selected data:	ITO/PEDOT:PSS/P3HT–Zn2(ZnTCPP)–PCBM/MoO3/Ag

Film thickness, *d*	100	nm	
Device area, *A*	0.025	cm²	

2)

Series resistance compensation?	TRUE	
Series resistance, *Rs*	5	Ω
Excluded voltages V_int >	1000000	V

3)

Built in voltage compensation?	TRUE	
V_BI value	−0.1	V
Exclude V_int <	0.00	V

4)

Relative dielectric constant, ε,	3.5	
Internal voltage range selected for fitting		
min	0.01	
max	0.8	

5)

Fitted?	TRUE	
Fit results:		
μ0 =	1.60E–03	cm²/Vs
γ =	4.00E–03	cm^{1/2}/V^{1/2}
Field range of good fit:		
min	2.48E+04	V/cm
max	7.82E+04	V/cm
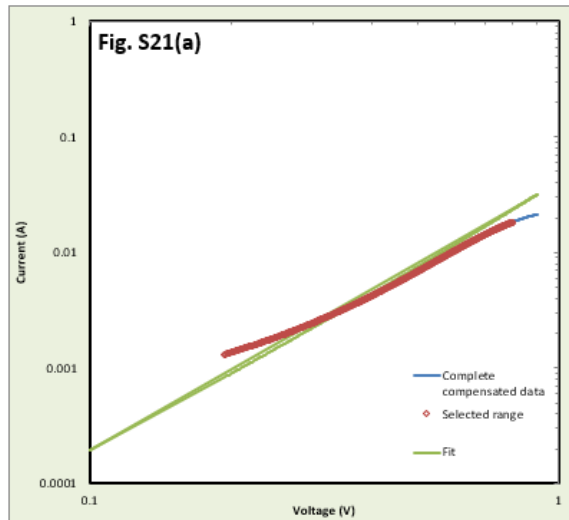
Mobility at selected electric field = 3.20E–03 cm²/Vs
at *F* = 3.00E+04 V/cm
Good fit at this electric field

Fig. S21(a)

---

1)

	Raw data			Selected data
Filename:	P3HT–Zn2(ZnTCPP)–PCBM electron only device		Description of selected data:	ITO/ZnO/P3HT–Zn2(ZnTCPP)–PCBM/BCP/Ag

Film thickness, *d*	100	nm	
Device area, *A*	0.025	cm²	

2)

Series resistance compensation?	FALSE	
Series resistance, *Rs*	N/A	Ω
Excluded voltages V_int >	1000000	V

3)

Built in voltage compensation?	TRUE	
V_BI value	−0.15	V
Exclude V_int <	0.00	V

4)

Relative dielectric constant, ε,	3.5	
Internal voltage range selected for fitting		
min	0.01	
max	1	

5)

Fitted?	TRUE	
Fit results:		
μ0 =	1.27E–03	cm²/Vs
γ =	3.00E–03	cm^{1/2}/V^{1/2}
Field range of good fit:		
min	2.59E+04	V/cm
max	1.01E+05	V/cm
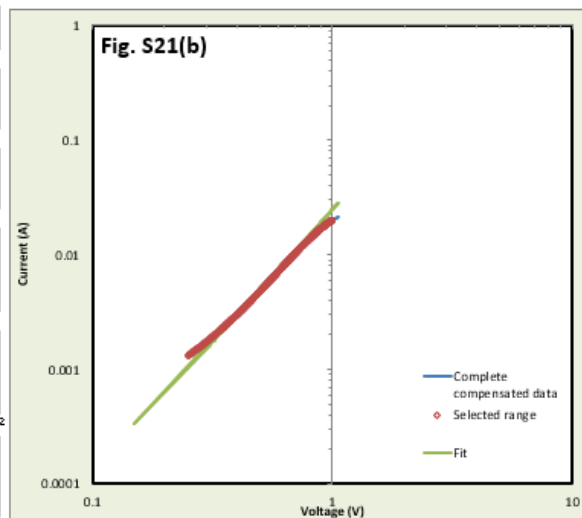
Mobility at selected electric field = 2.14E–03 cm²/Vs
at *F* = 3.00E+04 V/cm
Good fit at this electric field

Fig. S21(b)

Chapter 4 MONs for enhanced performance of OPVs
Supplementary Information

Status: **Complete**

1)

	Raw data
Filename:	P3HT-Zn2(ZnTCPP)-PCBM hole only

	Selected data
Description of selected data:	ITO/PEDOT:PSS/P3HT-Zn2(ZnTCPP)-PCBM/MoO3/Ag

Film thickness, d	150	nm
Device area, A	0.025	cm²

2)

Series resistance compensation?	TRUE	
Series resistance, R_s	10	Ω
Excluded voltages V_int >	1000000	V

3)

Built in voltage compensation?	TRUE	
V_BI value	-0.1	V
Exclude V_int <	0.00	V

4)

Relative dielectric constant, ε_r	3.5	
Internal voltage range selected for fitting		
min	0.01	
max	1	

5)

Fitted?	TRUE	
Fit results:		
μ_0 =	1.27E-03	cm²/Vs
γ =	2.94E-03	cm^{1/2}/V^{1/2}
Field range of good fit:		
min	1.73E+04	V/cm
max	6.10E+04	V/cm
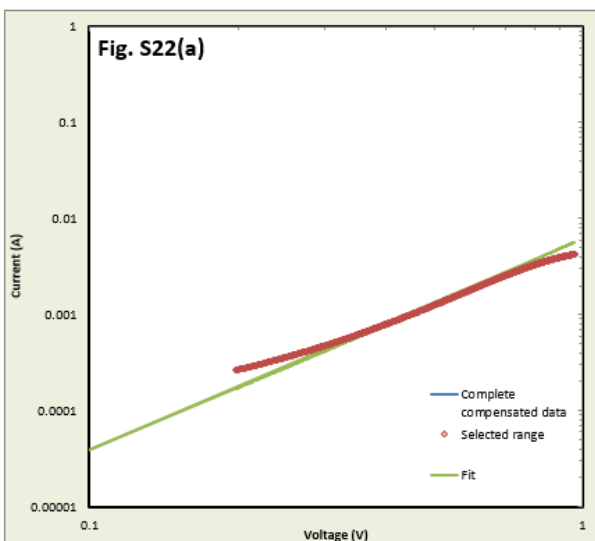
Mobility at selected electric field =	2.12E-03	cm²/Vs
at F =	3.00E+04	V/cm

Good fit at this electric field

Fig. S22(a)

Status: **Complete**

1)

	Raw data
Filename:	P3HT-Zn2(ZnTCPP)PCBM electron only

	Selected data
Description of selected data:	ITO/ZnO/P3HT-Zn2(ZnTCPP)PCBM/BCP/Ag

Film thickness, d	150	nm
Device area, A	0.025	cm²

2)

Series resistance compensation?	TRUE	
Series resistance, R_s	20	Ω
Excluded voltages V_int >	1000000	V

3)

Built in voltage compensation?	TRUE	
V_BI value	-0.1	V
Exclude V_int <	0.00	V

4)

Relative dielectric constant, ε_r	3.5	
Internal voltage range selected for fitting		
min	0.01	
max	1	

5)

Fitted?	TRUE	
Fit results:		
μ_0 =	1.79E-03	cm²/Vs
γ =	1.00E-03	cm^{1/2}/V^{1/2}
Field range of good fit:		
min	1.48E+04	V/cm
max	6.15E+04	V/cm
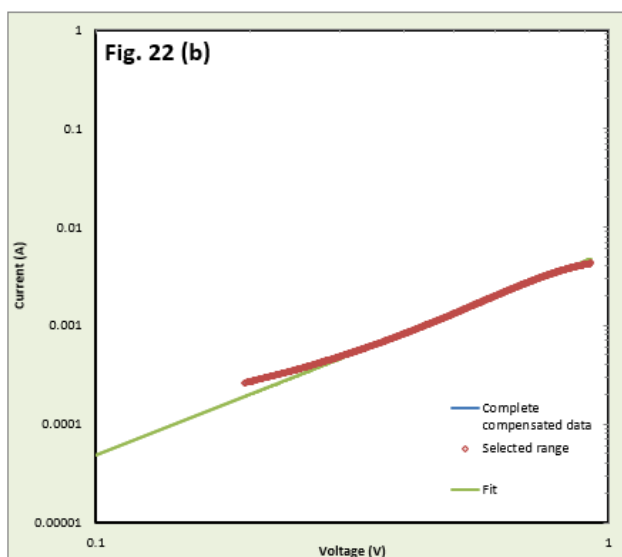
Mobility at selected electric field =	2.13E-03	cm²/Vs
at F =	3.00E+04	V/cm

Good fit at this electric field

Fig. 22 (b)

The devices were prepared following the same procedure described in the experimental section for photovoltaic devices, except that of the metal electrode. The mobilities were determined by fitting the dark current to the model of a single carrier SCLC current with field dependent mobility[20], which is described as

$$J = [(9\ \varepsilon_r \varepsilon_0\ \mu_0 V^2)/8L^3]\ \exp(\beta \sqrt{V}/L)$$

Where, J is the current, μ_0 is the zero-field mobility, ε_0 is the permittivity of free space, ε_r is the relative permittivity of the material, V is the effective voltage, and L is the thickness of the active layer.

10. GI-WAXS

The GIWAXS thin film measurements were performed with a Xeuss 2.0 system (Xenons, France). The Sheffield machine is fitted with a MetalJet (Excillum, Sweden) liquid gallium X-ray source, providing a 9.24 keV X-ray beam collimated to a beam spot of 400 µm laterally at the sample position, measuring the full sample length. X-ray diffraction patterns were acquired with a Pilatus3R 1M 2D detector (Dectris, Switzerland). The sample to detector distance was calibrated using a silver behenate calibrant standard in transmission geometry. Samples were measured in GI-WAXS geometry near the critical angle (calculated to probe the entire film thickness) and under vacuum atmosphere to minimise the background scatter.

Figure S4.23. GI-WAXS 2-D detector images of a. Pristine P3HT film; b. P3HT-ZnTCPP blend film. The corresponding 1-D cross sections are shown in Figure 4.
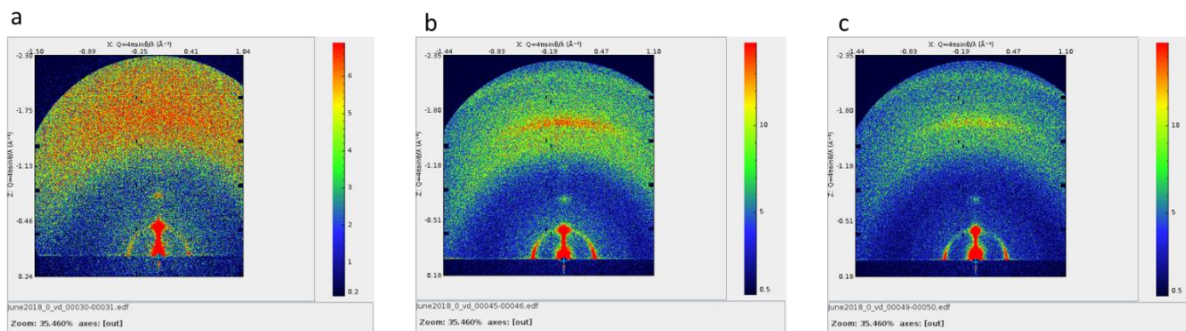
Figure S 4.24. GI-WAXS 2-D detector images of a. Thermal annealed, b. Solvent annealed, and c. Solvent+thermal annealed P3HT-Zn$_2$(ZnTCPP)-PCBM device active layers.

Table S4.4. Scherrer analysis and calculation of crystallite sizes from the 100 and 010 P3HT peaks.

Sample	$B_f{}^{hkl} \cos \theta_{hkl}$		D, nm
	100, $2\theta_{100} = 5.4°$	010, $2\theta_{100} = 24.0°$	
P3HT	0.012	0.013	10.96± 0.7
P3HT-Zn$_2$(ZnTCPP)	0.013	0.014	11.39±0.8
P3HT-Zn$_2$(ZnTCPP)-PCBM	0.011	0.012	13.59±0.7

11. AFM – Morphological investigation of the device active layers

11.1 P3HT-Zn$_2$(ZnTCPP)-PCBM active layers and the corresponding Fourier transformations used to extract the domain length scale
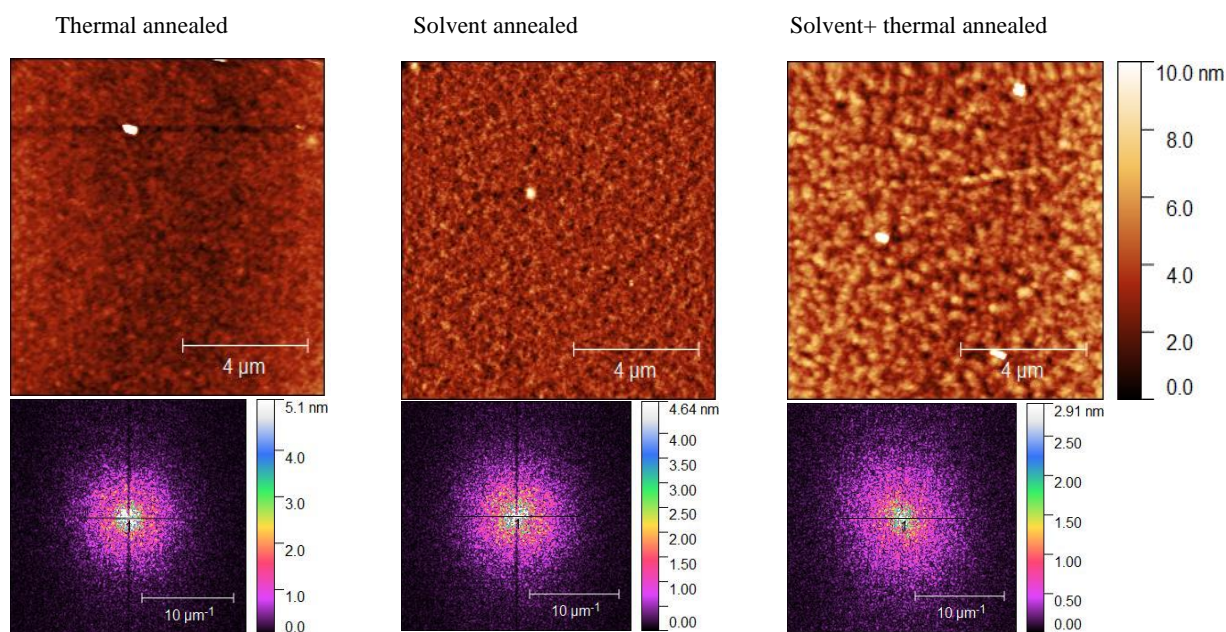
Figure 4.25. Investigation of changes in the morphology of the device active layer during the different annealing procedures followed for performance optimisation: a. P3HT-Zn$_2$(ZnTCPP)-PCBM film: thermal annealed at 120°C for 10 minutes; b: solvent vapour annealed in a column saturated with chlorobenzene vapour at 120°C for 5 minutes; c: solvent annealed like in (b) for 10 minutes followed by thermal annealing at 120°C for 5 minutes;

11.2 P3HT-PCBM active layers and the corresponding Fourier transformations used to extract the domain length scale

Thermal annealed   Solvent annealed   Solvent+ thermal annealed
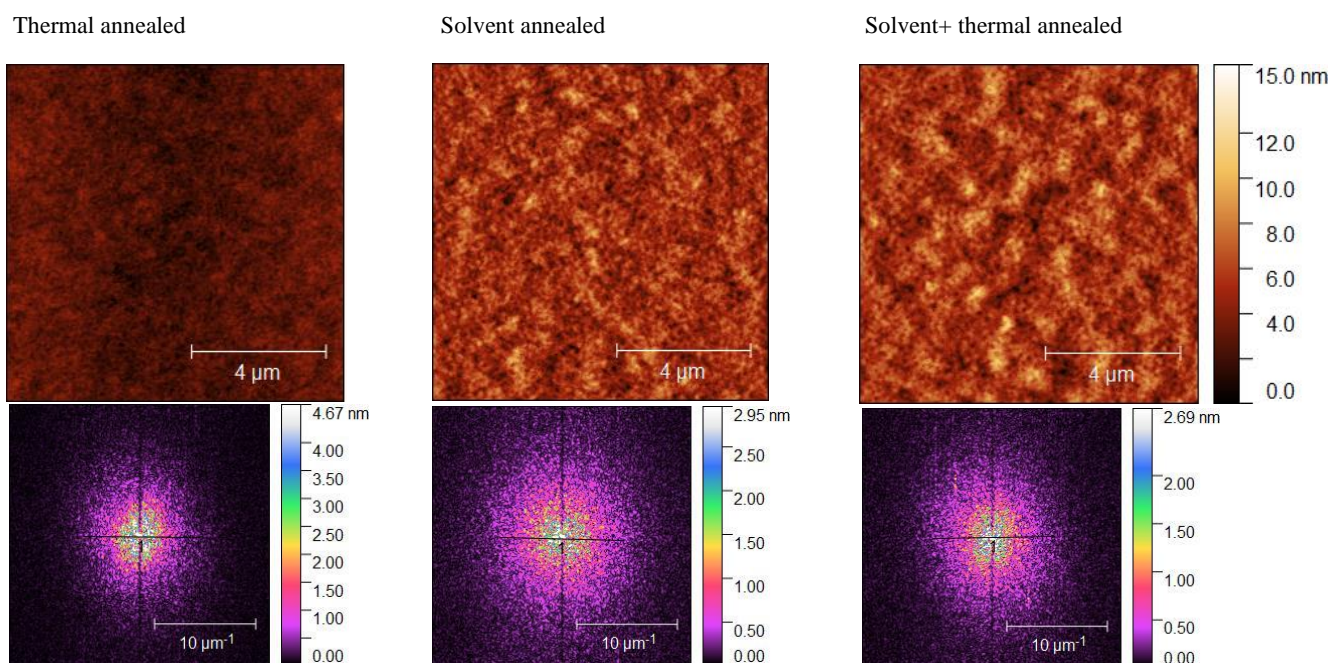
Figure 4.26. Investigation of changes in the morphology of the device active layer during the different annealing procedures followed for performance optimisation: a. P3HT-PCBM film: thermal annealed at 120°C for 10 minutes; b: solvent vapour annealed in a column saturated with chlorobenzene vapour at 120°C for 5 minutes; c: solvent annealed like in (b) for 10 minutes followed by thermal annealing at 120°C for 5 minutes;

12. Spectroscopic ellipsometry

For fitting of the data, J. A. Woollam WVASE32 Software was used. During the fitting, reasonable boundaries were set for model parameters to restrict them to physically meaningful values. Fitting in the range of 700−900 nm was performed first using a Cauchy model and the thickness value determined by a step-profiler as the initial guess to obtain a good estimate of film thickness. Then, a B-spline model incorporating a Kramers Kronig model was used to fit the n and k were fitted in the desired wavelength range with the thickness fixed. Finally, both

thickness and optical functions were allowed to vary in the last fitting run to verify that a reasonable solution has been obtained.
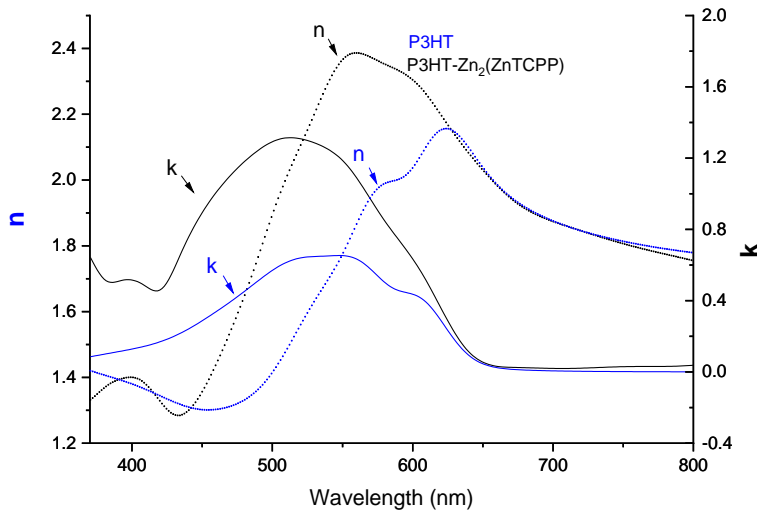
Figure S 4.27. The extinction coefficient spectra and wavelength dependant refractive index plots of P3HT and P3HT-Zn$_2$(ZnTCPP) extracted using spectroscopic ellipsometry;
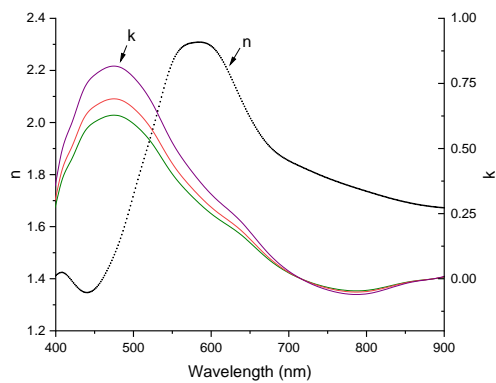
Figure S 4.28. The optical properties of the device active layer as a function of annealing conditions extracted using spectroscopic ellipsometry

13. References

1.   Zhao, M. *et al.* Ultrathin 2D Metal-Organic Framework Nanosheets. *Adv. Mater.* **27**, 7372–7378 (2015).

2.   Singh, A., Dey, A. & Iyer, P. K. Influence of molar mass ratio, annealing temperature and cathode buffer layer on power conversion efficiency of P3HT:PC71BM based organic bulk heterojunction solar cell. *Org. Electron. physics, Mater. Appl.* **51**, 428–434 (2017).

3.   Oh, I. S., Ji, C. H. & Oh, S. Y. Effects of Ytterbium on Electrical and Optical Properties of BCP / Ag / WO 3 Transparent Electrode Based Organic Photovoltaic Cells. **12**, 156–162 (2016).

4.   Wang, D. *et al.* Effect of a cathode buffer layer on the stability of organic solar cells. *Semicond. Sci. Technol.* **30**, (2015).

5.   Tseng, C. A. *et al.* The effects of fluorine-contained molecules on improving the polymer solar cell by curing the anomalous S-shaped I-V curve. *ACS Appl. Mater. Interfaces* **7**, 6683–6689 (2015).

6.   Qin, D., Wang, W., Wang, M., Jin, S. & Zhang, J. The dependence of the cathode architecture on the photoactive layer morphology in bulk-heterojunction polymeric solar cells. *Semicond. Sci. Technol.* **29**, (2014).

7.   Colsmann, A., Junge, J., Kayser, C., Wellinger, T. & Lemmer, U. Optimization of electron transport and cathode materials for efficient organic solar cells. *Org. Optoelectron. Photonics II* **6192**, 619220 (2006).

8.   Feng, Z., Hou, Y. & Lei, D. The influence of electrode buffer layers on the performance of polymer photovoltaic devices. *Renew. Energy* **35**, 1175–1178 (2010).

9.   Yi Wang, Z., Lee, S. H., Kim, D. H., Kim, J. H. & Park, J. G. Effect of NiOx thin layer fabricated by oxygen-plasma treatment on polymer photovoltaic cell. *Sol. Energy Mater. Sol. Cells* **94**, 1591–1596 (2010).

10.   Lee, D. *et al.* Transparent electrode with ZnO nanoparticles in tandem organic solar cells. *Sol. Energy Mater. Sol. Cells* **95**, 365–368 (2011).

11. J.K. Baral, R., Izquierdo, M., Packirisamy & Truong, V.-V. Improved polymer solar cell performance by engineering of cathode interface. *Eur. Phys. J. Appl. Phys.* **55**, 30202 (2011).

12. Qin, D. *et al.* The manageable formation of the gradient-layered polymer/fullerene blend films via the addition of bathocuproine and their applications in organic solar cells. *Phys. Status Solidi A* **1156**, 1150–1156 (2012).

13. Tseng, W. H. *et al.* Enhancements in device efficiency of poly(3-hexylthiophene): [6,6]-phenyl C 61-butyric acid methyl ester based solar cells with incorporation of bathocuproine. *Thin Solid Films* **520**, 5413–5416 (2012).

14. Cheng, G., Tong, W. Y., Low, K. H. & Che, C. M. Thermal-annealing-free inverted polymer solar cells using ZnO/Cs 2CO 3 bilayer as electron-selective layer. *Sol. Energy Mater. Sol. Cells* **103**, 164–170 (2012).

15. Jung, G. H. & Lee, J. L. Origin of gap states in the electron transport layer of organic solar cells. *J. Mater. Chem. A* **1**, 3034–3039 (2013).

16. Xu, K., Kim, D. H., Lee, S. H. & Kim, T. W. Enhancement of the power conversion efficiency for organic photovoltaic cells with a Liq/bathocuproine electron transport bilayer. *Thin Solid Films* **547**, 116–119 (2013).

17. Li, J. *et al.* A new alcohol-soluble electron-transporting molecule for efficient inverted polymer solar cells. *Org. Electron. physics, Mater. Appl.* **14**, 2164–2171 (2013).

18. Xiao, T. *et al.* Improved efficiency and stability of inverted polymer solar cells with a solution-processed BPhen interlayer and polystyrene beads. *Org. Electron. physics, Mater. Appl.* **14**, 2555–2563 (2013).

19. Williams, G. & Aziz, H. The effect of charge extraction layers on the photo-stability of vacuum-deposited versus solution-coated organic solar cells. *Org. Electron. physics, Mater. Appl.* **15**, 47–56 (2014).

20. Blakesley, J. C. *et al.* Towards reliable charge-mobility benchmark measurements for organic semiconductors. *Org. Electron.* **15**, 1263–1272 (2014).

Chapter 5

Tuning Energy Levels and Active Layer Morphology of Organic Photovoltaic Devices with Metal-Organic Framework Nanosheets

Kezia Sasitharan[a], Johannes Frisch[b,c], Ahmed Iraqi[a], David G. Lidzey[d], Marcus Baer[b,c], Jonathan A. Foster[a*]

[a]Department of Chemistry, The University of Sheffield, Dainton Building, Brook Hill, S3 7HF, Sheffield, UK.

[b] Interface Design, Helmholtz-Zentrum Berlin für Materialien und Energie GmbH (HZB), Berlin, 12489 Germany

[c] Energy Materials In-Situ Laboratory Berlin (EMIL), Helmholtz-Zentrum Berlin für Materialien und Energie GmbH, Berlin, 12489 Germany

[d]Department of Physics and Astronomy, The University of Sheffield, Hicks Building, Hounsfield Road, S3 7RH, Sheffield, UK

Graphical abstract

Main text

Author contributions

Kezia Sasitharan   Synthesised and characterised the MONs, prepared the photovoltaic devices and carried out the relevant analyses, prepared samples and carried out the photoemission measurements, analysed all the experimental data and drafted the manuscript.

Johannes Frisch   Trained KS in the photoemission measurements, aided with analysis of data and editing of the manuscript.

Ahmed Iraqi   Helped with data discussion and editing of the manuscript.

David G. Lidzey   Helped with data discussion and editing of the manuscript.

Marcus Baer   Supervised the photoemission part of the project and helped with editing of the manuscript.

Jonathan A. Foster   Supervised the project, helped with data discussion and aided with drafting of the manuscript.

5.1 Publication Main Text

Abstract

Metal-organic framework nanosheets are emerging as promising additives to enhance the performance of organic photovoltaics, thanks to their diverse and tunable optoelectronics. We recently showed that addition of zinc-porphyrin based MONs as ternary components within P3HT-PCBM solar cells resulted in remarkable improvements in device performance. In this work, we aim to take advantage of the modular structure of MONs to better understand how to design MONs for use in OPV devices. We seek to investigate the effect of tuning the energy level alignment of the MONs by using different combinations of metal ions and ligands. Detailed investigations of the electronic and optical properties and their performance in P3HT-PCBM OPV devices were conducted. As compared to the reference OPV devices, we found that $Zn_2(ZnTCPP)$ MONs doubled the device performance, whereas $Cu_2(ZnTPyP)$ did not affect the device performance and $Cu_2(CuTCPP)$ halved the device performance. With the help of photoemission, absorption and atomic force microscopy investigations, we identified three different mechanisms by which MONs can influence the photoactive layer – light absorption, energy level alignment and morphological changes. Different metal ions and ligands were found to have small but significant effects on the light absorption and energy level alignment properties of the MONs. However, nanosheet thickness was found to be a crucial parameter in enabling the MONs to optimise device morphology in order to achieve significant improvements in performance. We anticipate this study will aid the design of MONs and other 2D materials for use in other organic light harvesting and emitting devices.

Introduction

Solar energy has been identified as a clean and efficient energy for sustainable power generation.[1–3] Organic photovoltaics (OPV) have huge potential as a sustainable technology due to their ease of processability, high absorption co-efficient and flexibility.[4–8] Termed "bulk heterojunction," the active layer of these devices consists of a blend of two organic materials with different optoelectronic properties.[9–13] Organic semiconductors typically show low charge mobility and therefore the bulk heterojunction blend of donor-acceptor components is usually maintained thin to achieve better charge collection.[14–16] One strategy is to create tandem structures with multiple absorption layers to enable complementary absorption and enhanced photovoltaic conversion.[17] However, this approach is accompanied with increased fabrication

costs and complexity.[18] Ternary organic solar cells with an auxiliary third component incorporated into the donor/acceptor photoactive system is a promising approach that has been investigated extensively to broaden the absorption range of OPVs.[19–22] A typical ternary blend consists of an additional donor or acceptor component, generally expected to have complementary absorption. Besides the light absorption benefit, other factors that influence device efficiency like morphology, charge carrier mobility, fill factor (FF) and open circuit voltage (Voc) have been shown to greatly improve the power conversion efficiency (PCE) values in many investigations of adding a third component to the active layer of a binary host.[23] Various third components investigated in ternary bulk heterojunctions include donor polymers, small molecules, dye molecules, fullerene derivatives as a second acceptor, quantum dots and various semiconducting nanomaterials. [24–26] A key requirement of these ternary components is aligning the band-gaps to create new charge transport pathways and avoid creating recombination centres.[27–29]

Metal-organic framework nanosheets (MONs) are an emerging class of two-dimensional materials with a modular structure in which organic linkers are coordinated to metal ions.[30,31] These materials have shown enormous potential in a wide range of applications including sensing, catalysis, separation membranes, energy harvesting and storage.[32–35] In recent years, these materials have been investigated in organic electronics with remarkable results, thanks to their nanoscopic dimensions and tunable optoelectronic properties.[36] Bis(dithiolato)nickel MONs when incorporated as hole buffer layer in OLED led to a 2-fold enhancement in device lifetime.[37] With the first example of a tellurophene based MON electron extraction layer in a functional solar cell reported in 2018, this application has received considerable interest.[38] Porphyrin based MONs on ITO, embedded with fullerenes were recently demonstrated to work as a liquid-junction solar cell.[39] Following this, our group demonstrated the first example of using MONs in the photoactive layer of OPVs where-in the incorporation of MONs in the P3HT-PCBM solar cell resulted in a near doubling of the PCE.[40] Essentially this reported system is a ternary bulk heterojunction device with MON as the third component in P3HT-PCBM host device, enabling morphology control. Detailed analysis of this system showed that MONs acted as templates which increased the crystallinity of the donor polymer and thereby resulting in a balanced charge mobility and improved device performance metrics. This set the stage for MONs as diverse tunable materials with the capability of enhancing the performance of organic electronic devices when systematically engineered with the right linker components for the desired application.

Porphyrins are attractive candidates for organic photovoltaics because of their favourable absorption, high molar extinction coefficient, high quantum efficiency of about 80%, strong π-π interaction with fullerenes, compatibility with most solvents and additives commonly employed in OPV fabrication procedures and the potential to promote efficient electron transfer at the donor-acceptor interfaces.[41-50] Interactions between P3HT and porphyrins leading to favourable optoelectronic properties have been investigated by many groups. Recently Kilbey and coworkers demonstrated the use of a porphyrin functionalised P3HT system that promotes miscibility with PCBM in a BHJ layer.[47] Bronstein and co-workers showed that the introduction of a platinated porphyrin unit to P3HT led to increase in charge mobilities of upto an order of a magnitude.[49] In another interesting report, co-ordination of zinc porphyrin with imidazole functionalised polythiophene copolymer showed extended absorption and a concentration dependant photo-induced energy transfer.[50] These structures were observed to disrupt the polymer organisation which the authors attribute as the cause for modest PCEs. Generally, in literature metallized porphyrins were found to be better than the non-metallised ones in mediating OPV efficiencies and the type of metal-ion in the porphyrin centre is known to control the energy levels and the electron transport properties.[51] The J-type aggregation property of porphyrins have been utilized to fabricate many novel nanopatterned structures and tested in OPVs as well.[41,49,52] While most of these works are interesting chemical modifications that enable tuning the optoelectronic properties of P3HT, the effect on performance enhancement of the OPV device is usually found to be very low. This has been attributed to the tendency of porphyrins to crystallize/aggregate into small recombination centres within the photoactive layer. This effect is observed in our own work as well, where the porphyrin MONs showed a near doubling of PCE (upto 5.2%) whilst the porphyrin molecule when investigated by itself as a ternary component led to a PCE of 1.38% only. This establishes that organising the porphyrin units into a two-dimensional network structure as in the case with MONs is important to achieve the doubling effect in device efficiency.

While the role of the $Zn_2(ZnTCPP)$ MONs in acting as templates to enable crystallization of the P3HT grains and favouring an ideal bulk heterojunction morphology for charge dissociation and transport was experimentally proven in our work, the energy level alignment was not yet probed. However, while investigating such novel systems as additives in existing OPV systems, it is important to probe the energetic alignment between the different components in the active layer to understand the fundamental physical processes that govern the device function and performance enhancement.[53] In this work we explore two additional

analogous MON systems copper tetrakis(4-carboxyphenyl) porphyrin $Cu_2(CuTCPP)$ and copper zinc tetrapyridyl porphyrin $Cu_2(ZnTPyP)$ as ternary components and investigate the OPV performance, along with the energy level alignment studies. It is observed that $Zn_2(ZnTCPP)$ remains the best candidate in terms of simultaneously improving all the device performance parameters (Jsc, Voc, FF and PCE). With the use of photoemission spectroscopy, we analyse the alignment of energy levels at the various interfaces within the ternary devices thereby presenting a detailed account of the energy landscape in the MON based device active layers. In addition to this, a comparison of the optoelectronics and the morphology of the different MON systems helps to understand the device physics and the drive behind exceptional energy conversion in the $Zn_2(ZnTCPP)$ based ternary system. This work demonstrates that along with the ideal positioning of the MON frontier energy levels with respect to the donor and the acceptor, achieving a favourable active layer morphology and enhancement of light absorption are features of paramount importance for a significant improvement in device performance.

Results
Synthesis and characterisation of MOFs
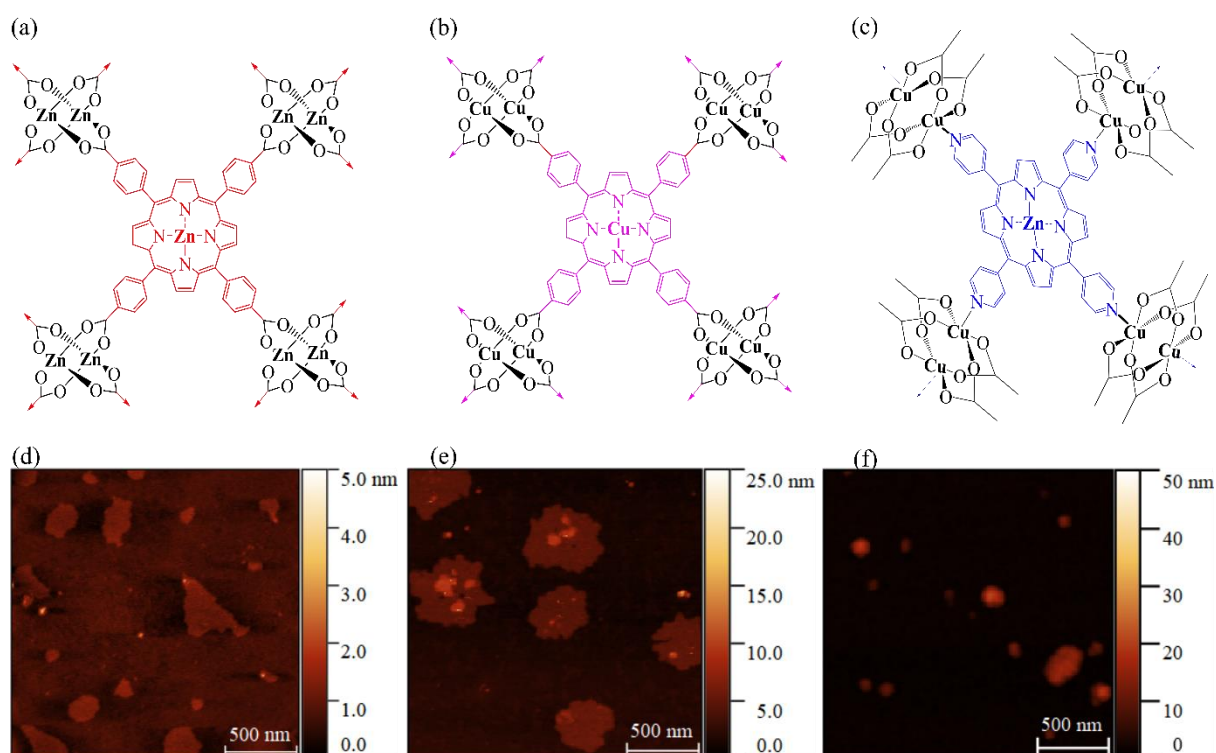
Figure 5.1 Structures and AFM images of $Zn_2(ZnTCPP)$. $Cu_2(CuTCPP)$ and $Cu_2(ZnTPyP)$ MONs used in this work.

The bulk MOFs were prepared via a solvothermal technique, similar to the method described in our previous work. Square planar building blocks based on tetraarylporphyrins – TCPP ((tetrakis(4-carboxyphenyl) porphyrin) and TPyP (5,10,15,20-tetra-4-pyridyl-21H,23H-porphine) have been used in this work. These ligands offer two distinct metal binding sites – a structural metal binding site at the carboxy and pyridyl ends, and another metal binding site within the porphyrin cavity. TCPP was heated with the metal precursor in a DMF: ethanol mixture at 80°C for 24 hours resulting in the black microcrystalline MOF as the product. These M-TCPP (M=Zn, Cu or Co) MOFs are known as porphyrin paddlewheel frameworks where one TCPP ligand is connected by four metal paddlewheel nodes ($M_2(COO)_4$ resulting in a two-dimensional layered structure. During the reaction, the TCPP ligand also gets metallated with the M^{2+} ions. These layered sheets are further stacked in an AB pattern, which means the metal atoms in the centre of the porphyrin rings are aligned with the metal atoms in the paddlewheel nodes forming a 2D MOF structure. In our synthesis, zinc nitrate and copper nitrate were used as the metal precursors for Zn_2(ZnTCPP) and Cu_2(CuTCPP) respectively. For the third system Cu_2(ZnTPyP) .we adapted a method reported previously for a 2D Cu MOF formed by mixing TPyP with copper acetate in chloroform.[54]. The previous MONs were homometallic, therefore the metal precursors were introduced directly in stoichiometric ratios to facilitate the formation of the metalloporphyrin centre and the paddlewheels. However, in this third system, to get the bimetallic configuration, we first metallated the TPyP ligand by reacting it with zinc nitrate in a 1:1 stoichiometric ratio. The resulting Zn-TPyP ligand was then solvothermally reacted with copper acetate to form Cu_2(ZnTPyP) MOF where all the four pyridyl groups of ZnTPyP are coordinated to four different Cu(II) atoms of the Cu_2(OAc) units. The 2D layers stack in an AB sequence such that the zinc atoms in the middle of the TPyP rings are aligned with the copper atoms in the paddlewheel nodes. **Figure 5.1(a-c)** shows the structures of the three MOFs with their metalloporphyrin centres and the paddlewheel metal nodes. The powder X-ray diffraction patterns and other solid state analysis of the synthesized MOFs showed good agreement with the previously reported analogous structures in literature and have been included in the supplementary information.

Exfoliation into MONs

The layered MOFs were then suspended in ethanol (5mg/6ml) and sonicated for one hour in an ultrasonic bath followed by centrifugation at 1500 rpm for 10 minutes to remove the larger unexfoliated particles. The supernatant consisting of the exfoliated MONs was collected and 20uL of it was deposited onto freshly cleaved mica (preheated to 80°C) for AFM images which

are shown in **Figure 5.1(d-f).** The $Zn_2(ZnTCPP)$ MONs were consistent in size dimensions with our previous paper and are 1nm thin with a lateral size distribution ranging between 50nm and 200nm. The $Cu_2(CuTCPP)$ MONs were found to be between 4-5nm in height and between 400-600 nm in lateral dimensions. The $Cu_2(ZnTPyP)$ MONs were found to be between 15-40 nm in height and their lateral dimensions were found to be between 50-400 nm. Thus, the $Zn_2(ZnTCPP)$ MONs are approaching monolayer thickness, the $Cu_2(CuTCPP)$ MONs are about three layer thick and have a larger lateral dimension of about 0.5um whereas the $Cu_2(ZnTPyP)$ MONs are few layers thicker, more particle-like and less sheet-like of the three systems explored here.

Optoelectronic features
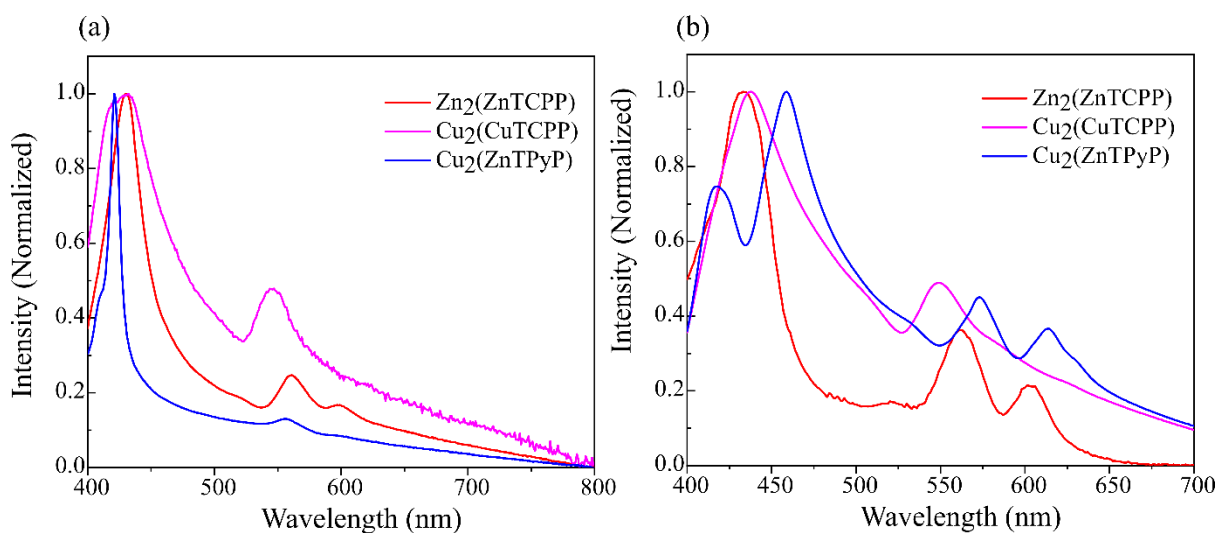
Figure 5.2 (a) Solution-state absorption and (b) Thin-film absorption spectroscopy of the different MONs used in this work.

The UV-Vis absorption spectra of the MONs were collected in ethanolic solutions and in films spin-coated from suspending MONs in chlorobenzene. In solutions all MONs show a strong absorption range of 400-600 nm with the absorption maxima related to the soret-band of the porphyrin ring and the other peaks from the Q-bands. All the bands are ascribed to π-π* transitions. If the metal is changed in the porphyrin skeleton, the spectrum can change in two ways – variation of the intensity of the long wavelength band and shifting of the whole spectrum. We observed that in the solution state (**Figure 5.2a**), $Zn_2(ZnTCPP)$ has a S-band at 432nm, and two Q-bands at 564 and 603 nm. $Cu_2(CuTCPP)$ has its absorption maxima at 435 nm and only a single Q band at 550nm. The $Cu_2(ZnTPyP)$ being made of a different porphyrin unit with the pyridyl substituents has distinct absorption features the TCPP ones characterised by a much narrower S-band at 422 nm and two Q bands at 556nm and 607 nm. In the film state

(**Figure 5.2b**), there is a broader absorption observed which is attributed to the enhanced stacking of the porphyrins.

Incorporation into ternary blend OPV devices

The application of MONs as ternary additives in bulk heterojunction OPV devices was investigated in optimised P3HT-PCBM host devices. For the active layer, MONs were mixed with P3HT-PCBM with a loading of 20% by weight (methods detailed in supplementary information) and the resulting ternary blend was spin coated onto PEDOT:PSS coated ITO, followed by BCP/Ag as the buffer layer and the back contact.
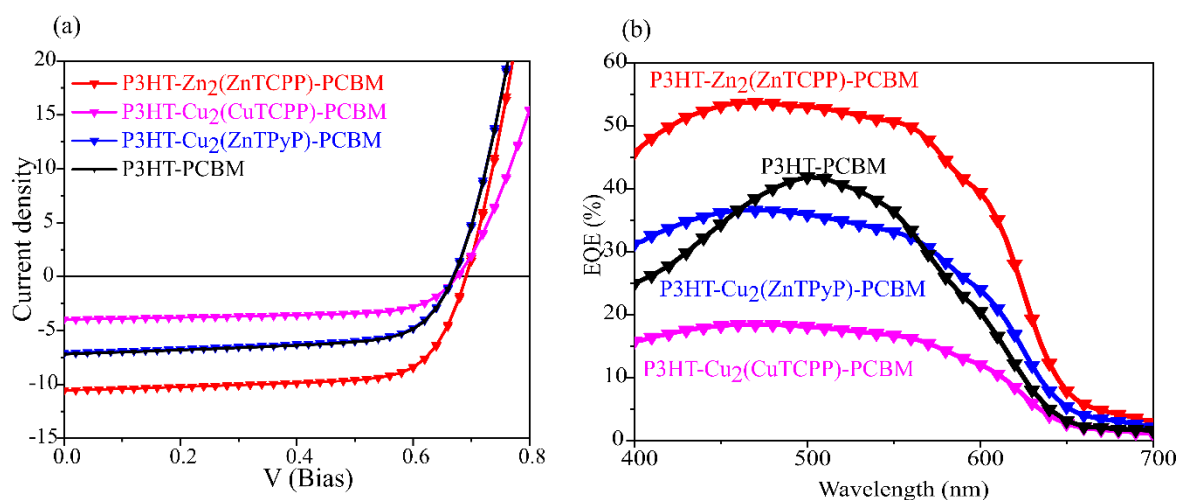
Figure 5.3 (a) Current-voltage curves and (b) EQE spectra of the different P3HT-MON-PCBM configurations used in this work.

The current-voltage response (J-V curve) of the devices are shown in **Figure 5.3a**. In contrast to $Zn_2(ZnTCPP)$ which was previously found to result in significant improvements in the PCE, addition of $Cu_2(CuTCPP)$was found to substantially decrease the performance whilst $Cu_2(ZnTPyP)$ resulted in no change. The external quantum efficiency measurements (EQE) shown in **Figure 5.3b** were conducted to gain insight into the photoresponse of the ternary systems across the wavelength range 400 nm to 700 nm. The Jsc's calculated from EQE are consistent with the measured values, with <5% error. When compared with the P3HT-PCBM devices, all the P3HT:MON:PCBM systems demonstrate a broader EQE spectra which is attributed to the absorption contributions from the porphyrin units. The P3HT: $Zn_2(ZnTCPP)$:PCBM devices show a strong and uniform photoresponse between 400 to 560 nm, with a maximum EQE at 55%. In comparison with the reference P3HT-PCBM, there is enhanced photoresponse in the region 400 to 450 nm which corresponds to the S absorption
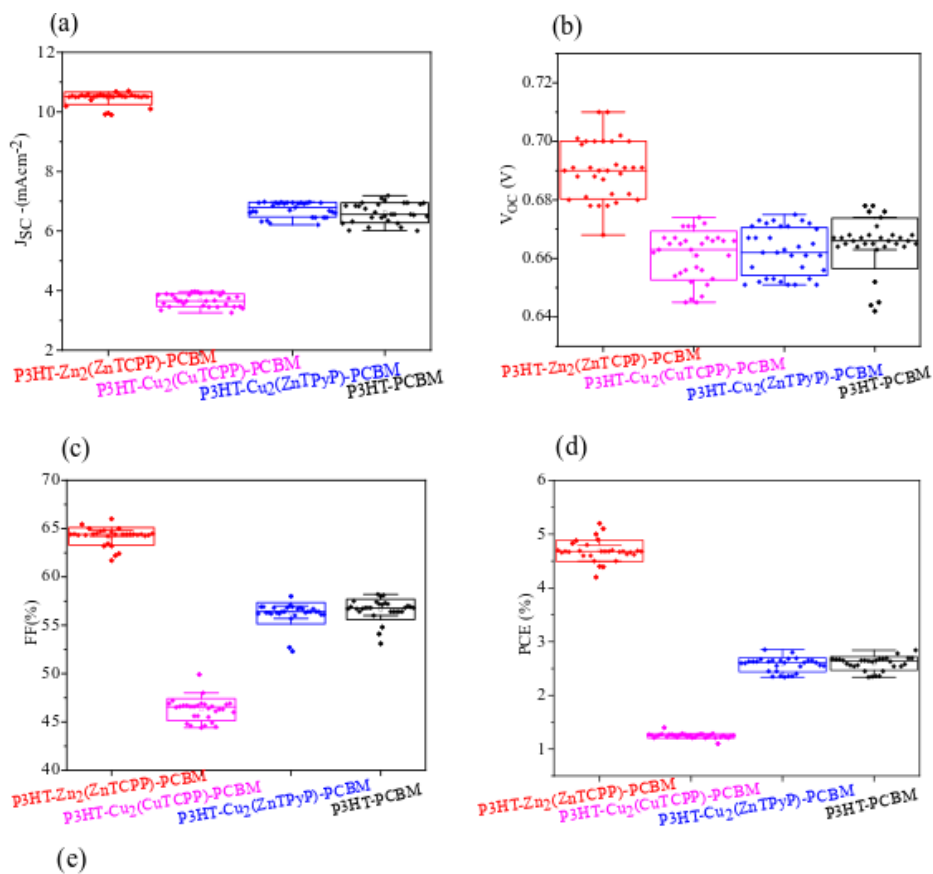
Figure 5.4 Box plots representing the statistical analysis of the different device performance parametric - (a) Jsc, (b)Voc, (c) FF, (d) PCE of the different device configurations and a table listing the average and standard deviation values calculated form 30devices for each configuration.

band of porphyrins and additional photoresponse in the region 600nm to 650 nm, attributed to the increased crystallinity of P3HT dealt with in detail in our previous work. The P3HT-Cu_2(CuTCPP)-PCBM devices show a uniform photoresponse in the 400nm to 600nm region, but with much reduced intensity and with the maximum EQE being only 18%. In comparison, the P3HT:Cu_2(ZnTPyP):PCBM system shows a similar uniform photoresponse across 400 nm to 600 nm with an EQE maxima at 36%. In addition the enhanced absorption contribution in the S band region, there is a pronounced shoulder at 610 nm which corresponds to the second Q-band associated with this MONs. These findings confirm that the MONs are photoactive in

the films, with the porphyrin unts contributing to net light absorption. It is noteworthy that the photoresponse in the primary absorption region of P3HT-PCBM is weakened by 5% with the incorporation of $Cu_2(ZnTPyP)$ and by 30% in the case of $Cu_2(CuTCPP)$. This indicates there have been changes in the active layer morphology and charge transport pathways within these devices, and this will be explored in the later sections.

The device figures of merit averaged over 30 devices for each P3HT-MON-PCBM combination are plotted as a function of the active layer composition in **Figure 5.4(a-d).** Looking in detail at how each of the performance metric is affected **(Figure 5.4e**), $Zn_2(ZnTCPP)$ causes an increase in absorption in the films as compared to P3HT-PCBM blend, contributing to an increase in short-circuit current density (Jsc) by 4 mA/cm^2. Furthermore, an increase in Voc by 0.3V and FF by ~8% suggests a reduced recombination rate within the ternary bulk heterojunction, cumulatively leading to an improved PCE of 4.69%. Both $Cu_2(CuTCPP)$ and $Cu_2(ZnTPyP)$ left the Voc unchanged than the pristine P3HT-PCBM devices. This tells us that the effective donor-acceptor energy gap i.e $E_{Fullerene\ LUMO}$- $E_{P3HT\ HOMO}$) remained unaffected with the loading of MONs. While $Cu_2(ZnTPyP)$ did not cause any statistically significant reduction in device performance, $Cu_2(CuTCPP)$ decreased the Jsc by 3mA/cm^2 and the FF by ~10%. This large decrease in FF along with the decreased quantum efficiency for this device observed above confirms there are clear differences in the charge transport pathways and (or) evolution of the photoactive nanostructure with the incorporation of each type of MON which need to be probed.

Photoemission studies

UV Photoemission spectroscopy (UPS) measurements were performed to gain a comprehensive understanding of the energy level alignment at all the interfaces within the MON based ternary bulk heterojunction devices in this work and to understand the influence of these energy levels position on the observed power conversion efficiencies. taking into account that the optical band gap and the electronic band gap differ by a value equal to the exciton binding energy, UPS and UV-vis absorption spectroscopy is generally acceptable as a superior method to determine the position of the frontier occupied and unoccupied energy leaves with respect to the Fermi level (E_F) in the device. In photoemission, absorption of a photon in the UV region leads to excitation of an electron into an energy level above the vacuum level. The relation between the kinetic energy of this released electron (E_{kin}) and the binding energy of the electrons in the material is $E_{kin} = h\nu - E_b$ where $h\nu$ is the energy of the photon that was absorbed, and E_b is the binding energy. The work function of the deposited

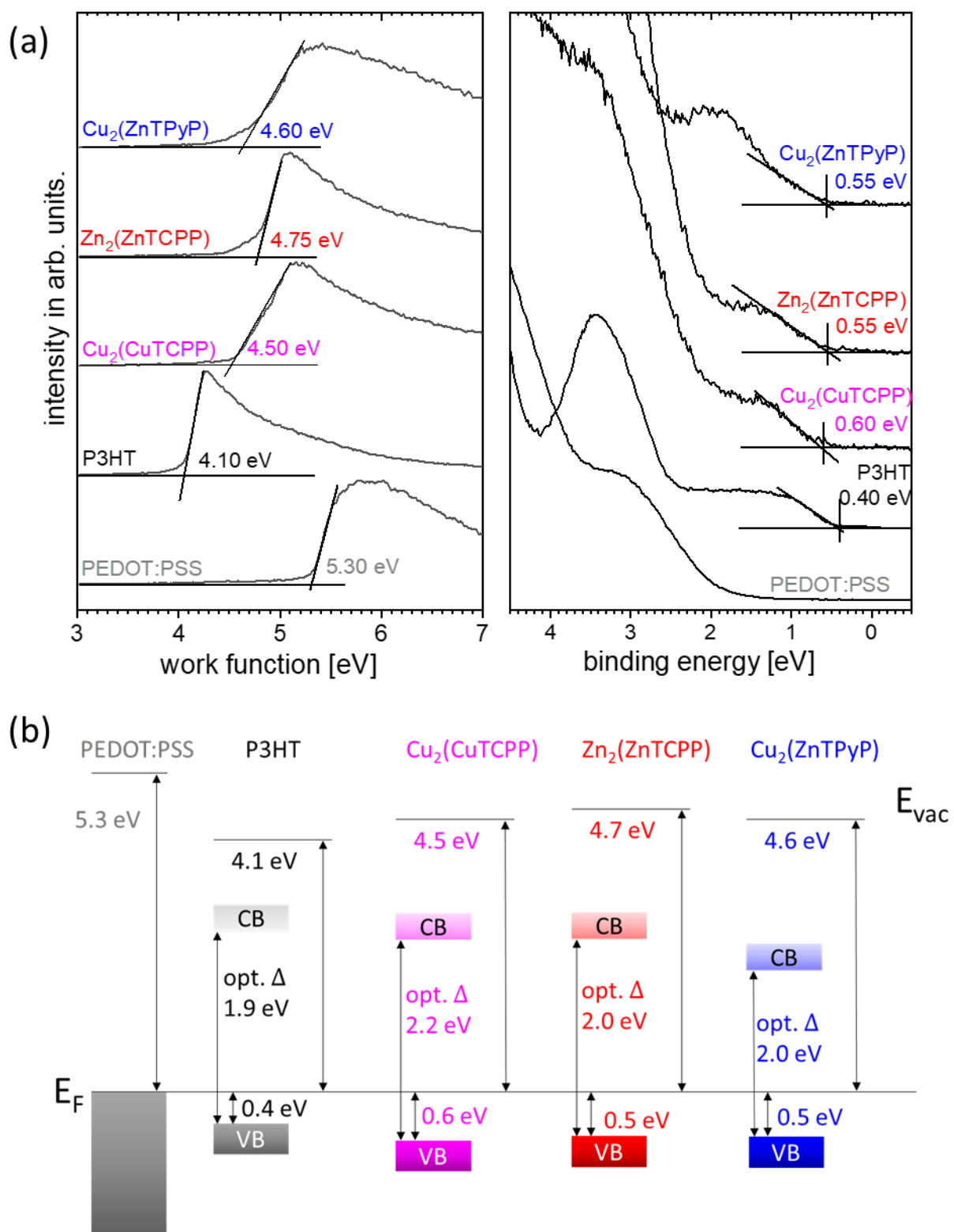material can be determined by measuring the secondary electron cut-off (SECO) (lowest

Figure 5.5 The seco and valence band spectra of P3HT, and the MONs deposited on PEDOT:PSS; and a summary of the evaluated values.

kinetic energy range of the photoelectron spectrum) which mainly comprises of inelastically scattered photoelectrons. The high kinetic energy range of the spectrum gives the occupied valence level positions (VB onset, see **Figure 5.5** right part). The VB onset energy distance to the E_F corresponds to the hole-injection barrier (HIB). The ionisation energy (IE) can be obtained by adding the hole-injection barrier (HIB) to the sample Φ.

The valence band (VB) spectra and SECOs of P3HT spin coated on PEDOT:PSS are shown in **Figure 5.5**. The Φ of PEDOT:PSS was found to be 5.3 eV. A representative VB spectrum and SECO of P3HT on PEDOT:PSS are shown in the **Figure 5.5**. The low binding energy edge of the polymer valence band corresponds to the position of the highest occupied molecular orbital (HOMO). Using a value of 2 eV as the optical band gap of P3HT (in solid state), we can estimate the position of the conduction band (CB). The position of the CB with respect to E_F gives the hole injection barrier, which we estimate to be 0.40eV. The vacuum level, fermi level, HOMO and LUMO levels are summarized in **Figure 5.5**. The electron affinity can be calculated by subtracting the optical gap from the measured IE.

The Φ PEDT:PSS is reduced to 4.10 eV upon P3HT deposition. This can be explained by taking into account the small ionization energy (IE) of P3HT with respect to the hight Φ of PEDT:PSS. The IE of P3HT was determined to 4.50 eV (by adding the HIB of 0,40 eV to the P3HT Φ of 4.50 eV). Since the IE of P3HT is lower than the Φ of PEDOT:PSS, assuming vacuum level alignment at the interface would mean that a part of the filled VB states will be above the E_F which is forbidden by electronic equilibrium. Thus, electrons from P3HT are transferred at the interface to PEDOT:PSS and an interface dipole develops inducing an electric field that pins the frontier P3HT energy levels with respect to the E_F (Fermi-level pinning).[55,56]

For characterising the work function and ionization energies of MONs, we have deposited them via spin-coating onto PDOT:PSS films. It should be noted that the morphology of the surface plays a very important role in determining the work function, and the resulting ionisation energy value. Since MONs are anisotropic materials that are spin-coated from suspensions, rather than solutions, the resultant film is made of MON islands on top of the PEDOT:PSS substrate. We must be aware that the calculated ionization energies can be an overestimate than under the real operating conditions because of this uneven surface coverage. The calculated values are based on the measured Φ that is averaged due to the measurement technique over a large area of mostly MON islands with some pristine PEDOT:PSS surfaces. With this assumption, we have measured the Φ and HIB of the three MON systems and

estimated based on these measurements the IE (summarized in **figure 5.5**). In all the MONs, we observe the existence of filled gap states which act as pinning levels and as a consequence the Φ is reduced. Based on these calculations, we then proceed to decipher the energy level alignment in the device active layers.

To build the ternary bulk heterojunction energy level alignment (**Figure 5.6**), the starting point is the PEDOT:PSS-P3HT interface. Since the MONs are added into the active layer in the device we assumed vacuum level alignment between the P3HT-MON interface and have built the energy level alignment at the two-fold heterojunction assuming that the MONs are positioned away from the anode towards the cathode, i.e in between P3HT and PCBM. This is the ideal working position for these materials in the functional solar cell. The resultant new valence band onsets for the MONs are shown in **Figure 5.6**.

The energy level diagrams of all the P3HT-MON-PCBM combinations thus look workable and do not cause detrimental traps for the charge carriers. These results are important in that they provide an insight into the energy positioning of the MONs in the devices, and with all the MONs showing a workable alignment explains why the Voc of the devices do not change. In comparison, it appears that the VB of $Zn_2ZnTCPP$ is ideally positioned between that of P3HT and the HOMO level of PCBM, whereas the VB of $Cu_2(CuTCPP)$ is closer to that of P3HT, and the VB of $Cu_2(ZnTPyP)$ is closer to the HOMO level of PCBM. While these shifts are subtle, these findings provide an insight into why the $Zn_2(ZnTCPP)$ may be superior in enabling performance enhancement in this setting. However, these are not sufficient to explain why $Cu_2(CuTCPP)$ devices have a reduced Jsc and FF, and why $Cu_2(ZnTPyP)$ does not cause the same doubling in PCE as $Zn_2(ZnTCPP)$.
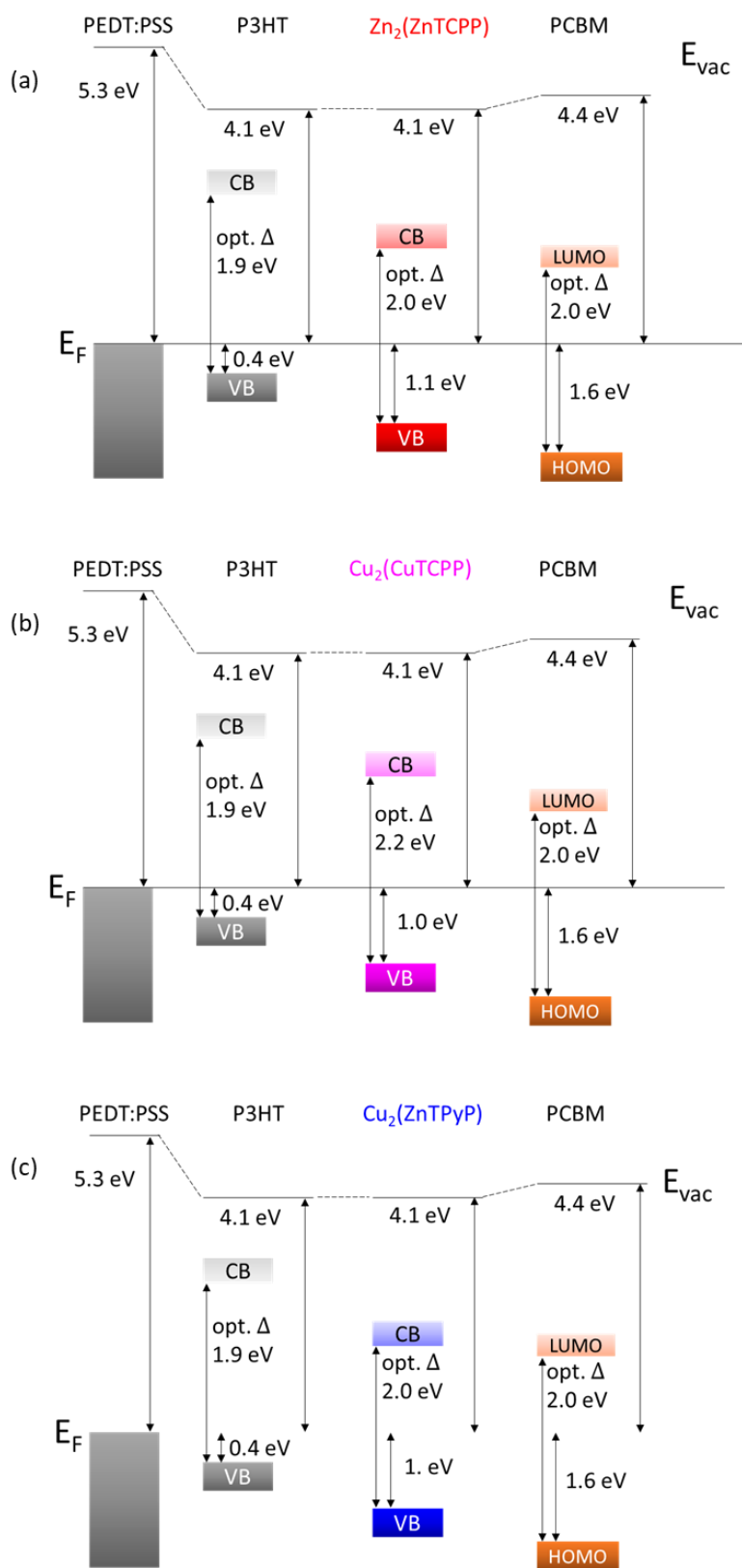
Figure 5.6. Energy level alignment for the P3HT-MON-PCBM configurations

Morphological studies – AFM

(a)

(b)

(c)

(d)
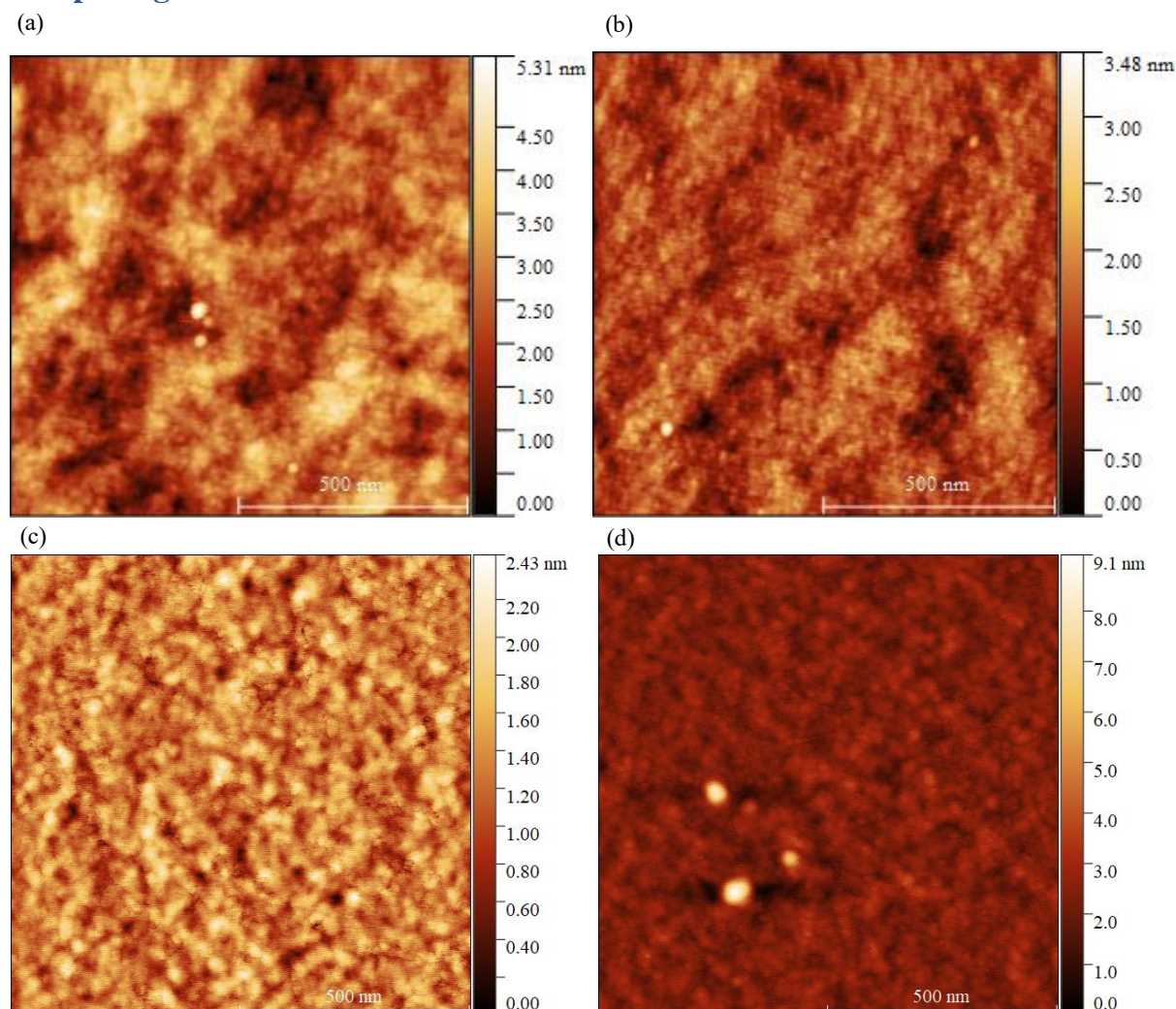
Figure 5.7. AFM height profile images of (a) P3HT-PCBM; (b) P3HT-ZnTCPP-PCBM; (c)P3HT-CuTCPP-PCBM; (d) P3HT-CuZnTPyP-PCBM active layers

AFM imaging of the ternary blend active layers (**Figure 5.7**) was conducted to look into the effect that MONs have on the active layer morphology. A spatial Fast-Fourier transform was applied to the images to extract the grain size (phase separation length scales) according to the literature methods with the detailed evaluation result listed in the ESI. This gives information about the evolution of the nanostructure and domain sizes in the active layer. As reported previously, the grain size in P3HT-PCBM active layer are in the range of 10-15 nm whereas with the addition of $Zn_2ZnTCPP$ in the active layer, the grain sizes were found to reduce to about 6-10 nm.[40] Large and loosely packed PCBM will inhibit the crystallinity of the polymer and create an unfavourable environment for efficient exciton dissociation. With the Zn_2(ZnTCPP) MONs acting as templates for a higher fraction of the polymers to crystallize

first, overgrowth of PCBM is prevented and well-defined smaller grain sizes which are more favourable for charge carrier transport and within the exciton diffusion length are created. This change in grain size is thus correlated to the observations on change in crystallinity of P3HT in the presence of $Zn_2ZnTCPP$ leading to effective manipulation of the grain sizes and with the newly created 10nm length scale, the domains are constrained in the same scale as the exciton diffusion length. In the case of devices with $Cu_2(CuTCPP)$ and $Cu_2(ZnTPyP)$ in the active layer, it is observed that the grain sizes are larger than that found in the control devices (about 12 nm for $Cu_2(ZnTPyP)$ and upto 47 nm for the $Cu_2(CuTCPP)$ containing films. This can partially be due to the large sizes of these nanosheets. The $Cu_2(CuTCPP)$ being greater than 400nm in lateral size, is too large to allow for the same favourable effects that we observed with the inclusion of the ZnTCPP MONs. The CuZnTPyP system on the other hand has more particle like nature and is about ¬50 nm in height, so is several layers thick. This clearly states that the morphological effects introduced in the active layer by ZnTCPP cannot be generalized to any MON system, but specifically tailored in terms of the MON dimensions itself.

Device active layer	FFT – Inverse space value	Calculated grain size
P3HT-PCBM	$100 \ \mu m^{-1}$	10nm
P3HT-ZnTCPP-PCBM	$115 \ \mu m^{-1}$	8.7nm
P3HT-CuTCPP-PCBM	$21.09 \ \mu m^{-1}$	47.4nm
P3HT-CuZnTPyP-PCBM	$79 \ \mu m^{-1}$	12.7nm

Discussion

There are three different ways in which the MONs can influence the photoactive layer – light absorption, energy level alignment and morphological changes. With porphyrin units being the main organic component of the MON structures, the absorption contribution from the MON structures are complementary to that of P3HT and PCBM. Substituting the porphyrin centre with different metals does influence the absorption spectra to some extent, and of the three MONs, the $Zn_2(ZnTCPP)$ has the best spectral coverage with respect to the other components, thanks to its highly intense S band at 430nm and the two Q bands at 564 and 604 nm

respectively. This along with the highest molar extinction coefficient makes the $Zn_2(ZnTCPP)$ a better light absorbing ternary component as can be observed in the EQE spectra as well. The $Cu_2(CuTCPP)$ MONs only have one Q absorption band, hence offer a narrower absorption range. It is also more scattery and less absorbing with a very low molar extinction coefficient. The $Cu_2(ZnTPyP)$ MON system does offer a good absorption range with its S-band shoulder peaks and two Q-bands.

All the MONs have a workable energy level position, with $Zn_2(ZnTCPP)$ being relatively in the middle of P3HT-PCBM levels, thus ideally positioned. $Cu_2(CuTCPP)$ has a 0.2eV drop in the valence band onset making it closer to P3HT than $Zn_2(ZnTCPP)$, whereas replacing the ligand with TPyP raises the VB of $Cu_2(ZnTPyP)$ by 0.15 eV. Nevertheless, we do not see a drop in Voc when any of the MONs are added into the devices.

We conclude that the morphological changes are key to the drastic change in device performances we observed. We have shown that changing the ligand and metal composition in the MONs disrupts the device/blend morphology. Our previous work attributed the bulk of the improvement in P3HT-PCBM device performance to an increase in crystallinity of P3HT due to templating effects by the MONs. This was proven by GI-WAXS analysis, AFM grain size investigations and the contributions from the enhanced crystalline regions can be seen in the absorption spectra of the photoactive films and EQE spectra of the solar cells as well. The key driving force behind this templating effect is the favourable size dimensions of the MONs themselves. With monolayer thickness (1nm) and a lateral size dimension between 50-200 nm, the $Zn_2(ZnTCPP)$ MONs are ideally suited for incorporation into the device thin films.

The $Cu_2(CuTPP)$ MONs being quite large in size - >500 nm and about 4nm thick, are not ideal for the photoactive layers. The large sized flakes of nanosheets reduce the donor-acceptor interface available in the photoactive layer and thus the charges produced in the P3HT and PCBM are less able to travel. This explains the drop in Jsc and FF of the $Cu_2(CuTCPP)$ incorporated devices, and the decrease in the EQE of the primary P3HT-PCBM wavelength range by 18%. The $Cu_2(ZnTPyP)$ MONs with their ~30nm thickness when incorporated in 150nm device can be obstructive to some extent. The more particle -like and less sheet-like morphology means the propensity to offer templating effect for the polymer chain ordering is no longer available and the large thickness is only more likely to reduce the P3HT-PCBM in some parts and accounts for the 5.5 drop in EQE % at the P3HT-PCBM region.

The grain size evaluations from the AFM images of the photoactive layers confirm this hypothesis, as the $Zn_2(ZnTCPP)$ MONs lead to smaller grain sizes, favouring charge percolation pathways and transport. The $Cu_2(CuTCPP)$ MONs lead to the formation of larger overgrown grain sizes which exceed the exciton diffusion length for this polymer system, thereby proving the breakage/disruption of the P3HT-PCBM interfaces. The $Cu_2(ZnTPyP)$ MONs lead to a slight increase in the grain sizes, and the particle like morphology seems to create some aggregation centres of MONs in the films as well.

Conclusion

In conclusion, this study is a systematic evaluation of MONs as potentially tunable additives in OPVs. The modular nature of MONs allows for creation of a diverse range of metal-ligand combinations, thus providing opportunities for tunability of optoelectronic properties. By investigating a series of porphyrin-based MONs and their influence on the device performance parameters f the archetypal P3HT-PCBM devices, we have established some design rules to be considered before incorporating MONs in OPVs. We have found that for a MON to act as an ideal ternary component in a bulk-heterojunction device, the absorption, morphology and energy level alignment are key features to be considered. While the energy-level alignment is necessary to facilitate a trap-free charge transport, the complementary absorption is an added advantage in pushing the current density of the devices. Monolayer nanosheets with optimal lateral sizes have been found to favour the crystallinity of the polymer via a templating effect and the formation of well-defined smaller grain sizes leading to efficient charge percolation pathways. Having few-layer nanosheets with larger than 500nm lateral sizes or thicker nanosheets (more particle-like) do not assist in templating the crystallinity and are more likely to cause disruption of the donor/acceptor interface. Thus, this study offers valuable insights for MON design which could allow us to develop higher performing devices.

Author contributions

KS carried out the synthesis and characterisation of MONs, device fabrication, testing, sample preparation for all the analytical experiments, the related data analysis and drafted the manuscript. JF trained KS on the photoemission measurements, analysis and aided in editing the manuscript. AI and D.G.L helped with data discussion. MB supervised the photoemission studies. JAF supervised the project, helped with data discussion and manuscript editing.

Conflicts of interest

DGL is a co-founder and Chairman of the materials science company Ossila Ltd, that retails materials and equipment used in organic optoelectronic device research and development.

Acknowledgements

References

1   Z. Liu, S. E. Sofia, H. S. Laine, M. Woodhouse, S. Wieghold, I. M. Peters and T. Buonassisi, *Energy and Environmental Science*, 2020, **13**, 12–23.

2   D. Sandor, S. Fulton, J. Engel-Cox, C. Peck and S. Peterson, *Sustainability (Switzerland)*, , DOI:10.3390/su10010160.

3   T. Kirchartz and U. Rau, *Physica Status Solidi (A) Applications and Materials Science*, 2008, **205**, 2737–2751.

4   H. Yao, Y. Cui, D. Qian, C. S. Ponseca, A. Honarfar, Y. Xu, J. Xin, Z. Chen, L. Hong, B. Gao, R. Yu, Y. Zu, W. Ma, P. Chabera, T. Pullerits, A. Yartsev, F. Gao and J. Hou, *Journal of the American Chemical Society*, 2019, jacs.8b12937.

5   A. Kiriy and F. C. Krebs, in *Advances in Polymer Science*, Springer New York LLC, 2017, vol. 272, pp. 351–376.

6   T. Kirchartz, K. Taretto and U. Rau, *Journal of Physical Chemistry C*, 2009, **113**, 17958–17966.

7   J. Nelson, J. Kirkpatrick and P. Ravirajan, *Physical Review B - Condensed Matter and Materials Physics*, , DOI:10.1103/PhysRevB.69.035337.

8   C. W. Tang, *Applied Physics Letters*, 1986, **48**, 183–185.

9   J. Zhao, Y. Li, G. Yang, K. Jiang, H. Lin, H. Ade, W. Ma and H. Yan, *Nature Energy*, , DOI:10.1038/NENERGY.2015.27.

10   S. Sandén, N. M. Wilson, O. J. Sandberg and R. Österbacka, *Applied Physics Letters*, , DOI:10.1063/1.4949016.

11   B. Xiao, P. Calado, R. C. I. MacKenzie, T. Kirchartz, J. Yan and J. Nelson, *Physical Review Applied*, , DOI:10.1103/physrevapplied.14.024034.

12   D. Abbaszadeh, *Chem. Mater.*, 2019, **31**, 6380–6386.

13   X. Yang, J. Loos, S. C. Veenstra, W. J. H. Verhees, M. M. Wienk, J. M. Kroon, M. A. J. Michels and R. A. J. Janssen, *Nano Letters*, 2005, **5**, 579–583.

14   X. Gong, M. Tong, F. G. Brunetti, J. Seo, Y. Sun, D. Moses, F. Wudl and A. J. Heeger, *Advanced Materials (Weinheim, Germany)*, 2011, **23**, 2272–2277.

15   yuanbao Lin, Y. Firdaus, F. H. Isikgor, M. I. Nugraha, E. Yengel, G. T. Harrison, R. Hallani, A. El Labban, H. Faber, C. Ma, X. Zheng, A. S. Subbiah, C. T. Howells, O. M. Bakr, I. McCulloch, S. De Wolf, L. Tsetseris and T. D. Anthopoulos, *ACS Energy Letters*, , DOI:10.1021/acsenergylett.0c01421.

16   E. L. Ratcliff, B. Zacher and N. R. Armstrong, *Journal of Physical Chemistry Letters*, 2011, 2, 1337–1350.

17   L. Meng, Y. Zhang, X. Wan, C. Li, X. Zhang, Y. Wang, X. Ke, Z. Xiao, L. Ding, R. Xia, H. L. Yip, Y. Cao and Y. Chen, *Science*, 2018, **361**, 1094–1098.

18   Y. Wang, X. Ke, Z. Xiao, L. Ding, R. Xia and H. Yip, *Science*, 2018, **1098**, 1094–1098.

19   L. Zhan, S. Li, T. K. Lau, Y. Cui, X. Lu, M. Shi, C. Z. Li, H. Li, J. Hou and H. Chen, *Energy and Environmental Science*, 2020, **13**, 635–645.

20   W. Zhao, S. Li, S. Zhang, X. Liu and J. Hou, *Advanced Materials*, , DOI:10.1002/adma.201604059.

21   B. Fan, W. Zhong, X. F. Jiang, Q. Yin, L. Ying, F. Huang and Y. Cao, *Advanced Energy Materials*, , DOI:10.1002/aenm.201602127.

22   T. Ameri, P. Khoram, J. Min and C. J. Brabec, *Advanced Materials*, 2013, 25, 4245–4266.

23   L. Lu, M. A. Kelly, W. You and L. Yu, *Nature Photonics*, 2015, **9**, 491–500.

24   X. A. Jeanbourquin, A. Rahmanudin, X. Yu, M. Johnson, N. Guijarro, L. Yao and K. Sivula, *ACS Applied Materials and Interfaces*, 2017, **9**, 27825–27831.

25   T. Y. Huang, D. Patra, Y. S. Hsiao, S. H. Chang, C. G. Wu, K. C. Ho and C. W. Chu, *Journal of Materials Chemistry A*, 2015, **3**, 10512–10518.

26   L. Lu, T. Xu, W. Chen, E. S. Landry and L. Yu, *Nature Photonics*, 2014, **8**, 716–722.

27   R. Yu, H. Yao and J. Hou, *Advanced Energy Materials*, ,
DOI:10.1002/aenm.201702814.

28   H. Lu, J. Zhang, J. Chen, Q. Liu, X. Gong, S. Feng, X. Xu, W. Ma and Z. Bo,
Advanced Materials, 2016, **28**, 9559–9566.

29   T. Liu, Y. Guo, Y. Yi, L. Huo, X. Xue, X. Sun, H. Fu, W. Xiong, D. Meng, Z. Wang,
F. Liu, T. P. Russell and Y. Sun, *Advanced Materials*, 2016, **28**, 10008–10015.

30   J. A. Foster, S. Henke, A. Schneemann, R. A. Fischer and A. K. Cheetham, *Chem.
Commun.*, 2016, **52**, 10474–10477.

31   D. J. Ashworth and J. A. Foster, *Journal of Materials Chemistry A*, 2018, **6**, 16292–
16307.

32   J. Nicks, J. Zhang and J. A. Foster, *Chemical Communications*, 2019, **55**, 8788–8791.

33   S. Kim, H. Wang and Y. M. Lee, *Angewandte Chemie International Edition*, ,
DOI:10.1002/anie.201814349.

34   W. Zhao, J. Peng, W. Wang, S. Liu, Q. Zhao and W. Huang, *Coordination Chemistry
Reviews*, 2018, **377**, 44–63.

35   D. J. Ashworth, T. M. Roseveare, A. Schneemann, M. Flint, I. D. Bernáldes, P.
Vervoorts, R. A. Fischer, L. Brammer and J. A. Foster, *Inorganic Chemistry*, 2019, **58**,
10837–10845.

36   Y. Zheng, F. Sun, X. Han, J. Xu and X. Bu, *Advanced Optical Materials*, 2020,
2000110.

37   S. Liu, Y.-C. Wang, C.-M. Chang, T. Yasuda, N. Fukui, H. Maeda, P. Long, K.
Nakazato, W.-B. Jian, W. Xie, K. Tsukagoshi and H. Nishihara, *Nanoscale*, 2020, 0–7.

38   W. Xing, P. Ye, J. Lu, X. Wu, Y. Chen, T. Zhu, A. Peng and H. Huang, *Journal of
Power Sources*, 2018, **401**, 13–19.

39   C. Liu, C. Wang, H. Wang, T. Wang and J. Jiang, *European Journal of Inorganic
Chemistry*, 2019, **2019**, 4815–4819.

40   K. Sasitharan, D. G. Bossanyi, N. Vaenas, A. J. Parnell, J. Clark, A. Iraqi, D. G.

Lidzey and J. A. Foster, *Journal of Materials Chemistry A*, 2020, **8**, 6067–6075.

41   P. D. W. Boyd and C. A. Reed, *Accounts of Chemical Research*, 2005, **38**, 235–242.

42   J. K. Sprafke, D. V. Kondratuk, M. Wykes, A. L. Thompson, M. Hoffmann, R. Drevinskas, W. H. Chen, C. K. Yong, J. Kärnbratt, J. E. Bullock, M. Malfois, M. R. Wasielewski, B. Albinsson, L. M. Herz, D. Zigmantas, D. Beljonne and H. L. Anderson, *Journal of the American Chemical Society*, 2011, **133**, 17262–17273.

43   T. G. Pedersen, T. B. Lynge, P. K. Kristensen and P. M. Johansen, in *Thin Solid Films*, Elsevier, 2005, vol. 477, pp. 182–186.

44   X. Liu, C. Huang and M. Li, *Journal of Physical Chemistry C*, 2016, **120**, 27148–27158.

45   W. J. Belcher, K. I. Wagner and P. C. Dastoor, *Solar Energy Materials and Solar Cells*, 2007, **91**, 447–452.

46   M. G. Walter, A. B. Rudine and C. C. Wamser, *Journal of Porphyrins and Phthalocyanines*, 2010, **14**, 759–792.

47   Z. D. Seibers, G. S. Collier, B. W. Hopkins, E. S. Boone, T. P. Le, E. D. Gomez and S. M. Kilbey, *Soft Matter*, , DOI:10.1039/d0sm01244k.

48   P. D. W. Boyd, M. C. Hodgson, C. E. F. Rickard, A. G. Oliver, L. Chaker, P. J. Brothers, R. D. Bolskar, F. S. Tham and C. A. Reed, *Journal of the American Chemical Society*, 1999, **121**, 10487–10495.

49   R. E. Andernach, S. Rossbauer, R. S. Ashraf, H. Faber, T. D. Anthopoulos, I. McCulloch, M. Heeney and H. A. Bronstein, *ChemPhysChem*, 2015, **16**, 1223–1230.

50   M. Chevrier, J. Kesters, C. Blayo, S. Richeter, A. Van Der Lee, O. Coulembier, M. Surin, A. Mehdi, R. Lazzaroni, R. C. Evans, W. Maes, P. Dubois and S. Clément, *Macromolecular Chemistry and Physics*, 2016, **217**, 445–458.

51   S. Wang, M. Wang, Z. Chen and X. Yang, *Journal of Materials Chemistry A*, 2015, **3**, 21051–21059.

52   J. H. Lee, H. Jintoku, Y. Okazaki, T. Sagawa, M. Takafuji and H. Ihara, *Solar Energy Materials and Solar Cells*, 2015, **140**, 428–438.

53   N. Koch, *ChemPhysChem*, 2007, 8, 1438–1455.

54   A. Sengupta, S. Datta, C. Su, T. S. Herng, J. Ding, J. J. Vittal and K. P. Loh, *ACS Applied Materials and Interfaces*, 2016, **8**, 16154–16159.

55   Q. D. Yang, H. W. Li, Y. Cheng, Z. Guan, T. Liu, T. W. Ng, C. S. Lee and S. W. Tsang, *ACS Applied Materials and Interfaces*, 2016, **8**, 7283–7290.

56   R. C. Shallcross, T. Stubhan, E. L. Ratcliff, A. Kahn, C. J. Brabec and N. R. Armstrong, *Journal of Physical Chemistry Letters*, 2015, **6**, 1303–1309.

5.2 Publication Supplementary Information

Tuning Energy Levels and Active Layer Morphology of Organic Photovoltaic Devices with Metal-Organic Framework Nanosheets

Kezia Sasitharan, Johannes Frisch, Ahmed Iraqi, David G Lidzey, Marcus Baer and Jonathan A Foster

Supplementary information

Table of contents

1. General experimental procedures

Commercial solvents and reagents were used without further purification. Synthesis of organic ligands was carried out in dry glassware with a nitrogen overpressure. Solvothermal synthesis of metal-organic frameworks was undertaken using borosilicate vials with Teflon faced rubber lined caps.

NMR spectra were recorded on a Bruker Advance DPX 400 spectrometer. Chemical shifts for ^1H are reported in ppm on the δ scale; ^1H chemical shifts were referenced to the residual solvent peak. All coupling constants are reported in Hz. Mass spectra were collected using a Bruker Reflex III MALDI-TOF spectrometer. Elemental analyses were obtained on a vario MICRO CHNS elemental analyzer equipped with a thermal conductivity detector. X-Ray powder diffraction patterns were collected using a Bruker D8 Advance powder diffractometer equipped with a copper K_α source (λ=1.5418 Å) operating at 40 kV and 40 mA. The instrument was fitted with an energy-dispersive LYNXEYE detector. Measurements were carried out using a fixed goniometer stage with a rotating flat plate sample holder. UV-Vis absorption spectra were collected on a Cary 5000 UV-Vis-NIR instrument using a 1 cm internal length quartz cuvette.

Nanoscopic characterisation was performed using a Bruker Multimode 5 AFM, operating in soft-tapping mode under ambient conditions. Bruker OTESPA-R3 cantilever were used, with a drive amplitude and nominal resonance frequency of 20.4 mV and 290 kHz, respectively. Images were processed using standard techniques with free Gwyddion software.

UPS measurements were performed at the beamline PM4 at the synchrotron light source BESSY II (Berlin, Germany). Spectra were collected with a hemispherical electron energy analyzer (Scienta SES 100) using an excitation photon energy of 30 eV for UPS. The secondary electron cutoff (SECO) spectra were recorded with a sample bias of −10 V to clear the analyzer work function. The error of binding energy (BE) and work function values reported is estimated to be smaller than ±0.05 eV.

2 Syntheses
2.1 Synthesis of *meso-tetracarboxyphenyl porphyrin* (TCPP) ligand

10 mL of pyrrole (98%, light brown solution) was distilled under vacuum at 80°C to give 5 mL of a clear solution. 4-formylbenzoic acid (3.0 g, 20 mmol) was dissolved in propionic acid (100 mL) and freshly distilled pyrrole (1.4 mL, 20 mmol) was added by syringe. The solution immediately darkened and was refluxed for 15 hours. The mixture was chilled in a fridge for

10 hours before collection of the solid by vacuum filtration. The solid was washed with hot water (2 x 20 mL) and dried under vacuum to give the product as a black powder (3.23 g, 4.0 mmol, 80 %). Elemental Analysis (%) calculated for $C_{48}H_{30}N_4O_8$: Expected: C, 72.91; H, 3.82; N, 7.09. Found: C, 72.95; H, 4.08; N, 6.82

λ_{max} (nm): 420 (π-π^*)

^{1}H-NMR (d$_6$-DMSO) δ/ppm: 8.85 (8H, s, β-pyrrolic H), 8.38 (8H, d, J = 8.0, Ar-H), 8.32 (8H, d, J = 8.0, Ar-H), -2.95 (2H, s, internal pyrrole NH).

MALDI-TOF: m/z 791.2 ([MH]$^+$)

2.2 Synthesis of TPyP

10 mL of pyrrole (98%, light brown solution) was distilled under vacuum at 80°C to give 5ml of a clear solution. 4-pyridine-carboxaldehyde (3.16 Ml, 3.35 mmol) was dispersed in propionic acid (75ml). This mixture was heated to 100°C under reflux. A mixture of pyrrole (2.32 ml, 3.34 mmol) and propionic acid (10ml, 0.13 mmol) was added slowly and the resulting mixture is heated to 141°C for 24 hours. The mixture was chilled in the fridge for about 12 hours before adding hot water to the solution to force the TPyP out of solution. The solid was collected by vacuum filtration and washed with hot water (4x20ml) and dried under vacuum to give the product as a black powder.

2.3 Metallation of TPyP with Zn

Zinc (II) was inserted into the porphyrin monomers by standard methods. An excess of Zinc Nitrate (1.1mmol) was added to 0.63 mmol of TPyP in 50 mL DMF. The solution was refluxed for 1 hour, after which a small sample fo the reaction mixture was extracted and analysed by using UV-Vis spectroscopy. The spectrum indicated that the metal insertion was complete with the four Q bands of the free base collapsing into two. The DMF was rotavaped off and the ZnTPyP was washed with hot water (60°C, 2x20mL).

2.4 Synthesis of bulk Zn$_2$(Zn-TCPP)(DMF)

H_2TCPP (7.9 mg, 0.03 mmol), Zn(NO$_3$)$_2$.3H$_2$O (8.9 mg, 0.09 mmol), DMF (1.5 mL) and ethanol (0.5 mL) were mixed at room temperature and heated at 80°C for 24 hours. Purple crystals were collected by centrifugation at 4500 RPM for 10 minutes and repeatedly washed in ethanol until the supernatant became clear (Yield 87%)

Elemental analysis $C_{48}H_{24}N_4O_8Zn_3(H_2O)_4(DMF)_3$: Expected C, 53.57; H, 4.50; N, 8.33 Found C, 52.76; H, 4.77; N, 8.88.

A slight excess of Zn around the edge of the MOF and possible nitrate counter ions could be the reason for lower carbon content and higher nitrogen.

2.5 Synthesis of bulk $Cu_2(Cu\text{-}TCPP)(DMF)$

H_2TCPP (23.7 mg, 5 mmol), $Cu(NO_3)_2.3H_2O$ (21.6 mg, 15 mmol), DMF (4.5 mL) and ethanol (1.5 mL) were mixed at room temperature and heated at 80°C for 24 hours. Purple powder was collected by centrifugation at 4500 RPM for 10 minutes and repeatedly washed in ethanol until the supernatant became clear (Yield 83.8%)

Elemental analysis $C_{48}H_{24}N_4O_8Cu_3(H_2O)_4(DMF)_3$: Expected C, 54.05; H, 4.22; N, 7.74; Found C, 53.45; H, 4.44; N, 8.04

2.7 Synthesis of bulk $Cu_2(Zn\text{-}TPyP)(DMF)$

ZnTPyP (7.9 mg, 0.03 mmol), $Cu(NO_3)_2.3H_2O$ (8.9 mg, 0.09 mmol), DMF (1.5 mL) and ethanol (0.5 mL) were mixed at room temperature and heated at 80°C for 24 hours. Black powdery product was collected by centrifugation at 4500 RPM for 10 minutes and repeatedly washed in ethanol until the supernatant became clear (Yield 74%)

2.8 Exfoliation of MOF into MONs

5 mg of MOF was added to a 12 mL glass vial along with 6 mL of the desired solvent. The sample was mixed in a vortex mixer for 30 seconds to disperse the sediment. The samples were sonicated using a Fisherbrand Elmasonic P 30H ultrasonic bath (2.75 L, 380/350 W, UNSPSC 42281712) filled with water. Samples were sonicated for 60 min at a frequency of 80 kHz with 100% power and the temperature was thermostatically maintained at 16-20°C using a steel cooling coil. Sonication was applied using a sweep mode and samples were rotated through the water using an overhead stirrer to minimise variation due to ultrasound "hot-spots". Following sonication, the vials were transferred to centrifuge tubes and centrifuged at 1500 RPM for 10 minutes to remove non-exfoliated particles.

3   Structural characterisations

XRD of MOF and MONs
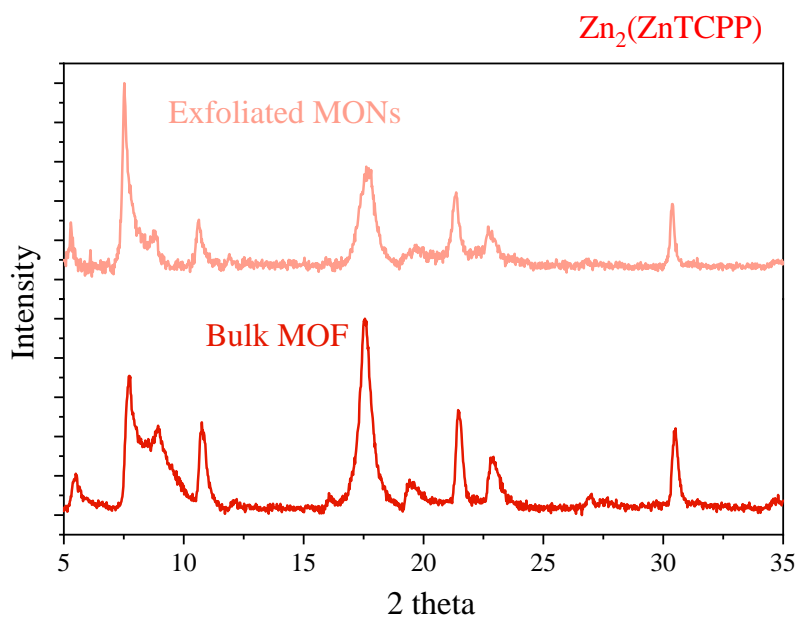
Figure S5.1 XRD patterns of bulk Zn$_2$(ZnTCPP) MOF and exfoliated MONs
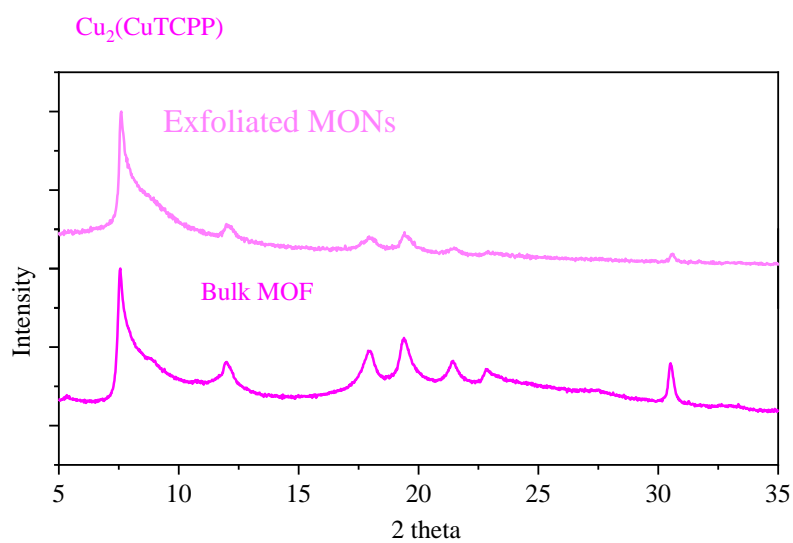
Figure S5.2 XRD patterns of bulk Cu$_2$(CuTCPP) MOF and exfoliated MONs
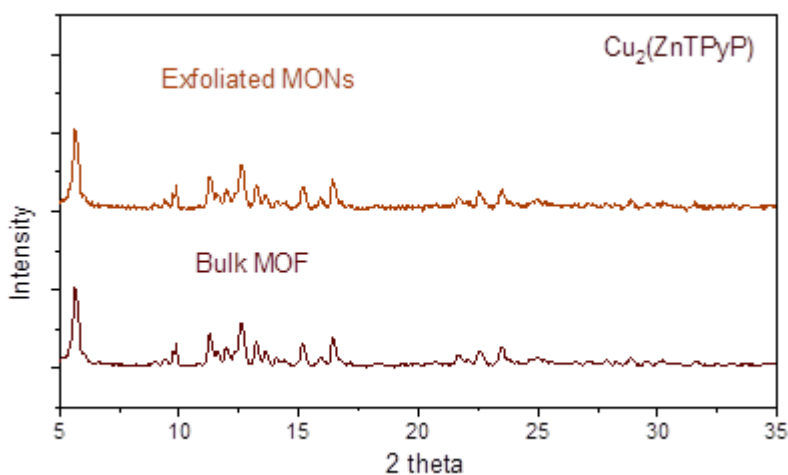
Figure S5.3 XRD patterns of bulk Cu$_2$(ZnTPyP) MOF and exfoliated MONs

4 Molar extinction coefficient

a. Zn$_2$(ZnTCPP) MONs
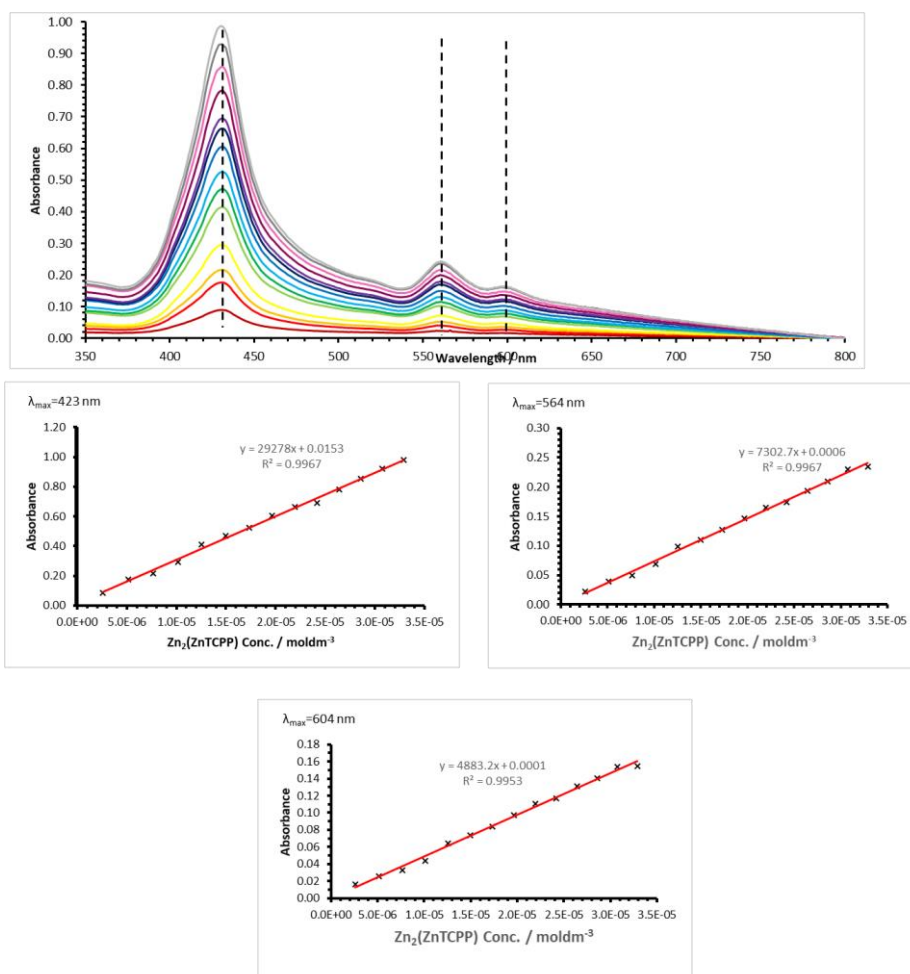
Figure S5.4 Molar extinction coefficient calculation for Zn$_2$(ZnTCPP) MONs

b. Cu₂(CuTCPP) MONs
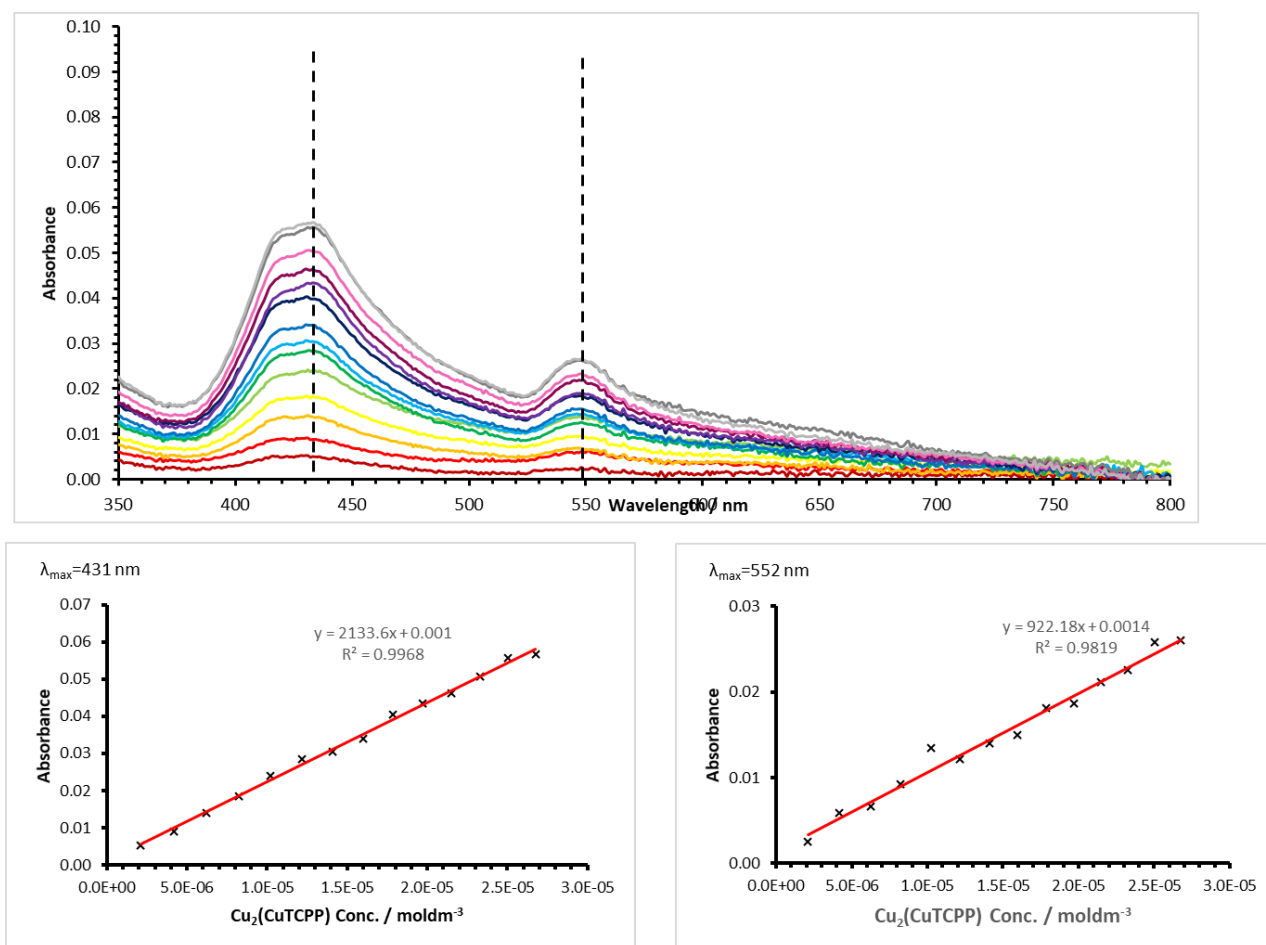
Figure S5.5 Molar extinction coefficient calculation of Cu₂(CuTCPP) MONs
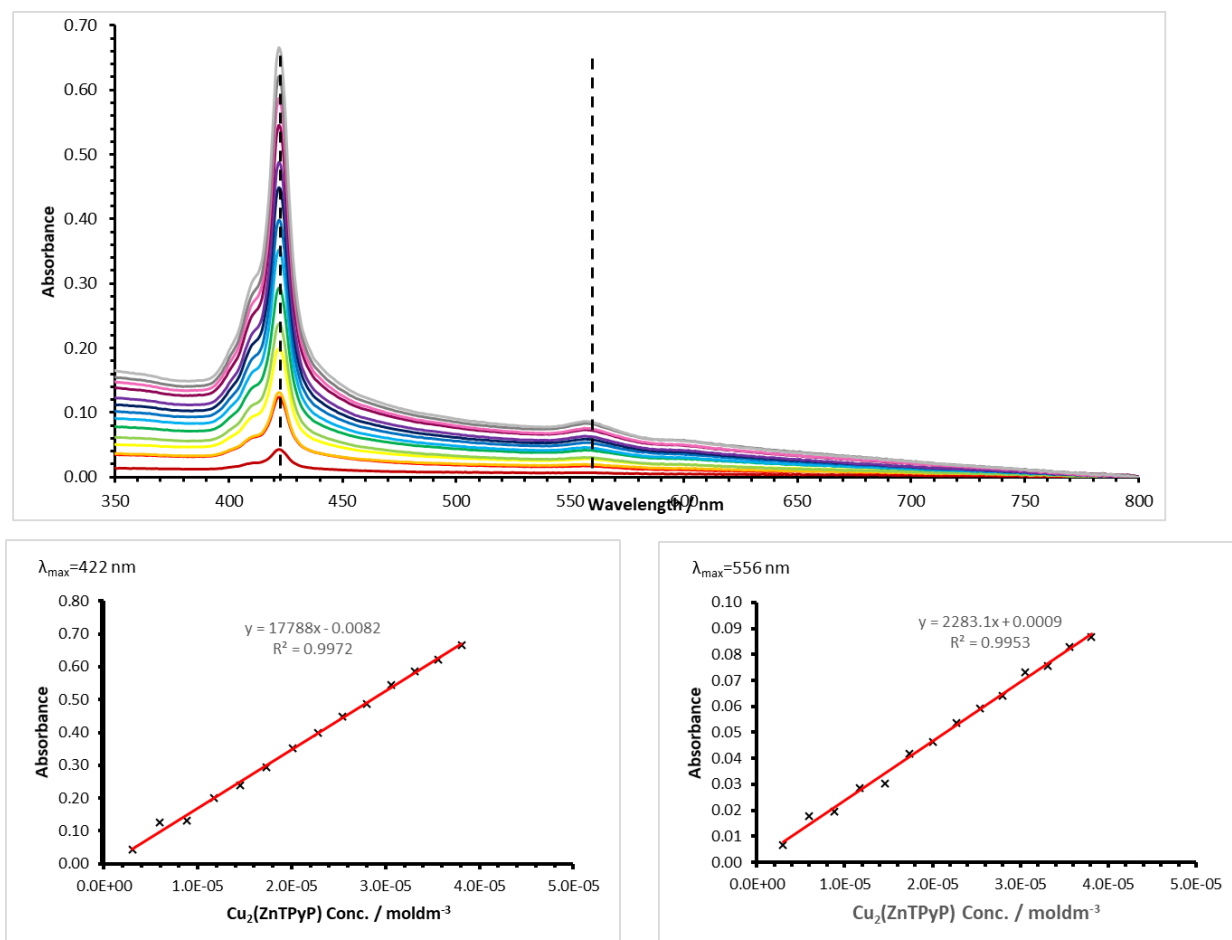
c. Cu₂(ZnTPyP) MONs

Figure S5.6 Molar extinction coefficient calculation of Cu₂(ZnTPyP) MONs

5   AFM imaging of various MONs

a. **Zn₂(ZnTCPP) MONs**
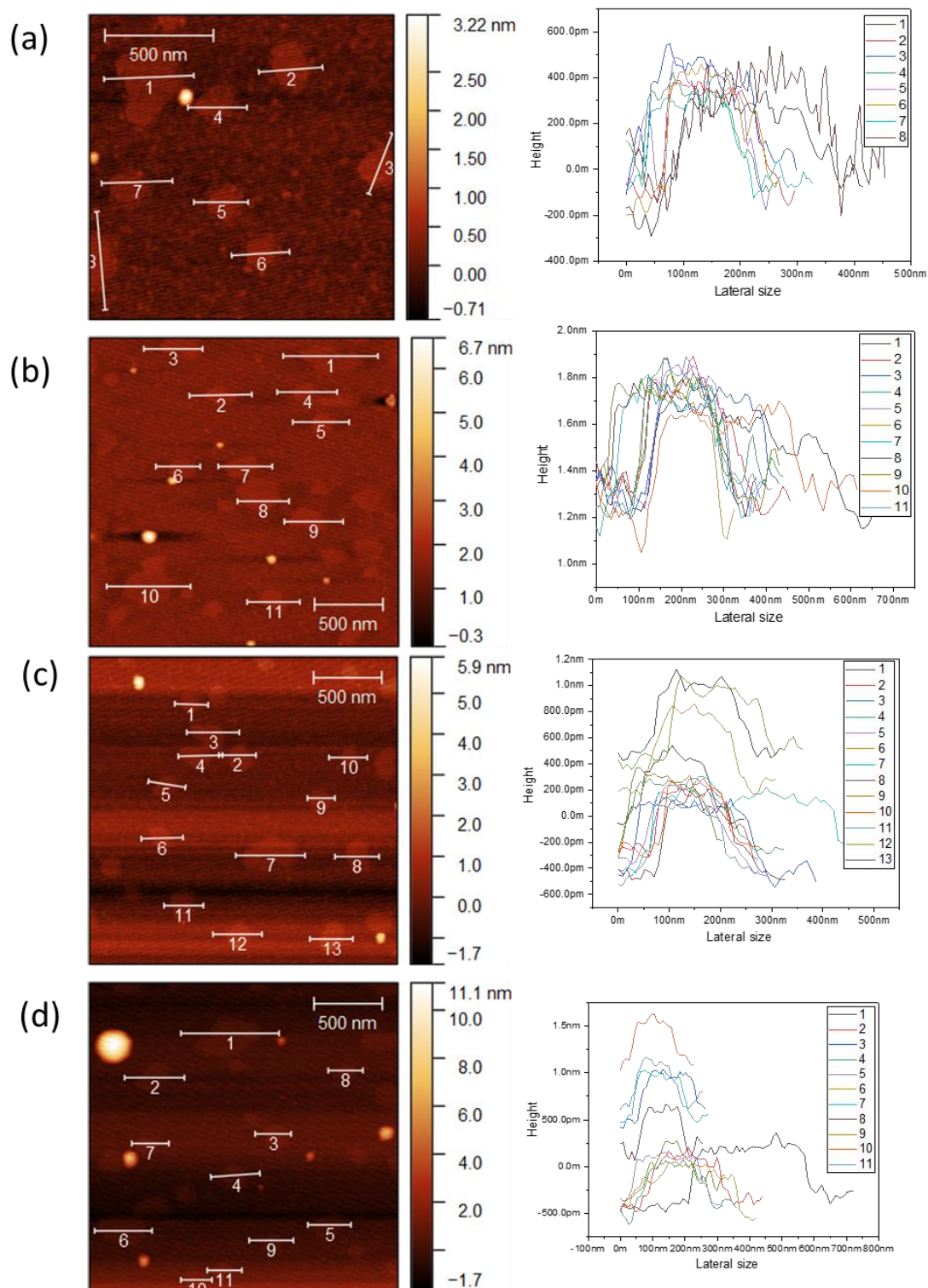
Figure S5.7 AFM images and corresponding height profiles of Zn₂(ZnTCPP) MONs

b. Cu₂(CuTCPP) MONs
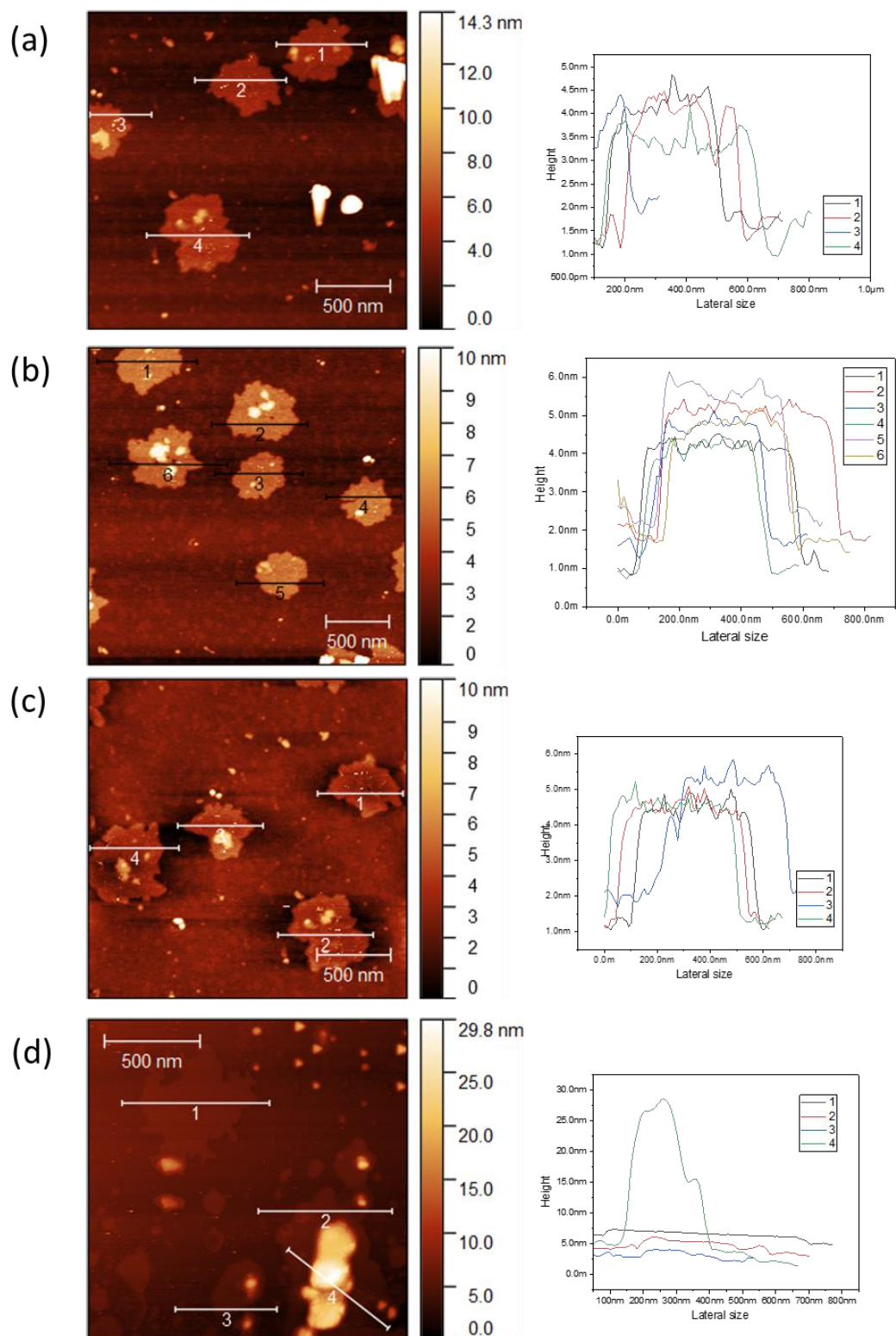
Figure S5.8 AFM images and corresponding height profiles of Cu₂(CuTCPP) MONs
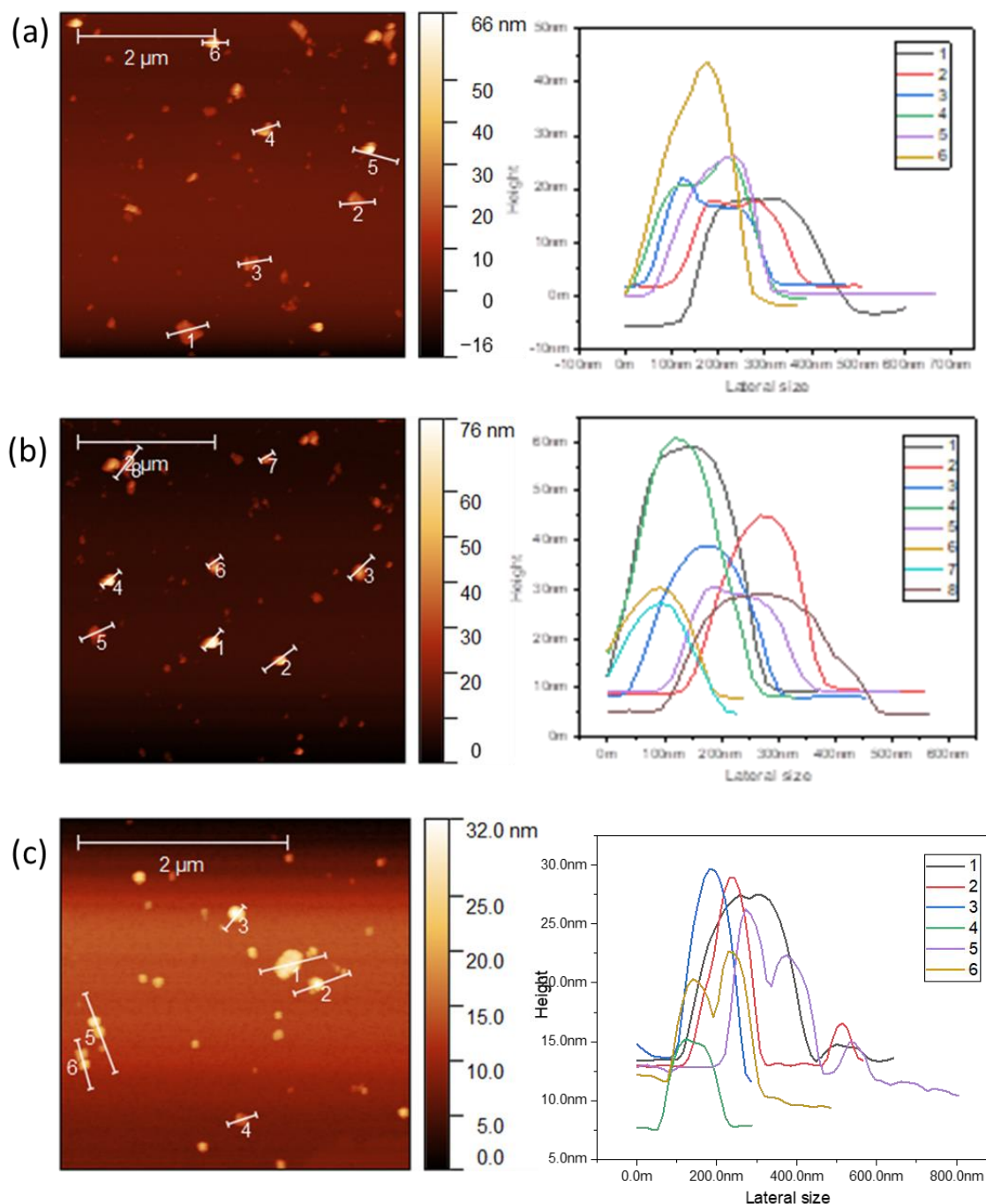
c. **Cu₂(ZnTPyP) MONs**

Figure S5.9 AFM images and corresponding height profiles for Cu₂(ZnTPyP) MONs

6   Fabrication of devices

a.   Preparation of substrates

Pre-patterned ITO Glass substrates (20 mm x 15 mm) of 20 ohm/square resistance (Ossila) were cleaned via hellmenex (1-3vol%) in boiling DI water (10-minute sonication), followed

by further washing in boiling DI water (10-minute sonication) and finally 5-10 minutes sonication in isopropyl alcohol. The substrates were dried with a nitrogen gun and placed in a UV-Ozone cleaner for 10 minutes to ensure removal of any surface particulates.

b. Deposition of PEDOT:PSS

PEDOT:PSS solution (Al4083, Ossila) was brought to room temperature, filtered through a 0.45 µm PVDF filter into an amber vial and dynamically spin-coated (45 µL) onto room-temp substrates at 6000 rpm, to achieve a film ~25 nm. The PEDOT:PSS coated substrates were placed on a hotplate at 110 °C for 15 minutes. This was followed by further annealing in the glovebox at 110 °C for 15 minutes to remove any surface moisture. After 15 minutes annealing in the glovebox, the ITO/PEDOT samples were cooled to room temperature before active layer deposition.

c. Active layer deposition

P3HT (Sigma Aldrich) and PCBM (99% purity, supplied by Ossila) were used as received. P3HT (10mg/mL) was dissolved in chlorobenzene (CB) solvent. After heating at 60 °C for 10 minutes followed by cooling towards room temperature, the solution was filtered through a 0.45 um PTFE filter. The P3HT solution in chlorobenzene was then mixed with 5mg MONs MONs (1:0.5 wt/wt ratio of P3HT:MON) and stirred at 60 °C for an hour. Then 10 mg of PCBM was added and the final P3HT:MON:PCBM (1:0.5:1 wt/wt ratio) was heated at 70°C for an hour and cooled to room temperature prior to spin coating. The solutions were then spin-cast onto ITO/PEDOT at 1000 rpm under a nitrogen atmosphere in a glove box, forming films of ~150 nm as determined by dektak. For control devices, 1:1(wt/wt) (P3HT:PCBM) were spin cast at 2000 rpm in the same method as above to give films of ~150nm. Solvent-vapour annealing of the films was carried out by placing the coated substrates in a sealed metal container containing 20uL of solvent chlorobenzene) for 5 minutes.

d. Top contact deposition and encapsulation

The ITO/PEDOT:PSS/Active layer substrates were placed under a vacuum of <2E-6 mBar before thermally evaporating BCP (5nm) and Silver (100nm) layers using a shadow mask. The devices were encapsulated using an epoxy resin (Ossila, E131).
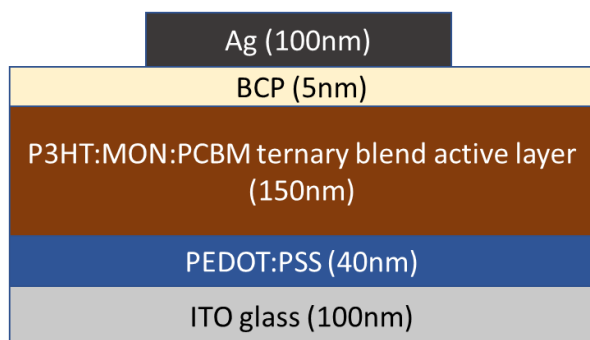
Figure S5.10 The architecture of solar cells prepared in this work.

7   Device testing

Device performance was determined under ambient conditions by measuring J–V curves using a Newport 92251A-1000 solar simulator, with devices illuminated through a 0.0256 cm^2 aperture mask. Before each set of measurements, the intensity was calibrated to 100 mW cm^{-2} using an NREL certified silicon reference cell. The applied bias was swept from 0.0 to +1.2 V and back again at a scan speed of 0.4 V s^{-1} using a Keithley 237 source measure unit.

8.   Bilayer devices

Bilayer devices were prepared in the same way as the bulk heterojunctions, except for the active layer. Instead of pre-mixing the P3HT-PCBM and MONs, each component was individually spin-coated orthogonally before the back contact fabrication.

Table S5.1 Solar cell performance parametrics for the bilayer devices with configuration ITO/PEDOT:PSS/P3HT/ZnTCPP/BCP/Ag

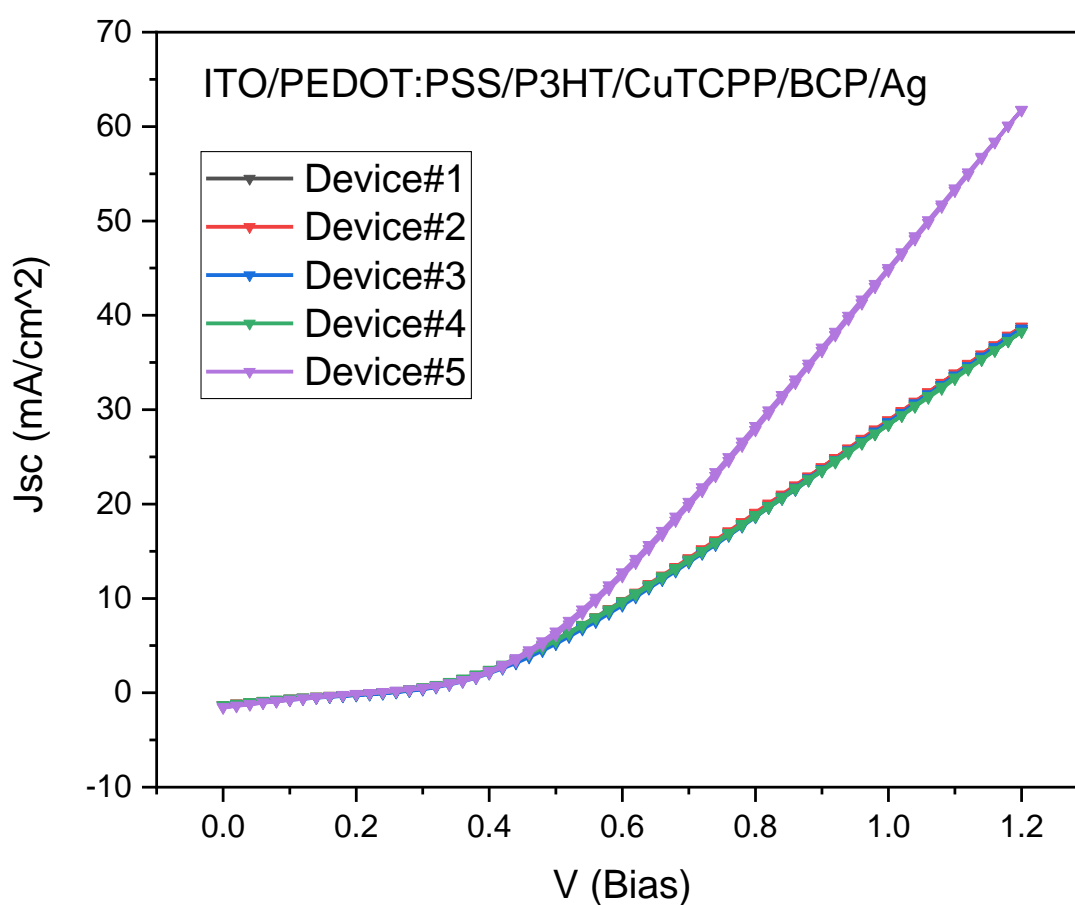| Device	Jsc	Voc	FF	PCE
Device#1	-3.52	0.16	26.4	0.15
Device#2	-3.27	0.19	26.68	0.16
Device#3	-3.58	0.16	26.31	0.15
Device#4	-2.92	0.08	25.30	0.06
Device#5	-2.98	0.15	26.13	0.11
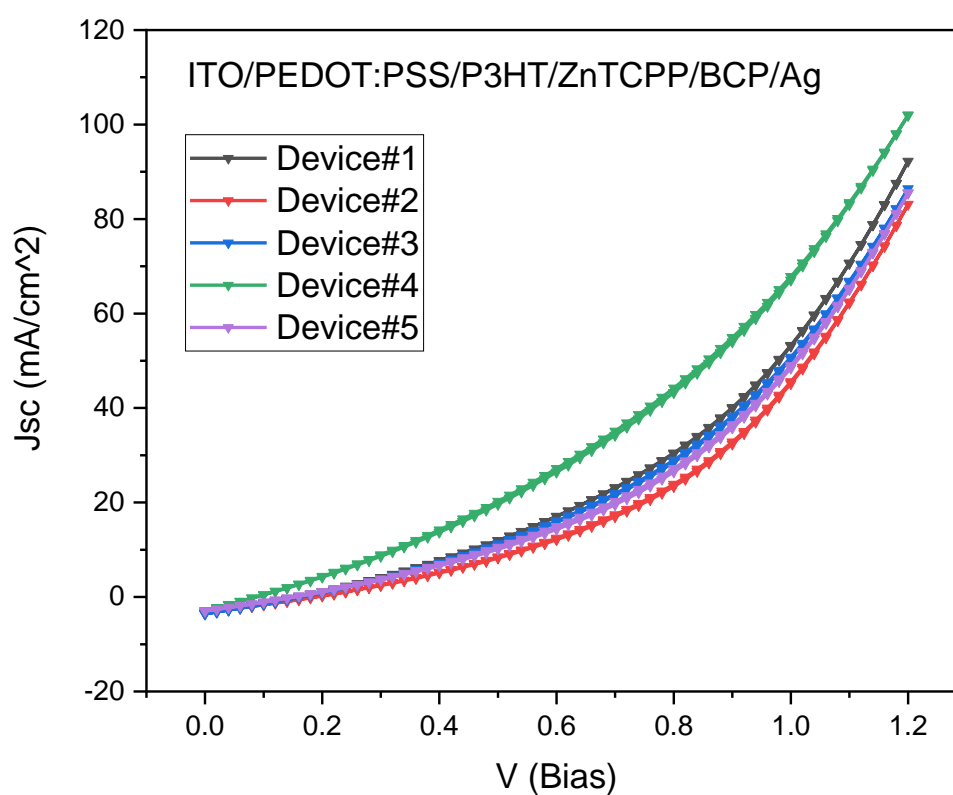
Figure S5.11 J-V curves of the devices ITO/PEDOT:PSS/P3HT/ZnTCPP/BCP/Ag listed in table S5.1

Table S5.2 Solar cell performance paramterics for the bilayer devices with the configuration ITO/PEDOT:PSS/ZnTCPP/PCBM/Ag

Device	Jsc	Voc	FF	PCE
Device#1	-3.48	0.55	31.94	0.62
Device#2	-3	0.63	37.40	0.71
Device#3	-3.09	0.34	24.94	0.26
Device#4	-3.29	0.64	33.10	0.69
Device#5	-3.32	0.58	29.95	0.58
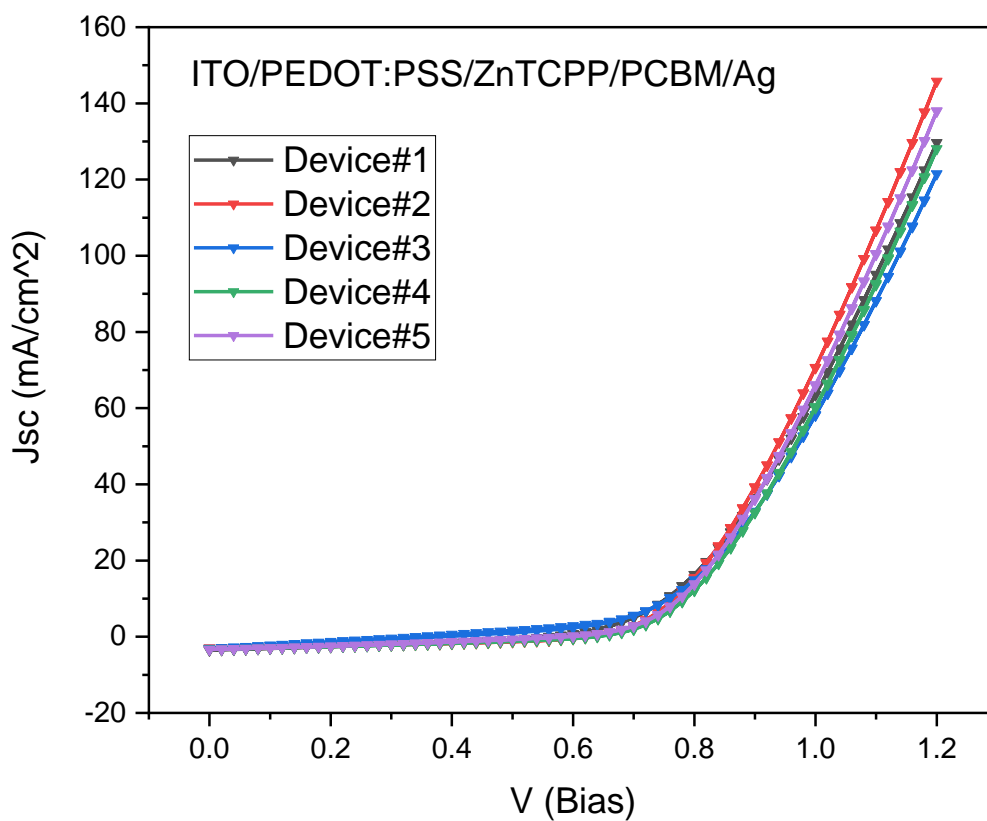
Figure S5.12 J-V curves for the devices with the configuration ITO/ PEDOT:PSS/ ZnTCPP/ PCBM/ Ag listed in table S5.2

Table S5.3 Solar cell performance parametrics for the devices with configuration
ITO/PEDOT:PSS/P3HT/CuTCPP/BCP/Ag

Device	Jsc	Voc	FF	PCE
Device#1	-1.33	0.23	20.72	0.06
Device#2	-1.31	0.24	20.60	0.06
Device#3	-1.42	0.25	20.83	0.07
Device#4	-1.32	0.23	20.80	0.06
Device#5	-1.55	0.23	21.61	0.08

Figure S5.13 J-V curves of the devices with configuration ITO/ PEDOT:PSS/ P3HT/
CuTCPP/ BCP/Ag listed in table S5.3

Table S5.4 Solar cell performance parametrics for devices with configuration ITO/PEDOT:PSS/CuTCPP/PCBM/Ag

Device	Jsc	Voc	FF	PCE
Device#1	-1.68	0.04	24.02	0.02
Device#2	-1.81	0.09	24.56	0.03
Device#3	-1.71	0.05	24.56	0.02
Device#4	-1.89	0.05	24.70	0.02
Device#5	-1.35	0.06	24.88	0.02
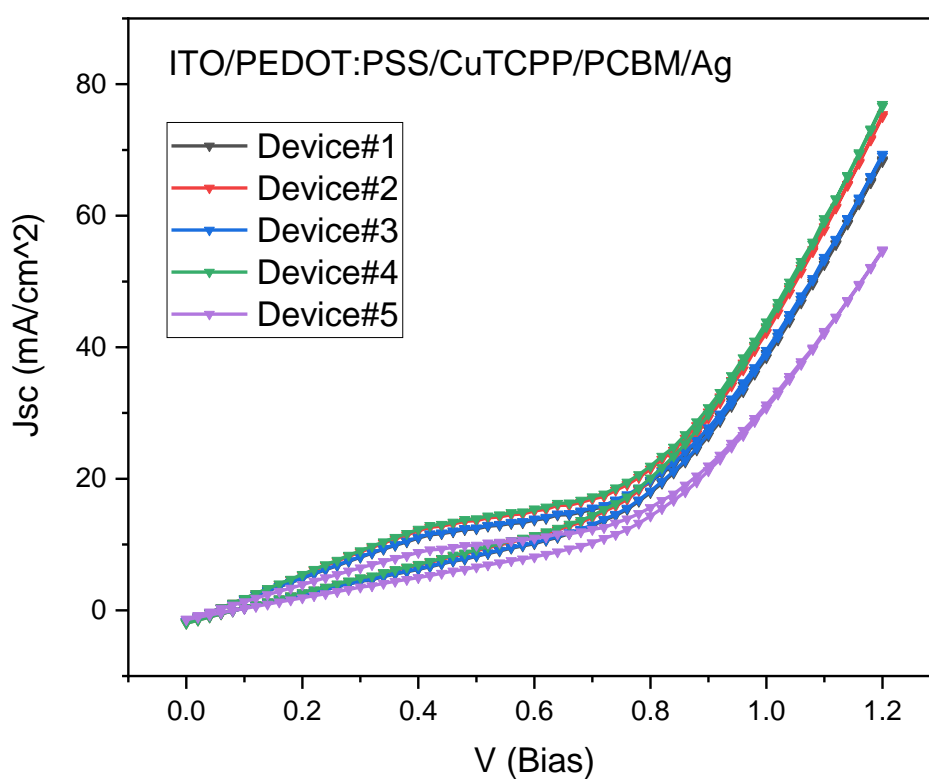
Figure S5.14 J-V curves of solar cells from table S5.4 of the configuration ITO/PEDOT:PSS/CuTCPP/PCBM/Ag

Table S5.5 Solar cell performance parametrics for devices with the configuration
ITO/PEDOT:PSS/P3HT/CuZnTPyP/BCP/Ag

Device	Jsc	Voc	FF	PCE
Device#1	-1.44	0.37	29.51	0.23
Device#2	-1.41	0.31	28.81	0.20
Device#3	-1.42	0.40	29.87	0.18
Device#4	-1.41	0.21	26.57	0.11
Device#5	-1.44	0.43	29.95	0.15
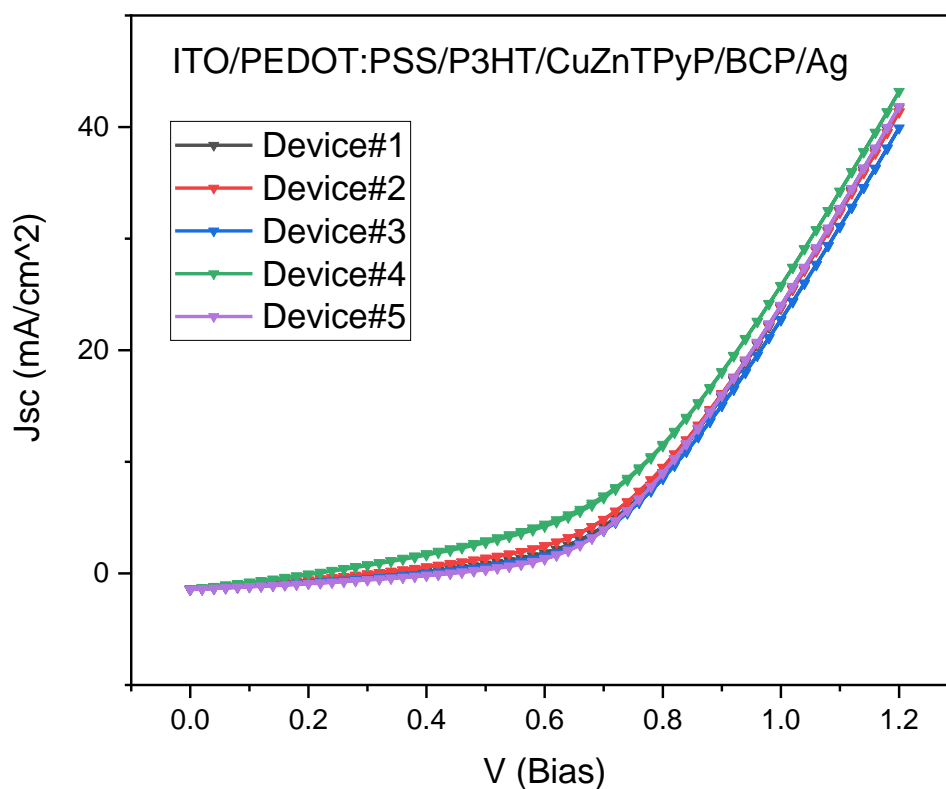
Figure S5.15 J-V curves of the solar cells from table S5.5 of the configuration
ITO/PEDOT:PSS/P3HT/CuZnTPyP/BCP/Ag

Table S5.6 Solar cell performance parametrics for devices with the configuration ITO/PEDOT:PSS/CuZnTPyP/PCBM/Ag

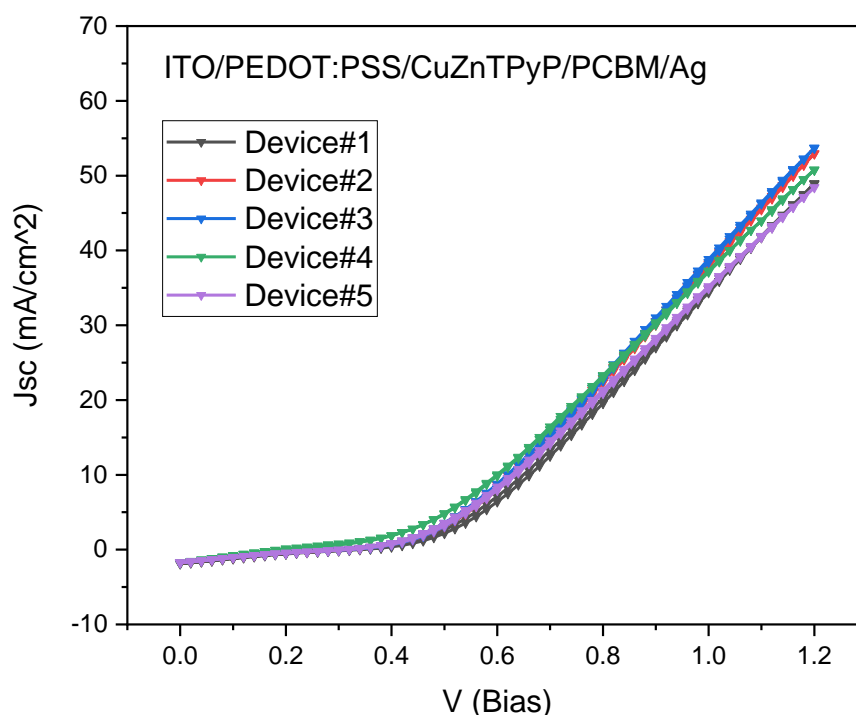| Device	Jsc	Voc	FF	PCE
Device#1	-1.88	0.34	20.59	0.13
Device#2	-1.78	0.32	19.86	0.11
Device#3	-1.75	0.32	19.80	0.11
Device#4	-1.74	0.19	24.00	0.07
Device#5	-1.75	0.32	20.44	0.11

Figure S5.16 J-V curves of the solar cells with the configuration ITO/PEDOT:PSS/CuZnTPyP/PCBM/Ag, listed in table S5.6

9. Photoemission investigations
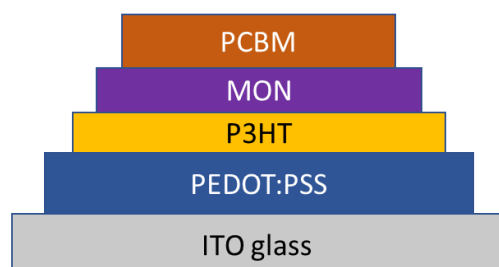
Figure S5.17 Schematic representation of the different interfaces studies using photoemission techniques in this work.

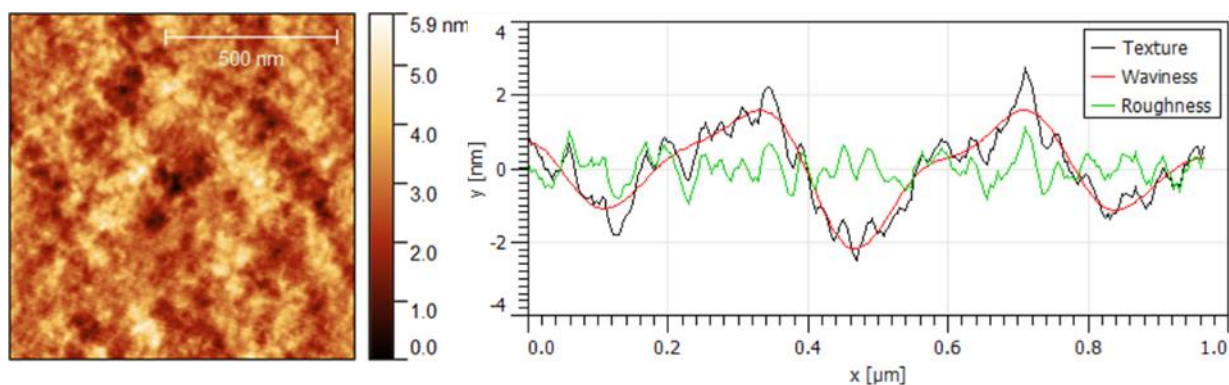## 9.1 AFM images of the substrates used for MON layer deposition

Figure S5.18 AFM image and the corresponding profile of roughness of the PEDOT:PSS layer on ITO substrates.
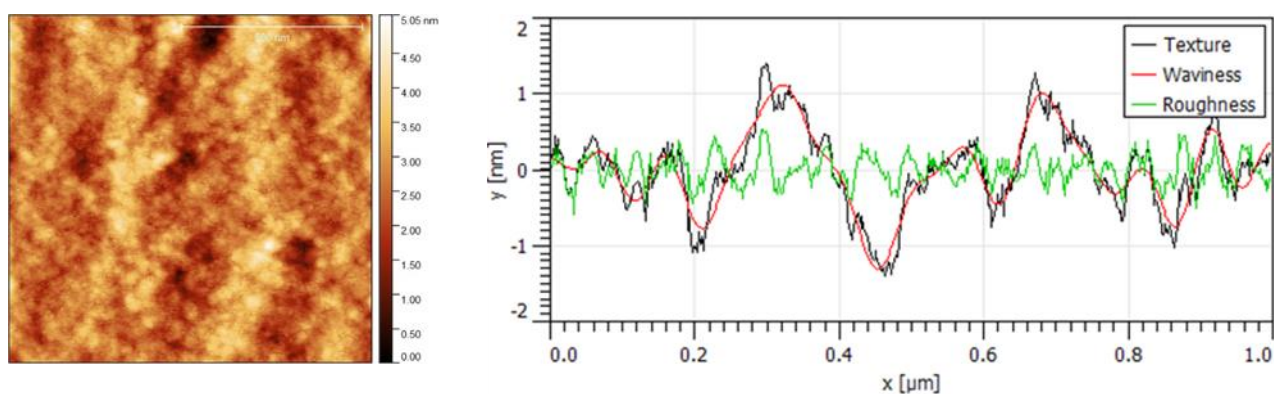

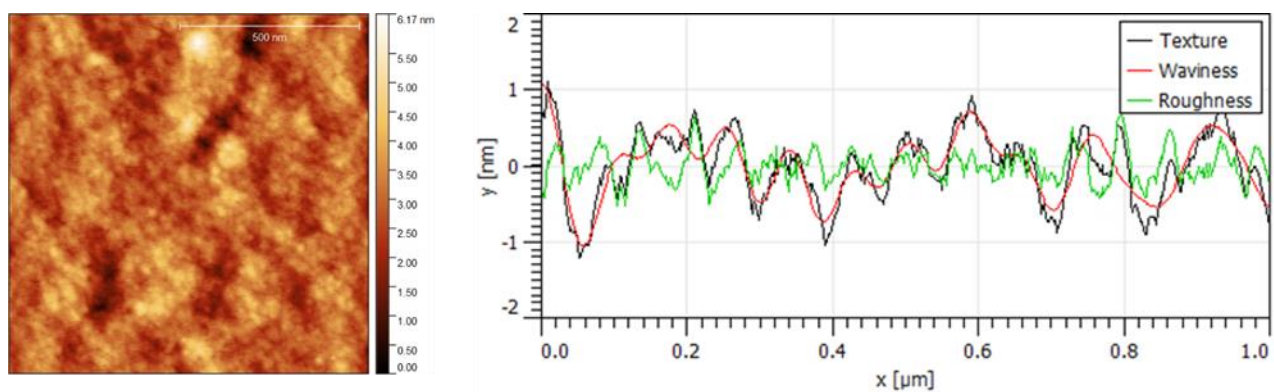Figure S5.19 AFM image and corresponding roughness profile of the P3HT films spin-coated onto PEDOT:PSS.

Figure S5.20 AFM image and corresponding roughness P3HT crosslinked on PEDOT:PSS
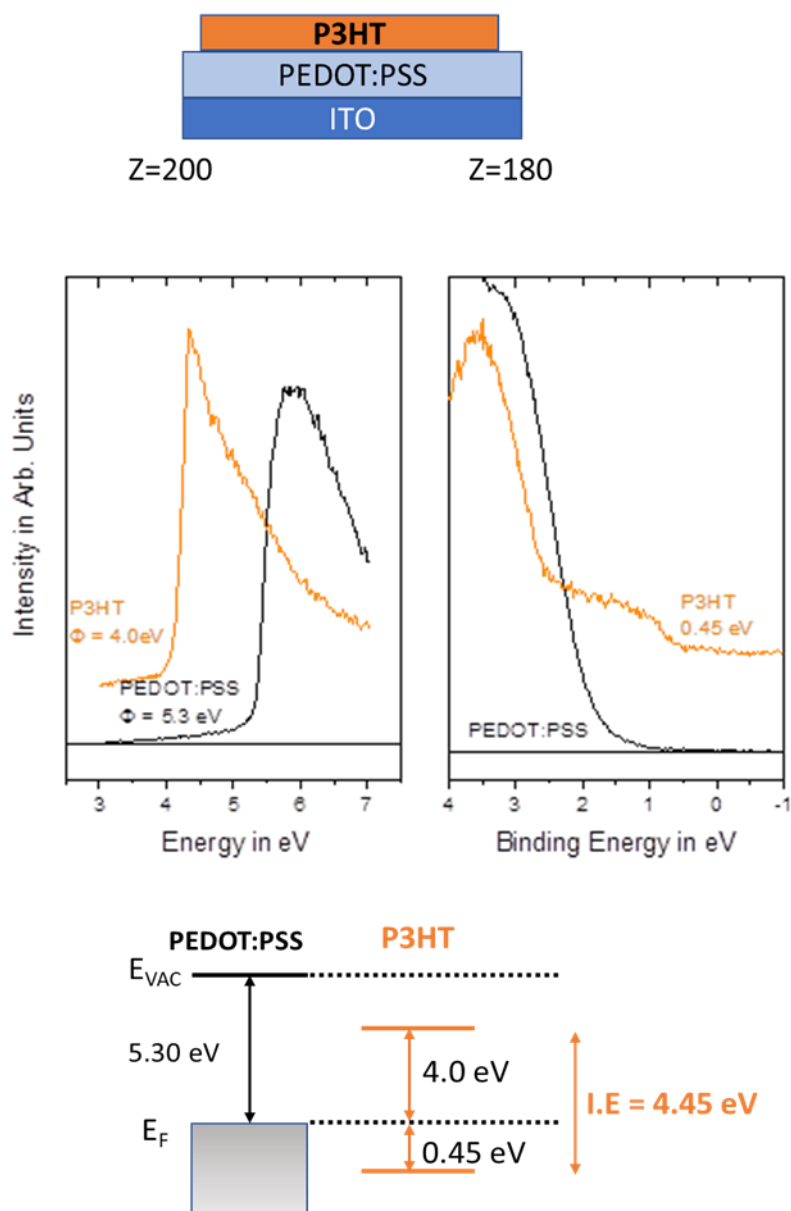
9.2 P3HT/PEDOT interface

Figure S5.21 Photoemission investigation of the P3HT/PEDOT:PSS reference substrate.

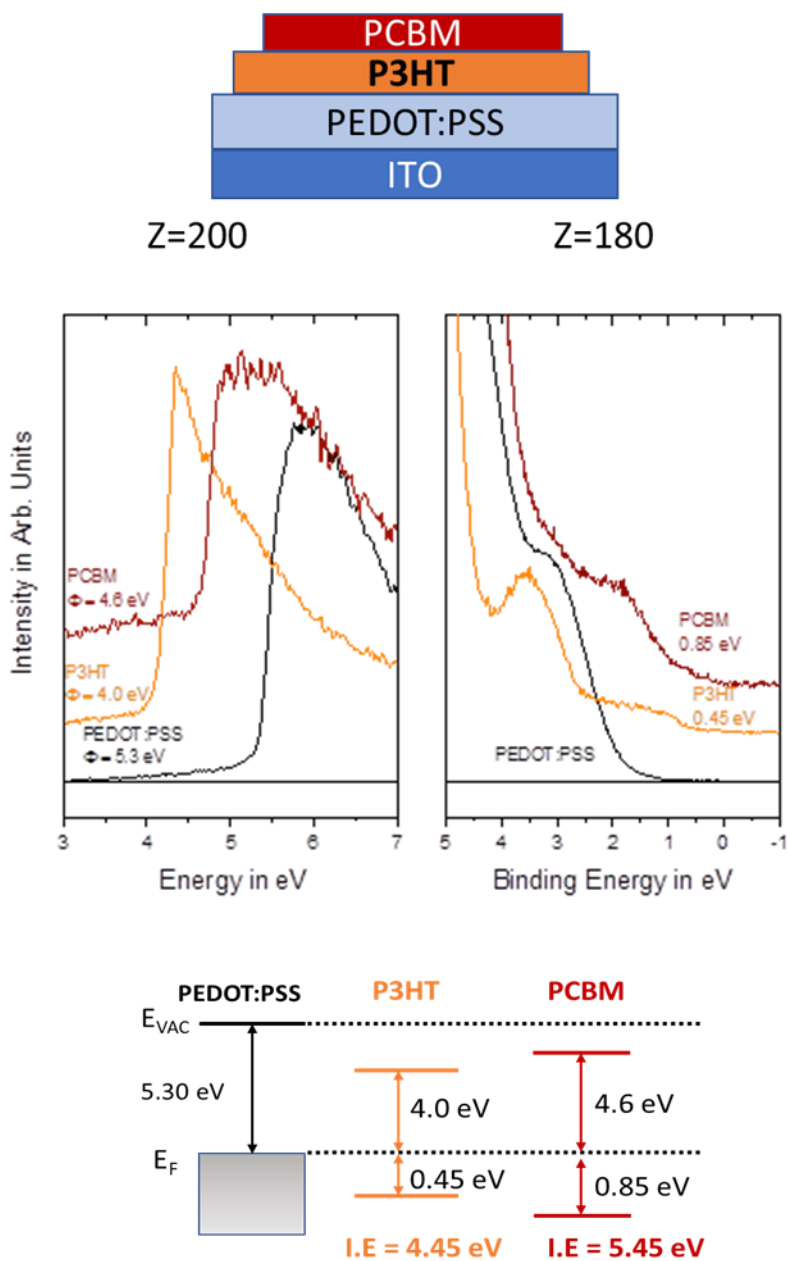## 9.3 P3HT/PCBM interface – reference device

Figure S5.22 Photoemission investigation of the P3HT/PCBM reference interface on PEDOT:PSS,

10. AFM imaging of bulk heterojunctions and Fast fourier transform for grain size calculations
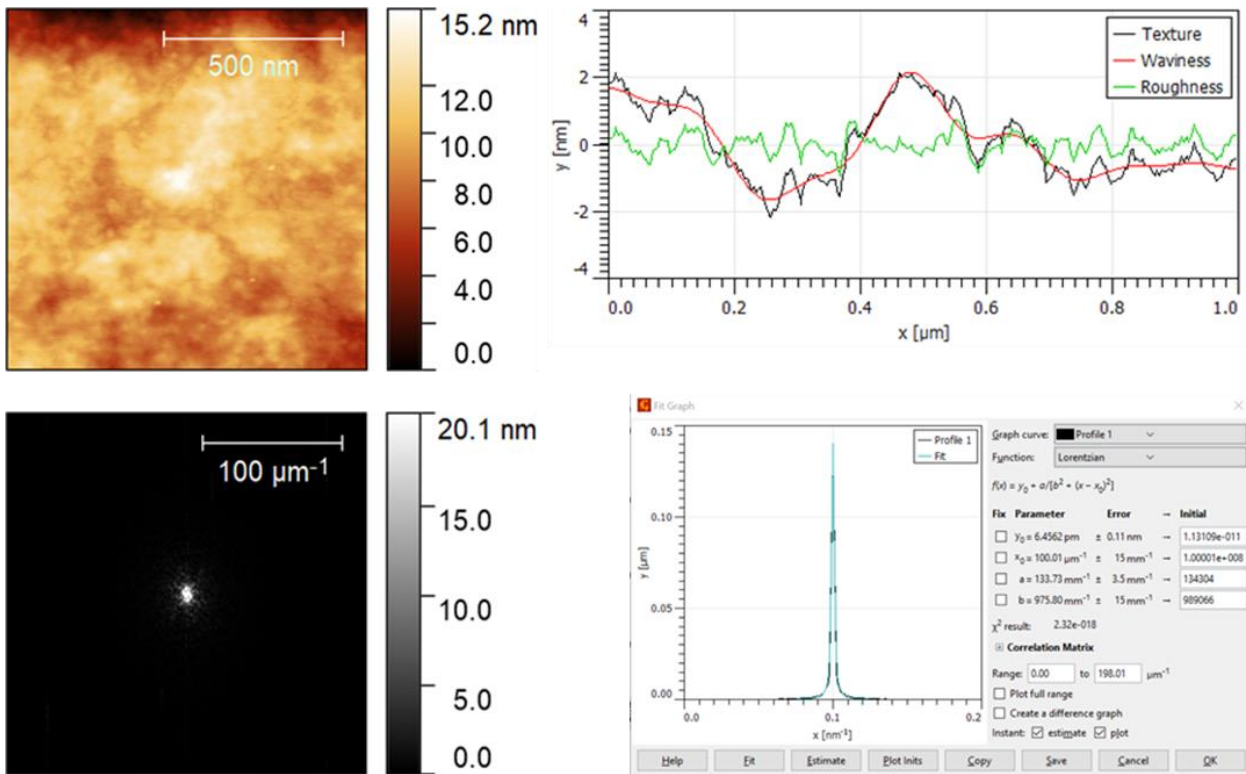
10.1 P3HT-PCBM

Figure S5.23 AFM image of P3HT-PCBM bulk heterojunction film, the corresponding roughness profile and the fast Fourier transformation for grain size calculations.

Figure S5.24 AFM image of P3HT-ZnTCPP-PCBM bulk heterojunction film, the corresponding roughness profile and the fast Fourier transformation for grain size calculations.
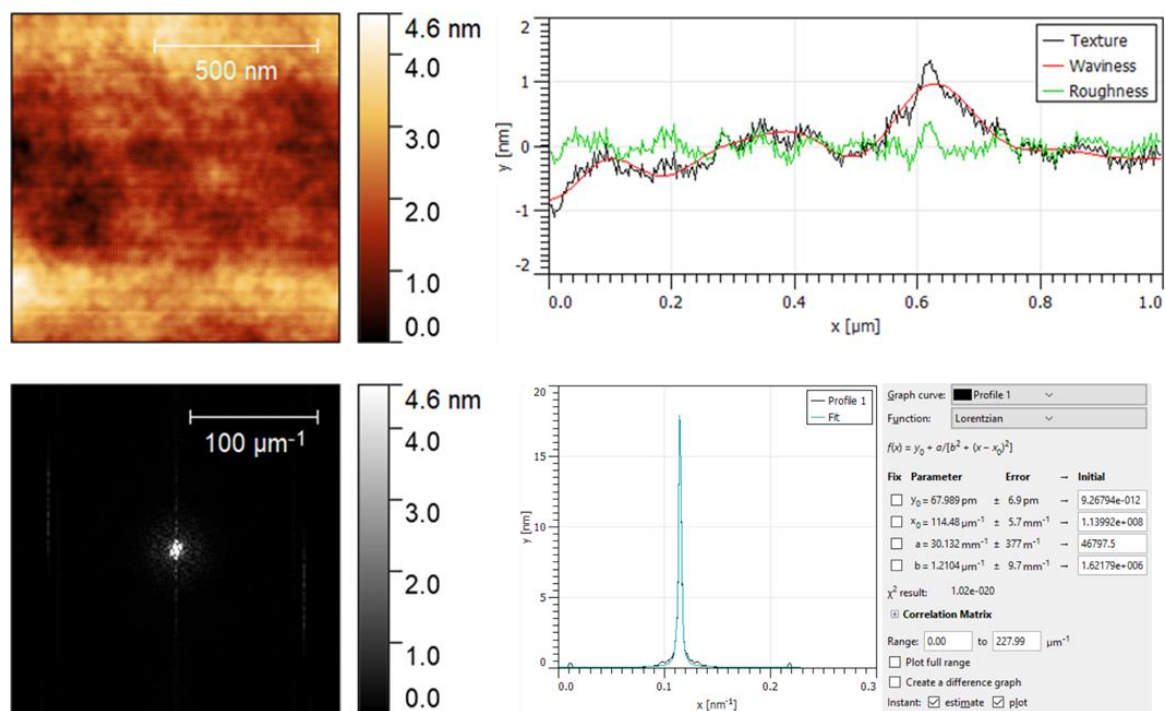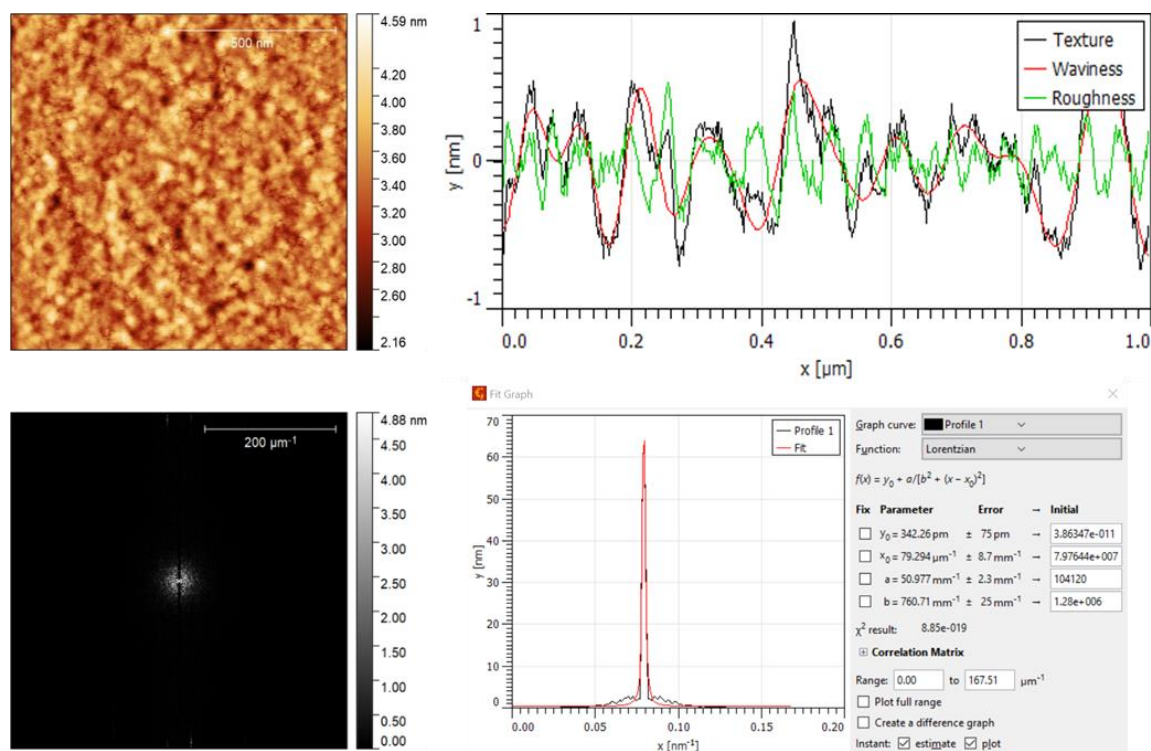
Figure S5.25 AFM image of P3HT-CuTCPP-PCBM bulk heterojunction film, the corresponding roughness profile and the fast Fourier transformation for grain size calculations.

10.4 P3HT-CuZnTPyP-PCBM
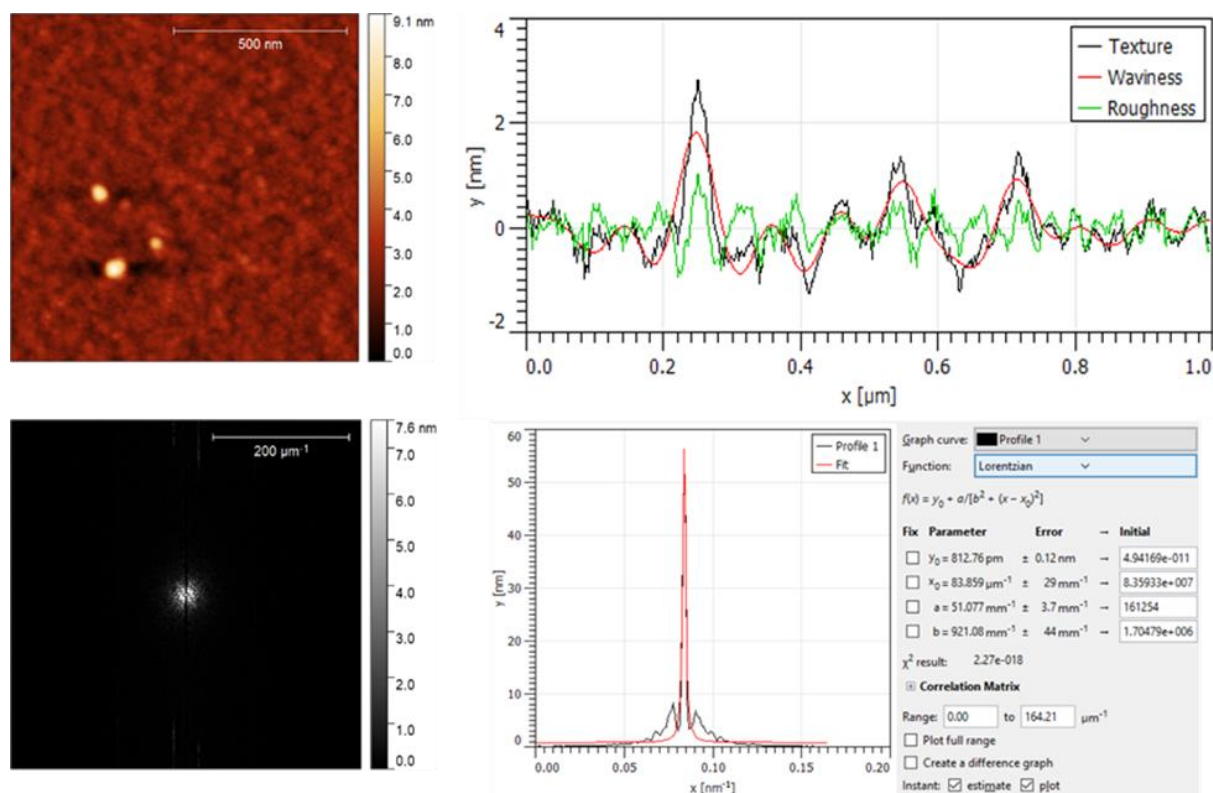
Figure S5.26 AFM images of P3HT-CuZnTPyP-PCBM bulk heterojunction, the corresponding roughness profile and the fast Fourier transformation calculations.

Table S5.7 Summary of the grain size calculations

Device active layer	FFT – Inverse space value	Calculated grain size
P3HT-PCBM	100 μm^{-1}	10nm
P3HT-ZnTCPP-PCBM	115 μm^{-1}	8.7nm
P3HT-CuTCPP-PCBM	21.09 μm^{-1}	47.4nm
P3HT-CuZnTPyP-PCBM	48.9 μm^{-1}	20.4nm

Chapter 6

Metal-Organic Framework Nanosheets as Templates to Enhance Performance in Semi-Crystalline Organic Photovoltaic Cells

Kezia Sasitharan [a], Rachel Kilbride[b], Emma Spooner [b], Jenny Clark [b], Ahmed Iraqi [a], David G. Lidzey [b] and Jonathan A. Foster *[a]

[a]Department of Chemistry, The University of Sheffield, Dainton Building, Brook Hill, S3 7HF, Sheffield, UK.
[b]Department of Physics and Astronomy, The University of Sheffield, Hicks Building, Hounsfield Road, S3 7RH, Sheffield, UK

Graphical abstract
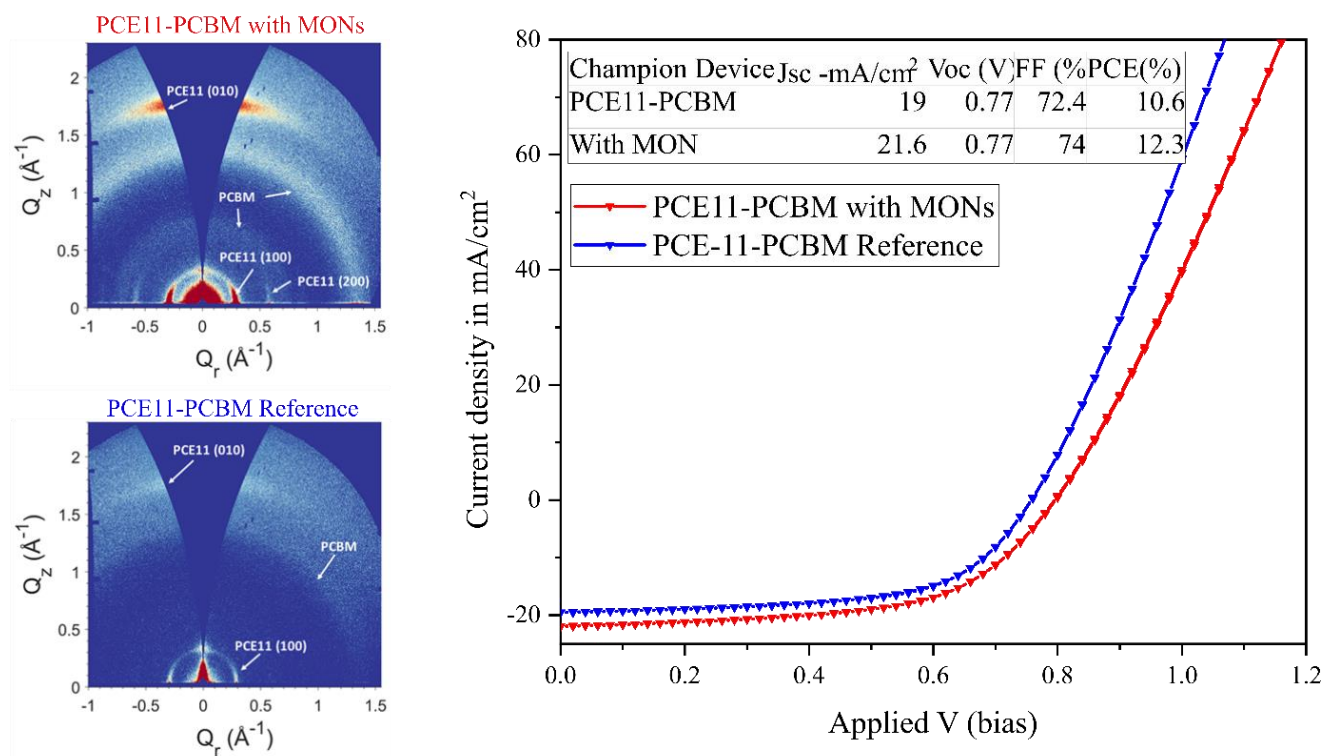
Author contributions

Kezia Sasitharan   Synthesized and characterised the MONs, prepared the photovoltaic devices and carried out the relevant analyses, prepared the samples for GI-WAXS measurement, analysed the experimental results and drafted the manuscript.

Rachel Kilbride   Collected the GIWAXS data and helped with data discussion.

Emma Spooner   Assisted with EQE measurements and data discussion.

Jenny Clark   Aided with data discussion.

Ahmed Iraqi   Aided with data discussion.

David G. Lidzey   Aided with data discussion.

Jonathan A. Foster   Supervised the project, aided with data discussion and drafting of the manuscript.

6.1 Publication main text

Abstract

We demonstrate that the inclusion of metal-organic framework nanosheets (MONs), in the preparation of bulk heterojunction organic photovoltaics (OPVs) increases its performance. The power conversion efficiency of devices based on the polymer PffBT4T-2OD were shown to increase from 10.6% to 12.3% with the incorporation of MONs into the active layer. Detailed studies revealed that the presence of the nanosheets resulted in a higher fraction of face-on oriented polymer crystals in the films. The improved bulk-heterojunction morphology is correlated with an increased fill-factor and improvements in current density. This effect was found to be generalizable to devices based on other semi-crystalline polymers including P3HT-PCBM, P3HT-ICBA, but was not observed for amorphous polymers such as PCDTBT. PTB7-Th and fully crystalline PBDB-T. Our results not only demonstrate the potential of MONs as additives within OPVs but also provide important scientific insights that will facilitate further improvement in the morphology and performance of organic solar cells and other electronic devices.

Introduction

Organic photovoltaics (OPVs) are a promising technology for conversion of solar energy to electricity with the added advantage of large area fabrication, low toxicity, and faster energy payback time.[1–4] The photoactive layers in a bulk heterojunction OPV device typically consist of an electron donating polymer and an electron accepting molecule, finely mixed at the nanoscale level.[5–7] In recent years, a new series of high-performing donor polymers were discovered with strong temperature-dependant aggregation (TDA) properties.[8] These semi-crystalline polymers are fully disordered (disaggregated) at elevated temperatures, but upon cooling form highly ordered aggregates. This polymer family has enabled various high-performance devices that form well-controlled and near optimal blend morphologies. The crystallinity and favoured photoactive layer morphology of these polymer based systems are easily tunable via methods such as solution optimisation, annealing, solvent additives etc.[8–11] These TDA based polymers have also been explored in ternary (multicomponent) OPVs with their low band gaps offering extended light absorption in the near IR region, cascaded energy level alignment, improved nanoscale morphology, improved charge mobility and stability. This field has progressed rapidly over the last 5 years with improved donor polymers such as PCE12, PCE14 and novel non-fullerene acceptors such as ITIC, Y6.[2,12–17] The preparation of better

hole transport materials and the use of tandem architectures have pushed the record for OPV performance to >18% as of 2020, making this an increasingly competitive field.[18,19]

Metal-organic framework nanosheets (MONs) are graphene-like two-dimensional materials, composed of organic linkers coordinated to metal-ions or clusters.[20–22] These materials combine the high surface areas and nanoscopic dimensions of two-dimensional materials with opto-electronic tunability that arises out of their modular structure. These properties have enabled promising progress in the use of MONs in separation, catalysis, sensing and most recently in electronic devices.[21–25] The band gap tunability of MONs has allowed for their incorporation into a number of electronic devices including OLEDs and OPVs as electron extraction layers, electron donors and buffer layers.[26–29] Recently, A.K.Y Jen and co-workers demonstrated the use of MONs as an electron extraction layer at the perovskite/cathode interface leading to a 22.02% efficient perovskite solar cell.[30] The short span of time in which MONs have developed and enabled major breakthroughs in different kinds of photovoltaic devices is remarkable.

We recently reported the first example showing incorporation of MONs into the photoactive layer of OPV bulk heterojunctions.[31] Porphyrin MONs were added to the archetypal P3HT-PCBM architecture through a simple spin-coating method to create a ternary blend solar cell. Remarkably, the addition of MONs resulted in a near doubling in device power conversion efficiency from 2.7% to 5.2%.[31] Detailed investigations into the morphology of the active layer using AFM, wide angle X-ray and dark injection measurements showed that the relative proportion of crystalline regions in the thin films is improved upon incorporation of MONs. Thus, MONs act as templates to increase the crystallinity of the otherwise semi-crystalline polymer P3HT leading to more balanced charge mobility and improved device performance metrics.

Encouraged by this remarkable improvement in performance we sought to investigate the effect of adding MONs to the active layer of other OPV devices to better understand the mechanism and create higher performing devices. We investigated a range of other devices to understand the effect of MONs in the presence of different fullerene acceptors, semi-crystalline, crystalline and amorphous polymers. In the process, we created what to our knowledge are the highest performing fullerene-based device reported in the literature. We then undertook detailed analysis of this system to understand the mechanism behind performance enhancement. A comparison of these findings with our previous report on the P3HT-MON-PCBM system

confirms that MONs can act as templates for enhanced crystallization of the polymer chains leading to improved light absorption, charge transport and solar cell performance.
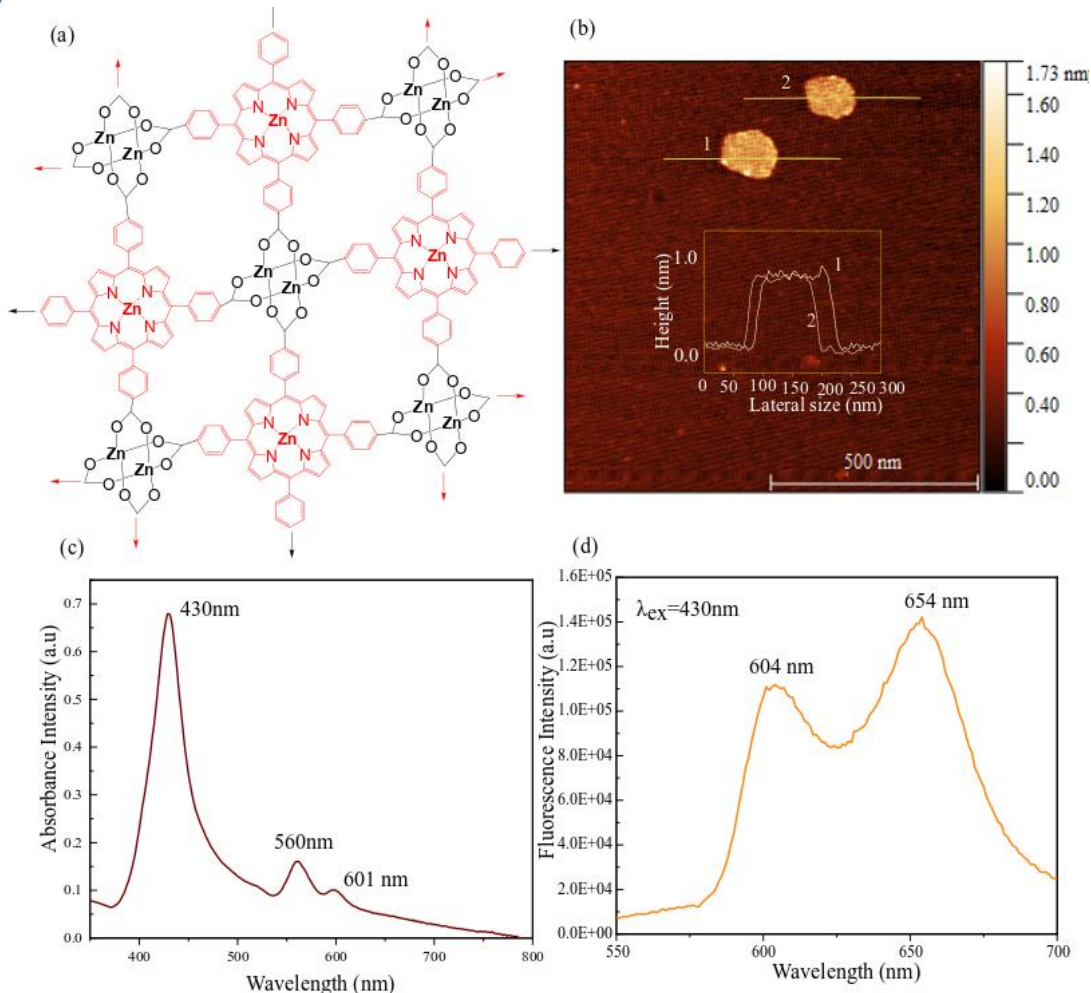
Results
Synthesis of MONs

Figure 6.1. (A) Structure of the MONs used in this study with one TCPP linker connected to four paddlewheel units and forming an extended structure, (b)AFM image of the monolayer nanosheets (inset: the height profile of the MONs); (c) Solution-state absorption spectra for a 25µM suspension of MONs in ethanol; (d) Solution state fluorescence spectra of MONs in ethanol with an excitation wavelength of 430nm.

Zn_2(ZnTCPP) bulk MOF was synthesised by the solvothermal reaction of tetrakis(4-carboxyphenyl) porphyrin (TCPP) and zinc nitrate in ethanol: DMF (3:1). TCPP is known to have a high degree of connectivity and pre-organisation, and in this structure is connected by zinc paddlewheel clusters as inorganic secondary building units.[31] The layered MOF was suspended in the solvent, sonicated in an ultrasonic bath to aid exfoliation of the MONs. The resultant MONs were centrifuged at 1500 rpm for 10 minutes to remove any unexfoliated larger particles. The final solutions was predominantly monolayer Zn_2(ZnTCPP) MONs suspended

in the solvent of choice. **Figure 6.1a** shows a structure of the MONs, showing each TCPP ligand to be connected to four paddlewheel units to form an extended structure. The MON suspensions were collected, and a known amount was drop cast onto pre-heated mica substrates for AFM imaging. **Figure 6.1b** shows a representative AFM image with the height profile of the predominantly monolayer MONs shown in the inset. The MONs, being constructed out of porphyrin units, exhibit ideal absorption properties with bands at 435nm, 564nm and 601nm. **Figure 6.1c** shows the solution state absorption spectra for a 25 µM suspension of MONs in ethanol and **Figure 6.1d** shows the fluorescence emission spectra obtained at an excitation wavelength of 430 nm. The two emission bands characteristic of the Zn-TCPP system at 604 nm and 654 nm are observed. These optoelectronic results demonstrate that the porphyrin based MONs absorb in the range of wavelength that overlaps well with the visible region of the solar spectrum and they absorb complementarily to some of the most commonly employed OPV polymers making them ideal ternary components.

OPV device fabrication

For this work, 20 batches of exfoliated MONs (5mg/mL) in ethanol were aggregated, the solvent evaporated and stored until needed. A weighed amount of MON was then re-suspended in chlorobenzene and sonicated for 10minutes before the preparation of the ternary solutions, for screening the various polymer-fullerene combinations studied in this work. The devices in this work have an inverted configuration and the different layers are in the order ITO:ZnO:Active layer:MoO$_3$:Ag. To test the photovoltaic properties, JV curves were recorded while the devices were illuminated using a Newport AM 1.5 solar simulator calibrated against an NREL standard silicon solar cell. In all cases, an aperture mask was placed on top of the device to ensure the light exposed area of the device was limited to 2.6 mm^2. The supporting information lists the device preparation and the optimization of the percentage by weight loading of MONs in each type of active layer.

The following polymers were chosen for investigation in this study due to their different degrees of crystallinity: poly(3-hexylthiophene) (**P3HT**), poly[N-9″-hepta-decanyl-2,7-carbazole-*alt*-5,5-(4′,7′-di-2-thienyl-2′,1′,3′-benzothiadiazole)] (**PCDTBT)**, poly[4,8-bis(5-(2-ethylhexyl)thiophen-2-yl)benzo[1,2-b;4,5-b′]dithiophene-2,6-diyl-alt-(4-(2-ethylhexyl)-3-fluorothieno[3,4-b]thiophene-)-2-carboxylate-2-6-diyl] (**PBT7-Th**), poly[(2,6-(4,8-bis(5-(2-ethylhexyl)thiophen-2-yl)benzo[1,2-b:4,5-b′]dithiophene)-*co*-(1,3-di(5-thiophene-2-yl)-5,7-bis(2-ethylhexyl)benzo[1,2-c:4,5-c′]dithiophene-4,8-dione)] (**PBDB-T)** and poly[(5,6-difluoro-2,1,3-benzothiadiazol-4,7-diyl)-alt-(3,3‴-di(2-octyldodecyl)-2,2′;5′,2″;5″,2‴-

quaterthiophen-5,5‴-diyl)] (**PffBT4T-2OD**). PffBT4T-2OD will be hereafter referred to as **PCE-11**, its commercial name.

Table 6.1 The OPV performance results from the champion (best-performing) devices for each polymer-MON-fullerene inverted configuration, compared to the reference devices without the MONs.

Device configuration	Jsc (-mA/cm^2)	Voc (V)	FF (%)	PCE (%)
P3HT-ICBA	6.23	0.87	56.06	3.04
P3HT-MON-ICBA	12.0	0.85	60	6.12
PCDTBT-PCBM	9.07	0.89	67.31	5.44
PCDTBT-MON-PCBM	9.54	0.89	66.32	5.63
PTB7-Th-PCBM	13.08	0.83	56	6.1
PTB7Th-MON-PCBM	13.32	0.84	58.9	6.59
PBDBT-PCBM	12.5	0.89	63.67	7.08
PBDBT-MON-PCBM	13.7	0.89	64.1	7.8
PCE11-PCBM	19	0.77	72.4	10.6
PCE11-MON-PCBM	21.6	0.77	74	12.3

P3HT is the prototypical semicrystalline polymer. **PCDTBT** is a representative amorphous bulk heterojunction system with a bilayer lamellar arrangement.[32] **PTB7-Th** polymer is a donor-acceptor type system reported as consisting of amorphous phases intermixed in largely disordered aggregates.[33] **PBDB-T** is one of the highest performing donor polymers with a rigid and planar backbone and forms large crystalline/highly ordered aggregates when cast as films.[34] PffBT4T-2OD (hereafter referred to as **PCE-11**, its commercial name) exhibits temperature dependant aggregation behaviour with the ability to be engineered into highly crystalline domains.[35] The polymers were combined with different fullerene acceptors (PCBM, ICBA), to form BHJ devices. Ternary blends with between 10% and 20% of MONs were produced by adding the MONs to the mixture prior to spin coating. The performance of each device was optimised as described in the ESI. Key metrics for the "champion" devices with and without MONs are detailed in table 6.1. In the following discussion we focus on relating the crystallinity of the polymers to the device performance.

P3HT is the prototypical semicrystalline polymer. Building on our previous studies on P3HT-MON-PCBM system,[31] **P3HT-ICBA** devices incorporating an improved fullerene acceptor were investigated. Incorporation of 20% by weight of MONs into the active layer of these devices resulted in a near doubling of PCE from 3.04% to 6.10% (**Figure 6.2a**). Underlying the improvement in PCE is an increase in the Jsc of the devices with MONs by 6 mA/cm^2 an improvement in the fill factor by about 4% compared to those without whilst the Voc remains unaffected. Analysis of the absorption spectra of the films (**Figure 6.2b**) showed there is an enhancement of the absorption coefficient in the P3HT region with well-pronounced peaks corresponding to the crystalline regions of P3HT. This matches our previous detailed observation in P3HT-PCBM films (although the device architecture was conventional in the previous study, whereas inverted in the present study) and shows that the templating effect of MONs on P3HT is generalizable irrespective of the type of fullerene acceptor or device architecture being used.

PCDTBT is a representative amorphous bulk heterojunction system with a bilayer lamellar arrangement.[32] In contrast to the P3HT-PCBM and P3HT-ICBA results, no pronounced enhancement in PCE was observed upon incorporation of MONs into amorphous **PCDTBT-PCBM** devices. The concentration of MONs was evaluated at weight % loadings of 5, 10 and 15. At above 15%, the devices have not been studied because at these concentrations, the ~90nm thin films became increasingly rougher and uneven. But up to 15% by weight addition of MONs, we find that the Jsc increases marginally up to 0.5mA/cm^2. (**Figure 6.2c**). This is a
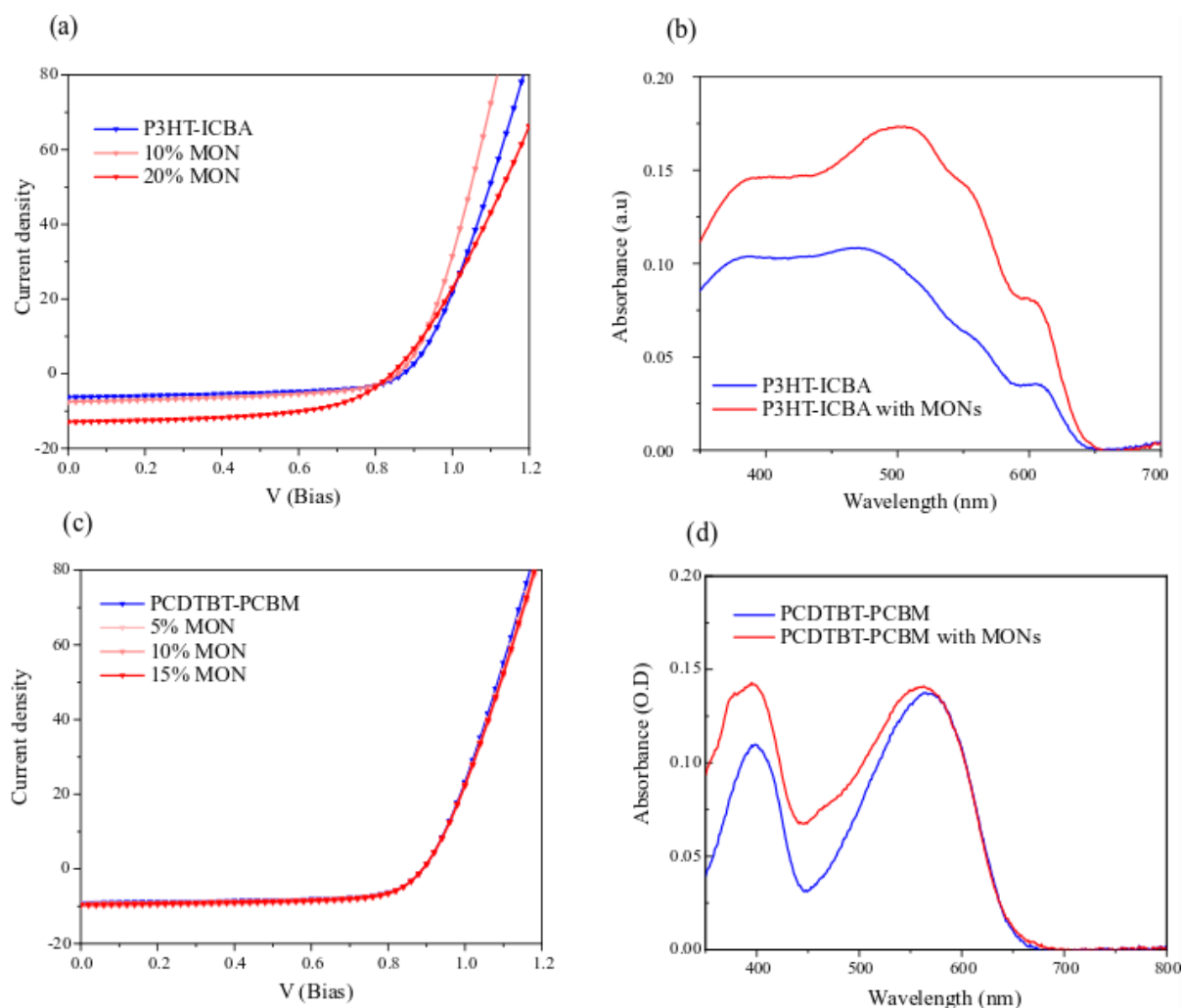

Figure 6.2.(a) Comparison of J-V curve of P3HT-ICBA with and without the addition of MONs; and (b) the corresponding thin-film absorption spectra; (c) Comparison of J-V curves of the PCDTBT-PCBM devices with and without the MONs; (d) and the corresponding absorption spectra.

very nominal rise and can be attributed to additional absorbance from the porphyrin units. The Voc remains unchanged. The FF decreased by 1% and the overall PCE of the device remains at 5%. On comparing the absorption spectra of the films with and without MONs (**Figure 6.2d**), the optical density was found to increase slightly in the wavelength range 400-550 nm, which matches the absorption profile of the porphyrin units in the MON structure. We infer that the

amorphous nature of the polymer means that the increase in the fraction of crystalline material observed in semi-crystalline systems cannot occur so no corresponding increase in performance is observed. Interestingly, PCDTBT has been reported to show a limited short range order due to π-π stacking between polymers normal to the plane of the substrate.[32] However, as outlined later in this paper, templating is expected to take place by ordering polymer chains perpendicular to the nanosheets which is not likely to be applicable in this case.

PTB7-Th polymer is a donor-acceptor type system reported as consisting of amorphous phases intermixed in largely disordered aggregates.[33] Amorphous **PTB7-Th-PCBM** devices show marginal, but not statistically significant, improvements to the device PCE upon incorporation of MONs (**Figure 6.3a**). At 5% weight loading of MONs in PTB7-Th: PCBM devices, the Jsc and FF improve by 0.3mA/cm^2 and ~3% respectively, whilst the Voc remains unchanged leading to an increase in PCE from 6% to 6.5%. The absorption spectra for the devices with MONs (**Figure 6.3b**) show a slight increase in the wavelength region 400-750 nm. Since the porphyrins only absorb till 550nm, it is unclear whether the increased absorbance in the longer wavelength region arises from thickness effects in the film or from changes to film crystallinity. A few previous literature reports have shown this class of polymers can occasionally result in improved aggregation features when combined with highly crystalline small molecules and other additives.[8,33,36–45] However, morphological and chain packing
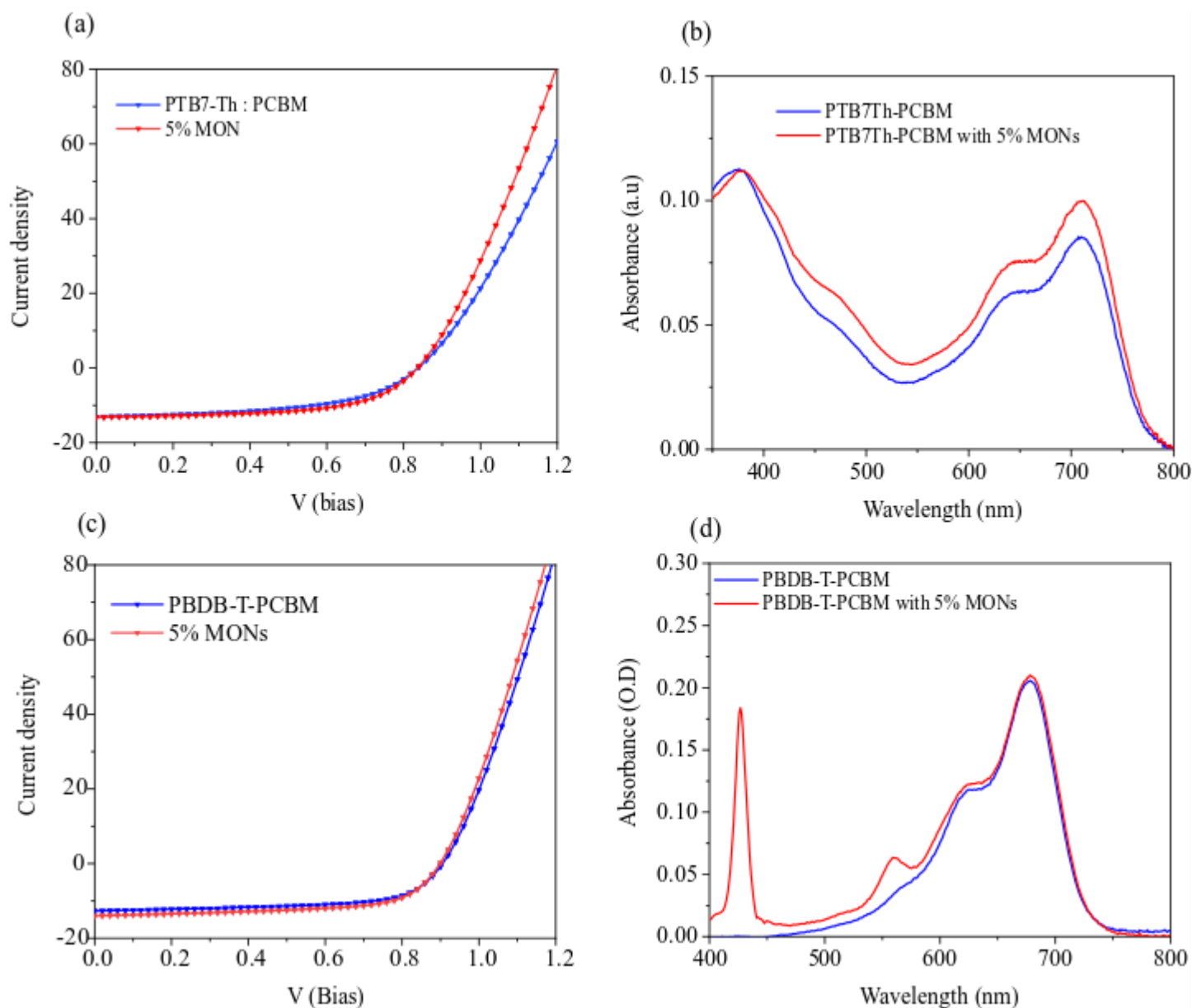
Figure 6.3.(a) J-V curves of the PtB7-Th-PCBM device with and without MONs; (b) Absorption spectra of thin-films of PTB7-Th-PCBM and PTB7-Th-MON-PCBM; (c) J-V curves of PBDB-T-PCBM with and without MONs;

studies on these polymers support the existence of a major fraction of amorphous regions in the photoactive layer with very short correlation lengths, similar to PCDTBT.[33,46,4739] We therefore conclude that the MONs templating effect is not significant in this system and the small improvements observed are due to increased absorption by the nanosheets.

Predominantly crystalline **PBDB-T:PCBM** devices showed an increase in PCE from 7.1% to 7.8% upon incorporation of a 5 wt% loading of MONs (**Figure 6.3c**). There is an underlying increase in Jsc by 1mA/cm^2 and FF by 1% with no change in Voc. This polymer does not absorb in the porphyrin absorption region, hence the contribution from the S-band of

MON in the absorption spectra at 430nm can be clearly seen (**Figure 6.3d**). The Q-absorption band of porphyrins at 564nm can also be seen here, contributing to an increase in absorbance intensity. These findings explain the 1mA/cm^2 increase in Jsc, the second highest increase (after P3HT) among the polymers investigated so far. Being highly crystalline in nature, it is unclear whether any further improvements can, or need be made to the morphology of this polymer system. Therefore, in this case the contribution of MONs is only to raise the absorbance in the <500nm spectral region.
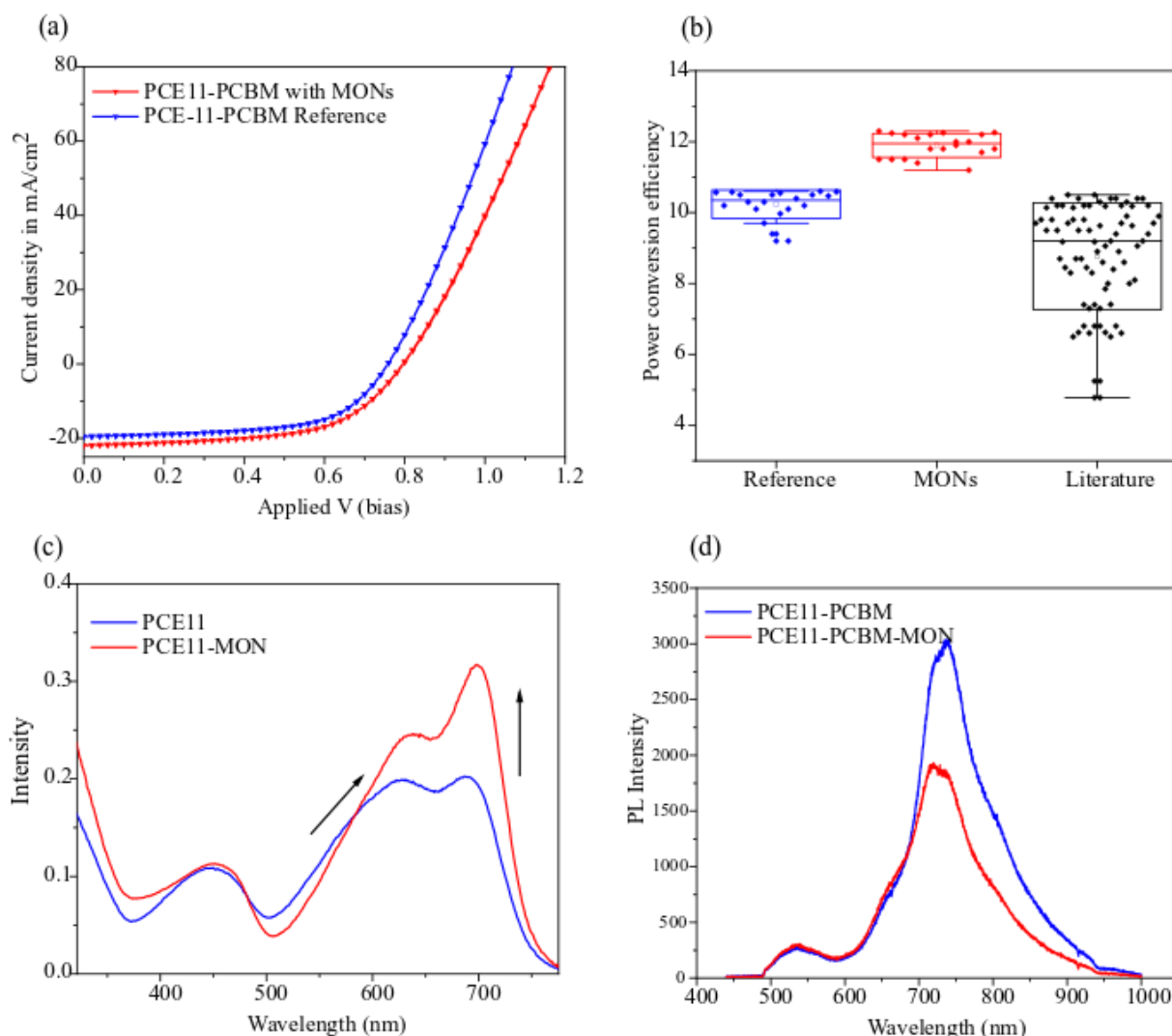

Figure 6.4. (a) J-V curve of the PCE11-PCBM and PCE11-MON-PCBM devices, (b) Box plots showing the distribution of the PCEs obtained from the 20 reference and 20 MON based devices that were prepared in this study to check the statistical significance of the obtained results and performance enhancement; (c) Absorbance spectra of thin-films of PCE-11 and PCE-11-MON (20% by weight loading); (d) Photoluminescence spectra of the PCE-PCBM and PCE-11-MON-PCBM films.

Semi-crystalline **PCE11-PCBM** devices showed a remarkable increase in performance parameters upon incorporation of MONs with a PCE of 12.3% for the champion device as compared to 10.60% for the reference device (**Figure 6.4a**). The Jsc increased by 3 mA/cm^2,

the fill factor increased by 2% and the Voc remained unaffected within the error range. At 12.3% this device is the best performing fullerene-based device reported in the literature to date. This system was therefore chosen to study the mechanism of performance enhancement in detail. **Figure 6.4b** shows the statistical analysis of the PCE (%) obtained from 20 reference devices and 20 MON based devices prepared in this work. This enables us to be confident that the performance enhancement observed is not a one-off effect but is consistent and reproducible. We have also analysed the works in literature (**Figure 6.4b**) that have reported OPV devices based on this PCE-11 polymer to test the significance of this enhancement that MONs have brought about. Table S6.1, supplementary information lists the literature values, references, and the methodology used for the literature search. Upon comparing with the results from 47 literature reports, we found that our MON incorporated PCE-11-PCBM devices with a mean PCE of 11.90±0.34% are the highest reported so far for this class of polymer, and also our champion device at 12.30% is the best fullerene based OPV reported so far, to the best of our knowledge.

Optoelectronic characterisations

The thin film optoelectronic electronic characterisations offer key insights into light absorption and exciton generation in the photoactive layer. A comparison of the thin-film absorption spectra of the pristine polymer with that of a polymer-MON blend provided useful information about the light absorbing units in the films and modifications to the polymer chain ordering brought about by the MONs (**Figure 6.4c**). The polymer PCE-11 has a characteristic absorption spectrum with bands at 450 nm, 560nm and 700nm. With the addition of MONs, we observe that the vibronic peak at 560 nm, is red shifted accompanied by an increase in intensity at 700 nm. These findings correspond to aggregation of the polymer chains. This is the first evidence of possible role of MONs in enhancing the crystallinity of the polymer by acting as templates, similar to the role played by the MONs in our P3HT-PCBM devices. Photoluminescence (PL) quenching measurements are useful to understand the charge generation processes and to confirm the exciton dissociation process in the solar cells. PL quenching is a simple technique to quantify the efficiency of exciton dissociation as it probes the charge transfer at the donor-acceptor interface. The occurrence of charge transfer between PCE-11 and PCBM is already known.[48,49] Hence, here we compared the PL signals (thickness correction applied) obtained from the PCE-11-PCBM thin films before and after incorporation of MONs (**Figure 6.4d**). Thus, by keeping the other components – polymer and fullerene constant, we were able to quantify the effect in exciton dissociation that is contributed by the MONs in our OPVs. By

integrating the area under the curve, we found that the MON containing films exhibit a higher PL quenching efficiency by 42% as compared to the pristine films without MONs. It is therefore apparent that with the addition of MONs, exciton dissociation is better. These changes in the absorption and PL spectra of the polymer-PCBM blend with the addition of MONs explains the improved Jsc and FF values observed.

Morphological role of MONs – GIWAXS studies

In order to investigate how the incorporation of MONs affects the molecular packing of the polymer chains in the blends we employ grazing incidence wide angle X-ray scattering (GI-WAXS) studies. It is important to note that semi-crystalline polymers typically organise into lamellar crystalline domains, having a face-to-face π-π stacking between backbones and lamellar stacking through the side chains. To probe the packing arrangement in our systems we compared the patterns obtained from PCE11: PCBM reference device films and the PCE11:MON:PCBM device films. The corresponding two-dimensional patterns of the blend films are shown in **Figure 6.5a-b** , and the out of plane and in-plane one-dimensional GIWAXS profiles are depicted in **Figure 6.5c-d**. (For further information, please look at **Figures S6.5 to S6.12, supplementary information**). The reference PCE11: PCBM films showed well-defined lamellar peaks (100) of the polymer at 0.29 Å^{-1} and a weak π-π stacking peak at 1.80 Å^{-1}. The PCBM ring is visible at 1.4 Å^{-1}. With the addition of MONs, the PCE11: MON: PCBM films show all the in-plane stacking peaks as observed in the pristine polymer and PCBM films with no shifts in position. This indicates that the donor polymer and acceptor fullerene maintain their molecular structure in the ternary blend even upon the incorporation of MON. However, an additional second order polymer peak corresponding to 200 lamellar stacking is visible at 0.585 Angstrom^{-1}. There is also an additional PCBM peak observed at 0.64 Angstroms^{-1}. PCBM is largely found to be amorphous with short range isotropic structural order, as expected. The increase in intensity of the (100) polymer peak and appearance of the (200) peak indicate an increase in long range molecular order of the polymer PCE-11 upon incorporation of MONs. Thus, a higher percentage of the polymer is found to be orientated face-on with respect to the substrate with the incorporation of MONs in the films.
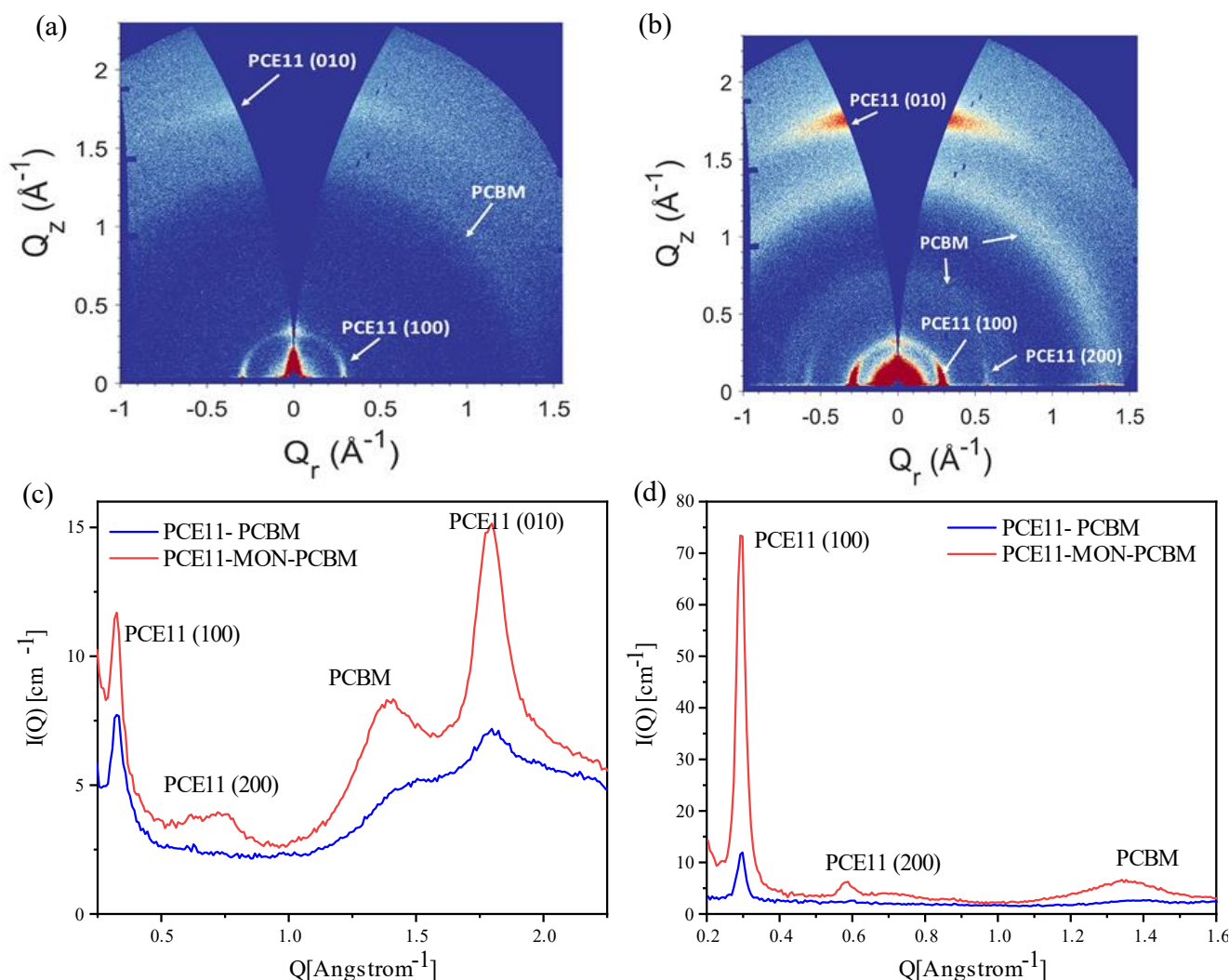
Figure 6.5. (a) GIWAXS investigations on the active layer films: (a) 20D detector image of PCE11-PCBM films; (b) 2D detector image of PCE11-MON-PCBM film; (c) Comparison of the out of plane radial integration and (d) the in-plane radial integration on the PCE-11-PCBM films and PCE-11-MON-PCBM films.

We then evaluated the molecular organisation in the out-of plane direction and found the 010 peak which is the characteristic peak of π-π stacking shifted from 1.84 Å^{-1} to 1.79 Å^{-1} upon incorporation for MONs in the films. This peak shift corresponds to an increase in the π-π stacking distance. The π-π coherence length (crystal coherence length), which is quantified by the full-width half maximum of the 010 diffraction peak using the Scherrer equation increases from 1.88 nm to 4.57 nm. The coherence length is an indication of paracrystallinity. The increased coherence length indicates an increase in the lattice ordering. This enables the creation of a more ordered charge transport pathway. Therefore, our GI-WAXS results confirm the increase in film crystallinity rationale and the MONs indeed influence the molecular packing into well-ordered domains. There is appearance of an additional PCBM peak observed at 0.64 Å in the MON incorporated films. This indicates that MONs favour the maintenance of

short range isotropic structural order in PCBM. Since the MONs are promoting/templating the crystallization of polymer, this prevents PCBM from forming overgrown aggregates in the film and they retain their short-range order while the polymers crystallize out first. This provides an avenue for stronger phase separation between PCE-11 and PCBM which is desirable for efficient charge transport.

AFM imaging and grain size analysis

We also performed AFM imaging of the reference and MON based device films and observed the formation of homogeneous films which explains the >70% FF in all devices (**Figure 6.6**). A spatial Fourier transform function was applied to extract the grain size from the AFM images. In the reference devices, the length scale was found to be ~32 nm; and upon incorporation of MONs, the length scale is modified to 25 nm. This shows that all films have domains that are within the favourable range for exciton splitting, hence high Jsc values are observed in the devices. The reduced grain sizes in the MON incorporated films is an added evidence for the formation of well-defined charge transport pathways.
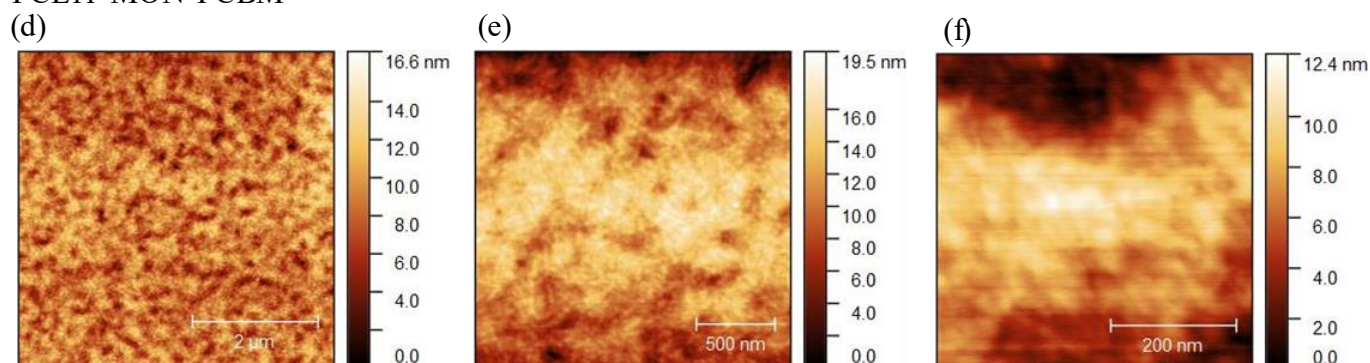
PCE11-PCBM
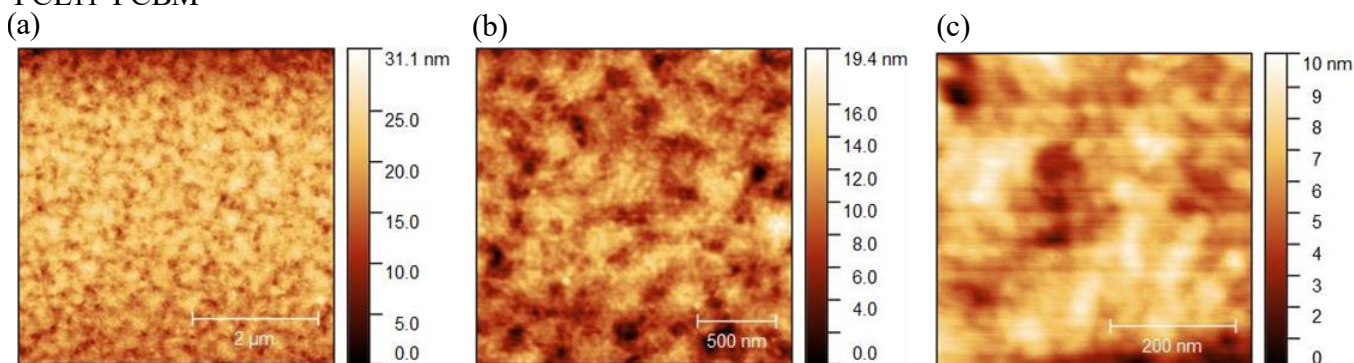
PCE11-MON-PCBM

Figure 6.6. AFM imaging of the films: (a-c) PCE11-PCBM films; (d-f) PCE11-MON-PCBM films

Charge mobility investigations

To quantify the influence of the improved active layer morphology created by MONs on the percolated charge transport pathways, we measured the charge carrier mobility for holes and electrons individually using the space-charge limited current (SCLC) model. Hole-only and electron-only devices were prepared by adjusting the buffer layers and the dark injection curves were fitted to the Mott-Guorney model to measure the charge mobility for holes and electrons in the PCE-11:PCBM and PCE11:MON:PCBM blends. As shown in (Table S6.3, ESI), the hole mobility of PffBT4T-2OD is quite high and is quite well balanced with the electron mobility (~10^{-3} $cm^2V^{-1}s^{-1}$). This explains the observation of >10% efficiency in all devices, including the references. With the incorporation of MONs, there is a slight improvement in both mobilities and the electron and hole mobilities continue to remain well balanced. Thus, the change in the molecular ordering of the donor polymer with the incorporation of MONs affects the formation of percolation pathways for charge transport by improving both the hole and electron mobilities.

Discussion

Nanoscale morphology has been established as one of the controlling factors in the device performance of bulk heterojunction polymer solar cells. Donor polymers, especially the TDA type ones, have been previously shown to change from a disordered to a more ordered conformation due to a variety of reasons such as decreased solution temperature. The morphology of the devices, with small scale interpenetrating domains will allow for an efficient splitting of excitons, but increases the possibility of non-geminate recombination, which could lower the fill factor. Large domains induced by a strong phase separation will reduce non-geminate recombination but cause a less efficient charge carrier generation, which would lower Jsc. Improving the active layer crystallinity is important in OPV devices because of its direct implication in device performance and stability. The ordering of the conjugated polymer units in the films is often correlated with exciton and charge transport properties. Increase in crystallinity of the photoactive films has also been shown to be associated with the overall device stability, as the amorphous regions in the films were found to contain more triplet states leading to device degradation.[35] The material crystallinity is also a key determinant of triplet lifetimes for a broad range of polymer structures. Therefore, development of new materials and additives for tailoring the crystallinity in OPVs is an important development in this field.

In the various solar cell examples that we have incorporated MONs into, we have observed that the nature of the polymer determines the influence of MONs in the performance. In the fully crystalline polymer system PBDB-T which predominantly absorbs in the wavelength range 500-800nm, the contribution towards increased light absorption by MONs, translating into a higher Jsc and PCE is evident. Similarly, in a fully amorphous polymer systems such as PCDTBT, PTB7-Th, there is a contribution from the absorption of the porphyrin units in MONs itself that assists in raising the Jsc by a small value.

Significant performance enhancement is observed only in cases where the nature of the donor polymer is semi-crystalline. This concept was introduced by us in the P3HT-PCBM system (conventional architecture) where MONs lead to an enhancement of power conversion efficiency. In this work we extended this to evaluate the P3HT-ICBA system (inverted architecture) which showed the same doubling effect in PCE leading to 6% devices and the PCE11-PCBM system which showed a record breaking efficiency of 12.3%. These systems exhibit an increase in the absorption coefficient accompanied by a red-shifted absorption spectrum which is related to the packing order of the polymer chains in the films.

We then investigated in detail the role played by MONs within the PCE11-PCBM devices in influencing the molecular packing arrangement of the films when the polymer-MON blends are spin-coated. The GI-WAXS analysis provides evidence for the improved crystallinity in the active layer blends with MONs. Addition of MONs promotes face-on orientation of the PCE-11 chains, resulting in stronger π-π stacking out-of-plane and stronger lamellar stacking in-plane. This is the best orientation for photovoltaic devices because charge transport takes place in perpendicular direction. The PCE-11 peaks from GIWAXS analysis are higher in intensity than the reference devices and second order lamellar peak is visible in the presence of MONs. These observations indicate increased crystallinity and self-organisation of PCE-11 in the presence of MONs.

Scherrer analysis shows that the π-π stacking crystal correlation length of the polymer increases from 1.88 nm to 4.57 nm after the addition of MONs. This is a very favourable change as there are more ordered charge transport pathways within the active layer, leading to reduced non-geminate recombinations and increased Jsc. This adds up to the observed solar cell performance metrics where upon incorporation of MONs the Jsc improves from 19 to ~22 mA/cm^2 whereas the Voc remains constant. The better charge percolation pathways thus introduced improves the hole and electron mobility of the system to some extent. The grain

sizes in the films also decrease marginally and offer better charge transport. PCE-11 is a well-optimised system with very little room for further improvement in terms of charge mobility. However, the molecular packing of the polymer on the substrate is largely dependent on the preparation conditions owing to the poor solubility and temperature dependant agglomeration of the polymer chains. MONs therefore act as templates to promote crystallization and self-organisation of these polymer chains during the spin-coating process leading to a statistically significant improvement in power conversion efficiency.

Conclusions

Here we have demonstrated the generalizability of porphyrin-based MONs as ideal templating candidates for improving the crystallinity in OPV devices leading to the highest performing fullerene based OPV reported so far. Their favourable absorption properties, nanoscopic size dimensions and solution processability enable MONs to be easily integrated into the thin-film photoactive layers in OPVs. We selected and screened a series of OPV polymers ranging in their properties as crystalline, semi-crystalline and amorphous. The fully crystalline and amorphous polymer systems only benefitted from the additional light-absorption of the porphyrin units in MONs, leading to small increases in Jsc value. In contrast, the semi-crystalline polymer systems show remarkable improvements in Jsc, FF and result in higher power conversion efficiency devices. Building on from our previously reported 5.2% MON based P3HT-PCBM device, in this work we demonstrated a 6% PCE in P3HT-ICBA and a 12.3% PCE in PCE11-PCBM devices upon incorporation of MONs. GI-WAXS, AFM and dark injection studies show that the MONs improved the polymer crystallinity, prevent PCBM aggregations, generate longer charge percolation pathways and enable better phase separation between PCE-11 and PCBM leading to the record power conversion efficiency.

These results demonstrate and establish the templating effect of MONs as an applicable concept for improving the performance in semi-crystalline polymer-based devices. With the rise of polymer based non-fullerene acceptors, MONs can be potentially tuned as electron donors for the creation of higher performing fullerene-free OPVs. Facilitation of better ordering and crystallinity are also desirable properties for other applications such as OLEDs and OFETs. Therefore, MONs have established themselves as an important class of 2D materials with the potential to create a new generation of organic electronic devices with improved structural ordering and performance. References

1   K. Leo, *Nat. Rev. Mater.*, 2016, **1**, 16056.

2   L. Duan and A. Uddin, *Advanced Science*, 2020, 7.

3   S. Günes, H. Neugebauer and N. S. Sariciftci, *Chemical Reviews*, 2007, 107, 1324–1338.

4   T. Ameri, P. Khoram, J. Min and C. J. Brabec, *Advanced Materials*, 2013, 25, 4245–4266.

5   F. Yang and S. R. Forrest, *ACS Nano*, 2008, **2**, 1022–1032.

6   A. Wadsworth, M. Moser, A. Marks, M. S. Little, N. Gasparini, C. J. Brabec, D. Baran and I. McCulloch, *Chemical Society Reviews*, 2019, 48, 1596–1625.

7   J. E. Allen and C. T. Black, *ACS Nano*, 2011, **5**, 7986–7991.

8   H. Hu, P. C. Y. Chow, G. Zhang, T. Ma, J. Liu, G. Yang and H. Yan, *Accounts of Chemical Research*, 2017, **50**, 2519–2528.

9   M. Y. Aliouat, D. Ksenzov, S. Escoubas, J. Ackermann, D. Thiaudière, C. Mocuta, M. C. Benoudia, D. Duche, O. Thomas and S. Grigorian, *Materials*, 2020, **13**, 3092.

10   P. Li, Y. Zhang, T. Yu, Q. Zhang, J.-P. Masse, Y. Yang, R. Izquierdo, B. Sun and D. Ma, *Solar RRL*, 2020, **4**, 2000239.

11   D. Baran, T. Kirchartz, S. Wheeler, S. Dimitrov, M. Abdelsamie, J. Gorman, R. S. Ashraf, S. Holliday, A. Wadsworth, N. Gasparini, P. Kaienburg, H. Yan, A. Amassian, C. J. Brabec, J. R. Durrant and I. McCulloch, *Energy and Environmental Science*, 2016, **9**, 3783–3793.

12   Y. Yang, Z. G. Zhang, H. Bin, S. Chen, L. Gao, L. Xue, C. Yang and Y. Li, *Journal of the American Chemical Society*, 2016, **138**, 15011–15018.

13   Y. Lin, J. Wang, Z. G. Zhang, H. Bai, Y. Li, D. Zhu and X. Zhan, *Advanced Materials*, 2015, **27**, 1170–1174.

14   Z. Wang, J. Ji, W. Lin, Y. Yao, K. Zheng and Z. Liang, *Advanced Functional Materials*, , DOI:10.1002/adfm.202001564.

15   L. Perdigón-Toro, H. Zhang, A. Markina, J. Yuan, S. M. Hosseini, C. M. Wolff, G. Zuo, M. Stolterfoht, Y. Zou, F. Gao, D. Andrienko, S. Shoaee and D. Neher, *Advanced Materials*, 2020, **32**, 1906763.

16   J. Wu, J. Lee, Y. C. Chin, H. Yao, H. Cha, J. Luke, J. Hou, J. S. Kim and J. R. Durrant, *Energy and Environmental Science*, 2020, **13**, 2422–2430.

17   L. Zhan, S. Li, T. K. Lau, Y. Cui, X. Lu, M. Shi, C. Z. Li, H. Li, J. Hou and H. Chen, *Energy and Environmental Science*, 2020, **13**, 635–645.

18   yuanbao Lin, Y. Firdaus, F. H. Isikgor, M. I. Nugraha, E. Yengel, G. T. Harrison, R. Hallani, A. El Labban, H. Faber, C. Ma, X. Zheng, A. S. Subbiah, C. T. Howells, O. M. Bakr, I. McCulloch, S. De Wolf, L. Tsetseris and T. D. Anthopoulos, *ACS Energy Letters*, , DOI:10.1021/acsenergylett.0c01421.

19   L. Meng, Y. Zhang, X. Wan, C. Li, X. Zhang, Y. Wang, X. Ke, Z. Xiao, L. Ding, R. Xia, H. L. Yip, Y. Cao and Y. Chen, *Science*, 2018, **361**, 1094–1098.

20   D. J. Ashworth and J. A. Foster, *Journal of Materials Chemistry A*, 2018, **6**, 16292–16307.

21   Y. Zheng, F. Sun, X. Han, J. Xu and X. Bu, *Advanced Optical Materials*, 2020, 2000110.

22   M. Zhao, Y. Huang, Y. Peng, Z. Huang, Q. Ma and H. Zhang, *Chemical Society Reviews*, 2018, **47**, 6267–6295.

23   S. Kim, H. Wang and Y. M. Lee, *Angewandte Chemie International Edition*, , DOI:10.1002/anie.201814349.

24   J. Liu, X. Song, T. Zhang, S. Liu, H. Wen and L. Chen, *Angewandte Chemie - International Edition*, 2020, 2–15.

25   Y. Peng and W. Yang, *Advanced Materials Interfaces*, 2019, **1901514**, 1–30.

26   S. Liu, Y.-C. Wang, C.-M. Chang, T. Yasuda, N. Fukui, H. Maeda, P. Long, K. Nakazato, W.-B. Jian, W. Xie, K. Tsukagoshi and H. Nishihara, *Nanoscale*, 2020, 0–7.

27   W. Xing, P. Ye, J. Lu, X. Wu, Y. Chen, T. Zhu, A. Peng and H. Huang, *Journal of Power Sources*, 2018, **401**, 13–19.

28   C. Liu, C. Wang, H. Wang, T. Wang and J. Jiang, *European Journal of Inorganic Chemistry*, 2019, **2019**, 4815–4819.

29   X. Hu, Z. Wang, B. Lin, C. Zhang, L. Cao, T. Wang, J. Zhang, C. Wang and W. Lin,

Chemistry - A European Journal, 2017, **23**, 8390–8394.

30   S. Wu, Z. Li, M. Li, Y. Diao, F. Lin, T. Liu, J. Zhang, P. Tieu, W. Gao, F. Qi, X. Pan, Z. Xu, Z. Zhu and A. K. Jen, *Nature Nanotechnology*, , DOI:10.1038/s41565-020-0765-7.

31   K. Sasitharan, D. G. Bossanyi, N. Vaenas, A. J. Parnell, J. Clark, A. Iraqi, D. G. Lidzey and J. A. Foster, *Journal of Materials Chemistry A*, 2020, **8**, 6067–6075.

32   N. Blouin, A. Michaud and M. Leclerc, *Advanced Materials*, 2007, **19**, 2295–2300.

33   B. A. Collins, Z. Li, J. R. Tumbleston, E. Gann, C. R. Mcneill and H. Ade, *Advanced Energy Materials*, 2013, **3**, 65–74.

34   W. Zhao, D. Qian, S. Zhang, S. Li, O. Inganäs, F. Gao and J. Hou, *Advanced Materials*, 2016, **28**, 4734–4739.

35   Y. Liu, J. Zhao, Z. Li, C. Mu, W. Ma, H. Hu, K. Jiang, H. Lin, H. Ade and H. Yan, *Nature Communications*, 2014, **5**, 1–8.

36   M. R. Hammond, R. J. Kline, A. A. Herzing, L. J. Richter, D. S. Germack, H. W. Ro, C. L. Soles, D. A. Fischer, T. Xu, L. Yu, M. F. Toney and D. M. Delongchamp, *ACS Nano*, 2011, **5**, 8248–8257.

37   L. Yang, Y. Chen, S. Chen, T. Dong, W. Deng, L. Lv, S. Yang, H. Yan and H. Huang, *Journal of Power Sources*, 2016, **324**, 538–546.

38   B. Ebenhoch, S. A. J. Thomson, K. Genevičius, G. Juška and I. D. W. Samuel, *Organic Electronics*, 2015, **22**, 62–68.

39   C. Wang, E. Gann, A. S. R. Chesman and C. R. McNeill, *AIP Advances*, 2019, **9**, 065024.

40   R. S. Bhatta and M. Tsige, *Polymer*, 2014, **55**, 2667–2672.

41   Z. Wu, C. Sun, S. Dong, X.-F. Jiang, S. Wu, H. Wu, H.-L. Yip, F. Huang and Y. Cao, *Journal of the American Chemical Society*, 2016, **138**, 2004–2013.

42   L. Lu, T. Xu, W. Chen, E. S. Landry and L. Yu, *Nature Photonics*, 2014, **8**, 716–722.

43   T.-Y. Juang, Y.-C. Hsu, B.-H. Jiang and C.-P. Chen, *Macromolecules (Washington, DC, United States)*, 2016, **49**, 7837–7843.

44   W. Li, Y. Yan, Y. Gong, J. Cai, F. Cai, R. S. Gurney, D. Liu, A. J. Pearson, D. G. Lidzey and T. Wang, *Advanced Functional Materials*, 2018, **28**, n/a.

45   F. Zhao, Y. Li, Z. Wang, Y. Yang, Z. Wang, G. He, J. Zhang, L. Jiang, T. Wang, Z. Wei, W. Ma, B. Li, A. Xia, Y. Li and C. Wang, *Advanced Energy Materials*, 2017, **7**, n/a.

46   J. Zhang, Y. Zhang, J. Fang, K. Lu, Z. Wang, W. Ma and Z. Wei, *Journal of the American Chemical Society*, 2015, **137**, 8176–8183.

47   Z. M. Beiley, E. T. Hoke, R. Noriega, J. Dacuña, G. F. Burkhard, J. A. Bartelt, A. Salleo, M. F. Toney and M. D. McGehee, *Advanced Energy Materials*, 2011, **1**, 954–962.

48   L. Duan, Y. Zhang, R. Deng, H. Yi and A. Uddin, *ACS Applied Energy Materials*, 2020, **3**, 5792–5803.

49   W. Li, J. Cai, F. Cai, Y. Yan, H. Yi, R. S. Gurney, D. Liu, A. Iraqi and T. Wang, *Nano Energy*, 2018, **44**, 155–163.

6.2 Publication Supplementary Information

Metal-Organic Framework Nanosheets as Templates to Enhance Performance in Semi-Crystalline Organic Photovoltaic Cells

Kezia Sasitharan, Rachel Kilbride, Emma Spooner, Jenny Clark, Ahmed Iraqi, David G. Lidzey and Jonathan A. Foster

1. General experimental procedures

2. Syntheses

3. Fabrication of the photovoltaic devices

4. Statistical analysis

5. Optimization of photovoltaic devices

6. GI-WAXS analysis

7. AFM imaging and grain size analysis

8. SCLC devices for charge carrier mobility measurements

9. References

1. General experimental procedures

Commercial solvents and reagents were used without further purification. Synthesis of organic ligands was carried out in dry glassware with a nitrogen overpressure. Solvothermal synthesis of metal-organic frameworks was undertaken using borosilicate vials with Teflon faced rubber lined caps.

NMR spectra were recorded on a Bruker Advance DPX 400 spectrometer. Chemical shifts for ^{1}H are reported in ppm on the δ scale; ^{1}H chemical shifts were referenced to the residual solvent peak. All coupling constants are reported in Hz. Mass spectra were collected using a Bruker Reflex III MALDI-TOF spectrometer. Elemental analyses were obtained on a vario MICRO CHNS elemental analyzer equipped with a thermal conductivity detector. X-Ray powder diffraction patterns were collected using a Bruker D8 Advance powder diffractometer equipped with a copper K_α source (λ=1.5418 Å) operating at 40 kV and 40 mA. The instrument was fitted with an energy-dispersive LYNXEYE detector. Measurements were carried out using a fixed goniometer stage with a rotating flat plate sample holder. IR spectroscopy was performed on a Perkin-Elmer Pyris TGA from 30-600°C at 10°C min^{-1}, under a 20 mL min^{-1} nitrogen flow. UV-Vis absorption spectra were collected on a Cary 5000 UV-Vis-NIR instrument using a 1 cm internal length quartz cuvette. PL spectra were recorded using a Horiba

FluoroMax spectrofluorometer using 500 nm excitation. The fluorescence emission was corrected for sample absorption at the excitation wavelength to produce an emission spectrum proportional to the fluorescence quantum efficiency.

Nanoscopic characterisation was performed using a Bruker Multimode 5 AFM, operating in soft-tapping mode under ambient conditions. Bruker OTESPA-R3 cantilever were used, with a drive amplitude and nominal resonance frequency of 20.4 mV and 290 kHz, respectively. Images were processed using standard techniques with the free Gwyddion software.

2. **Syntheses**

   a. **Synthesis of *meso-tetracarboxyphenyl porphyrin* (TCPP) ligand**

10 mL of pyrrole (98%, light brown solution) was distilled under vacuum at 80°C to give 5 mL of a clear solution. 4-formylbenzoic acid (3.0 g, 20 mmol) was dissolved in propionic acid (100 mL) and freshly distilled pyrrole (1.4 mL, 20 mmol) was added by syringe. The solution immediately darkened and was refluxed for 15 hours. The mixture was chilled in a fridge for 10 hours before collection of the solid by vacuum filtration. The solid was washed with hot water (2 x 20 mL) and dried under vacuum to give the product as a black powder (3.23 g, 4.0 mmol, 80 %). Elemental Analysis calculated for $C_{48}H_{30}N_4O_8$: Expected: C, 72.91; H, 3.82; N, 7.09. Found: C, 72.95; H, 4.08; N, 6.82

λ_{max} (nm): 420 (π-π^*)

^{1}H-NMR (d$_6$-DMSO) δ/ppm: 8.85 (8H, s, β-pyrrolic H), 8.38 (8H, d, J = 8.0, Ar-H), 8.32 (8H, d, J = 8.0, Ar-H), -2.95 (2H, s, internal pyrrole NH).

MALDI-TOF: m/z 791.2 ([MH]$^+$)

   b. **Synthesis of bulk Zn$_2$(Zn-TCPP)(DMF)**

H$_2$TCPP (7.9 mg, 0.03 mmol), Zn(NO$_3$)$_2$.3H$_2$O (8.9 mg, 0.09 mmol), DMF (1.5 mL) and ethanol (0.5 mL) were mixed at room temperature and heated at 80°C for 24 hours. Purple crystals were collected by centrifugation at 4500 RPM for 10 minutes and repeatedly washed in ethanol until the supernatant became clear (Yield 87%)

Elemental analysis $C_{48}H_{24}N_4O_8Zn_3(H_2O)_4(DMF)_3$: Expected C, 53.57; H, 4.50; N, 8.33 Found C, 52.76; H, 4.77; N, 8.88.

A slight excess of Zn around the edge of the MOF and possible nitrate counter ions could be the reason for lower carbon content and higher nitrogen.

   c. **Exfoliation of MOF into MONs**

5 mg of Zn_2(ZnTCPP) MOF was added to a 12 mL glass vial along with 6 mL of the desired solvent. The sample was mixed in a vortex mixer for 30 seconds to disperse the sediment. The samples were sonicated using a Fisherbrand Elmasonic P 30H ultrasonic bath (2.75 L, 380/350 W, UNSPSC 42281712) filled with water. Samples were sonicated for 60 min at a frequency of 80 kHz with 100% power and the temperature was thermostatically maintained at 16-20°C using a steel cooling coil. Sonication was applied using a sweep mode and samples were rotated through the water using an overhead stirrer to minimise variation due to ultrasound "hot-spots". Following sonication, the vials were transferred to centrifuge tubes and centrifuged at 1500 RPM for 10 minutes to remove non-exfoliated particles.
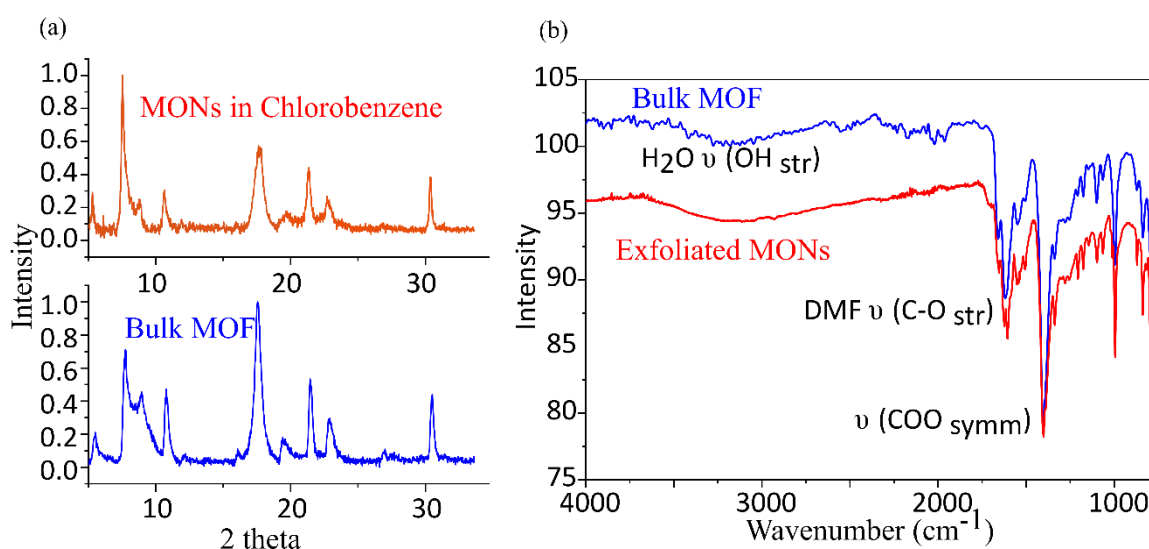

Figure S 6.1 (a) Powder diffraction pattern for as-synthesized Zn_2(ZnTCPP) MON in comparison with the synthesized bulk MOF. The diffraction patterns are in accordance with the previous reports[50] (b) FTIR spectra of Zn_2(ZnTCPP) bulk MOF in comparison with exfoliated MONs.

3. Fabrication of devices

a. Preparation of substrates

Pre-patterned ITO Glass substrates (20 mm x 15 mm) of 20 ohm/square resistance (Ossila) were cleaned via hellmenex (1-3vol%) in boiling DI water (10-minute sonication), followed by further washing in boiling DI water (10-minute sonication) and finally 5-10 minutes sonication in isopropyl alcohol. The substrates were dried with a nitrogen gun and placed in a UV-Ozone cleaner for 10 minutes to ensure removal of any surface particulates.

b. Deposition of ZnO

The precursor gel used to fabricate the ZnO electron transport layer was prepared by dissolving 0.2 g of zinc acetate dihydrate in 2ml 2-methoxyethanol with 55ul ethanolamine as stabilizer. The solution was then stirred in air for 12 hours to form a transparent gel which was spin-

coated at 3000 rpm onto the ITO surface. After being baked at 200°C for 60 min in air, the ZnO coated substrates were transferred into the N2 filled glovebox.

c. Active layer deposition

P3HT-ICBA

P3HT (Sigma Aldrich) and ICBA (99% purity, supplied by Ossila) were used as received. P3HT (10mg/mL) was dissolved in chlorobenzene (CB) solvent. After heating at 60 °C for 10 minutes followed by cooling towards room temperature, the solution was filtered through a 0.45 um PTFE filter. The P3HT solution in chlorobenzene was then mixed with a given wt% of ZnTCPP MONs (5%-20% tested for optimal concentration) and stirred at 60 °C for an hour. Then 10 mg of PCBM was added and the final P3HT:ZnTCPP:ICBA solution was heated at 70°C for an hour and cooled to room temperature prior to spin coating. The solutions were then spin-cast onto ITO/ZnO at 1000 rpm under a nitrogen atmosphere in a glove box, forming films of ∼150 nm as determined by dektak. For control devices, 1:1(wt/wt) (P3HT:ICBA) were spin cast at 2000 rpm in the same method as above to give films of ~150nm. Solvent-vapour annealing of the films was carried out by placing the coated substrates in a sealed metal container containing 20uL of solvent chlorobenzene) for 5 minutes.

PCDTBT-PC71BM

PCDTBT (Ossila) and PCBM (99% purity, supplied by Ossila) were used as received. PCDTBT (4mg/mL) was dissolved in chlorobenzene (CB) solvent. After heating at 60 °C for 10 minutes followed by cooling towards room temperature, the solution was filtered through a 0.45 um PTFE filter. The PCDTBT solution in chlorobenzene was then mixed with 5mg ZnTCPP MONs (1:0.5 wt/wt ratio of PCDTBT: ZnTCPP)) and stirred at 60 °C overnight. Then 16 mg of PCBM was added and the final PCDTBT: ZnTCPP: PCBM (1:0.5:4 wt/wt ratio) was heated at 70°C for an hour and cooled to room temperature prior to spin coating. The solutions were then spin-cast onto ITO/ZnO at 700 rpm under a nitrogen atmosphere in a glove box, forming films of ∼100 nm as determined by dektak. For control devices, 1:4(wt/wt) (PCDTBT: PCBM) were spin cast at 700 rpm in the same method as above to give films of ~90nm.

PTB7-Th-PC71BM

PTB7-Th (Ossila) and PCBM (99% purity, supplied by Ossila) were used as received. The solutions were made at 35mg/ml with a PTB7Th:PCBM ratio of (1:1.5). The PTB7-Th-PCBM solutions were made in chlorobenzene and set at 60°C for 10 minutes for dissolution. This was followed by cooling towards room temperature. Half of this solution was retained for the reference devices, and to the remaining PTB7-Th solution in chlorobenzene, 5% by weight of MONs was added. The solutions were

spin-cast at 2700 rpm for the reference devices and 3000 rpm for the MON devices, resulting in an active layer thickness of 120nm in both the cases.

PBDB-T-PC71BM

PBDB-T (Ossila) and PCBM (99% purity, supplied by Ossila) were used as received. PBDB-T:PCBM (20mg/mL) was dissolved in chlorobenzene (CB) solvent and set at 80°C overnight for dissolution. This was followed by cooling towards room temperature. And the solutions were ready for the reference devices. To another solution prepared in the same way, 5% by weight of MONs were added. The solutions were then spin-cast onto ITO/ZnO at 1000 rpm under a nitrogen atmosphere in a glove box, forming films of ~150 nm as determined by dektak. For the reference devices the speed of spin cast was 700 rpm to give films of ~150nm.

PffBT4T-2OD-PC71BM (also known as PCE11-PCBM)

To coat the active layer, for the reference devices we prepared an ink consisting of 1:1.2 wt ratio PffBT4T-2OD: PCBM dissolved at 9mg/ml in chlorobenzene. The solvent also contained 3% volume of 1,8-diiodooctane (DIO). The optimised MON based devices had 10% by weight of MONs added to the ink. The inks were stirred at 130°C for 6 hours before spin-coating to prevent polymer aggregation. The inks were spin-coated at 1000 rpm onto ZnO/ITO substrates held at 110°C. This heating of the substrates was found essential for uniform coating of film. Following annealing at 110°C for 10 minutes, the top electrode consisting of 10 nm of molybdenum oxide film capped by 100 nm Ag was thermal evaporated onto the active layer through a shadow mask. Finally, the devices were encapsulated using UV cured epoxy glue and a glass cover slip.

d. Top contact deposition and encapsulation

The ITO/ZnO/Active layer substrates were placed under a vacuum of <2E-6 mBar before thermally evaporating MoO_3 (5nm) and Silver (100nm) layers using a shadow mask. The devices were encapsulated using an epoxy resin (Ossila, E131).

e. Device testing

Device performance was determined under ambient conditions by measuring J–V curves using a Newport 92251A-1000 solar simulator, with devices illuminated through a 0.0256 cm^2 aperture mask. Before each set of measurements, the intensity was calibrated to 100 mW cm^{-2}

using an NREL certified silicon reference cell. The applied bias was swept from 0.0 to +1.2 V and back again at a scan speed of 0.4 V s^{-1} using a Keithley 237 source measure unit.

Table S 6.1 A summary of the device results from the above mentioned configurations, with the error bars obtained by statistical analysis on 20 devices, per configuration.

Device configuration	Jsc (-mA/cm^2)	Voc (V)	FF (%)	PCE (%)
P3HT-ICBA	6.0±0.23	0.87±0.01	55.5±0.5	2.8±0.3
P3HT-MON-ICBA	12.0±0.02	0.85±0.01	59±0.1	5.9±0.1
PCDTBT-PCBM	8.5±0.5	0.89±0.01	67.2±0.11	5.24±0.18
PCDTBT-MON-PCBM	9.2±0.3	0.89±0.01	66.30±0.02	5.4±0.2
PTB7-Th-PCBM	12.9±0.1	0.83±0.02	56±0.01	6.0±0.1
PTB7Th-MON-PCBM	13.14±0.2	0.84±0.02	58.4±0.5	6.20±0.39
PBDBT-PCBM	12.2±0.3	0.89±0.01	63.60±0.07	7.0±.08
PBDBT-MON-PCBM	13.6±0.1	0.89±0.02	64.0±0.1	7.4±0.4
PCE11-PCBM	18±1.02	0.77±0.01	71.5±0.9	9.7±0.89
PCE11-MON-PCBM	21.2±0.41	0.77±0.01	73.7±0.3	11.9±0.34

4. PffBT4T-2OD: PCBM statistical analysis

Literature PffBT4T-2OD devices – These results were obtained by using the keyword 'PffBT4T-2OD' in scifinder. The search yielded 126 research items. All these records were examined and the following results included in the box plot shown in Figure main text, with the aim to compare and investigate how highly performing our devices were with respect to the ones reported so far.

Table S 6.2 Literature reports on PCE-11 based OPV devices

Jsc (-mA/cm^2)	Voc (V)	FF (%)	PCE (%)	Ref
12.7	1	60	8.2	[1]
18.41	0.78	68.70	9.84	[2]
16.41	0.72	71.2	8.41	[3]
22.95	0.73	60	10.07	[4]
18.4	0.77	74	10.50	[5]
20.8	0.72	69.3	10.4	[6]
18.3	0.76	64	8.9	[7]
20.29	0.74	68.9	10.33	[8]
13.0	1.07	63	8.7	[9]
17.04	0.74	67	8.56	[10]
11.29	0.93	50	5.25	[11]
17.79	0.78	65.3	9.06	[12]
18.08	0.77	68.9	9.58	[13]
17.58	0.86	67.2	10.18	[14]
21.92	0.73	0.60	9.50	[15]
17.5	0.75	72.4	9.2	[16]
9.6	0.78	47.7	3.59	[17]
19.44	0.74	67.25	9.63	[18]
16.31	0.75	67	8.20	[19]
18.5	0.72	73	9.6	[20]
11.50	0.93	43	4.61	[21]
10.92	0.81	38	4.23	[22]
17.9	0.80	68.4	9.79	[23]

16.82	0.76	76.4	10.19	24
13.89	0.75	58.85	6.11	25
16.61	0.79	62.5	8.25	26
20.76	0.76	61.8	9.8	27
13.6	1.04	66.1	9.4	28
15.50	0.82	71	9.02	29
19.54	0.73	74.6	10.7	30
17.3	0.76	70	9.31	31
18.61	0.75	72.6	10.13	32
15.53	0.74	69	7.97	33
20.12	0.78	61.2	9.66	34
20.07	0.78	69	10.36	35
18.28	0.77	74.02	10.36	36
16.7	0.75	70	8.8	37
19.5	0.75	72.2	10.57	38
18.4	0.77	73.9	10.59	39
18.40	0.77	64	9.07	40
19.38	0.81	65	9.80	41
18.6	0.74	68	10.1	42
14.65	1.08	60	9.5	43
18.19	0.76	66.6	9.07	43
18.8	0.76	70	10.1	44
18.87	0.80	68.21	10.30	45
19.02	0.77	72.62	10.72	46
17.49	0.74	67.5	8.62	47

5. Optimisation stages to get to the 12.3% MON device

a. DIO addition – 3% by volume was found to be the optimum amount.
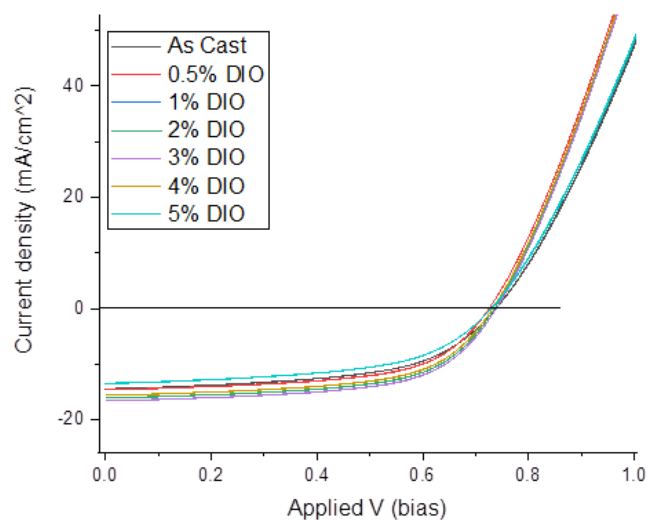

Figure S 6.2 Current-voltage curves of the PCE-11-PCBM devices with increased addition of DIO (1,8-diiodoctane), which is a plasticizer. 3% by volume is found to be the optimal amount.
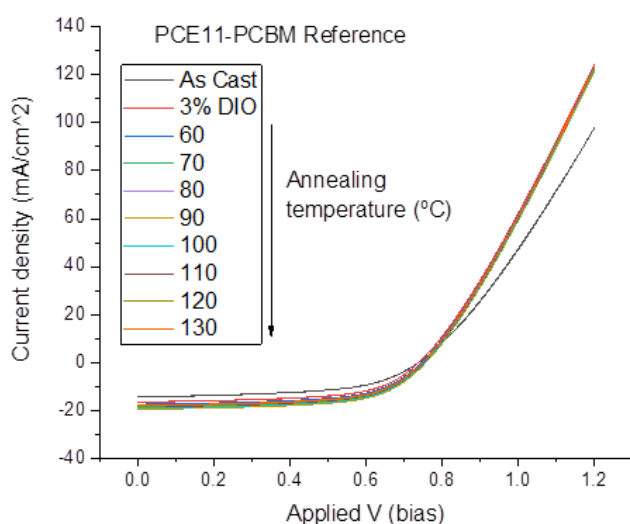
b. Optimisation of the Annealing temperature

Figure S 6.3 Current-voltage curves of the PCE11-PCBM reference devices evaluated at varying annealing temperatures.
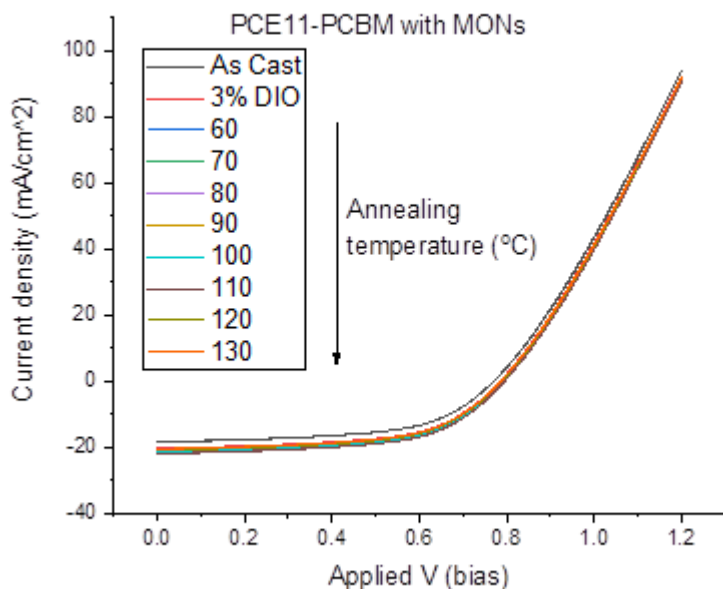
Figure S 6.4 Current-voltage curves of the PCE11-PCBM reference devices evaluated at varying annealing temperatures.

6.   GI-WAXS analysis

The GIWAXS thin film measurements were performed with a Xeuss 2.0 system (Xenons, France). The Sheffield machine is fitted with a MetalJet (Excillum, Sweden) liquid gallium X-ray source, providing a 9.24 keV X-ray beam collimated to a beam spot of 400 µm laterally at the sample position, measuring the full sample length. X-ray diffraction patterns were acquired with a Pilatus3R 1M 2D detector (Dectris, Switzerland). The sample to detector distance was calibrated using a silver behenate calibrant standard in transmission geometry. Samples were measured in GI-WAXS geometry near the critical angle (calculated to probe the entire film thickness) and under vacuum atmosphere to minimise the background scatter.

Measurement Details:

- Incident angle = 0.16 degrees

- Sample to detector distance = 307mm

- Sample chamber and flight tubes held under vacuum to remove background air scatter
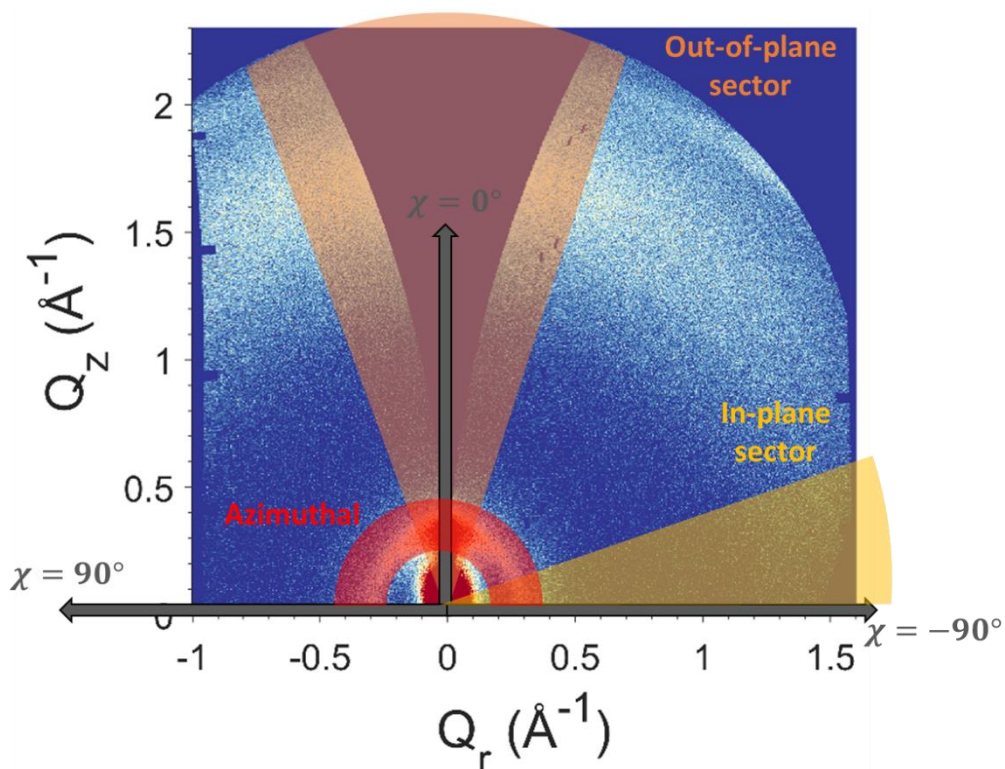
Figure S 6.5 A guide to the integration applied to the obtained GI-WAXS data in this work.

Data Processing details: The data was corrected, reshaped and reduced using the GIXSGUI MATLAB toolbox. [48]
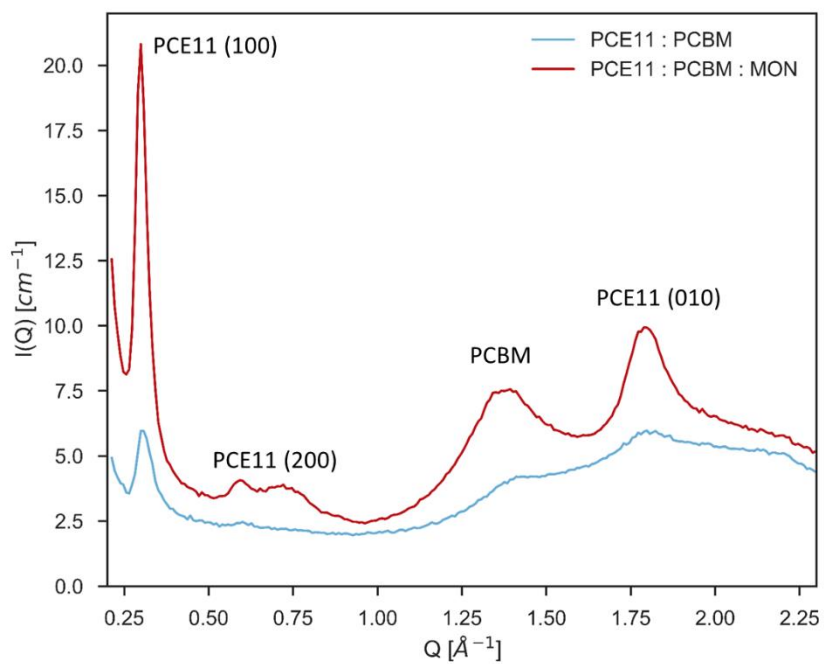

Figure S 6.6 Full radial integration of PCE11-PCBM and PCE11-MON-PCBM films
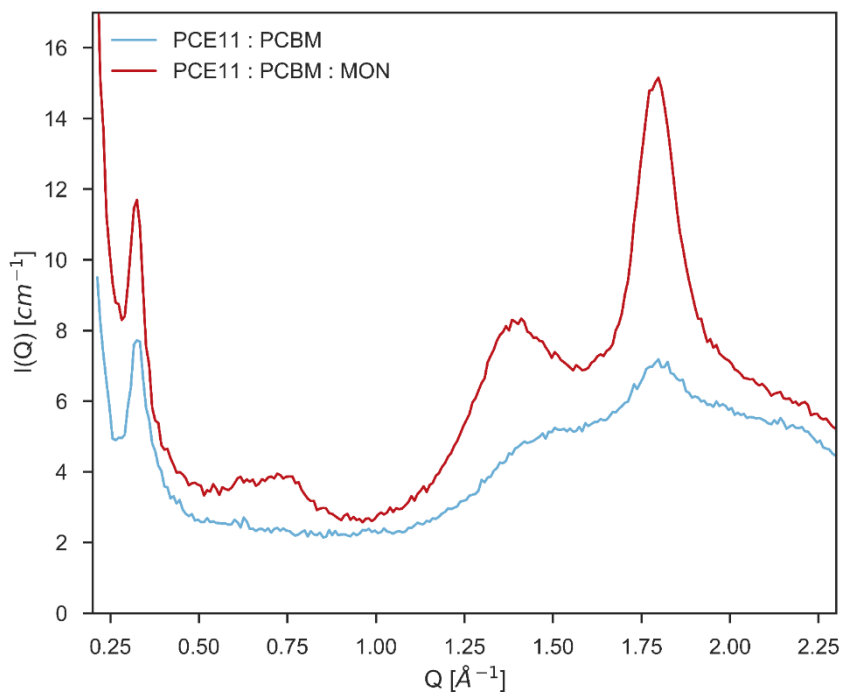
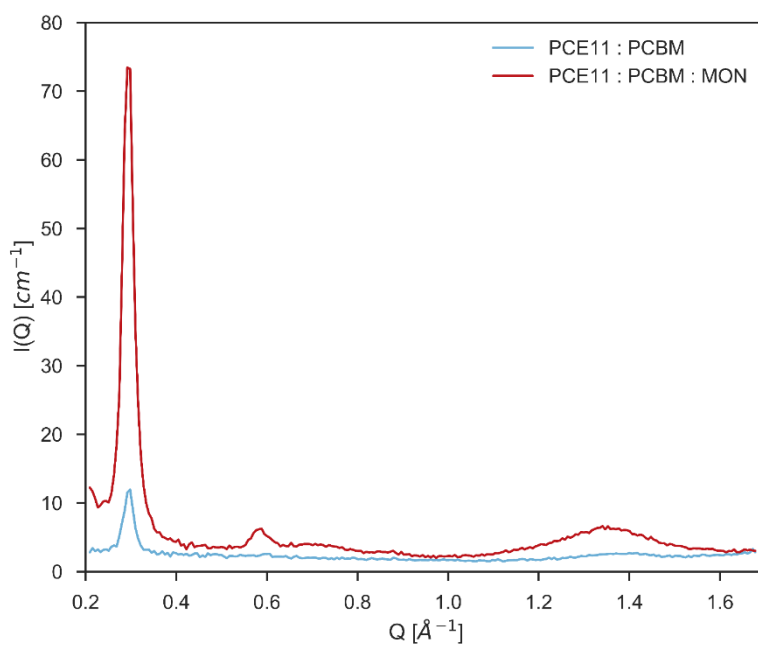Figure S 6.7 Out of plane radial integration of the GI-WAXS data

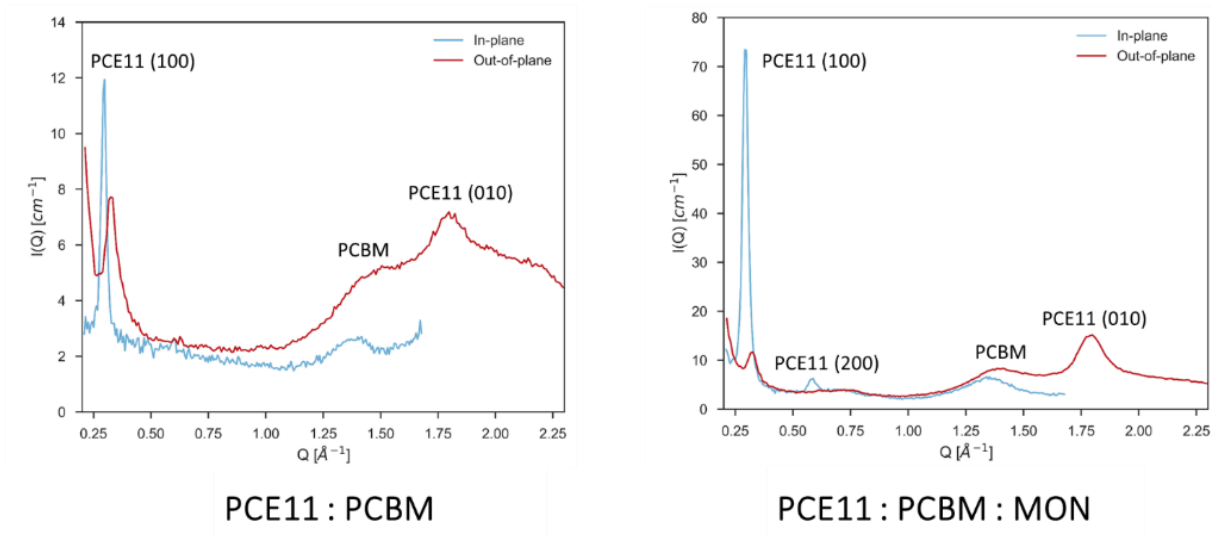Figure S 6.8 In-plane radial integration of the data

Figure S 6.9 Comparison of the in-plane and out-plane radial integrations

Orientation	Q (Å⁻¹)		d-spacing $(d = \frac{2\pi}{Q})$		Crystal Coherence Length CCL (a.u.)		Comment
	No MON	With MON	No MON	With MON	No MON	With MON	
In-plane	0.295	0.294	21.30	21.38	21.93	17.51	PCE11 lamellar (100)
	N/A	0.583	N/A	10.77	N/A	12.59	PCE11 lamellar (200)
	N/A	0.641	N/A	9.80	N/A	1.59	PCBM
	1.390	1.353	4.52	4.64	2.67	3.53	PCBM
Out-of-plane	0.328	0.321	19.18	19.60	6.40	8.11	PCE11 lamellar (100)
	N/A	0.664	N/A	9.46	N/A	1.79	PCBM
	1.484	1.416	4.23	4.44	1.47	2.02	PCBM
	1.839	1.794	3.42	3.50	1.88	4.57	PCE11 π-π stacking (010)

Crystallite Coherence Length (CCL) calculated using Scherrer equation:

$$CCL = \frac{\kappa\lambda}{\beta cos\theta}$$

Where:
κ = dimensionless shape factor (0.94)
λ = x-ray wavelength (0.134nm)
β = FWHM of P3HT (100) peak in radians
θ = Bragg angle in radians

Figure S 6.10 Tabulation of the peak Indexing and Scherrer analysis results on the films.

Orientation	Q (Å^{-1})		FWHM (Å^{-1})		Intensity (a.u.)	
	No MON	With MON	No MON	With MON	No MON	With MON
In-plane	0.295	0.294	0.02695	0.03083	8.65542	68.443
	N/A	0.583	N/A	0.04701	N/A	2.638
	N/A	0.641	N/A	0.37281	N/A	1.95977
	1.390	1.353	0.22382	0.16913	1.00233	2.958
Out-of-plane	0.328	0.321	0.09235	0.07284	4.58533	7.411
	N/A	0.664	N/A	0.33155	N/A	1.378
	1.484	1.416	0.40617	0.2954	2.76909	5.092
	1.839	1.794	0.32058	0.13176	4.40289	7.90039

Figure S 6.11 The gaussian peak fitting results tabulated showing a comparison of the Q values, full-width half maxima and the peak intensities with and without MONs in the PCE11-PCBM system.
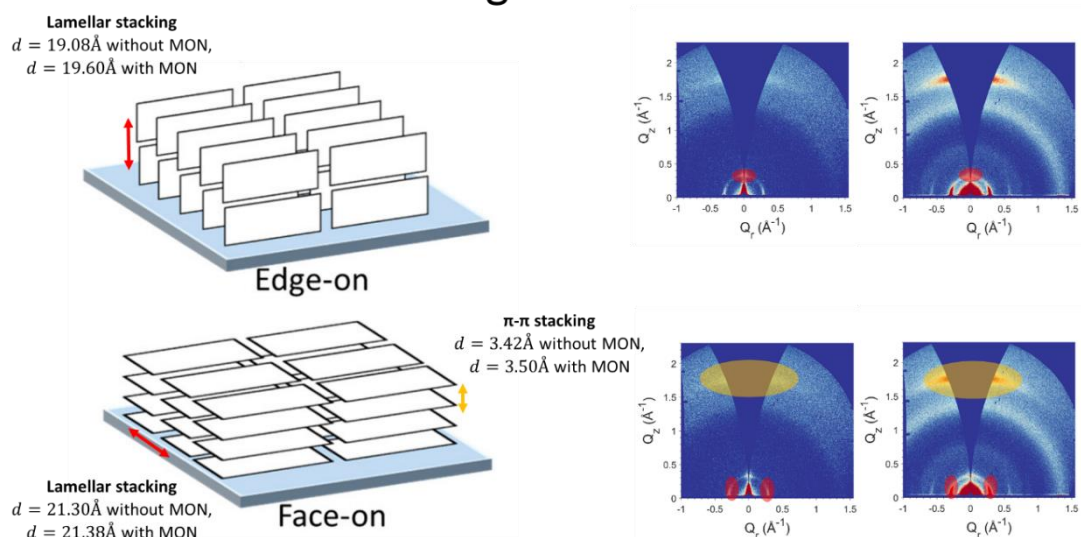
Figure S 6.12 Comparison of the PCE11 molecular packing (d-spacing values) in the films with and without MONs.

7. AFM imaging and grain size analysis
a. PCE11-PCBM scan size = 5um

b. PCE11-PCBM scan size = 2um

c. PCE11-PCBM scan size = 500 nm
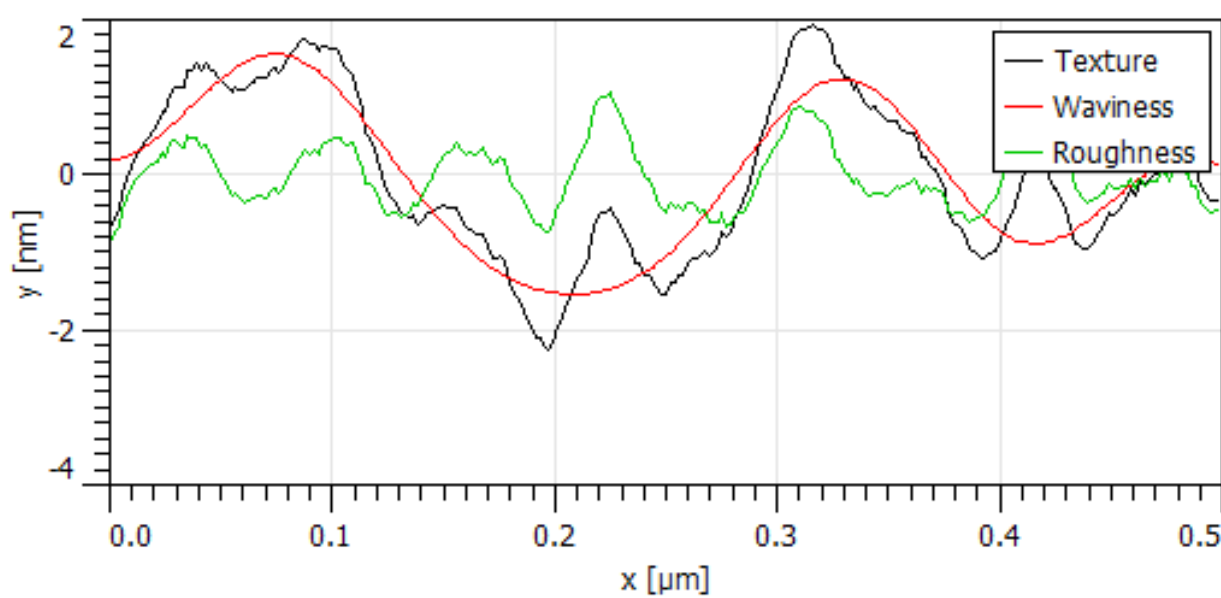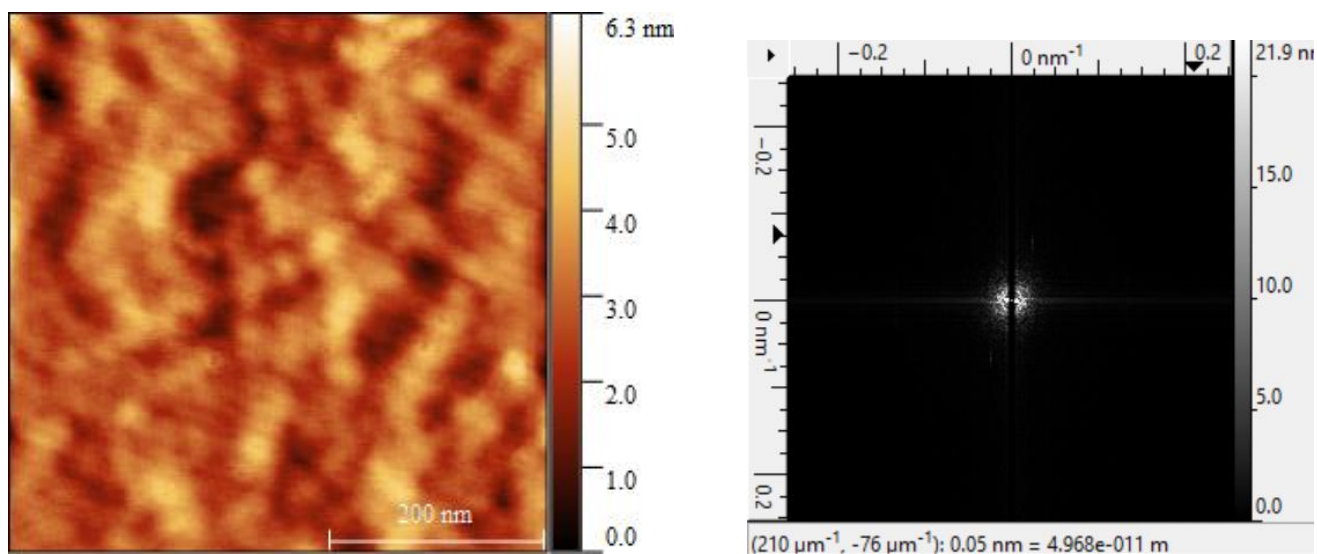
d. PCE11-PCBM-MONs scan size = 5um
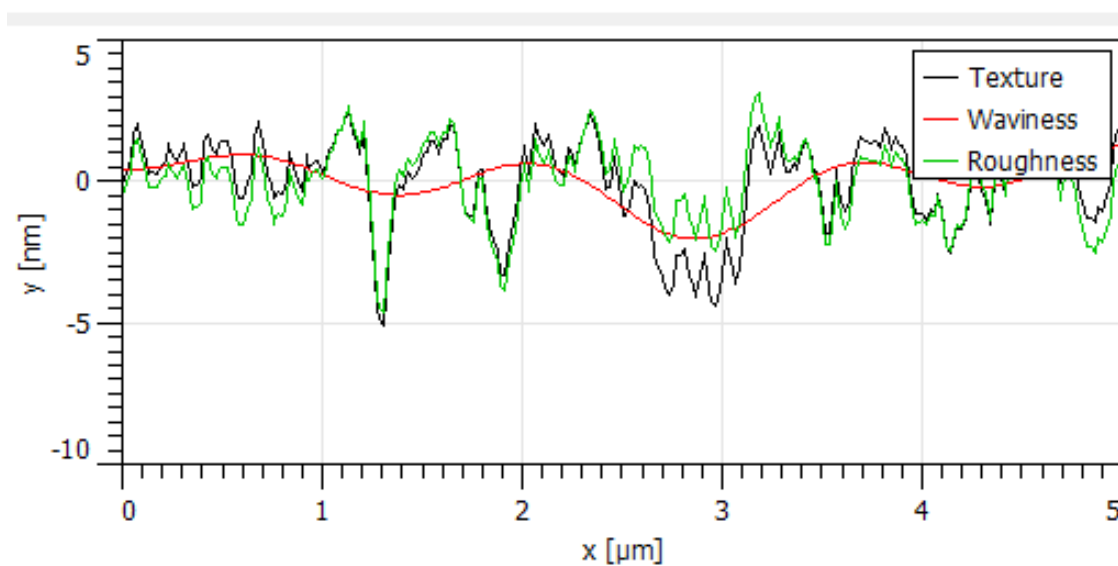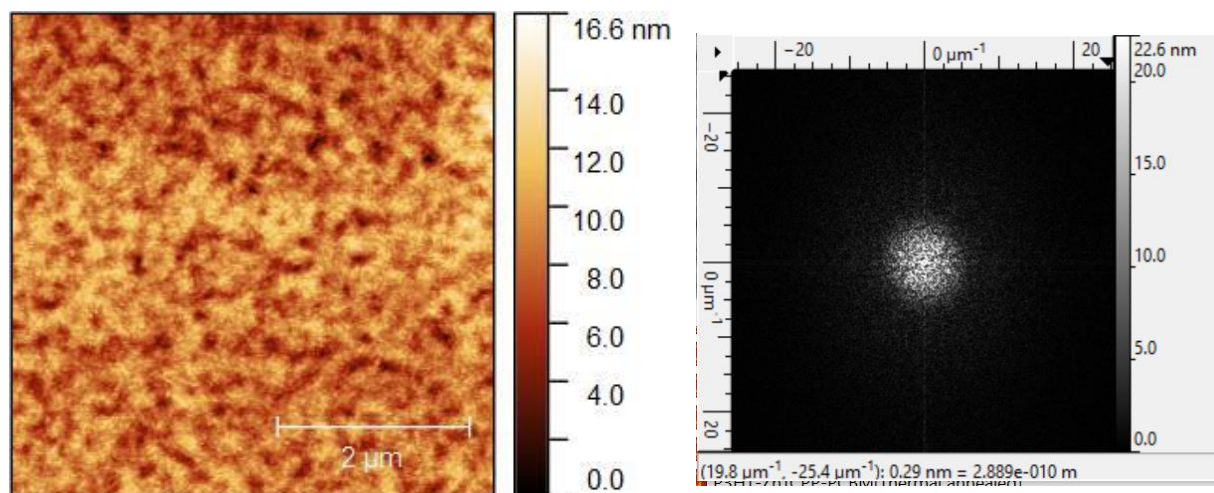
e. PCE11-PCBM-MONs scan size = 2um
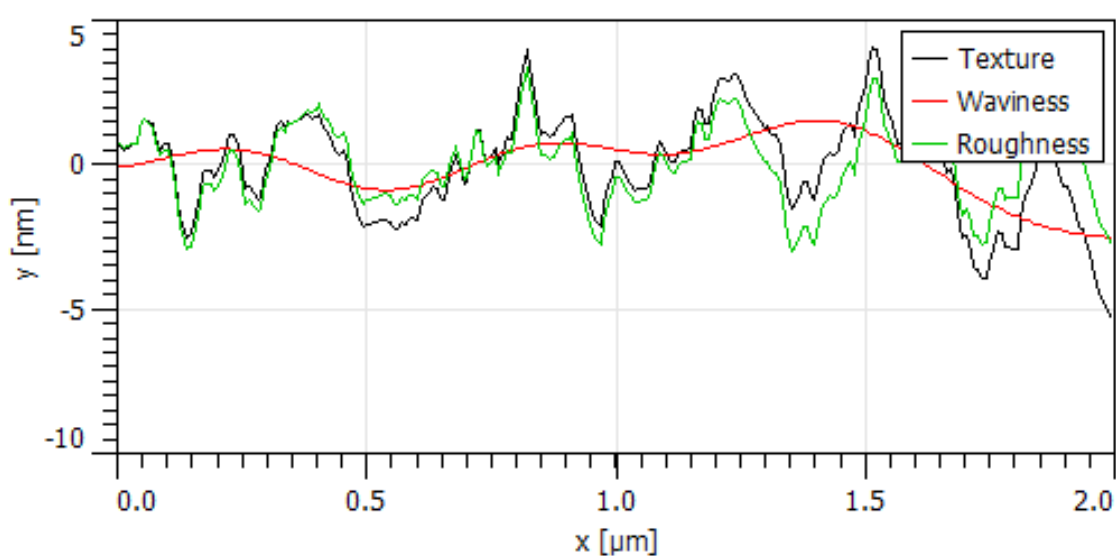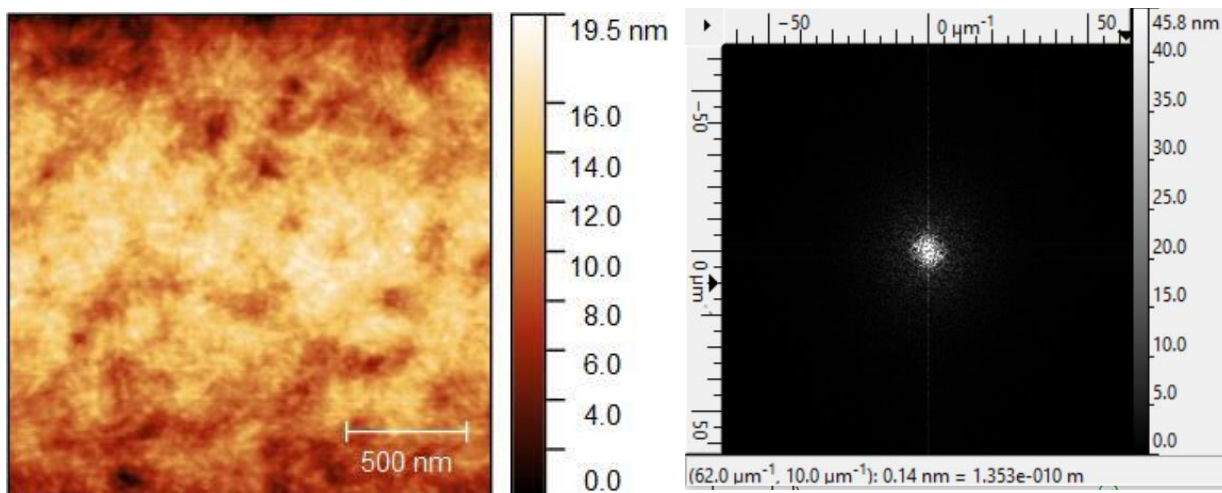
f. PCE11-PCBM-MONa scan size = 500nm
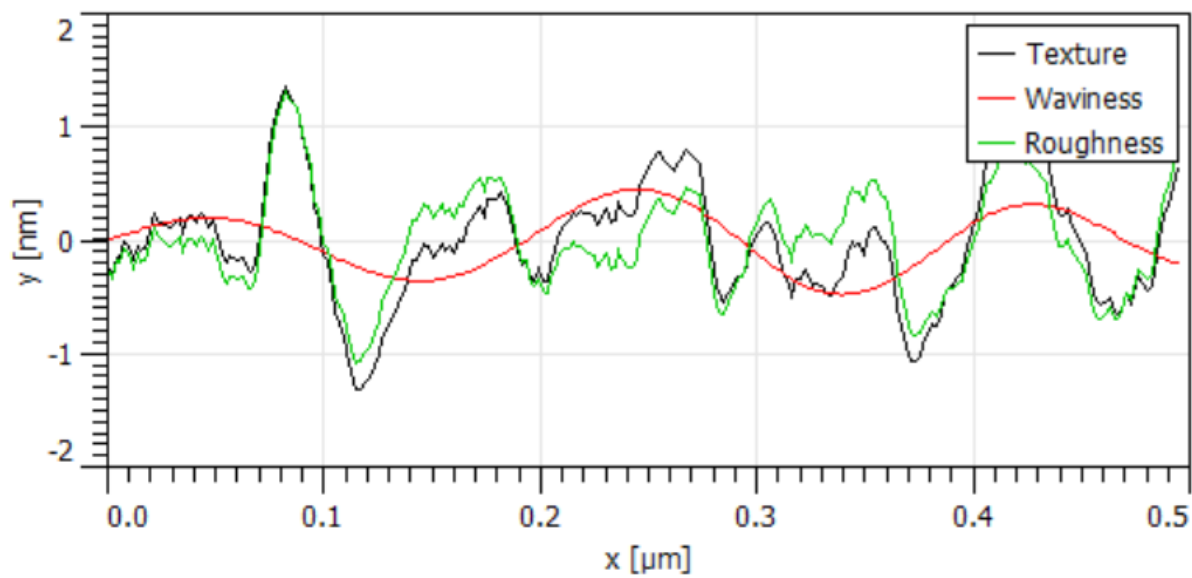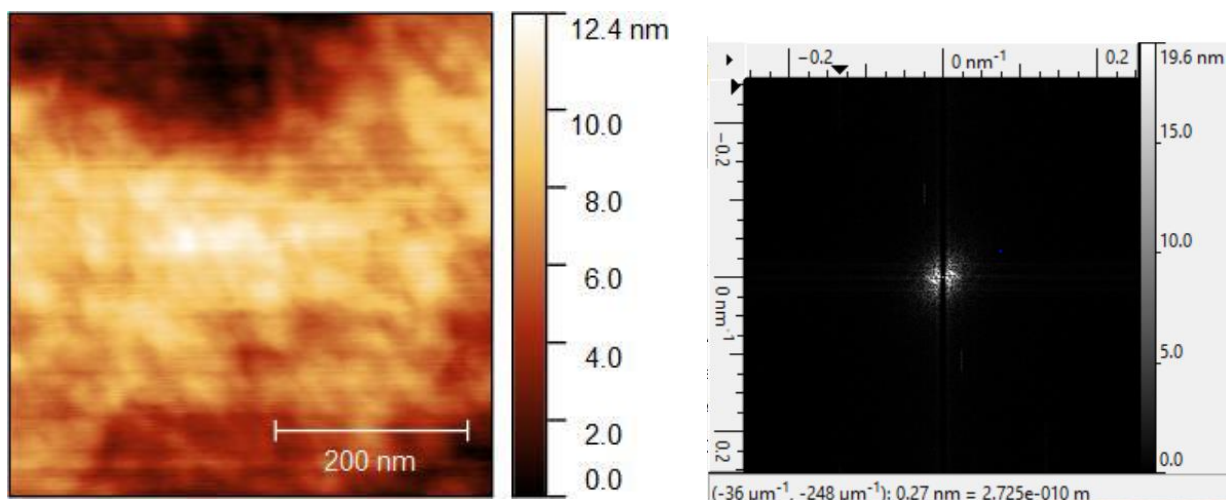
8. SCLC devices for charge carrier mobility measurement

The investigation of space-charge limited electron-only or hole-only devices for extraction of mobility values is a well-known and reliable method. Space-charge limited currents were tested in h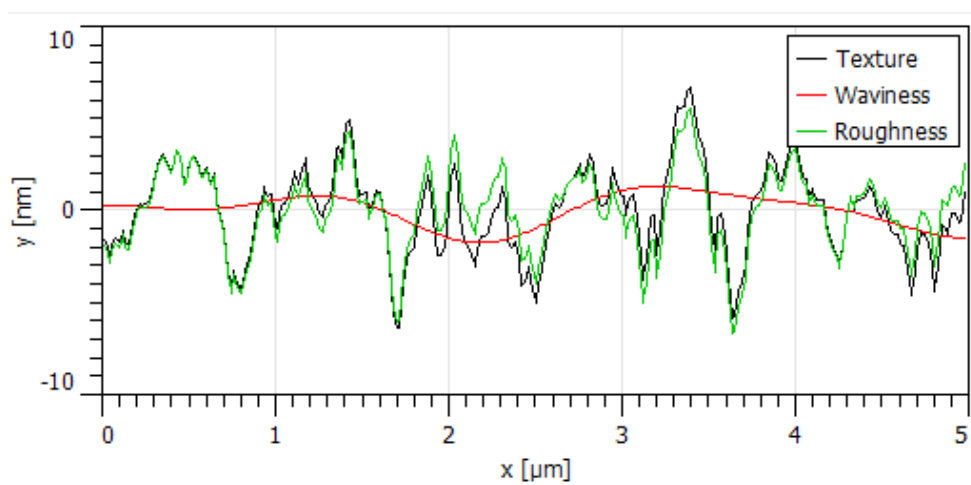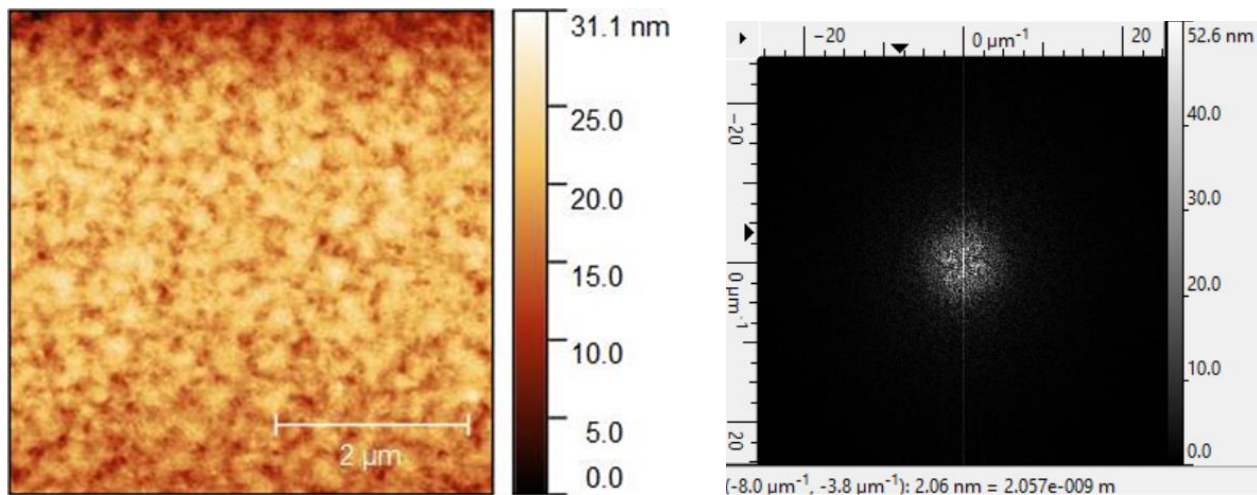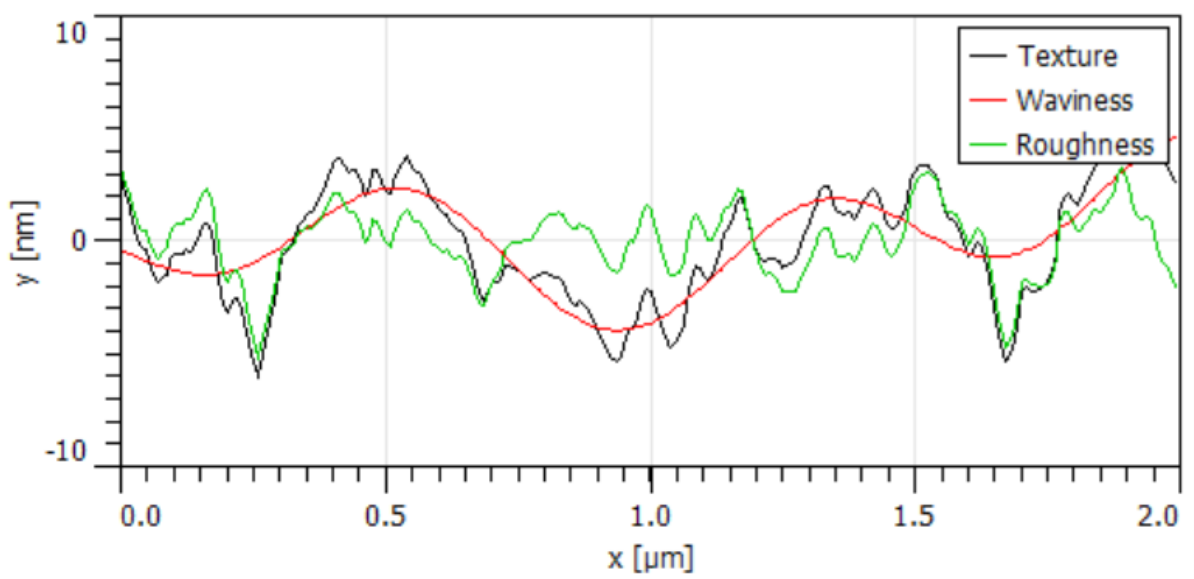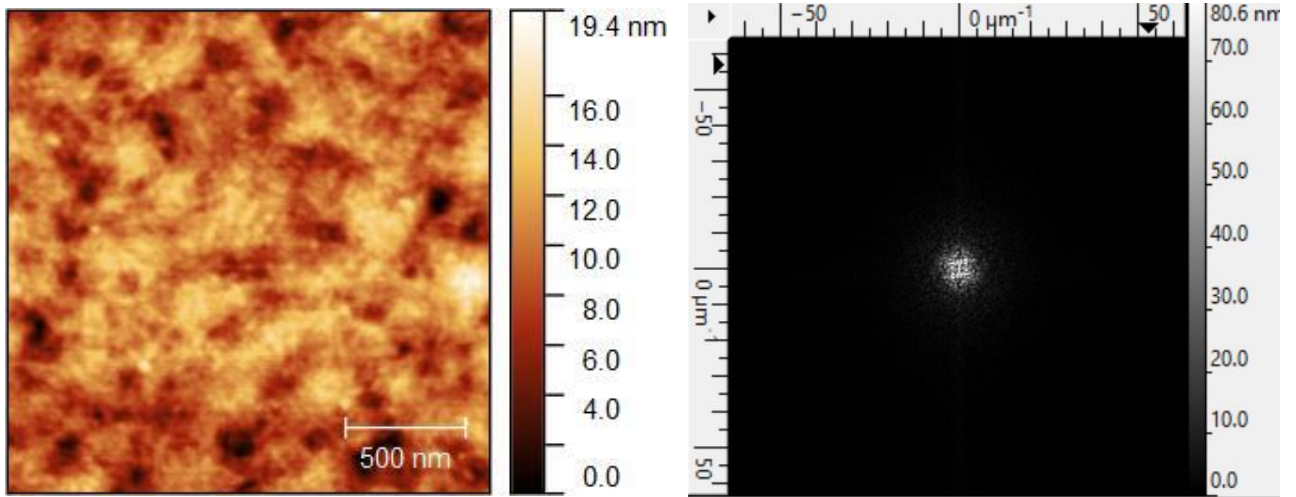ole only devices with the configuration ITO:PEDOT/PSS:active layer:MoO$_3$:Ag and a well-established protocol from literature was used for data fitting and analysis[49]. The hole mobility was determined by fitting the dark current to the model of a single carrier SCLC current with field dependent mobility based on Mott-Gurney law (Figure S19a-S22b, ESI). Electron only devices were fabricated with the configuration ITO:ZnO:Active layer:BCP:Ag to extract the electron mobility.

Table S 6.3 Hole mobility and electron mobility extracted from SCLC holes only and electrons only devices for different thicknesses of active layer; Number of devices tested for each thickness=3.

Device	Thickness	μh (Hole mobility)	μe (Electron mobility)	μh/μe
PCE-11/PCBM	150 nm	1.35 X10^{-3}	1.40 X10^{-3}	0.96
PCE11/MON/PCBM	150nm	2.07 X10^{-3}	2.29 X10^{-3}	0.90

Status: Complete

1)
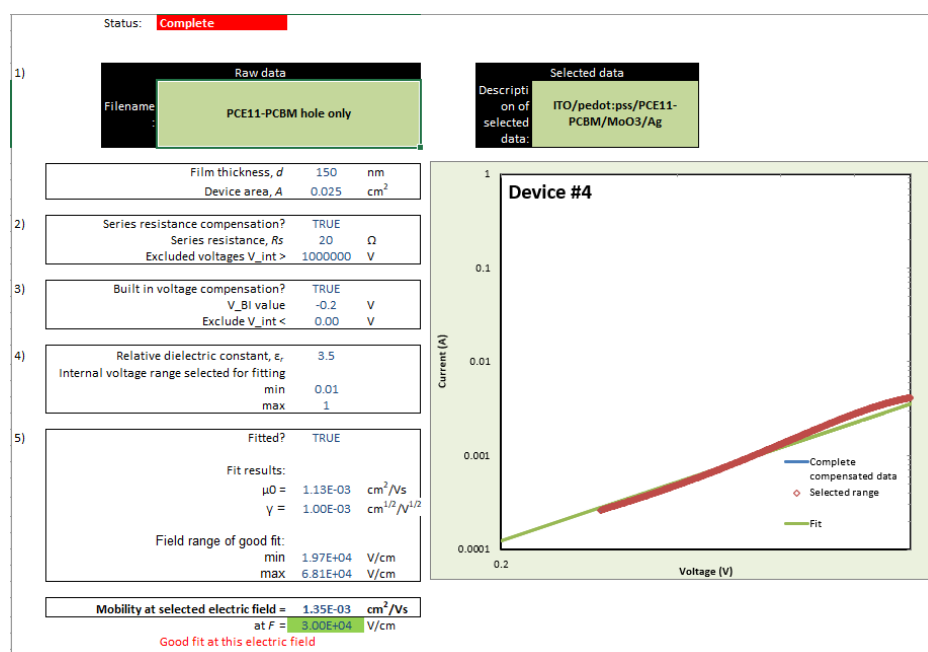
Raw data

Filename: PCE11-Zn2(ZnTCPP)-PCBM hole only

Selected data

Description of selected data: ITO/PEDOT:PSS/PCE11-Zn2(ZnTCPP)-PCBM/MoO3/Ag

Film thickness, d	150	nm
Device area, A	0.025	cm^2

2)

Series resistance compensation?	TRUE	
Series resistance, Rs	10	Ω
Excluded voltages V_int >	1000000	V

3)

Built in voltage compensation?	TRUE	
V_BI value	-0.1	V
Exclude V_int <	0.00	V

4)

Relative dielectric constant, ε_r	3.5	
Internal voltage range selected for fitting		
min	0.01	
max	1	

5)

Fitted?	TRUE	

Fit results:

$\mu 0 =$	1.27E-03	cm^2/Vs
$\gamma =$	2.82E-03	cm$^{1/2}$/V$^{1/2}$

Field range of good fit:

min	1.77E+04	V/cm
max	6.24E+04	V/cm

Mobility at selected electric field =	2.07E-03	cm^2/Vs
at $F =$	3.00E+04	V/cm

Good fit at this electric field

Device #3

Current (A) vs Voltage (V)

Legend: Complete compensated data; Selected range; Fit

Status: Complete

1)
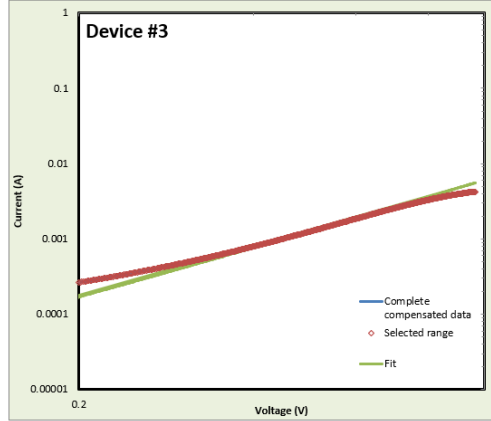
Raw data

Filename: PCE11-Zn2(ZnTCPP)PCBM electron only

Selected data

Description of selected data: ITO/ZnO/PCE11-Zn2(ZnTCPP)PCBM/BCP/Ag

Film thickness, d	150	nm
Device area, A	0.025	cm^2

2)

Series resistance compensation?	TRUE	
Series resistance, Rs	20	Ω
Excluded voltages V_int >	1000000	V

3)

Built in voltage compensation?	TRUE	
V_BI value	-0.1	V
Exclude V_int <	0.00	V

4)

Relative dielectric constant, ε_r	3.5	
Internal voltage range selected for fitting		
min	0.01	
max	1	

5)

Fitted?	TRUE	

Fit results:

$\mu 0 =$	1.79E-03	cm^2/Vs
$\gamma =$	1.40E-03	cm$^{1/2}$/V$^{1/2}$

Field range of good fit:

min	1.40E+04	V/cm
max	6.15E+04	V/cm

Mobility at selected electric field =	2.29E-03	cm^2/Vs
at $F =$	3.00E+04	V/cm

Good fit at this electric field

Device#2

Current (A) vs Voltage (V)

Legend: Complete compensated data; Selected range; Fit

1)

Raw data		Selected data	
Filename:	PCE11-PCBM electron only	Description of selected data:	ITO/ZnO/PCE11-PCBM/BCP/Ag

Film thickness, d	150	nm
Device area, A	0.025	cm^2

2)

Series resistance compensation?	TRUE	
Series resistance, Rs	20	Ω
Excluded voltages V_int >	1000000	V

3)

Built in voltage compensation?	TRUE	
V_BI value	-0.2	V
Exclude V_int <	0.00	V

4)

Relative dielectric constant, ε_r	3.5	
Internal voltage range selected for fitting		
min	0.01	
max	1	

5)

Fitted?	TRUE	
Fit results:		
μ_0 =	1.01E-03	cm^2/Vs
γ =	1.90E-03	$cm^{1/2}/V^{1/2}$
Field range of good fit:		
min	1.97E+04	V/cm
max	6.81E+04	V/cm

Mobility at selected electric field =	1.40E-03	cm^2/Vs
at F =	3.00E+04	V/cm
Good fit at this electric field		

Device#1

The devices were prepared following the same procedure described in the experimental section for photovoltaic devices, except that of the metal electrode. The mobilities were determined by fitting the dark current to the model of a single carrier SCLC current with field dependent mobility[49], which is described as

$$J = [(9\,\varepsilon_r\varepsilon_0\,\mu_0 V^2)/8L^3\,]\,\exp(\beta\sqrt{V}/L)$$

Where, J is the current, μ_0 is the zero-field mobility, ε_0 is the permittivity of free space, ε_r is the relative permittivity of the material, V is the effective voltage, and L is the thickness of the active layer.

References

1   X. Yi, C. H. Y. Ho, B. Gautam, L. Lei, A. H. Chowdhury, B. Bahrami, Q. Qiao and F. So, *Journal of Materials Chemistry C*, , DOI:10.1039/d0tc03969a.

2   P. Li, Y. Zhang, T. Yu, Q. Zhang, J.-P. Masse, Y. Yang, R. Izquierdo, B. Sun and D. Ma, *Solar RRL*, 2020, **4**, 2000239.

3   H. Gaspar, F. Figueira, K. Strutyński, M. Melle-Franco, D. Ivanou, J. P. C. Tomé, C. M. Pereira, L. Pereira, A. Mendes, J. C. Viana and G. Bernardo, *Materials*, 2020, **13**, 1267.

4   L. Duan, Y. Zhang, R. Deng, H. Yi and A. Uddin, *ACS Applied Energy Materials*, 2020, **3**, 5792–5803.

5   J. Zhang, W. Liu, M. Zhang, S. Xu, F. Liu and X. Zhu, *Journal of Materials Chemistry A*, 2020, **8**, 8661–8668.

6   M. Ren, G. Zhang, Z. Chen, J. Xiao, X. Jiao, Y. Zou, H. L. Yip and Y. Cao, *ACS Applied Materials and Interfaces*, 2020, **12**, 13077–13086.

7   D. Yang, B. Cao, V. Körstgens, N. Saxena, N. Li, C. Bilko, S. Grott, W. Chen, X. Jiang, J. E. Heger, S. Bernstorff and P. Müller-Buschbaum, *ACS Applied Energy Materials*, 2020, **3**, 2604–2613.

8   X. Zhang, P. Fan, S. Hou, Y. X. Zheng and J. Yu, *Solar Energy*, 2020, **198**, 535–541.

9   X. Yi, Z. Peng, B. Xu, D. Seyitliyev, C. H. Y. Ho, E. O. Danilov, T. Kim, J. R. Reynolds, A. Amassian, K. Gundogdu, H. Ade and F. So, *Advanced Energy Materials*, 2020, **10**, 1902430.

10   L. Duan, Y. Zhang, H. Yi, F. Haque, C. Xu, S. Wang and A. Uddin, *Materials Science in Semiconductor Processing*, 2020, **105**, 104750.

11   R. Zhao, B. Lin, J. Feng, C. Dou, Z. Ding, W. Ma, J. Liu and L. Wang, *Macromolecules*, 2019, **52**, 7081–7088.

12   L. Duan, H. Yi, Z. Wang, Y. Zhang, F. Haque, B. Sang, R. Deng and A. Uddin, *Sustainable Energy and Fuels*, 2019, **3**, 2456–2463.

13   L. Arunagiri, G. Zhang, H. Hu, H. Yao, K. Zhang, Y. Li, P. C. Y. Chow, H. Ade and H. Yan, *Advanced Functional Materials*, 2019, **29**, 1902478.

14   T. Liu, W. Gao, G. Zhang, L. Zhang, J. Xin, W. Ma, C. Yang, H. Yan, C. Zhan and J. Yao, *Solar RRL*, 2019, **3**, 1800376.

15   W. Zhang, R. Hu, X. Zeng, X. Su, Z. Chen, X. Zou, J. Peng, C. Zhang and A. Yartsev, *Polymers*, 2019, **11**, 408.

16   Y. Zhang, M. T. Sajjad, O. Blaszczyk, A. J. Parnell, A. Ruseckas, L. A. Serrano, G. Cooke and I. D. W. Samuel, *Chemistry of Materials*, 2019, **31**, 6548–6557.

17   M. Nazari, E. Cieplechowicz, T. A. Welsh and G. C. Welch, *New Journal of Chemistry*, 2019, **43**, 5187–5195.

18   X. Zhang, P. Fan, Y. Han and J. Yu, *Energy Technology*, 2019, **7**, 263–268.

19   L. Yan, Y. Wang, J. Wei, G. Ji, H. Gu, Z. Li, J. Zhang, Q. Luo, Z. Wang, X. Liu, B. Xu, Z. Wei and C. Q. Ma, *Journal of Materials Chemistry A*, 2019, **7**, 7099–7108.

20   B. Xu, I. Pelse, S. Agarkar, S. Ito, J. Zhang, X. Yi, Y. Chujo, S. Marder, F. So and J. R. Reynolds, *ACS Applied Materials and Interfaces*, 2018, **10**, 44583–44588.

21   H. Tan, Y. Long, J. Zhang, J. Zhu, J. Yang, J. Yu and W. Zhu, *Dyes and Pigments*, 2019, **162**, 797–801.

22   J. Farinhas, D. Molina, A. Olcina, C. Costa, L. Alcácer, F. Fernández-Lázaro, Á. Sastre-Santos and A. Charas, *Dyes and Pigments*, 2019, **161**, 188–196.

23   Z. Liu and N. Wang, *Journal of Power Sources*, 2018, **402**, 333–339.

24   R. Singh, S. R. Suranagi, J. Lee, H. Lee, M. Kim and K. Cho, *Scientific Reports*, 2018, **8**, 1–9.

25   Z. Bi, H. B. Naveed, Y. Mao, H. Yan and W. Ma, *Macromolecules*, 2018, **51**, 6682–6691.

26   C. Xu, M. Wright, D. Ping, H. Yi, X. Zhang, M. D. A. Mahmud, K. Sun, M. B. Upama, F. Haque and A. Uddin, *Organic Electronics*, 2018, **62**, 261–268.

27   C. Xu, M. Wright, N. K. Elumalai, M. A. Mahmud, V. R. Gonçales, M. B. Upama and A. Uddin, *Journal of Materials Science: Materials in Electronics*, 2018, **29**, 16437–16445.

28   G. Zhang, R. Xia, Z. Chen, J. Xiao, X. Zhao, S. Liu, H.-L. Yip and Y. Cao, *Advanced*

Energy Materials, 2018, **8**, 1801609.

29   M. Kim, J. Lee, D. H. Sin, H. Lee, H. Y. Woo and K. Cho, *ACS Applied Materials and Interfaces*, 2018, **10**, 25570–25579.

30   Y. Yan, W. Li, F. Cai, J. Cai, Z. Huang, R. S. Gurney, D. Liu, D. G. Lidzey, A. J. Pearson and T. Wang, *ACS Applied Energy Materials*, 2018, **1**, 3505–3512.

31   Y. Zhang, A. J. Parnell, O. Blaszczyk, A. J. Musser, I. D. W. Samuel, D. G. Lidzey and G. Bernardo, *Physical Chemistry Chemical Physics*, 2018, **20**, 19023–19029.

32   J. Zhao, S. Zhao, Z. Xu, D. Song, B. Qiao, D. Huang, Y. Zhu, Y. Li, Z. Li and Z. Qin, *ACS Applied Materials and Interfaces*, 2018, **10**, 24075–24081.

33   J. Wei, G. Ji, C. Zhang, L. Yan, Q. Luo, C. Wang, Q. Chen, J. Yang, L. Chen and C. Q. Ma, *ACS Nano*, 2018, **12**, 5518–5529.

34   C. Xu, M. Wright, N. K. Elumalai, M. A. Mahmud, D. Wang, V. R. Gonçales, M. B. Upama, F. Haque, J. J. Gooding and A. Uddin, *Applied Physics A: Materials Science and Processing*, 2018, **124**, 449.

35   J. Zhao, D. Song, B. Qiao, Z. Xu, D. Huang, M. Wang, X. Zhang, Y. Li, Y. Zhu and S. Zhao, *Organic Electronics*, 2018, **58**, 178–184.

36   M. Xiao, K. Zhang, Y. Jin, Q. Yin, W. Zhong, F. Huang and Y. Cao, *Nano Energy*, 2018, **48**, 53–62.

37   T. Umeyama, K. Igarashi, D. Sakamaki, S. Seki and H. Imahori, *Chemical Communications*, 2018, **54**, 405–408.

38   W. Li, J. Cai, F. Cai, Y. Yan, H. Yi, R. S. Gurney, D. Liu, A. Iraqi and T. Wang, *Nano Energy*, 2018, **44**, 155–163.

39   W. Li, Y. Yan, Y. Gong, J. Cai, F. Cai, R. S. Gurney, D. Liu, A. J. Pearson, D. G. Lidzey and T. Wang, *Advanced Functional Materials*, 2018, **28**, 1704212.

40   G. Ji, Y. Wang, Q. Luo, K. Han, M. Xie, L. Zhang, N. Wu, J. Lin, S. Xiao, Y. Q. Li, L. Q. Luo and C. Q. Ma, *ACS Applied Materials and Interfaces*, 2018, **10**, 943–954.

41   H. Cha, S. Wheeler, S. Holliday, S. D. Dimitrov, A. Wadsworth, H. H. Lee, D. Baran, I. McCulloch and J. R. Durrant, *Advanced Functional Materials*, 2018, **28**, 1704389.

42   G. Pirotte, S. Agarkar, B. Xu, J. Zhang, L. Lutsen, D. Vanderzande, H. Yan, P. Pollet, J. R. Reynolds, W. Maes and S. R. Marder, *Journal of Materials Chemistry A*, 2017, **5**, 18166–18175.

43   H. Cha, J. Wu, A. Wadsworth, J. Nagitta, S. Limbu, S. Pont, Z. Li, J. Searle, M. F. Wyatt, D. Baran, J. S. Kim, I. McCulloch and J. R. Durrant, *Advanced Materials*, , DOI:10.1002/adma.201701156.

44   J. Czolk, D. Landerer, M. Koppitz, D. Nass and A. Colsmann, *Advanced Materials Technologies*, 2016, **1**, 1600184.

45   Q. Sun, F. Zhang, Q. An, M. Zhang, X. Ma and J. Zhang, *ACS Applied Materials and Interfaces*, 2017, **9**, 8863–8871.

46   F. Zhao, Y. Li, Z. Wang, Y. Yang, Z. Wang, G. He, J. Zhang, L. Jiang, T. Wang, Z. Wei, W. Ma, B. Li, A. Xia, Y. Li and C. Wang, *Advanced Energy Materials*, 2017, **7**, 1602552.

47   Q. Sun, F. Zhang, Q. An, M. Zhang, J. Wang and J. Zhang, *Physical Chemistry Chemical Physics*, 2017, **19**, 709–716.

48   Z. Jiang, *Journal of Applied Crystallography*, 2015, **48**, 917–926.

49   J. C. Blakesley, F. A. Castro, W. Kylberg, G. F. A. Dibb, C. Arantes, R. Valaski, M. Cremona, J. Soo and J. Kim, *Organic Electronics*, 2014, **15**, 1263–1272.

50   M. Zhao, Y. Wang, Q. Ma, Y. Huang, X. Zhang, J. Ping, Z. Zhang, Q. Lu, Y. Yu, H. Xu, Y. Zhao and H. Zhang, *Advanced Materials*, 2015, **27**, 7372–7378.

Chapter 7

Conclusions

The use of metal-organic framework nanosheets (MONs) in the field of electronics has witnessed rapid progress in the recent years, enabling performance enhancement in various energy storage, light harvesting and emitting devices.[1–4] In this thesis, porphyrin-based paddlewheel MONs were evaluated as a new class of materials for use in OPV devices. Prior to the start of this work in 2017, there were no reports on the use of MONs in OPV devices. Porphyrin MONs were selected because of their high absorption and the propensity to form monolayer nanosheets.[5] Their nanoscopic dimensions and tunable band gaps meant that they could be engineered for use as ternary components in OPV devices. In this chapter, the scientific contribution of the chapters in this thesis and their relevance to the PV scientific community and MON research community are briefly summarized and discussed. A short outlook on future research directions and opportunities is provided in the end.

In **Chapter 4**, zinc-porphyrin based MONs were identified as potentially the first MON candidate to be evaluated for OPV applications.[4] Prior to this work, porphyrin based bulk metal-organic frameworks (MOFs) had been used in dye-sensitized solar cells with a PCE of <1%.[6] Although $Zn_2(ZnTCPP)$ had previously been shown to form MONs, we modified the procedure using our group's experience in ultrasonic exfoliation.[7–10] This method allowed us to produce predominantly monolayer nanosheets, thinner than those previously reported by other methods, although with smaller lateral dimensions. After structural and morphological investigations, these ultra-thin MONs were analysed for their optoelectronic properties and found to have band gaps ideally suited for enabling an energy cascade between P3HT and PCBM – the benchmark device in the field of OPVs. After optimisation, the MON incorporated ternary devices were found to outperform the reference P3HT-PCBM devices. GIWAXS, AFM, transient absorption, charge mobility and other optoelectronic investigations showed that the MONs acted as templates to enhance the crystallinity of P3HT in the device films. This resulted in other secondary effects – improved light absorption, enhanced hole mobility that indirectly contributed to more balanced charge mobility, well-defined smaller grain sizes and decreased recombination pathways. All these effects cumulatively contributed towards the near doubling of efficiency in the MON-based devices with the champion device demonstrating a

power conversion efficiency of 5.2% as compared to the 2.67% efficiency from the reference devices. The reference devices based on the bulk MOF and the porphyrin ligand molecule did not show the same enhancement in performance as the MONs, thereby highlighting the importance of the two-dimensional connectivity and nanoscopic dimensions of MONs for their application in OPV devices.

In **Chapter 5**, the advantage of the modular structure of MONs to fine tune the energy level alignment within the devices by using different combinations of metal ions and ligands was investigated. Cu_2(CuTCPP) MONs and Cu_2(ZnTPyP) MONs were compared with Zn_2(ZnTCPP) MONs in terms of their morphology, optoelectronic features, and influence on the device PCE of P3HT-PCBM OPVs. Most other 2D materials like Graphene and MoS_2 have thickness dependant bandgaps which are difficult to control.[11,12] In MONs however, the band gap arises from the chemical structure and the band gap is thus structurally tunable. With the use of photoemission techniques, the valence band, the hole injection barrier and ionization energies of the three MON systems were evaluated. A ternary bulk heterojunction energy level alignment model to systematically show the position of the energy levels of the three components in the active layer was also built. The choice of different metal ions was found to only have a small impact on the ionization energies of the MON and was not sufficient to explain the variations in device performances observed. The size of the nanosheets was found to play a significant role in influencing the device performance. Large sized nanosheets were detrimental to the PCEs because they reduce the interface between the donor P3HT and acceptor PCBM. This work demonstrates the importance of the ultrathin dimensions of the MONs and the potential of their modular structures in optimising the OPV device performance. In addition to these key findings about the role of MON morphology in enabling grain size control in OPV active layers, this work is also the first experimental evaluation of the band gap tunability of MONs.

In **Chapter 6**, the effect of adding the monolayer Zn_2(ZnTCPP) MONs to a series of different OPV polymers was investigated to further the understanding of the role of MONs and produce higher performing devices. In the case of amorphous polymers (PCDTBT, PBT7-Th) and fully crystalline polymers (PBDB-T), the only effect seen is the additional absorption contribution from the porphyrin units on MONs. This leads to slightly improved Jsc and FF with the PCE (%) improvements being less than 0.5. In contrast, devices based on semi-crystalline polymers showed significant enhancements in performance. As previously reported, P3HT-PCBM devices improved from 2.67% to 5.2% power conversion efficiencies with the

incorporation of MONs. In this work, P3HT-ICBA devices improved from 3% to 6% and PCE11-PCBM devices improved from 10.6% to 12.3%. The latter result in the best performing PCE11 device reported so far and also the best performing PCBM based OPV device to date. Based on the record efficiency obtained, we selected this system for detailed mechanistic investigations. GI-WAXS, AFM and charge mobility studies confirmed the creation of higher fraction of crystalline polymer in the films upon incorporation of MONs. Scherrer analysis showed the formation of longer well-ordered charge transport pathways. Consequently, an improvement was observed in the hole and electron mobilities and the grain size evaluations from the AFM images confirmed the formation of well-defined crystalline PCE-11 and the PCBM confined in its short-range order. Thus, MONs enabled the evolution of well-defined and highly crystalline nanoscale domains in the active layer. These findings confirm our hypotheses about MONs acting as templates for semi-crystalline polymers and aiding in improvement of their crystallinity and thereby the device performance.

Future work and outlook

Engineering the nanoscale composition and structure of the photoactive layer in OPVs is a crucial area of research to further enhance device performance efficiencies. The papers in this thesis contribute to this direction by establishing MONs as a novel class of materials that can impart additional light absorption and improved ordering of the polymer chains in the active layer. The research presented in Chapter 4 published earlier this year remains the first and only paper so far to investigate MONs in the active layer of an OPV device. The new opportunities opened up by the nanoscale dimensions in MONs allows incorporation within ternary blends for the first time, previously not possible with the bulk MOF systems. The optimised methods reported in this thesis will be valuable to others studying novel supramolecular materials, 2D materials, metal-organic materials or nanomaterials in OPV active layers and other organic electronic devices.

While extensive studies have been conducted on the effect of MONs on the morphology and energy level alignment within the ternary devices, a few avenues are yet to be explored. One such avenue is the effect of MONs on the long-term operational stability of these OPV devices. Complementary techniques to our AFM analysis such as small angle neutron scattering will be very useful to probe the bulk of the films and determine the overall change in morphology and grain sizes. Time-resolved photoluminescence measurements to probe the

changes in exciton diffusion length upon incorporation of MONs in OPVs is yet to be explored as well.

There is a wide scope for improving the optical, electronic and surface properties of MONs for the next generation of MONs for use in OPVs. While all the works in this thesis were limited to porphyrin -based MONs, the modularity of this class of materials opens the possibility to incorporate a wide range of well-absorbing ligands into the structure. Substituting the porphyrins for N-IR absorbing phthalocyanines is an ideal direction worth investigating. Phthalocyanine-based 2D MONs designed for energy storage applications have been shown to possess an intrinsic conductivity of 1.6 ± 0.2 cm^{2}V^{-1}s^{-1}.[13] This, along with their wider range of absorption wavelengths as compared to the porphyrin units, makes them ideal candidates for the next generation of MONs in OPVs.

Preliminary investigations of MONs in higher performing non-fullerene acceptors (ITIC) based devices showed device failures, and all the studies in this work were limited to fullerene-acceptor based systems. Understanding the cause of incompatibility between MONs and ITIC-based devices is another potential area worth investigating. Other novel acceptors like Y6 are interesting candidates to be explored as well.

MONs and other related materials such as COFs have been explored as interlayers for photovoltaic devices in the last couple of years. [14–16] These examples show promising results in improving the device efficiencies. While for ternary applications, we found that thinner, smaller lateral sizes of MONs were better to blend within the active-layer thin films, such considerations might not be needed for application as interlayers – thus offering greater flexibility in terms of MON size dimensions. The two-dimensional network could enable facile large area fabrication of the interlayers – ideal for pin-hole free extraction layer preparation. The surface functionalities of MONs can be tuned to aid for better adhesion of the subsequent layers, thereby providing simultaneous functions of carrier-extraction and morphology control. Conductive MONs based on thiolates, reported recently could be ideal candidates for this role.[17]

The key results from this work can also be used as a starting point to evaluate MONs in many related applications. The principles in this thesis can be applied to MON-based OFETs and OLEDs based on semi-crystalline polymers. The enhancement of charge mobility that is accompanied with the improved crystallinity imparted by MONs to these semi-crystalline polymers is expected to benefit the performance of OFETs and OLEDs as well. With the first

MON based perovskite solar cell reported this year, and with perovskites being closer to replacing commercial silicon technologies than OPVs, there lies another research direction for MONs in light harvesting.[16]

MONs possess a number of favourable properties that motivated this research such as their structural diversity, the higher surface area, being ultra-thin and physically flexible enough to stick closely to substrates, their ability to act as scaffolds and the band gap tunability. These features of MONs along with the utilization of their diverse chemical functionalities can usher in a new era of 2D materials for PV and other electronic applications.

References

1   C. Li, Q. Zhang, T. Li, B. He, P. Man, Z. Zhu, Z. Zhou, L. Wei, K. Zhang, G. Hong and Y. Yao, *Journal of Materials Chemistry A*, 2020, **8**, 3262–3269.

2   S. Liu, Y.-C. Wang, C.-M. Chang, T. Yasuda, N. Fukui, H. Maeda, P. Long, K. Nakazato, W.-B. Jian, W. Xie, K. Tsukagoshi and H. Nishihara, *Nanoscale*, 2020, 0–7.

3   M. Bonnema, F. Hossain, B. Nijssen and G. Holtgrieve, 2020, 0–25.

4   K. Sasitharan, D. G. Bossanyi, N. Vaenas, A. J. Parnell, J. Clark, A. Iraqi, D. G. Lidzey and J. A. Foster, *Journal of Materials Chemistry A*, 2020, **8**, 6067–6075.

5   D. J. Ashworth and J. A. Foster, *Journal of Materials Chemistry A*, 2018, **6**, 16292–16307.

6   B. C. Hawks, .

7   M. Zhao, Y. Wang, Q. Ma, Y. Huang, X. Zhang, J. Ping, Z. Zhang, Q. Lu, Y. Yu, H. Xu, Y. Zhao and H. Zhang, *Advanced Materials*, 2015, **27**, 7372–7378.

8   Y. Ding, Y. P. Chen, X. Zhang, L. Chen, Z. Dong, H. L. Jiang, H. Xu and H. C. Zhou, *Journal of the American Chemical Society*, 2017, **139**, 9136–9139.

9   M. Jian, H. Liu, T. Williams, J. Ma, H. Wang and X. Zhang, *Chemical Communications*, 2017, **53**, 13161–13164.

10   D. J. Ashworth, A. Cooper, M. Trueman, R. W. M. Al-Saedi, L. D. Smith, A. J. H. M. Meijer and J. A. Foster, *Chemistry - A European Journal*, 2018, **24**, 17986–17996.

11   M. Cox, A. Gorodetsky, B. Kim, K. S. Kim, Z. Jia, P. Kim, C. Nuckolls and I. Kymissis, *Applied Physics Letters*, 2011, **98**, 2–5.

12   M. Shanmugam, T. Bansal, C. A. Durcan and B. Yu, *Applied Physics Letters*, 2012, **100**, 1–5.

13   M. Wang, H. Shi, P. Zhang, Z. Liao, M. Wang, H. Zhong, F. Schwotzer, A. S. Nia, E. Zschech, S. Zhou, S. Kaskel, R. Dong and X. Feng, , DOI:10.1002/adfm.202002664.

14   W. Xing, P. Ye, J. Lu, X. Wu, Y. Chen, T. Zhu, A. Peng and H. Huang, *Journal of Power Sources*, 2018, **401**, 13–19.

15   M. G. Mohamed, C. C. Lee, A. F. M. EL-Mahdy, J. Lüder, M. H. Yu, Z. Li, Z. Zhu, C. C. Chueh and S. W. Kuo, *Journal of Materials Chemistry A*, 2020, **8**, 11448–11459.

16   S. Wu, Z. Li, M. Li, Y. Diao, F. Lin, T. Liu, J. Zhang, P. Tieu, W. Gao, F. Qi, X. Pan, Z. Xu, Z. Zhu and A. K. Jen, *Nature Nanotechnology*, , DOI:10.1038/s41565-020-0765-7.

17   Q. Zeng, L. Wang, Y. Huang, S.-L. Zheng, Y. He, J. He, W.-M. Liao, G. Xu, M. Zeller and Z. Xu, *Chemical communications (Cambridge, England)*, 2020, 2–5.